THE THERMAL RESPONSE OF BIOLOGICAL TISSUE SUBJECTED TO SHORT-PULSED IRRADIATIONS

by

KYUNGHAN KIM

A Dissertation submitted to the

Graduate School-New Brunswick

Rutgers, The State University of New Jersey

in partial fulfillment of the requirements

for the degree of

Doctor of Philosophy

Graduate Program in Mechanical and Aerospace Engineering

written under the direction of

Dr. Zhixiong Guo

and approved by

_____

_____

_____

_____

New Brunswick, New Jersey

[October, 2008]

ABSTRACT OF THE DISSERTATION

THE THERMAL RESPONSE OF BIOLOGICAL TISSUE SUBJECTED TO SHORT-PULSED IRRADIATIONS

By KYUNGHAN KIM

Dissertation Director:
Dr. Zhixiong Guo

A combined transient radiation and hyperbolic heat conduction model is developed to simulate heat transfer of biological tissue subjected to short pulsed irradiations. For modeling the ultrafast radiation heat transfer, the Transient Discrete Ordinate Method (TDOM) is developed in the two-dimensional axisymmetric cylindrical coordinates. The hyperbolic conduction model is solved by MacCormack's scheme with error terms correction. One combination model of radiation and heat conduction is that the radiation transfer is initiated by short pulse train irradiating until millisecond time scale and heat conduction transfer is followed. The temperature always increases by the radiation transfer and the heat is dissipated to the surrounding tissue by the hyperbolic heat conduction. The typical characteristic of the hyperbolic conduction is the thermal wave propagation rather than thermal diffusion with indefinite speed. It is found that the maximum local

temperatures are higher in the hyperbolic prediction than the parabolic prediction, which can be 7% higher in the modeled dermis tissue. After about 10 thermal relaxation times, thermal waves fade away and the predictions between the hyperbolic and parabolic models are closely consistent.

Other combination model is that radiation and conduction transfer always occurs together until a second time regime. The temperature prediction is compared with the experimental result provided by Dr. Kunal Mitra's group. Generally, the hyperbolic model combined with radiative heat transfer shows very similar result with the experimental data. It also shows high temperature increment near the laser deposition area compared with the parabolic model.

Own experimental study is conducted to evaluate the hyperbolic heat conduction phenomena. The fresh chicken tissue which is conserved the room temperature is suddenly contacted the ice block. Some of the results support the hyperbolic model by the temperature suddenly dropping rather that gradual temperature change.

The high absorbing tissue can enhance the radiation energy absorption and temperature increment is higher. The temperature increment is localized in the tissue surface region in the high scattering tissue. The focused laser beam played a role of temperature amplification around the focal region. The finer grid system is employed to catch up steep change of gradient of radiation energy absorption.

Acknowledgement

I would like to acknowledge and sincerely gratitude to my advisor Prof. Zhixiong Guo, for his support, guidance and mentorship through my study. Without consistent and patient advice from Prof. Guo, I could not fulfill Ph.D. degree. I would like to thank Prof. Yogesh Jaluria and Prof. Hao Lin for their invaluable advice and contributions. I would like to extend my thank to Prof. Kunar Mitra for providing experimental data and valuable suggestions on improving this dissertation.

The financial support as TA assistantship and Fellowship from the Mechanical Engineering department and research fund from Prof. Guo is great acknowledged.

I am thankful to my colleges, Haiyong Quan, Xiaoliang Wang, and JungBum Lee for enriching my life in Rutgers. I would like to thank Xiaoliang Wang for helping on experimental set up, and efforts for making our lab a better place to work.

I wish to thank my family, Wangsun Kim and Jungsoon Kim, for their endless support and mentorship over years and prayer to pursue my Ph.D. study.

Last but not least, I thank to my deepest appreciation and affection to my wife and best friend, Youjoung Her, for their continuous love, strong support, and prayer during my course of Ph.D study.

Dedication

To my wife and two daughters-Joanne and Claire

Table of Contents

List of Tables

List of Figures

List of Abbreviations

A	control surface
c	speed of light
c_t	speed of thermal wave
D	beam diameter of focused laser beam before focusing
E_{pulse}	energy per pulse
f	focal length
g	anisotropy factor
G	incident radiation
h^*	non-dimensional convective heat transfer coefficient
I	radiation intensity
N	number of angular direction (Chapter 2.3.1)
N	number of grid (except Chapter 2.3.1)
N_p	number of pulse of pulse train
n	reflective index
P_{ave}	average power of laser
q_0	amplitude of the pulse heat flux
$\mathbf{q}_{cond}$	conductive heat flux vector
$\mathbf{q}_{rad}$	radiative heat flux vector
Q_χ	non-dimensional variable of r directional conductive heat flux
Q_η	non-dimensional variable of z directional conductive heat flux

R	reflectance on the tissue surface
R	radial direction
R_i	radial grid size
r_f	beam width of focused beam in the focal plane
S	source term
T	temperature
t_p	laser pulse width
t_r	laser exposure time
V	control volume
w	angular weight
Z	axial direction
σ_a	absorption coefficient
σ_e	extinction coefficient
σ_s	scattering coefficient
ν_x, ν_y	Courant number
ν_i	beam width of focused beam inside of tissue
θ_{cr}	critical angle
θ_i	incident angle
χ	non-dimensional variable of r direction
ξ	non-dimensional variable of time
η	non-dimensional variable of z direction

τ thermal relaxation time

μ_1^l, μ_2^l, and μ_3^l directional cosine

α thermal diffusivity (Chapter 3)

θ non-dimensional variable of temperature

λ wavelength of the focused laser beam

ρ reflectivity

σ beam width of collimated beam

Φ scattering phase function

ω scattering albedo

Subscripts

b black body value

c collimated laser

d down stream

p control volume index

u upstream

w wall

Superscripts

d diffusive

l discrete direction index

s specular

Chapter 1

Introduction

1.1 The short-pulsed laser transport

Short-pulsed irradiation is accompanied with the use of pulsed lasers with pulse duration in the nano/picosecond time scale. Short-pulsed lasers can be used in a wide spectrum of emerging biomedical technologies such as in laser surgery and treatment [1-5], optical imaging and diagnostics [6-10], etc. The advantage of short pulsed laser is highlighted in laser ablation [11, 12], in which short pulsed laser has demonstrated the ability of ablating hard tissue like a tooth and middle ear tissue very effectively [13]. The short pulse laser is also applied to the spinal surgery [14] and to laser welding or soldering [15, 16]. The picosecond laser is proven to be efficient to remove tattoos in human tissue rather than nanosecond laser [17]. The short pulsed laser can be utilized in high-precision medical procedures like neurosurgery, ophthalmology, corneal surgery, and angioplasty since it provides the precise control of the output energy and able to control energy dissipation and the heat affected zone [18]. The optical imaging and diagnostics technology holds the possibility of providing information, both physiologically and morphologically, about interior of living tissue and organs minimizing any side effects [19, 20]. The major advantage is that the optical imaging

dose not use ionizing radiation unlike the X-rays, and that is has high spatial and temporal resolution unlike the magnetic resonance.

The concept of ultrafast radiation heat transfer [15, 21, 22] was introduced to differentiate the time-dependent radiation heat transfer associated with radiation propagation in the speed of light (i.e., the governing equation of radiation transfer is time-dependent) from the traditional transient radiation heat transfer in which the effect of time-dependent radiation propagation is negligible (i.e., the governing equation is still stationary) and only the boundary conditions are time-dependent. Ultrafast radiation heat transfer is significant when the pulsed irradiation time is not considerably longer than the characteristic radiation propagation time in the medium. In modern technological applications, it is often accompanied with the use of short-pulsed lasers. An excellent review by Kumar and Mitra [18] has summarized the applicability and techniques for solving one-dimensional (1-D) ultrafast radiation heat transfer problems. Guo and co-authors [15, 21-25] considered the modeling of 2-D and 3-D ultrafast radiation heat transfer and applications.

1.2 Thermal response incorporated with laser source

In application of laser tissue treatment such as laser welding, laser ablation, and laser phototherapy, the prediction of thermal response is of most critical interest. Laser welding of tissue is a surgical technique for bonding tissues, using a laser beam to activate photothermal bonds and/or photochemical bonds. Thermal energy is necessary to provide the activation force of photothermal bonds. Bass and Treat [26] reported that a proper temperature is 65°C in laser tissue welding to achieve optimum welding strength

in their review paper. Lobel *et al*. [27] recommend the surface temperature as 55°C to obtain good welding efficiency when CO_2 laser irradiated to the urinary bladder tissue. In laser tissue ablation procedure, Pierce [28] measured by the experimental method that the porcine tissue temperature is around 100 °C to achieve ablation effect. One example of phototherapy is the laser-assisted reshaping of cartilage technique. It is a surgical procedure designed to allow *in situ* treatment of deformities in the head and neck with less morbidity than traditional approach [29]. Diaz *el al*. [30] suggested that the mechanism responsible of laser reshaping is primarily associated with a phase transformation of cartilaginous bound water to free water taking place at a temperature of 65°C.

The understanding of heat transfer mechanism is then critical irradiating short pulse laser source. The heat transfer mechanism during laser irradiation is that the target tissue absorbs radiation energy which converts into heat. The irradiating targets begin to transfer this heat to their cooler surroundings mainly by thermal conduction, but this process takes some time and heat is initially confined to the targets during laser exposure [1]. At the end of an appropriately brief exposure, thermal conduction cools the targets and warms the surrounding tissue but the temperature should not reach to denaturing temperatures. The heated target tissue, with its specifically denatured or otherwise thermally damaged target, then slowly cools [1]. If the pulse width is shorter than the time it takes for the heat to dissipate into the surrounding tissue, most of the pulse energy causes photo thermal heating, avoiding destructive cumulative heating effects. In addition, pulsed output maximizes the peak power for a given average power. The purpose of short pulsed laser is to confine radiation energy to the heat-affected zone and to minimize

thermal damage induced by heat conduction to the surrounding tissue. Thus, the heat conduction process is also important in the prediction of accurate temperature response.

One review paper [31] compared several bio-heat transfer models for thermal prediction and concluded that the best practical approach for modeling of bio-heat transfer is the Pennes model as Eq. (1.1).

$$\rho C_p \frac{\partial T}{\partial t} = \nabla k \cdot (\nabla T) + Q_p + Q_s \tag{1.1}$$

Pennes [32] originally designed this equation to estimate the temperature distribution in the human forearm, but it has been extended many other applications [33, 34]. The storage of heat (LHS) is balanced by terms (RHS) describing conduction in tissue, convection between blood and tissue and heat generation. The second term of RHS in equation (1.1) is the so-called "perfusion term". This perfusion process is analogous to the process of mass transport between blood and tissue, which is confined primarily to the capillary bed of blood. It is noted that during short time laser irradiation perfusion loss is low and can be negligible [35]. The external heat source term Q_s corresponds to the heat generated by absorption of laser light and depends on the fluence rate and tissue absorption coefficient. Thus, the calculation of fluence rate and good modeling of bio-heat transfer problem can provide accurate temperature prediction. The experimental study for the measurement temperature with irradiation source was performed and numerical result was compared [36]. In the numerical part, the fluence rate is calculated by diffusion approximation to solve the light transport in turbid media and then the bio-heat transfer equation (1.1) was used to calculate the temperature profile. The results are shown in Figure 1.1. A CW laser with 2 W power was applied on a 2 mm spot to aorta tissue sample presented in Figure 1.1(a), while the samples in Figure 1.1(b) were

irradiated with 4 W on a 2.14 mm spot. The measured temperature rises were ~20 % lower than those predicted by the model at 65°C. Above this temperature range, the differences became more pronounced, especially in case of the sample irradiated with 2 W, which are heated more slowly. The deviation result can take place when fluence rate calculation or bio-heat transfer model is misled. Other deviation factor is water vaporization during laser irradiation of tissue surface. Torres *et al.* [36] corrected equation (1.1) by adding vaporization term and achieved more improving result. However, the deviation from experimental data still exists. The proper model to predict more accurately is still under development.

1.3 The hyperbolic heat conduction

The heat conduction term of Pennes' bio-heat transfer (1.1) is governed by the Fourier law. The traditional Fourier heat conduction is described by a parabolic diffusion equation which has an infinite speed of thermal propagation, indicating that a local change of temperature and/or heat generation causes an instantaneous perturbation in the temperature field. Thus, the diffusion equation has the unphysical property if a sudden change of temperature is made at some point on the body with extremely small amplitude at distant point. For a physical process occurring in a time interval shorter than that required for attaining thermal equilibrium, however, it has been noticed that heat wave theory [37-39] is more appropriate. The thermal wave postulate based on damped wave models leads to hyperbolic heat conduction equations and suggests a finite speed of thermal propagation.

Cattaneo [40] first expressed an explicit mathematical form of heat wave theory as,

$$\tau \frac{\partial \mathbf{q}}{\partial t} + \mathbf{q} = -k\nabla T \tag{1.2}$$

We shall call Eq. (1.2) Cattaneo's equation. When $\tau = 0$, Eq. (1.2) reduced to the Fourier's law. The thermal relaxation time, τ, in Eq. (1.2) is thought to be very small in nearly all practical and even exotic applications, so that as a practical it is believed that we get Fourier's law even on the shortest time scales of our daily lives. In fact, an understanding of time scales is the central object of scientific investigation of heat waves.

In 1980's, with the advent of ultrafast laser system, the hyperbolic heat conduction problem has been widely studied relating matter of short-pulsed laser metal heating. Qiu and Tien [40] validated hyperbolic conduction model comparing with experimental data with gold metal irradiating 96 *fs* pulsed laser. Though the thermal relaxation time of gold metal is extremely small as a 0.04 ps, high heat flux rate is incorporated together and the first term of LHS of Eq. (1.2) can not be negligible any more. Similarly, the thermal relaxation time of liquid has been known as $10^{-(9\sim11)}$ sec and it of metals is $10^{-(12\sim14)}$ sec [41].

However, the thermal relaxation time of nonhomogeneous material is suggested as quite large value, $10^{2\sim3}$ sec [41]. Also, Vedavarz et al. [38] examined the range of parameters over which this hyperbolic non-Fourier formulation is significant. They analyzed the thermal relaxation time for biological tissues and obtained a range of 1-100 sec at room temperature. Mitra et al. [39] experimentally measured the thermal relaxation time for processed bologna meat to be 15.5 ± 2.1 sec. Such large thermal

relaxation times reported for biological tissues make the thermal wave theory specifically significant in the thermal modeling of pulsed laser-tissue interactions.

The present study initiates with the belief that thermal relaxation time of live organ is large as mentioned early and can trigger hyperbolic conduction equation. Recently, Banerjee *et al.* [36] proved that hyperbolic model is closer to the experimental data rather than parabolic model with the 200 ps pulsed laser.

1.4 Objective of this study

The present dissertation is mainly focused to the numerical study. The experimental study is also conducted to validate hyperbolic heat conduction phenomena. The numerical result is compared with the experimental data which are provided by the Professor Kunar Mitra's group.

The present dissertation is composed of five parts. In the first part, the transient radiative transfer exposed to the short pulsed irradiation is studied. The formulation and numerical method is introduced. The tissue parametric study and laser beam characteristic study are then performed. In second part, transient heat transfer problem is studied. Both hyperbolic and parabolic heat conduction model are formulated and solved numerically. The solution is validated with existing analytical solution. In the third part, multi-time scale heat transfer problem with short pulsed laser is studied. By the limitation of short pulse laser exposure time until 1ms, the radiative heat transfer and conductive heat transfer is separated. In the fourth part, the experimental study is conducted to evaluate the hyperbolic conduction. The fresh chicken breast tissue is suddenly contacted

to the ice block. The temperature is monitored to investigate thermal wave propagation. In the fifth part, the numerical result is compared with the experimental data which is provided by the Professor Kunar Mitra's group. The short pulse laser is irradiated until order of 10 second regime. The radiative heat transfer and conductive heat transfer is combined to simulate this scenario. The aim of this chapter is to validate the hyperbolic heat conduction phenomena. The realistic tissue model is considered. The collimated and focused laser beams are compared.

1.5 The uniqueness of this study

To investigate the heat transfer in tissues with short-pulsed laser irradiation, the calculation of fluence rate and proper heat conduction model are critical. The fluence rate is calculated by solving the transient radiative transfer equation. The diffusion approximation which is simplified form of radiative transfer equation using scattering dominant medium is popularly used in the image reconstruction processes in optical tomography technique because it can be easily and fast simulated with even commercial software [50]. Furutsu and Yamada claimed that the diffusion coefficient is independent of absorption [50]. In early 1990's, Yoo *et al.* have shown that diffusion approximation fails to describe photon transport in optically thin and intermediate media even the media are scattering-dominated [73]. Thus, the radiative transfer model should be adopted the current study.

The numerical technique we developed is the Transient Discrete Ordinate Method (TDOM). Though this method has been developed for various geometric problems [21-25], the candidate extended it to the cylindrical medium for the first time. Another

common method for light transport problem is Monte Carlo method [8, 73, 74]. Generally the statistical Monte Carlo method is time consuming, and its results are subject to statistical errors.

Other important feature is to propose combined hyperbolic conduction model with radiation model, especially laser-tissue interaction problem. Though Banerjee *et al.* [75] considered numerical solution short-pulsed laser-tissue interaction problem, the fluence rate calculation depends on analytical function. Then applicable situation of analytical solution is restricted.

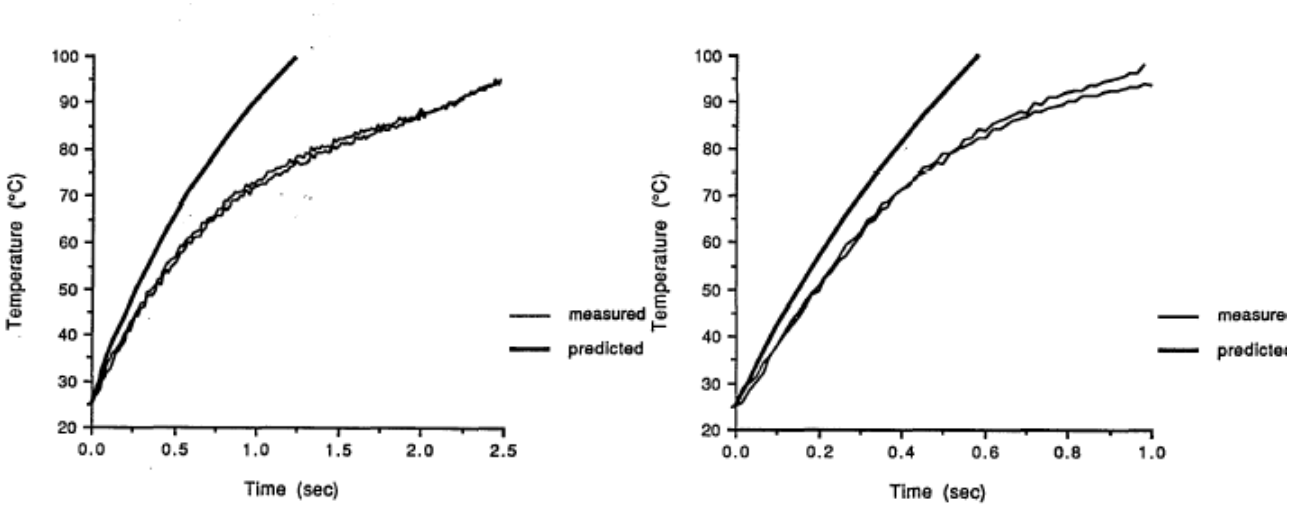

Figure 1.1 Comparison of temperature predicted by the Takata-Yoon model with those measured experimentally during irradiation of the aorta wall with (a) 2 W of laser power on a 2 mm spot and (b) 4 W on a 2.14 mm spot. [36]

Chapter 2

The transient radiative heat transfer exposed to short-pulsed irradiations

In this chapter, the transient radiative heat transfer with short-pulsed irradiation is modeled and solved by the numerical method. It is applied to the cylindrical geometric tissue. By employing various tissue optical properties, the radiation heat transfer is characterized. The several layered tissue model is also considered to simulate realistic tissue model. The laser pulse with picosecond regime is deposited to the cylindrical geometric tissue. Both collimated and focused laser beam are compared. To improve the numerical calculation efficiency, the nonuniform grid system is employed for the focused laser beam.

2.1 Mathematical models

2.1.1 The governing equation

The difference of short-pulsed radiative heat transfer from the traditional transient radiative heat transfer is that time-dependant radiative heat transfer is associated with radiation propagation in the speed of light. The traditional transient radiative heat transfer treats only boundary conditions and neglects the radiation propagation. However, the boundary is still stationary for the short-pulsed radiative heat transfer.

Solutions of short-pulse radiative heat transfer in 1D geometry have been reported in the literature [21, 43, 44]. Approaches that have extended to 2D geometries include the first order spherical harmonic (P_1) approximation [45], the discrete ordinate method [23], and the integral formulation [46]. However, the P_1 model underestimates the speed of light propagation [44] and the integral approach is difficult to apply to complex geometries. Guo and co authors solved the modeling of 2D and 3D short-pulse radiative heat transfer in Cartesian coordinate system [21-25]. In the present study, it is extended to the curvilinear coordinate system. Since the laser beam is Gaussian shape, the tissue geometry should be corresponds to the curvilinear coordinate system to predict accurate laser transport. Many research results have been developed using axisymmetric cylindrical coordinates system based on Monte Carlo (MC) simulation [47-49]. In MC simulations, the movements of photon packages within a medium are predicted via statistical analysis. Thus, there always exists statistical error. Whereas the DOM (Discrete Ordinate Method) is the deterministic approach, which can promise more accurate result [50]. The tissue shape is modeled with axisymmetric cylindrical medium and the Transient Discrete Ordinate Method (TDOM) is employed.

The pulses of a laser beam are incident into a tissue surface as shown in Figure 2.1. The pulsed laser radiation heat transfer can be formulated as a discretized form by the transient radiative transfer equation in the axisymmetric cylindrical coordinates system as Eq. (2.1):

$$\frac{1}{c}\frac{\partial I^l}{\partial t}+\frac{\mu_1^l}{r}\frac{\partial}{\partial r}[rI^l]-\frac{1}{r}\frac{\partial}{\partial \phi}[\mu_2^l I^l]+\mu_3^l\frac{\partial I^l}{\partial z}+\sigma_e I^l=\sigma_e S^l,\quad l=1,2,....,n, \qquad (2.1)$$

where c is the speed of light in the medium, μ_1^l, μ_2^l, and μ_3^l represent the directional cosines of a discrete ordinate direction and are expressed as:

$$\mu_1^l = \sin\theta\cos\phi, \quad \mu_2^l = \sin\theta\sin\phi, \quad \mu_3^l = \cos\theta \tag{2.2}$$

in which I^l is the directional radiation intensity, σ_e is the extinction coefficient that is the sum of the absorption coefficient, σ_a and the scattering coefficient, σ_s. The source term, S^l can be expressed as:

$$S^l = (1-\omega)I_b + \frac{\omega}{4\pi}\sum_{i=1}^{n} w^i \Phi(\hat{s}^i \to \hat{s}^l) I^i + \omega S_c^l, \; l = 1, 2, ..., n, \tag{2.3}$$

where scattering albedo $\omega = \sigma_s / \sigma_e$ is introduced. A quadrature set of n discrete ordinates with the appropriate angular weight w is used. The collimated laser source S_c^l in Eq. (2) is expressed by:

$$S_c^l = \frac{1}{4\pi} I_c \Phi(\hat{s}^c \to \hat{s}^l), \tag{2.4}$$

where the unit vector, $\hat{s}^c$, represents the laser incident direction. When the reduced scattering coefficient, $\sigma'_s = (1-g)\sigma_s$, is used, the unity scattering phase function, Φ, is considered and scattering coefficient switched to the reduced scattering coefficient.

In the present models the following assumptions are adopted:

(1) Tissue radiation emission is neglected because the tissue blackbody intensity is much smaller than the incident laser intensity.

(2) Tissue optical (absorption and scattering) property are thermally stable during the transient heat transfer process.

2.1.2 The incident laser profile

The characteristic of collimated laser beam profile is typically important in the present study. The short pulsed laser with t_p pulse duration has a Gaussian distribution both temporally and spatially. For normally incident irradiation, the beam intensity is specified as:

$$I_c(r,z,t) = (1-R)q_0 \exp\left\{-4\ln 2 \times [(t-z/c)/t_p - 1.5]^2\right\} \exp(-2r^2/\sigma^2) \exp(-\sigma_e z), \tag{2.5}$$

in which, R is the reflectance on the tissue surface, q_0 is the amplitude of the pulse heat flux, t_p is the pulse width, and σ is the beam radius varying with z which the peak intensity drops to the e^{-2} value. Here we consider pulse irradiation within $0 \le t \le 3t_p$.

If the focused laser beam is employed as a short pulsed laser source, the beam intensity can be specified as,

$$I_f(r,z,t) = (1-R)q_0 \exp\left\{-4\ln 2 \times [(t-z/c)/t_p - 1.5]^2\right\} \exp(-2r^2/{\nu_i}^2) \exp(-\sigma_e z) \times \frac{\int_0^{\nu_i} r \exp(-2r^2/\nu_i^2)dr}{\int_0^{r_f} r \exp(-2r^2/r_f^2)dr}, \tag{2.6}$$

where, ν_i is the beam radius at the certain axial location and it is also approximated that the maximum laser intensity drops to e^{-2} value. The r_f is the beam radius in the focal plane and it can be calculated as,

$$r_f = \frac{2}{\pi} \cdot \lambda \cdot \frac{f}{D}\ , \tag{2.7}$$

in which, λ is the wavelength of focused laser beam, f is the focal length, and D is the beam diameter before focusing. For example, λ= 514 nm, f = 400 mm, and D = 2mm, then the focused beam radius can be achieved as 0.065 mm. Last term of RHS is the laser beam energy compensation term, which provides the same amount of energy at the different axial location. The beam radius of the focused laser beam, ν_i can be specified by the geometric relationship as,

$$\nu_i = \left(-\frac{R_D - r_f}{R_D}\frac{Z_i}{f_D} + 1 \right), \qquad 0 \le Z_i \le f_D \tag{2.8 a}$$

$$\nu_i = \left(\frac{R_D - r_f}{R_D}\frac{Z_i}{f_D} - \frac{R_D - 2r_f}{R_D} \right), \qquad Z_i > f_D \tag{2.8 b}$$

The surface focused laser beam propagation is shown in Figure 2.2. The laser beam focused in the tissue medium and the propagation is shown in Figure 2.3. The treatment of focused laser beam for the numerical implementation is shown in Figure 2.4. In Figure 2.5, the laser propagation between collimated and focused beam is compared. For the collimated laser beam, the beam radius is always consistent as time advances. On the other hands, the beam radius changes in the tissue medium by incident angle and focal length. The high concentration of radiation energy then can be generated by the focused laser beam.

2.1.3 The absorbing radiation energy

Once the directional radiation intensity is calculated, the incident radiation (G) and the divergence of radiative heat flux ($\nabla \cdot \mathbf{q}_{rad}$) is calculated as:

$$G = \sum_{l=1}^{n} w^l I^l + I_c , \tag{2.9}$$

$$\nabla \cdot \mathbf{q}_{rad} = \sigma_a (4\pi I_b - G). \tag{2.10}$$

$\nabla \cdot \mathbf{q}_{rad}$ represents the absorbing radiation energy inside medium and black body emission I_b is neglected in present research by above mentioned general assumption.

2.1.4 The initial and boundary conditions

For the radiative heat transfer analysis, Snell's law and Fresnel's law [51] are adopted at the air-tissue interface because of the mismatch of refractive indices between the two media. For the normally incident laser radiation, the reflectance on the incident surface is

$$R = \left(\frac{n-1}{n+1} \right)^2, \tag{2.11}$$

where n is the refractive index of the tissue. For internal radiation at the tissue-air interface, total reflection occurs when the incident angle θ_i is not less than the critical angle, $\theta_{cr} = \sin^{-1}(1/n)$, because the refractive index of a biological tissue is greater than that of air. When $\theta_i < \theta_{cr}$, the reflection on the interface is purely specular and the reflectance is calculated by Fresnel's equation:

$$\rho^s = \frac{1}{2}\left[\frac{\tan^2(\theta_i - \theta_r)}{\tan^2(\theta_i + \theta_r)} + \frac{\sin^2(\theta_i - \theta_r)}{\sin^2(\theta_i + \theta_r)} \right], \tag{2.12}$$

where θ_r is the refraction angle predicted using Snell's law.

Since biologic tissues are generally highly scattering, photons reaching the other boundaries of the tissue cylinder have undergone multiple scattering events and the possibilities of photons passing through the boundary or reflecting back are almost equal.

Thus, we specify a diffuse reflectance (ρ^d) of 0.5 on such a kind of surfaces. The reflecting boundary conditions can be represented by [15, 25].

$$I_w^l = \rho^s I_w^{-l} + \frac{\rho^d}{\pi}\left[I_{cw} + \sum_{\hat{n}\cdot\hat{s}^j<0} w^j I_w^j \left|\hat{n}\cdot\hat{s}^j\right| \right]. \tag{2.13}$$

2.2 Properties of tissue

2.2.1 Optical properties of tissue

In order to discuss light transport in tissue medium, the knowledge of optical properties should be preceding. The optical properties can be changed by the laser wavelength. In past years, a host of investigators have reported value of the optical properties, but there exists a quite large variation in these reasons [52]:

(1) Model assumption (e.g., isotropic-anisotropic scattering or matched-mismatched boundaries)

(2) Measuring technique

(3) Experimental apparatus

(4) Calibration scheme

(5) Biological heterogeneities existence

Regardless of these problems, there is need to consolidate what has been measured, and the main trust of this literature survey is to present a summary of reported optical properties measurements.

Generally, the scattering of light by the organic tissue is much stronger than absorption in the specific wavelength (near infra red range), which is safe range of wavelength for human tissue. The optical properties have been studied by the literature

survey and are summarized in Figure 2.6 and Table 2.1. By the map of the optical properties, the most data set are congregated in the range of $0 < \sigma_a < 0.4\,mm^{-1}$ and $0 < \sigma_s^{'} < 4\,mm^{-1}$. It shows the reduced scattering coefficient is order of 10 times of absorption coefficient. In this chapter, mainly dermis tissue is demonstrated, but aorta tissue, heart tissue, and uterus tissue are compared.

2.3 Numerical schemes

2.3.1 Transient Discrete Ordinate Method (TDOM)

To solve the transient radiative transfer equation for cylindrical enclosure, the Transient Discrete Ordinate Method (TDOM) is employed. The discretized equation (2.1) in axisymmetric cylindrical geometry is complicated by the presence of the angular derivative term. The means of the axisymmetric cylinder is the system not depending on the angle of ψ as shown in Figure 2.1. Thus, we only interest one plane in the cylinder medium. All sliced medium in the cylinder will be identical. However, the axisymmetric system is different with 2-D planar medium since the angular directional intensity exists, radial and z-axial directional intensity as well. Carlson and Lathrop [53, 76] proposed a direct-differencing technique for calculating the angular derivatives at the quadrature points. Using this technique, the third term on the LHS of Eq. (2.1) can be rewritten as:

$$\frac{1}{r}\frac{\partial}{\partial \phi}[\mu_2^l I^l] = \frac{1}{r}[\alpha_{l+1/2} I^{l+1/2} - \alpha_{l-1/2} I^{l-1/2}]/w^l \tag{2.12}$$

where, the direction $l \pm 1/2$ defines the edges of the angular range of w^l, the two terms representing, respectively, the flow out of and into the angular range. A direct relationship between α_l and w^l can be drawn on the following relationship:

$$\alpha_{l+1/2} - \alpha_{l-1/2} = w^l \mu_1^l, \tag{2.14a}$$

$$\alpha_{1/2} = \alpha_{N+1/2} = 0\,,\ l = 1,2,3,\ldots,N\,. \tag{2.14b}$$

Then, the discretized form of equation (2.1) at one control volume cell is:

$$\frac{V}{c\Delta t}(I_p^l - I_p^{l0}) + \left|\mu_1^l\right|(A_{rd} I_{rd}^l - A_{ru} I_{ru}^l) - (A_{rd} - A_{rd})[(\alpha_{l+1/2} I_{p+1/2}^l - \alpha_{l+1/2} I_{p+1/2}^l)/w^l] + \left|\mu_3^l\right|(B_{zd} I_{zd}^l - A_{zu} I_{zu}^l) = \sigma_{ep} V(-I_p^l + S_p^l) \tag{2.15}$$

where, the subscripts *d*, *u*, and *p* stand for downstream, upstream, and the cell center, respectively. The diamond scheme is used to relating the up- and down- stream intensities in a control volume cell. The control volume is shown in Figure 2.7

The accuracy of the DOM solutions depends on the choice of the quadrature scheme. Although this choice is, in principle, arbitrary, a completely symmetric quadrature is preferred in order to preserve geometric invariance of the solution. In the present calculations, the S_{10} scheme is adopted for the angular direction discretization, where 120 angular directional intensities exist. Discrete ordinates of one quadrature for the S_{10} scheme are introduced in Table 2.2.

The final discretization equation for the cell intensity in a generalized form is:

$$I_p^l = \frac{\frac{1}{c\Delta t} I_p^{l0} + \sigma_{ep} S_p^l + \frac{A}{V}\left|\mu_1^l\right| I_{ru}^l + \frac{\left|\beta_p\right|}{V} I_{p-1/2}^l + \frac{B}{V}\left|\mu_3^l\right| I_{zu}^l}{\frac{1}{c\Delta t} + \sigma_{ep} + \frac{A}{V}\left|\mu_1^l\right| + \frac{\left|\beta_p\right|}{V} + \frac{B}{V}\left|\mu_3^l\right|} \tag{2.16}$$

Where;

$$A = A_{ru} + A_{rd} = 2\, r_p \Delta\phi\, \Delta z \tag{2.17a}$$

$$\beta_p = (A_{ru} - A_{rd})(\alpha_{l+1/2} + \alpha_{l-1/2})/w^l \tag{2.17b}$$

$$B = B_{ru} + B_{rd} = 2\, r_p \Delta r\, \Delta z \tag{2.17c}$$

$$V = r_p \Delta r \, \Delta\phi \, \Delta z \tag{2.17d}$$

2.3.2 The grid system

The grid is dived by 200 grids both radial and axial direction evenly in uniform grid system. The fine grid system is required to implement to the focused laser beam simulation. However, the accuracy and calculation time is always compromising problem. Thus, nonuniform grid systems are also employed, which grid systems supplies fine grid near laser deposition area and coarse grid other regions like as,

$$R_{i+1} = R_i + \Delta R \tag{2.17a}$$

$$\Delta R_i = \alpha_r \left(\beta_r - \exp(-\frac{\gamma_r \, i}{N}) \right) \tag{2.17b}$$

(Nonuniform grid system I) $\alpha_r = 0.0328$, $\beta_r = 2$, $\gamma_r = 10$, N=201

(Nonuniform grid system II) $\alpha_r = 0.0427$, $\beta_r = 1.5$, $\gamma_r = 25$, N=201

The nonuniform grid systems are plotted in Figure 2.8. The finer grid is employed to the laser deposition area, where the radiation energy is concentrated. By the implementation of nonuniform grid system, the calculation accuracy can be enhanced without severe drawback of calculation time and computer memory occupation. The change of grid size is shown in Figure 2.9 with various grid systems.

2.4 Results and discussion

Initially, the grid size influence is investigated in Figure 2.10. In the dermis tissue, the profiles of divergence of radiative heat flux along the optical axis are compared in the various grid size systems. The 100 grid system shows deviating result all time instants

but over 200 grid systems show similar tendency. The selection of 200 grid system is the reasonable choice considering both accuracy and calculation time. Thus, the 200 grid system is employed to calculate from now on.

In Figure 2.11, the contours of divergence of radiative heat flux are shown at certain time instant. As time advances, the radiation field propagates from the incident laser spot to the most inside tissue medium. At early time stage ($t > 100$ ps), the wave propagation by the radiation transfer is very obvious. Such a phenomenon could not be visualized if the time derivate term in the radiative transfer equation was neglected, nor could it be correctly predicted if a diffusion approximation that is commonly adopted in biomedical engineering field. A diffusion field clearly exists at $t = 500$ ps, when the influence of incident laser becomes weak and the magnitude of the radiation energy absorption becomes very small.

Figure 2.12 shows the temporal profiles of the divergence of radiative heat flux at different axial locations along the optical axis. The divergence of radiative heat flux represents the absorbed or deposited volumetric laser energy in the medium. At any locations, the absorbed radiation energy is found to increase rapidly to the maximum value with the input of a short pulse and then to decrease exponentially. Initially there is a very intense energy deposition at the location at the tissue surface. For $t > 40$ ps, the radiation energy deposition is even lower in the proximity of the laser incident spot that at other axial locations because the irradiation of incident pulse ends at 40 ps. This is different from continuous wave (CW) laser irradiation, in which the radiation energy deposition in the proximity of the incident spot is always the strongest. This unique feature of the proposed the short pulse laser transfer in tissue medium is of great

significance because it suggests that overheating to the certain tissue surface owing to larger energy deposition in the proximity of the laser spot can be avoided. The peak magnitude of absorption radiation energy becomes down in the deeper tissue medium and the time to reach of it also delays due to the flight time of the laser pulse.

In Figure 2.13, the accumulated divergence of radiative heat flux is shown. It represents the time integration of divergence of radiative heat flux until certain time. As long as heat transfer concepts, the accumulated divergence of radiative heat flux plays a role of the source term to increase temperature. During short time period-radiation transfer dominant period, the heat transfer by the thermal diffusion or thermal wave propagation is negligible and the absorption of radiation energy is accumulated without any thermal dissipation. The graphs shows the spatial variance of it along the dermis tissue optical axis at time instant of 500 ps, where the calculated results are compared with the simple Lambert-Beer's analyses. When scattering is neglected, the numerical result for the fully absorbing medium matches excellently with the Lambert-Beer's analysis. Since scattering in the dermis tissue is strong, the analytical result from simple Lambert-Beer's law does not match with the simulation. For absorbing-scattering tissues, therefore, Lambert-Beer's law may not be a good approximation. Instead accurate radiation transfer modeling is desirable.

In Figure 2.14, the contours of accumulated divergence of radiative heat flux are depicted. The distribution change of it is trivial as time proceeding and magnitude of it also is stationary, which means that the radiation energy absorption accumulated mainly during short time period (t = 100 ps). The radiation energy accumulation is mostly

confined to the laser deposition region. The distribution depends on the optical properties of tissue and laser characteristics such as beam radius, beam shape, and so on.

The parametric study of optical properties is conducted. In Figure 2.15, the contours of divergence of heat flux at certain time instant are shown with various scattering coefficient and $\sigma_a = 0.2\,mm^{-1}$. It is clearly observed that the low scattering medium penetrates inside medium deeply. As the scattering characteristics increases, the radiation energy is confined to near the surface medium. As time advances, the radiation field propagates inside medium. The speed of propagation is slow in high scattering medium. But magnitude of the absorbed energy is strong in high scattering medium.

In Figure 2.16, the contours of accumulated divergence of radiative heat flux at t = 400 ps, which time instant the radiation transfer is almost finished, with various scattering medium are plotted. Due to the low scattering influence, the radiation energy absorption is accumulated deeper inside medium. For the high scattering medium, the radiation energy absorption is concentrated near the surface medium. This can be explained with the optical penetration concepts. The extinction coefficient, which is summation of scattering and absorption coefficient, is inversely proportional to the optical penetration depth. It means that the higher extinction medium shows the short optical penetration depth.

In summarizing, the radiation absorption is limited in the tissue surface region with high absorbing radiation energy in high scattering medium.

To show this tendency clearly, the profiles of it along the optical axis is plotted in Figure 2.17. The profile of high scattering medium shows the steep gradient and strong radiation absorption exists in the surface area. It may cause the higher temperature mainly

around tissue surface region increment during laser irradiation. The scattering characteristic plays the important role of the radiation energy absorption if the absorption coefficient is relatively low.

In Figures 2.18 and 2.19, the influence of absorption coefficient is investigated with the fixed scattering coefficient, $\sigma_s' = 2\,mm^{-1}$. The difference of the divergence of radiative heat flux at certain time stage with the various absorption properties is not obvious. It is due that the variation of absorption coefficient is not sufficiently broaden and scattering event is still influential factor. More importantly, the maximum magnitude of accumulated divergence of radiative heat flux change rapidly as absorption coefficient increases. Still less optical penetration depth is observed in the high absorption medium.

The accumulated profiles of radiative heat flux along the optical axis are plotted in Figure 2.20. The absorption coefficient plays a role to increase radiation energy absorption near the surface region rather than optical penetration depth. It may cause high temperature increment during laser irradiation in the high absorption medium.

So far we investigated the optical properties are critical factors to determine radiation energy absorption. Sometimes, the radiation energy absorption is not sufficient in the low absorption medium to increase proper temperature level. Thus, the focused beam simulation is conducted to amplify radiation energy absorption. The focused laser beam can target specific area in the tissue medium and enhance the radiation energy concentration. In the Figure 2.21, the tissue geometric model is sketched. The tissue absorption coefficient is selectively low value as $\sigma_a = 0.015\,mm^{-1}$ and scattering coefficient is $\sigma_s' = 2\,mm^{-1}$. The collimated laser beam with 1mm radius and focused laser beam to the surface are compared.

For the focused laser beam simulation, the fine grid system is required to catch up the sudden gradient change of radiation energy absorption around focal region. However, the decreasing of grid size causes the calculation cost. Thus, the fine grid is employed around laser deposition area and coarse grid is employed other region. Keeping the same number of grid, the efficient calculation can be possible with the non uniform grid systems. Before using these grid systems, the validation procedure is performed in Figure 2.22. Due to the limitation of the analytical solution, the comparison among the various grid systems is conducted with the fully absorbing medium using the collimated laser beam. There exists perfect matching to the analytical solution with three grid systems.

With the scattering medium, the same comparison is performed in the Figure 2.23. In this case, the analytical solution does not exist and then only comparison among the grid systems is possible. Between two non uniform grid systems, the difference of profiles is trivial both radial and axial directions. The profiles with the non uniform grid systems shows more steep gradient and highly predicted at the tissue surface area compared with those of uniform grid system. However, the difference is not critical using collimated laser beam.

In Figure 2.24, the focused laser beam result is plotted. The higher magnitude of profile is predicted near the tissue surface with the non uniform grid systems. The steep gradient of profiles is also found out. The employing fine grid near the focal region may be helpful and the nonuniform grid system will be used to simulate the focused laser beam from now on.

The collimated laser and focused laser are compared with the divergence of radiative flux in Figure 2.25. The distribution difference is obvious in short time regime

at t = 20 ps and t = 40 ps. The radiation energy absorption is stronger and confined near the focal region using focused laser. This radiation absorption enhancement at specific region is beneficial factor using focused laser beam. As time passing, the diffusion process is dominant and the distribution becomes similar between two laser beam results.

In Figure 2.26, the accumulated divergence of radiative heat flux depicted at certain instants. For the focused laser beam, the absorption of radiation energy is accumulated to the surface region with a narrow width. The distribution of it using collimated laser is widely spread into the tissue inside both radial and axial directions. Again, the advantage of focused laser is to localize of absorbing radiation energy and amplify the radiation energy absorption.

Two laser beam systems are compared with axial profiles in Figure 2.27 with the accumulated divergence of radiative heat flux profile. Clearly, the higher and sharp gradient profile is observed in case of focused laser beam in the surface area. The maximum value of it is over five times of it for the collimated laser. Inside of the tissue medium, the difference of profiles becomes small.

In reality, the tissue is composed of multi layered medium and there exist many inhomogeneities such as blood vessels. Thus, more complicated and close to the real tissue model is introduced in Figure 2.28. The tissue is composed of three layered tissues, which are epidermis, dermis, and fatty tissue. The inhomogeneity medium is embedded with the high scattering coefficient. The optical properties of tissue are summarized in table 2.3. The epidermis tissue occupied very thin layer and shows the high absorbing characteristics. The beam is focused to the inhomogeneity location, where is located 2 mm below the tissue surface. The purpose of this simulation is to amplify radiation

energy absorption around inhomogeneity region. Both collimated and focused laser beam are simulated and compared.

In Figure 2.29, the 1 mm radius collimated laser beam is deposited. The divergence of radiative heat flux field is investigated as time proceeding. In early time stage, $\nabla \cdot q$ is concentrated around the laser deposition area and shows the high magnitude. As time advancing, the divergence of radiative heat flux field broadens inside of tissue medium and the quantity decreases due to the attenuation of light. At t = 80 ps, the discontinuity of divergence of radiative heat flux field along the Z = 2 mm line is absorbed since the inhomogeneity medium embedded. Similar discontinuity of field exists at t = 200 and 400 ps. Importantly, the strong absorption of radiation energy is found out in thin epidermis region, which means the most part of light is absorbed by epidermis region and hard to penetrate to the deep inside tissue medium.

The profiles of divergence of radiative heat flux along the optical axis are depicted in Figure 2.30 at sequential manner. The magnitude of profiles decreases as time marching and the field of divergence of radiative heat flux propagates deeply in the axial direction. High radiation energy absorption around tissue surface region is observed. At t = 200 ps, the axial profile shows almost flat shape.

In Figure 2.31, the accumulated divergence of radiative heat flux is depicted. As far as the distribution of it, there is no obvious difference at any time instants. It means that the absorption of radiation energy almost stored even until t = 40 ps. Critical region of it is the surface epidermis region that the radiation energy is mainly absorbed. Some distortion of profiles are shown along the Z = 2 mm due to the inhomogeneity medium. So far, we have studied with collimated laser beam source. The absorption of radiation

energy is weak inside tissue due to the higher absorbing epidermis tissue. It may not enough for laser treatment deep inside location. Thus, the laser beam is focused into specific region of inside tissue, the inhomogeneity medium.

The sequential development of divergence of radiative heat flux is shown in Figure 2.32. At t = 20 ps, the motion of focusing is well depicted and the higher energy absorption is found in the focal region. The absorption of radiation energy broadens around focal region at t = 40 ps. At longer time instant, i.e. from 80 ps, the radiation transport becomes diffused. The shape of distribution is quite similar with collimated laser beam result and the discontinuity of distribution in inhomogeneity region is observable at t = 200 ps and 400 ps.

The contours of accumulated divergence of radiative heat flux are depicted in Figure 2.33. At t = 20 ps, the focused laser beam propagation is well motioned and the converging angle of focused laser beam is 22.5º. The radiation energy is absorbed mostly in the focal region and surface region. As time advancing, the radiation energy absorption is accelerates to the focal region. Also, the diffusion phenomenon is dominant at the longer time instant.

The profiles of divergence of radiative heat flux along the optical axis are shown in Figure 2.34 (a). At early time instant, higher magnitude is predicted in the focal region, which is different aspect with collimated laser. As time marching, the profiles become flatter and show the small magnitude. Figure 2.35 (b) shows that the radiation energy absorption is mostly confined to the focal region. At t = 80 ps, the profile becomes stationary, which means radiation energy absorption finishes at that time instant. Of

course, the second peak of the profile is in the epidermis region due to the high absorbing characteristics.

The temporal profiles of divergence of radiative heat flux are compared between collimated laser beam and focused one in the Figure 2.36. For the collimated laser beam, the peak magnitude decreases deeper axial locations and higher value is predicted at the Z = 0. However, the higher value of profiles is predicted in the focal region for the collimated laser beam. It may be helpful to increase temperature rising at inhomogeneity region. The unique feature is observed at Z = 0 and Z = 1 mm locations for the focused laser beam. Different with collimated beam profiles, there exists second peak at the location of Z = 0 and Z = 1mm. The profiles decay exponentially after laser pulse passing certain location. The divergence of radiative flux field in focus region acts like a source term and it contribute the second peak at the location in front of focus region. More importantly, the absorption of radiation energy is strong at the focal point.

In Figure 2.37, the grid systems are compared. For the non uniform grid system, the profiles shows steep gradient, especially fine grid region. Thus, the nonuniform grid system is suitable for the implementation of focused laser beam.

2.5 Summary

The transient radiative transfer was studied when the 10 ps pulse laser deposited. The solution technique is the TDOM and the proper grid size is validated by the grid system test. The divergence of radiative heat flux field propagated from the tissue surface to inside medium. For the dermis tissue, it showed the stationary behavior at t = 500 ps and the divergence of radiative heat flux was accumulated mostly tissue surface area.

The optical properties are the main influential factor to determine the distribution of the accumulated of divergence of radiative heat flux. For the high scattering medium, the radiation energy absorption was limited to the tissue surface region and strong magnitude was predicted in this region. The absorption characteristics affected to the magnitude of the accumulation of radiation absorption energy rather than optical penetration since the tissue normally has high scattering event.

For the low absorbing tissue medium, the radiation energy absorption was restricted and focused laser beam was considered. To simulate the focused laser beam, fine grid system around the laser deposition area is employed. It was helpful to catch up steep change of gradient of radiation energy absorption. Strong radiation energy absorption was predicted in the focal region compared with collimated laser beam.

Realistic tissue model, which composed of three layered tissues and inhomogeneity tissue, was considered. For the collimated laser beam, the high radiation energy absorption was observed in the tissue surface region, epidermis tissue due to the high absorption tissue. For the focused laser beam, the maximum radiation energy absorption was predicted in the focal region, inhomogeneity tissue. The advantage of the focused laser beam is to amplify the radiation energy absorption at selective location.

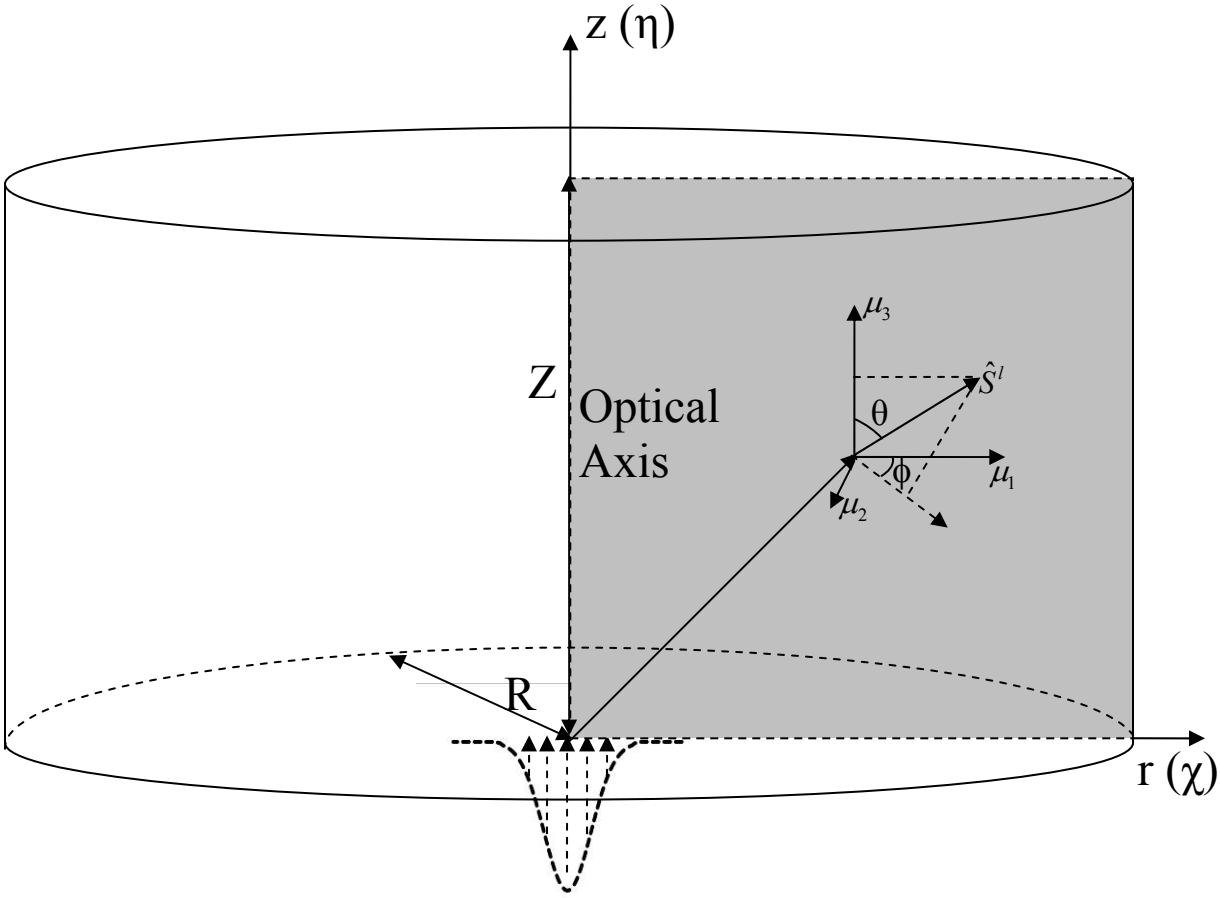

Figure 2.1 The sketch of tissue geometric and short pulse laser deposition

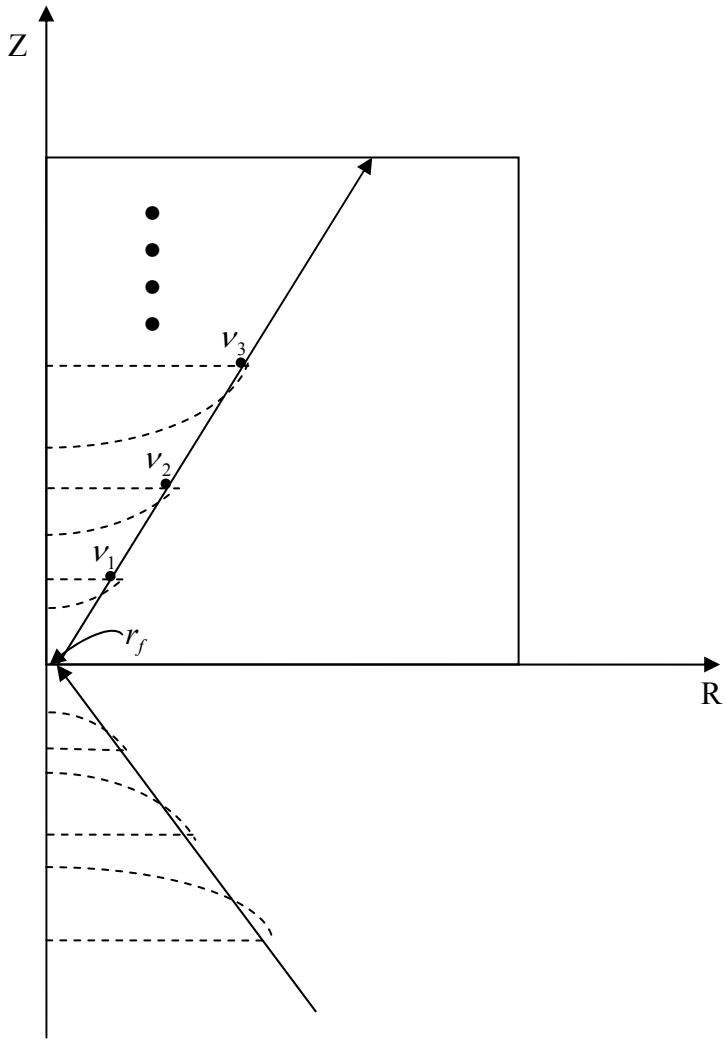

Figure 2.2 The implementation of propagation of surface focused laser beam

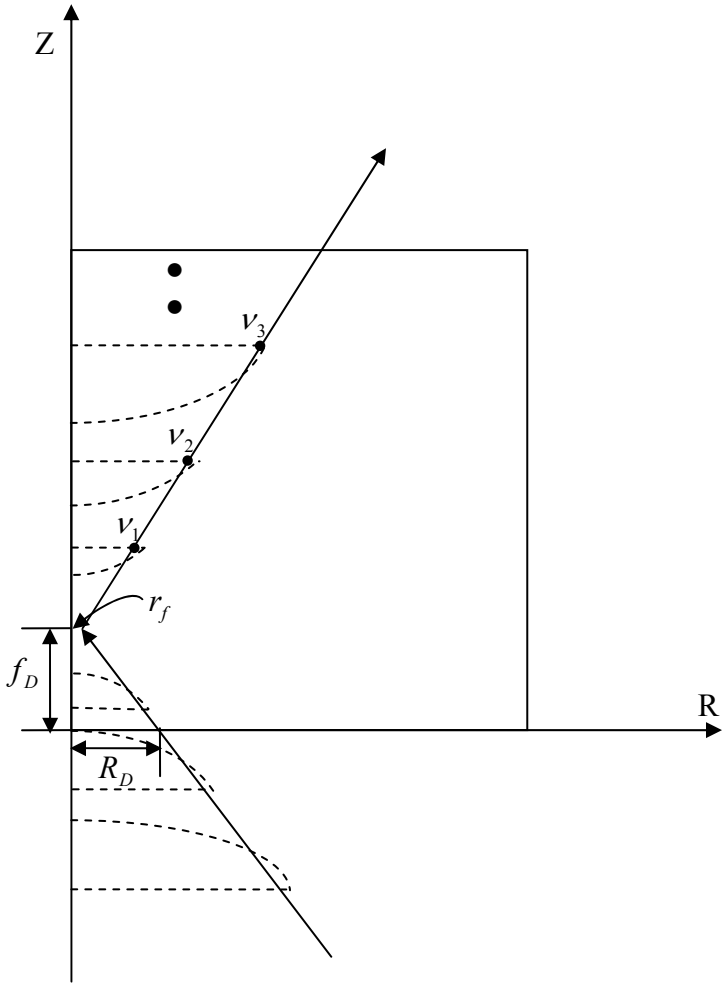

Figure 2.3 The implementation of propagation of focused laser beam into tissue medium

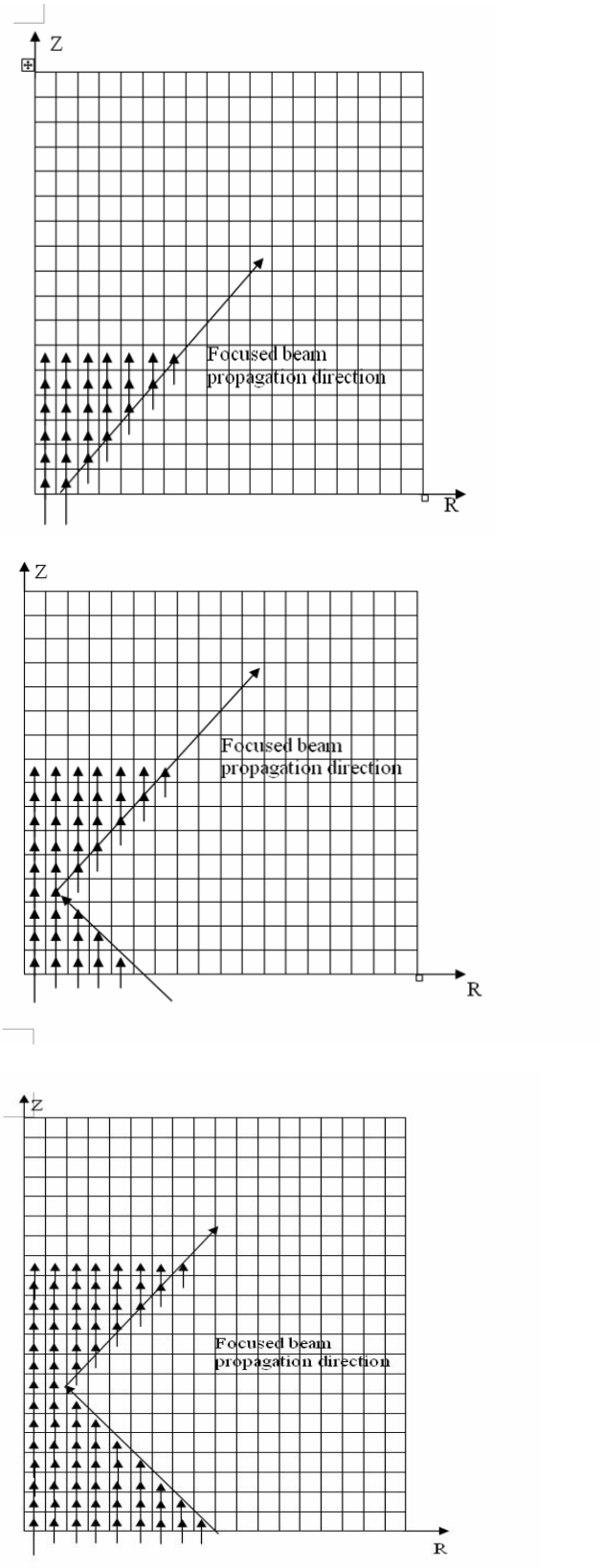

Figure 2.4 The focused laser beam treatment

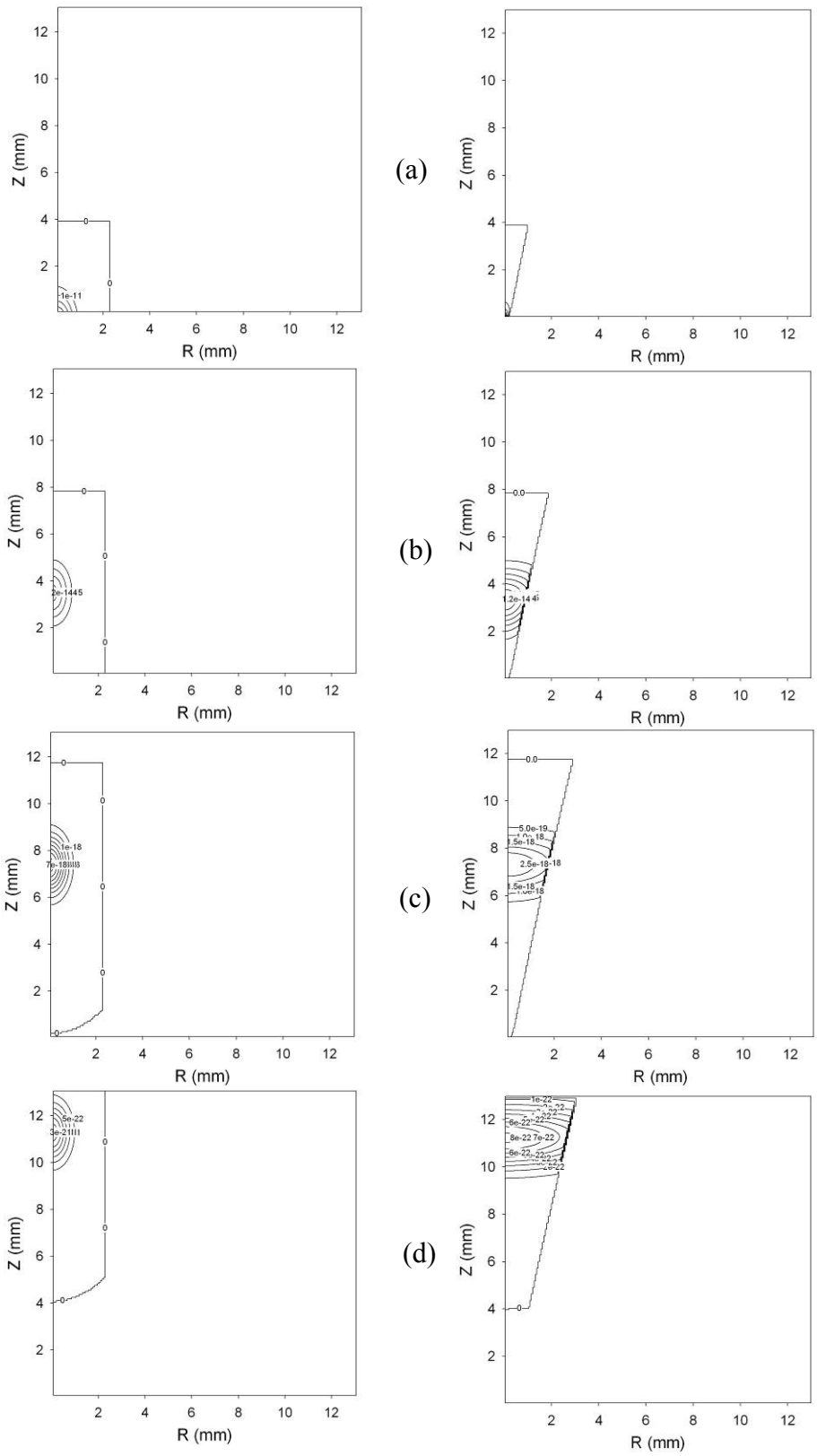

Figure 2.5 The comparison of laser beam propagation between collimated laser and focused laser at certain time instant: (a) t = 20 ps, (b) t = 40 ps, (c) t = 60 ps, and (d) t = 80ps.

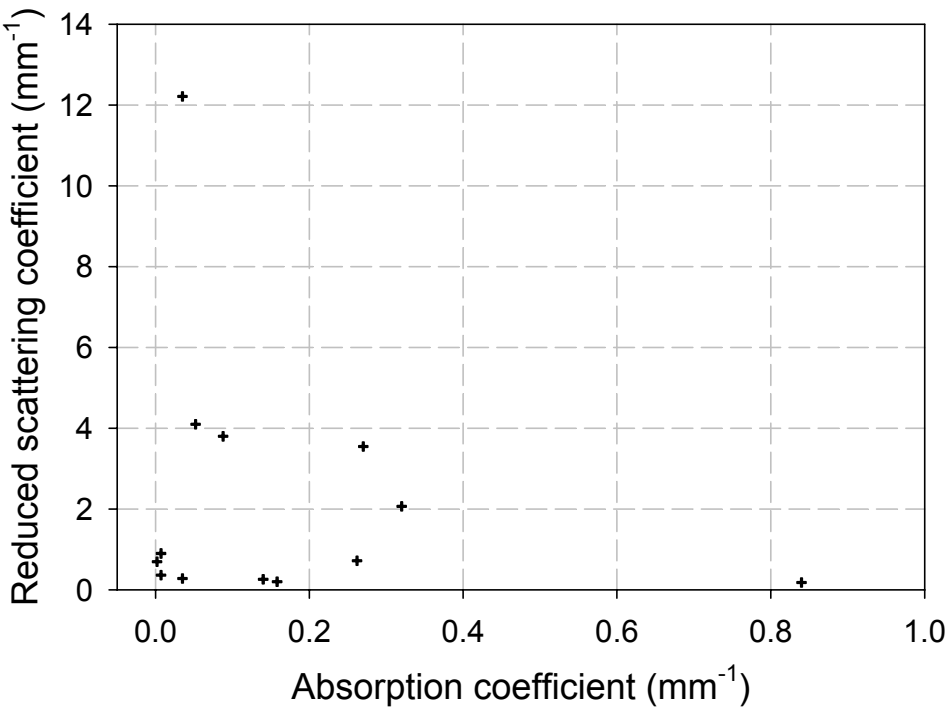

Figure 2.6 The optical property map of various tissues

TISSUE TYPE	WAVELENGTH (NM)	ABSORPTION (mm^{-1})	REDUCED SCATTERING (mm^{-1})	CITATION
HUMAN DERMIS	633	0.27	3.55	[52]
HUMAN AORTA	632.8	0.052	4.1	[52]
HEART (ENDOCARDIUM)	1060	0.007	0.367	[52]
HEAT (EPICARDIUM)	1060	0.035	0.284	[52]
HUMAN LIVER	630	0.32	2.07	[52]
COAGULATED LIVER	830	0.088	3.8	[83]
BRAIN (WHITE MATTER)	633	0.158	0.204	[52]
BRAIN (GRAY MATTER)	633	0.263	0.722	[52]
HUMAN BLADDER	633	0.14	0.264	[52]
HUMAN LUNG	630	0.84	0.18	[52]
HUMAN UTERUS	635	0.035	12.214	[52]
BREAST (NORMAL)	810	0.002	0.7	[84]
BREAST (TUMOR)	810	0.007	0.9	[84]

Table 2.1 The optical properties of various tissue

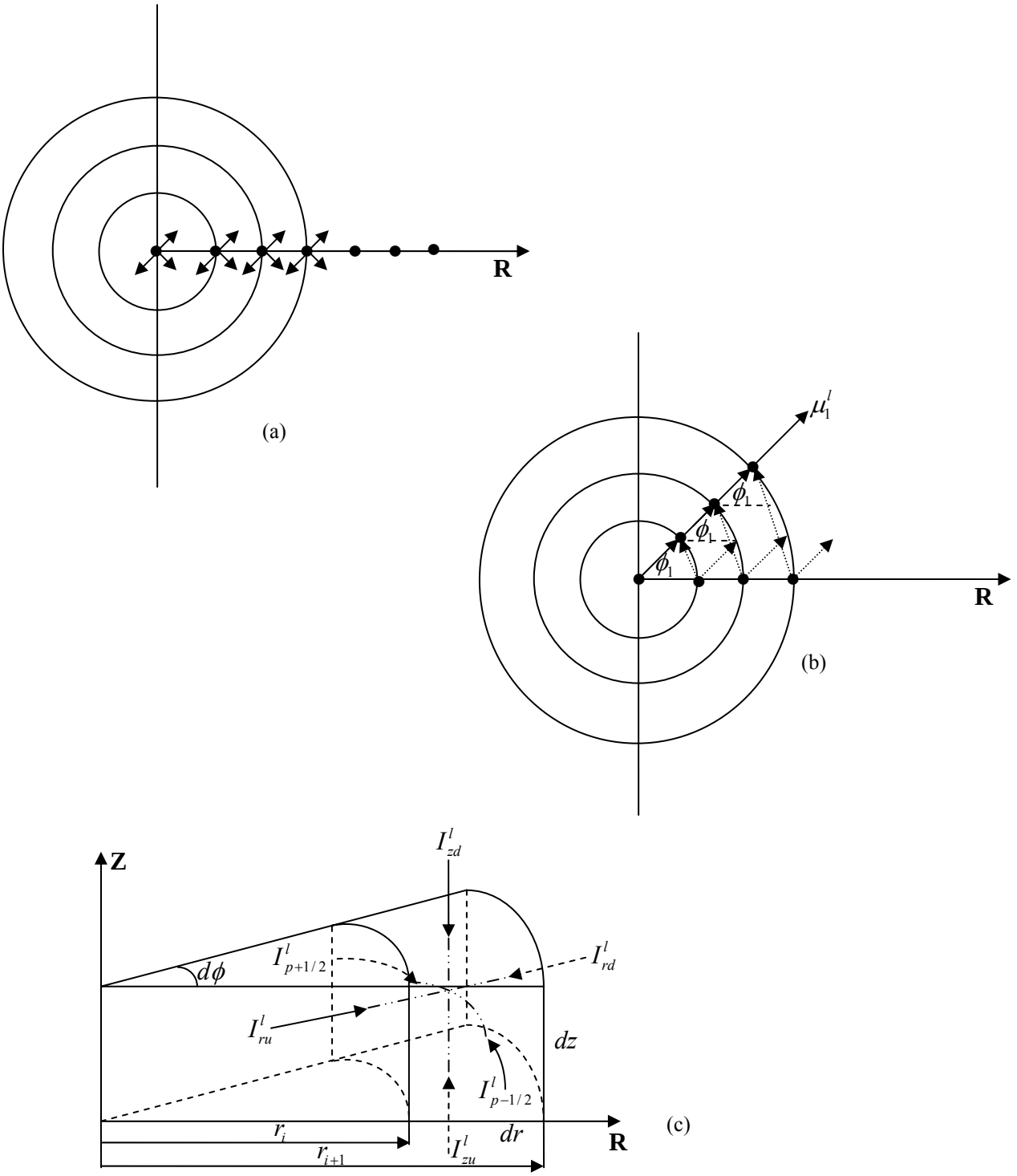

Figure 2.7 The control volume of the TDOM

l	μ_1	μ_2	μ_3	w
1	-0.137272	0.137272	-0.980975	0.0944411
2	0.137272	0.137272	-0.980975	0.0944411
3	-0.504689	0.137272	-0.852318	0.148395
4	-0.137272	0.504689	-0.852318	0.148395
5	0.137272	0.504689	-0.852318	0.148395
6	0.504689	0.137272	-0.852318	0.148395
7	-0.700413	0.137272	-0.700413	0.1149972
8	-0.504689	0.504689	-0.700413	0.0173701
9	-0.137272	0.700413	-0.700413	0.1149972
10	0. 137272	0.700413	-0.700413	0.1149972
11	0.504689	0.504689	-0.700413	0.0173701
12	0.700413	0.137272	-0.700413	0.1149972
13	-0.852318	0.137272	-0.504689	0.148395
14	-0.700413	0.504689	-0.504689	0.0173701
15	-0.504689	0.700413	-0.504689	0.0173701
16	-0.137272	0.852318	-0.504689	0.148395
17	0.137272	0.852318	-0.504689	0.148395
18	0.504689	0.700413	-0.504689	0.0173701
19	0.700413	0.504689	-0.504689	0.0173701
20	0.852318	0. 137272	-0.504689	0.148395
21	-0.980975	0. 137272	-0.137272	0.0944411
22	-0.852318	0.504689	-0.137272	0.148395
23	-0.700413	0.700413	-0.137272	0.1149972
24	-0.504689	0.852318	-0.137272	0.148395
25	-0.137272	0.980975	-0.137272	0.0944411
26	0.137272	0.980975	-0.137272	0.0944411
27	0.504689	0.852318	-0.137272	0.148395
28	0.700413	0.700413	-0.137272	0.1149972
29	0.852318	0.504689	-0.137272	0.148395
30	0.980975	0.137272	-0.137272	0.0944411

Table 2.2 The discrete ordinate and angular weight of one quadrature for S_{10} scheme.

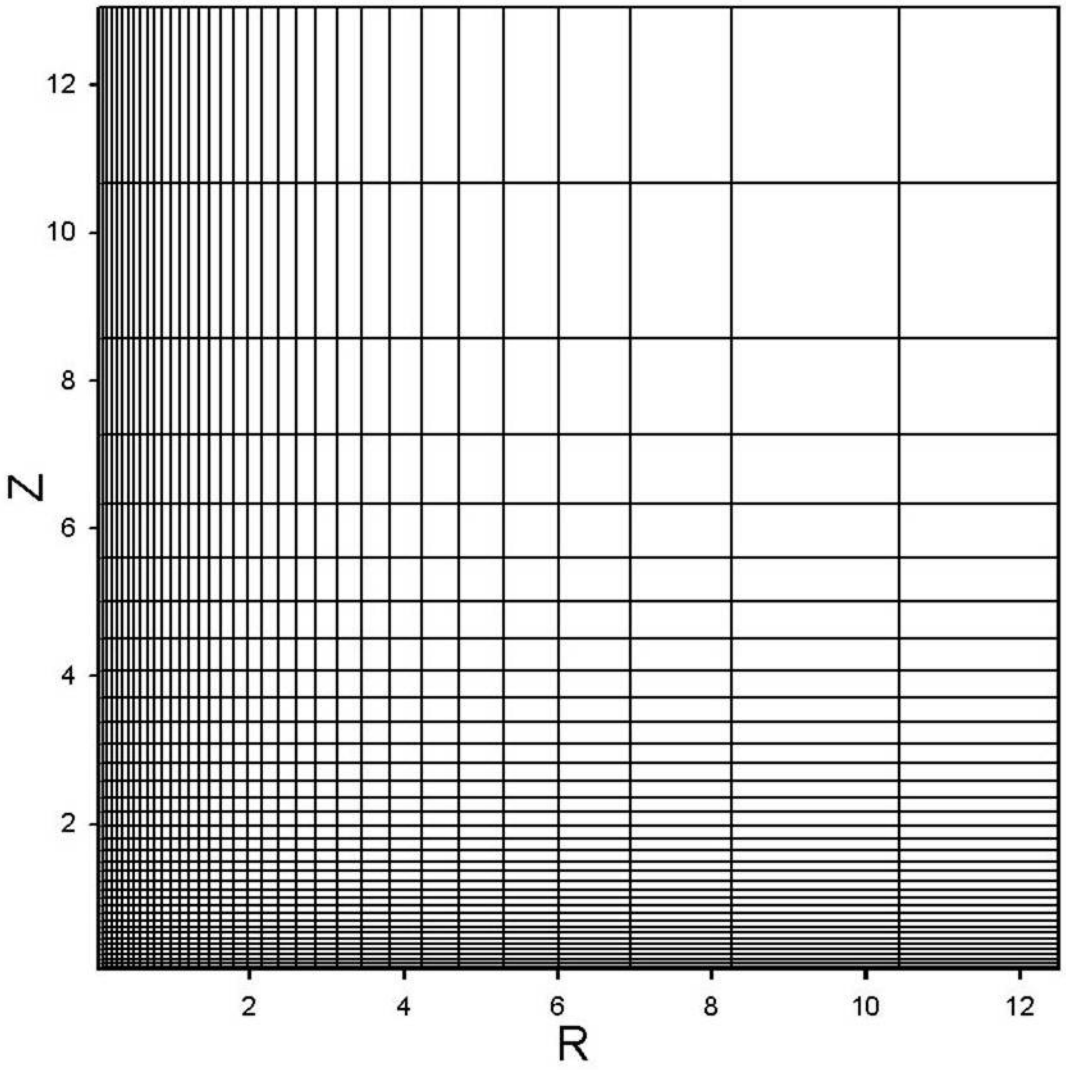

Figure 2.8 The nonuniform grid system

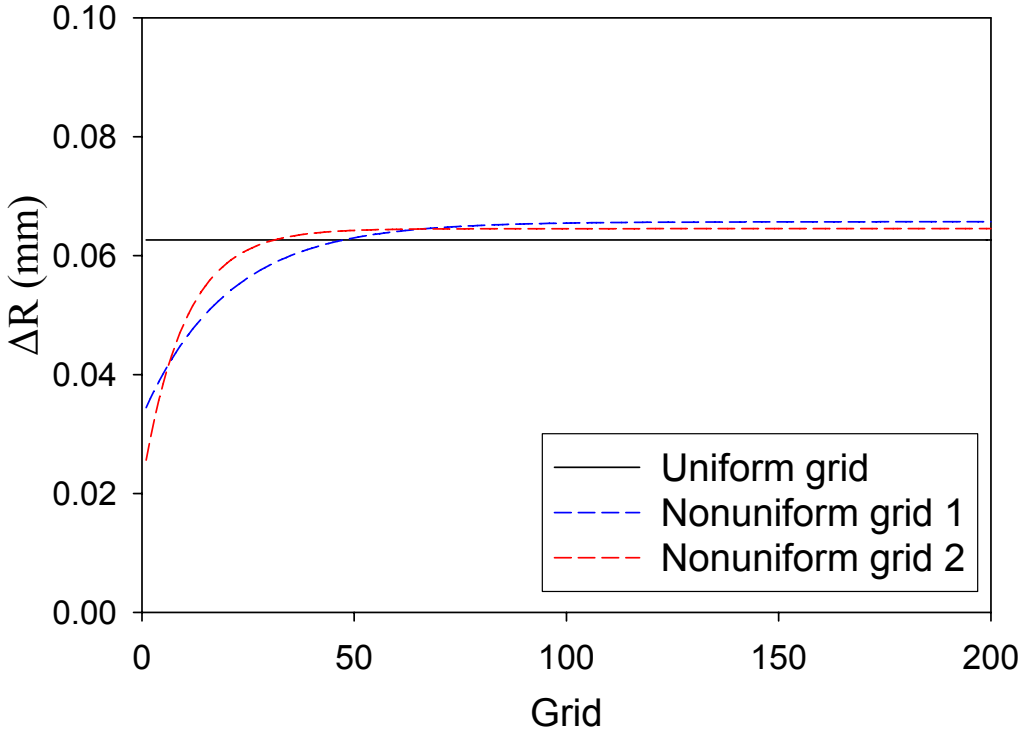

(a)

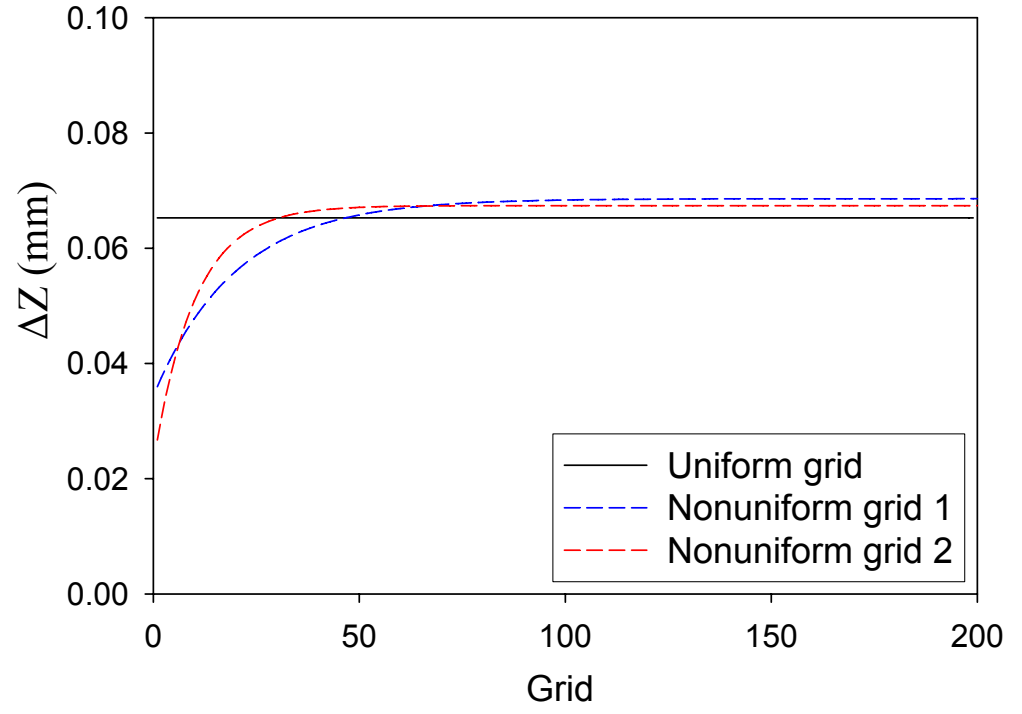

(b)

Figure 2.9 The comparison of grid size changing at different grid systems: (a) Change of grid size in the radial direction and (b) in the axial direction.

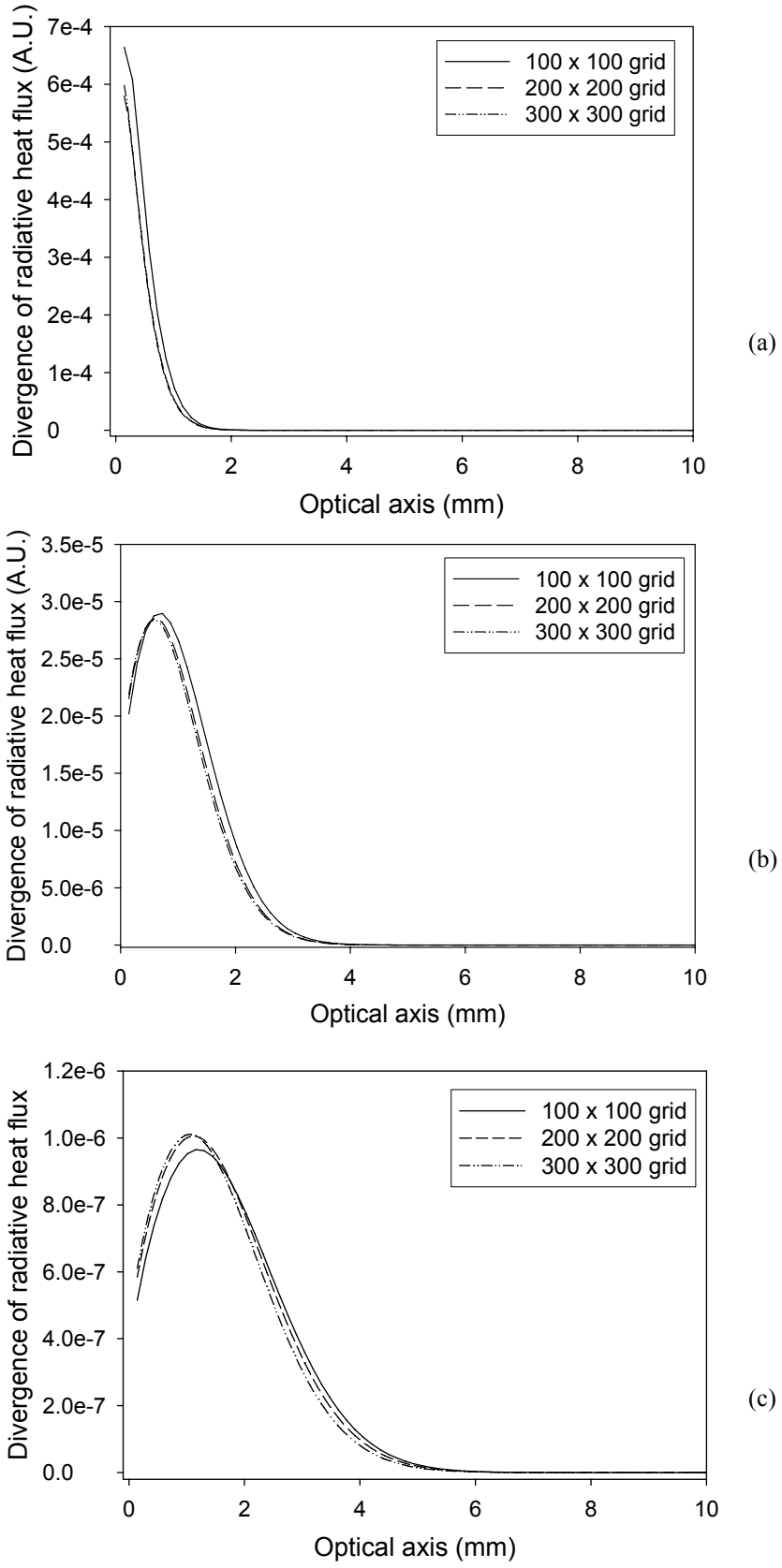

Figure 2.10 The influence of grid size for uniform grid system: (a) t = 20 ps, (b) t =50 ps, and (c) t =100 ps.

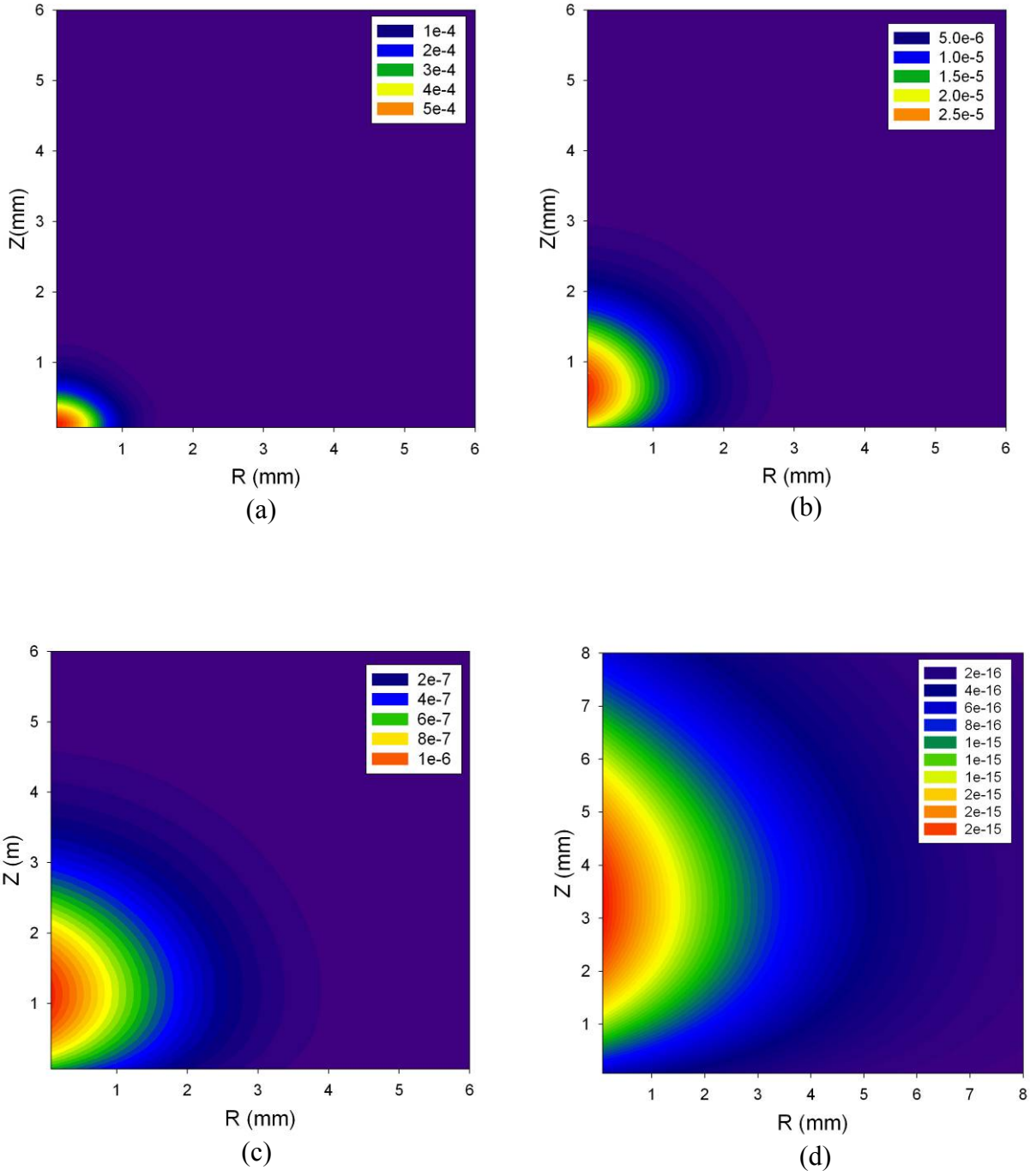

Figure 2.11 The contour of divergence of radiative heat flux at certain time instant: (a) t = 20 ps, (b) t = 50 ps, (c) t = 100 ps, and (d) t = 500 ps.

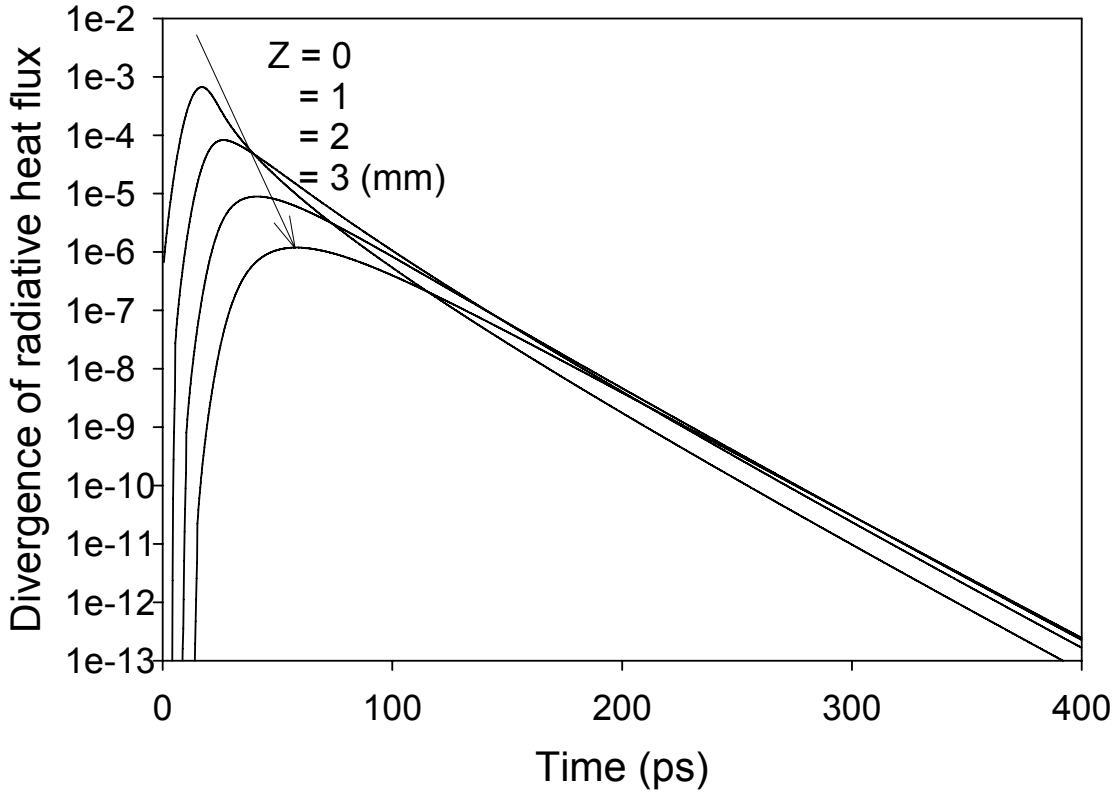

Figure 2.12 The temporal profiles of divergence of radiative heat flux along the optical axis.

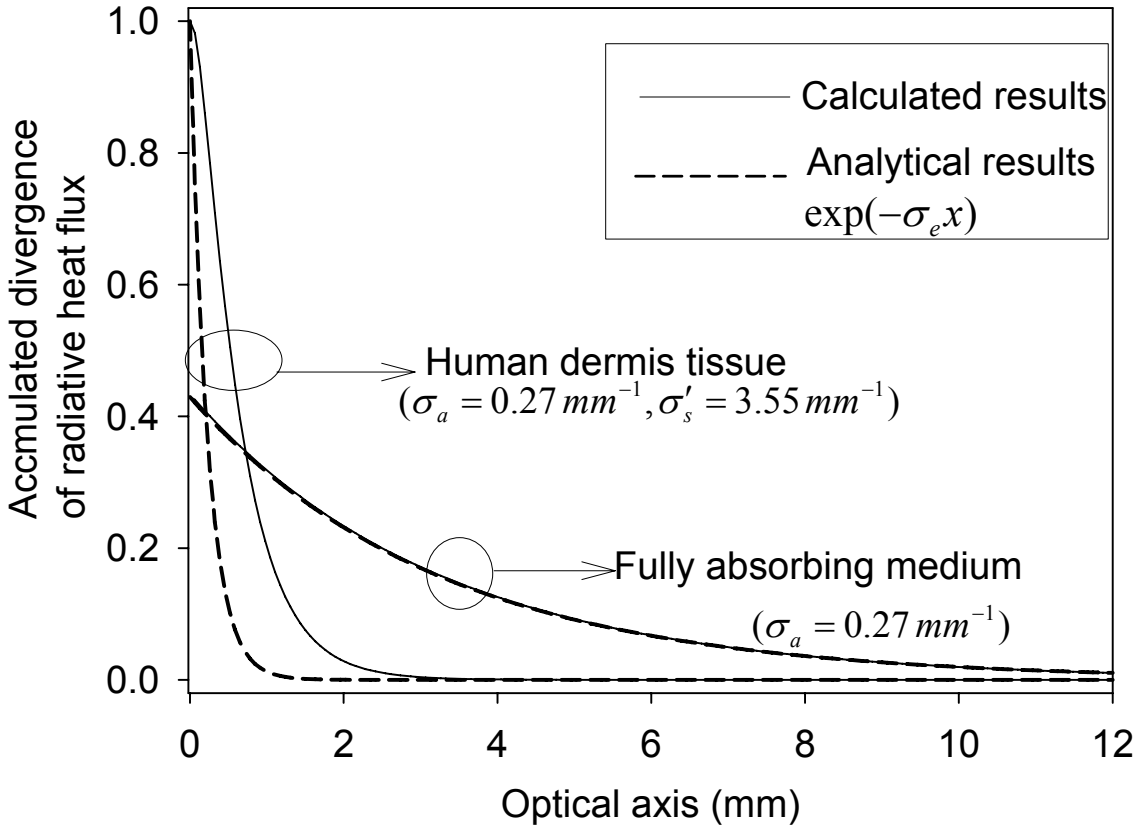

Figure 2.13 Comparisons of the accumulated divergence of radiative heat flux profiles along the cylinder centerline after 1ms pulse train irradiation predicted by the radiative heat transfer modeling and simple Lambert-Beer's analysis, respectively.

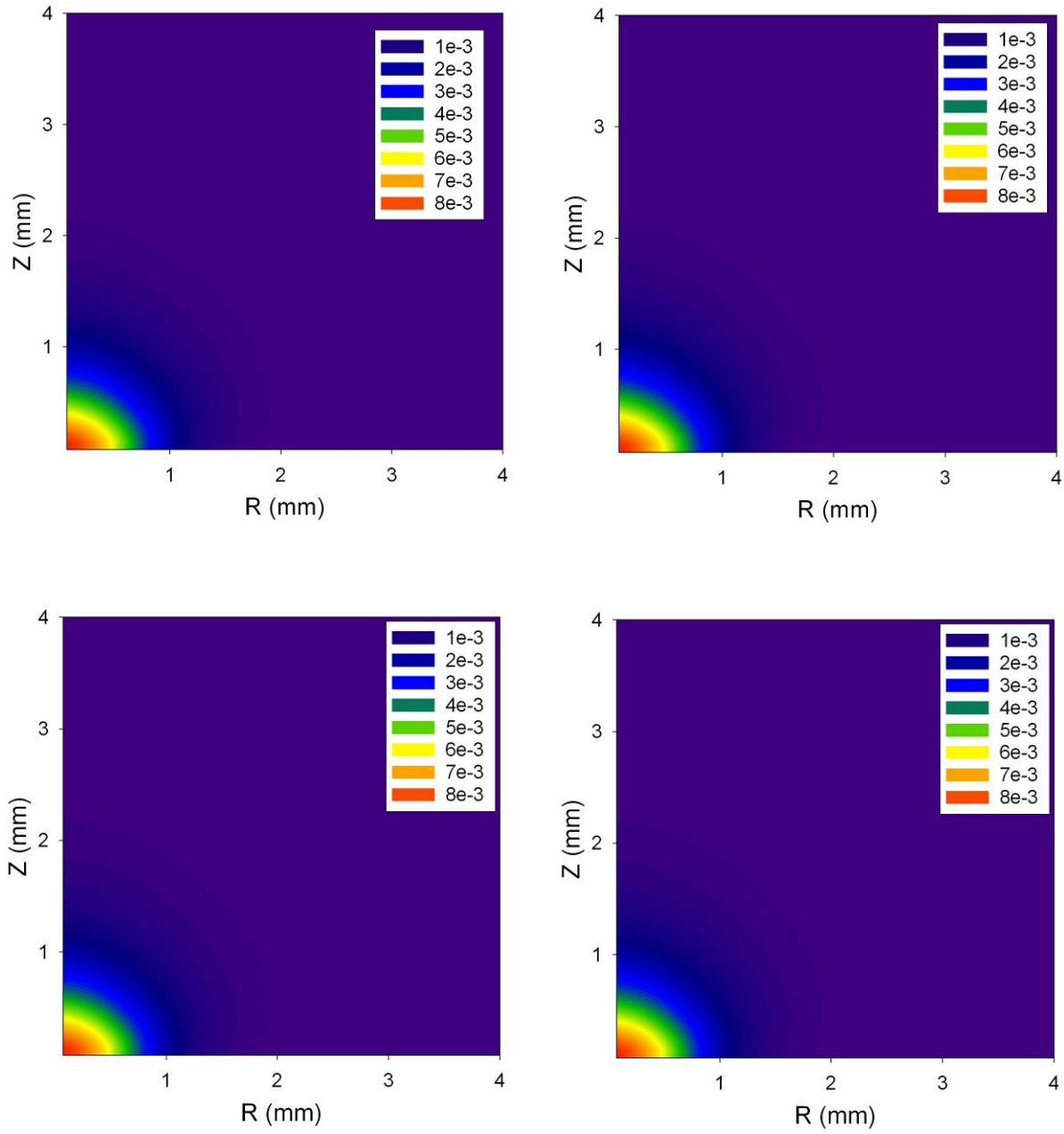

Figure 2.14 The contour of accumulated divergence of radiative heat flux at certain time instant: (a) t = 20 ps, (b) t = 50 ps, (c) t = 100 ps, and (d) t = 500 ps.

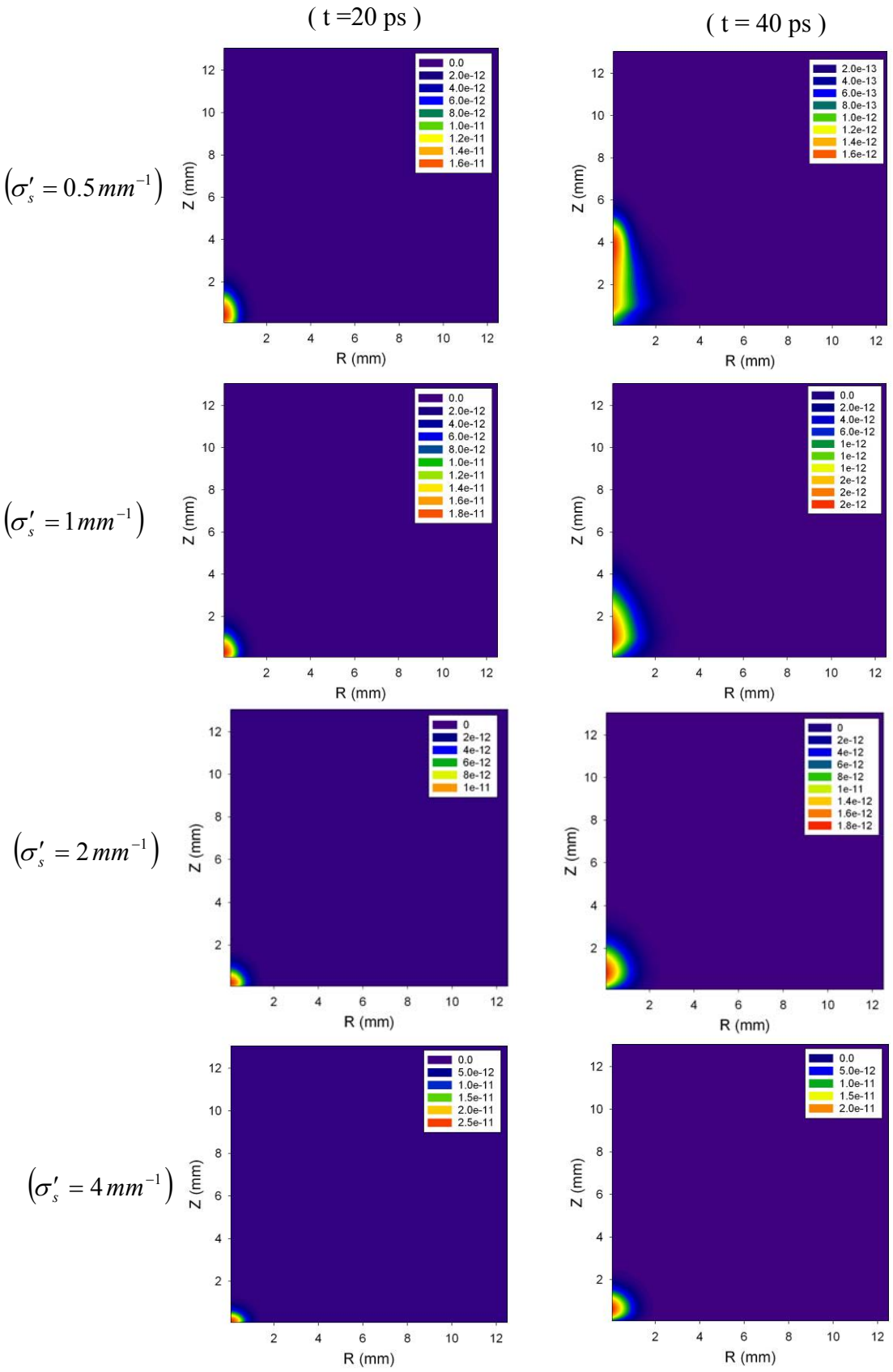

Figure 2.15 (a) The investigation of scattering coefficient influence at certain time instants

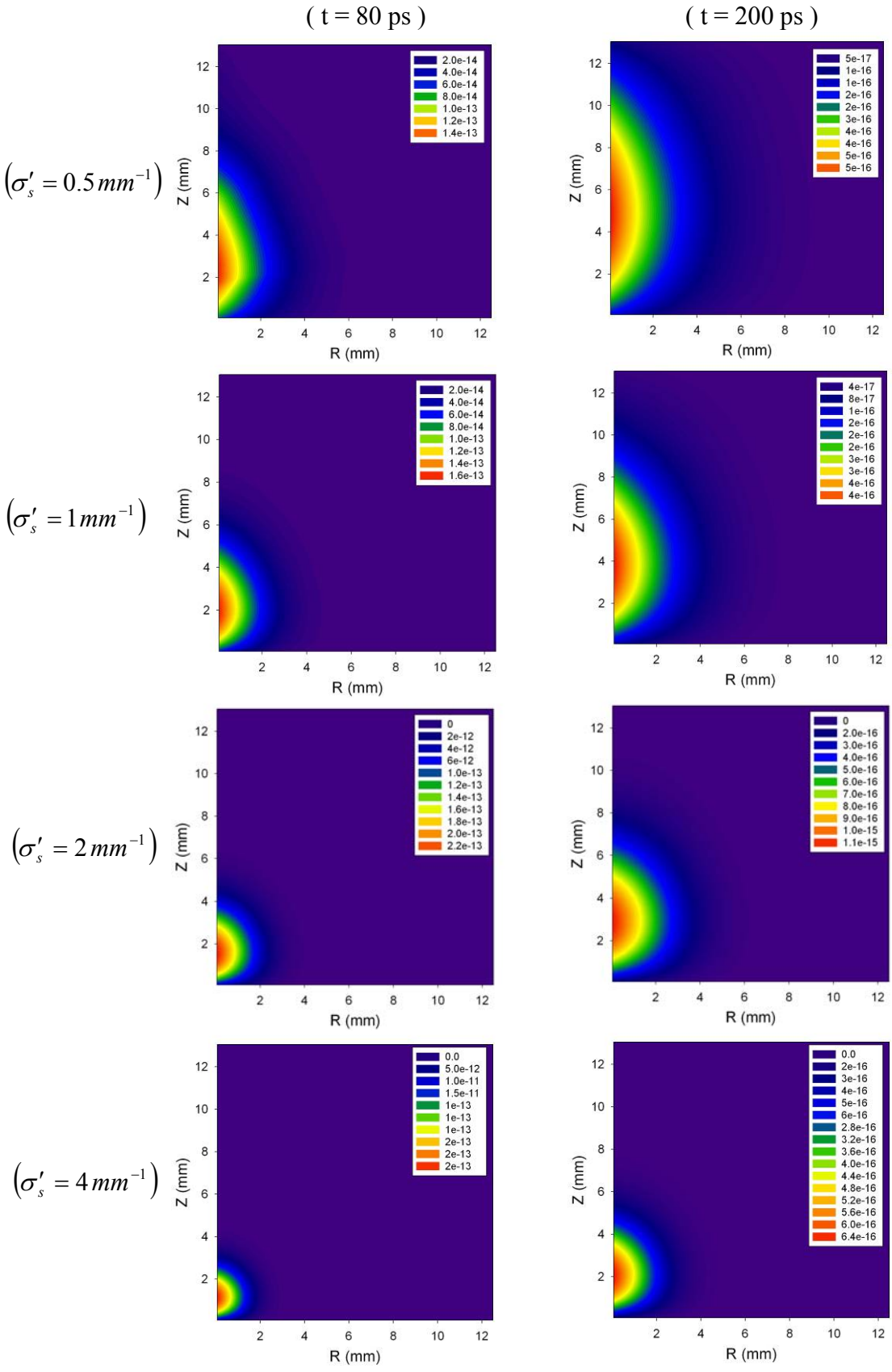

Figure 2.15 (b) The investigation of scattering coefficient influence at certain time instants

$\left(\sigma_s' = 0.5\,mm^{-1}\right)$

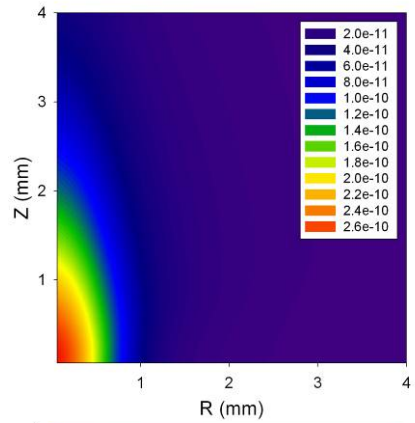

$\left(\sigma_s' = 1\,mm^{-1}\right)$

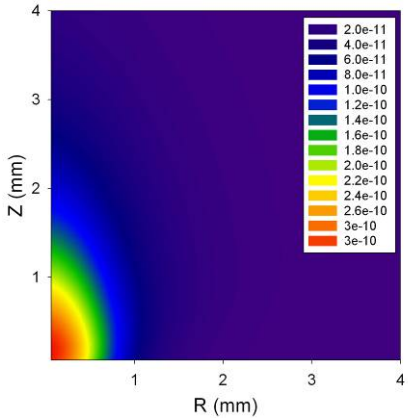

$\left(\sigma_s' = 2\,mm^{-1}\right)$

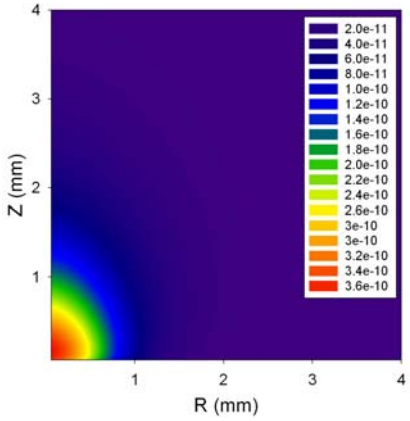

$\left(\sigma_s' = 4\,mm^{-1}\right)$

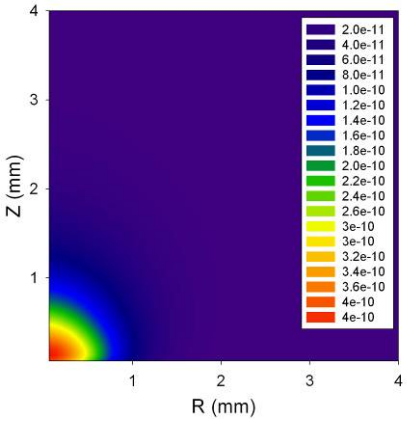

Figure 2.16 Contours of accumulated divergence of radiative heat flux at t = 400 ps.

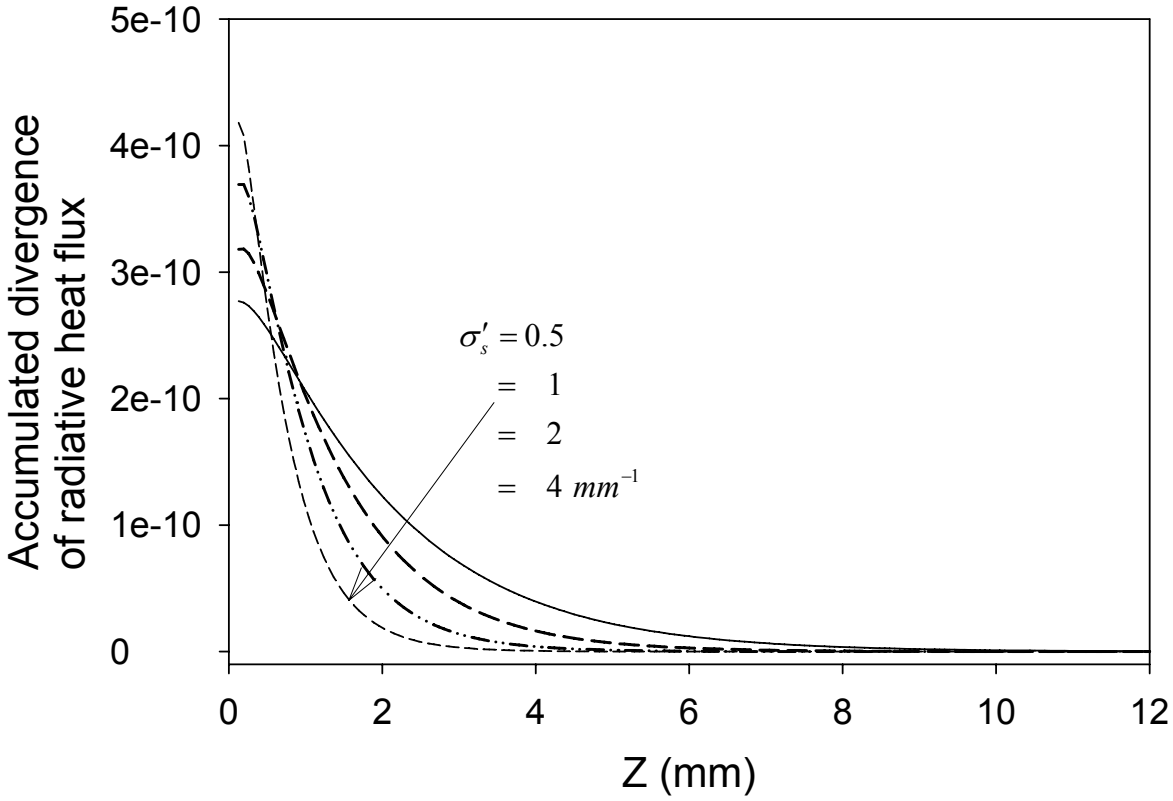

Figure 2.17 The comparison of accumulated divergence of radiative heat flux along the optical axis at t = 400 ps with various scattering coefficient medium.

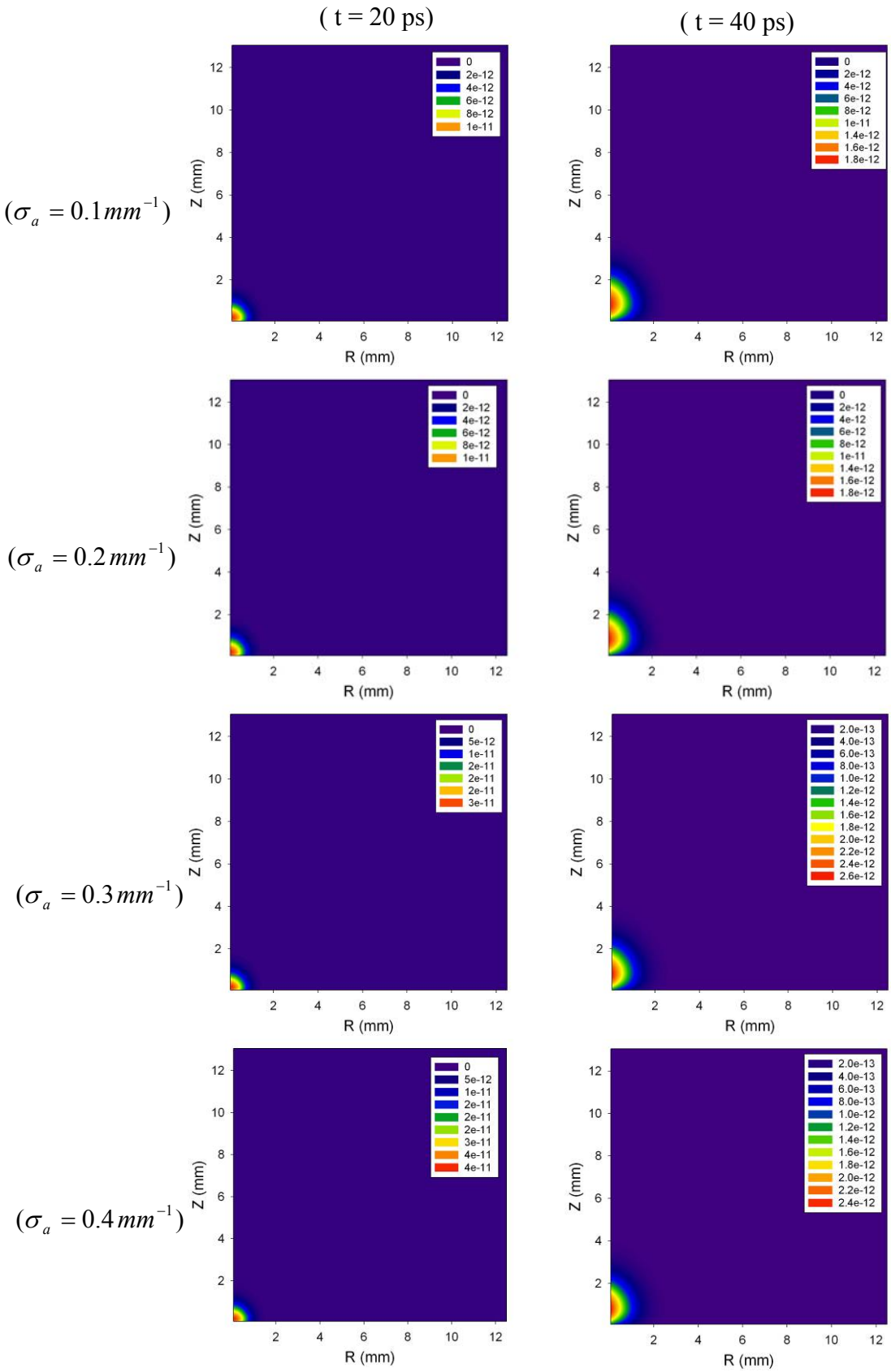

Figure 2.18 (a) The investigation of absorption coefficient influence at certain time instants

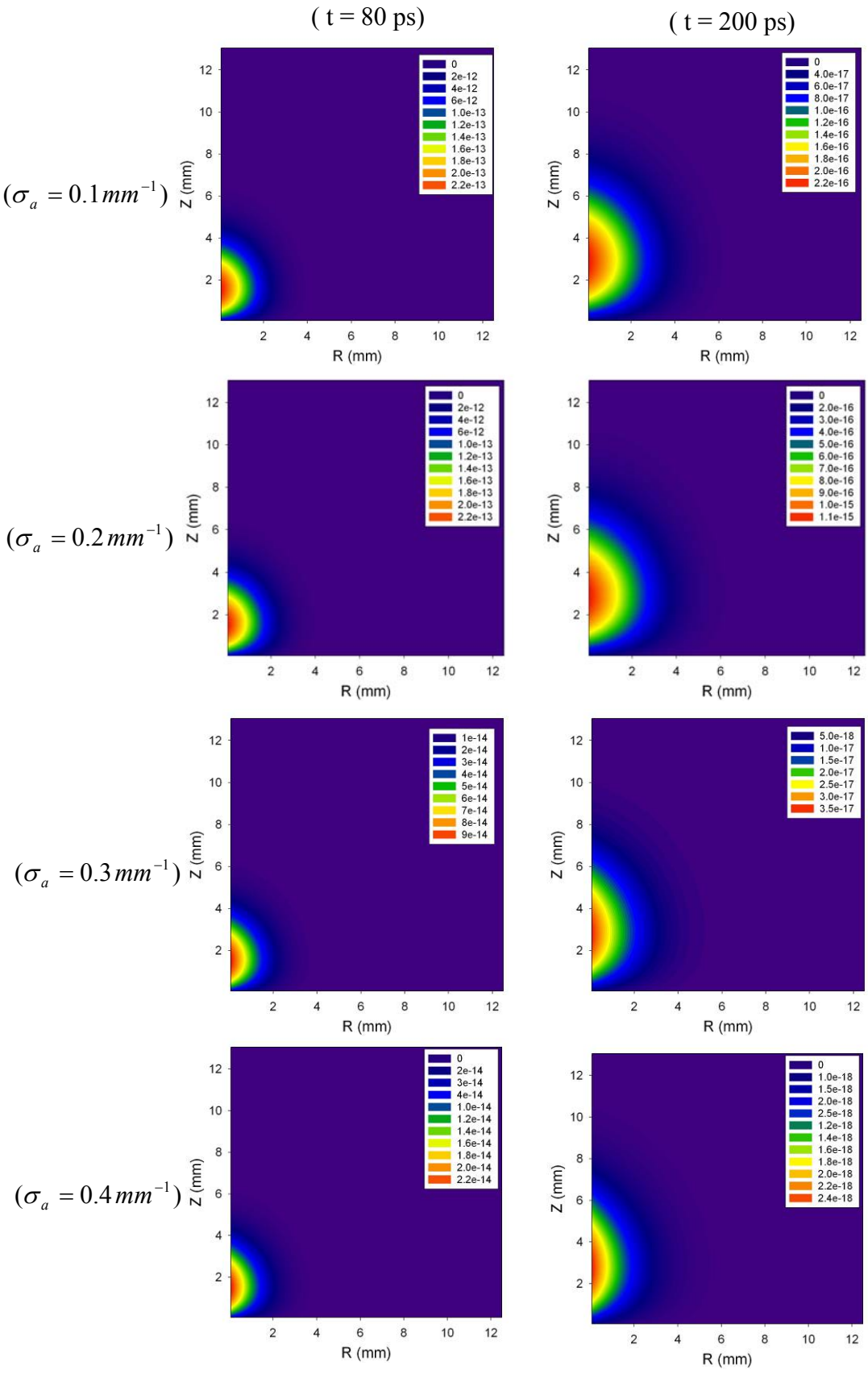

Figure 2.18 (b) The investigation of absorption coefficient influence at certain time instants

$(\sigma_a = 0.1 mm^{-1})$

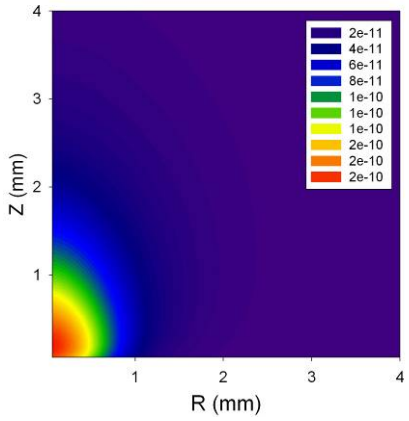

$(\sigma_a = 0.2 mm^{-1})$

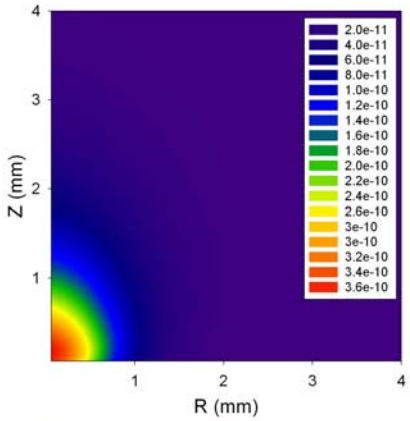

$(\sigma_a = 0.3 mm^{-1})$

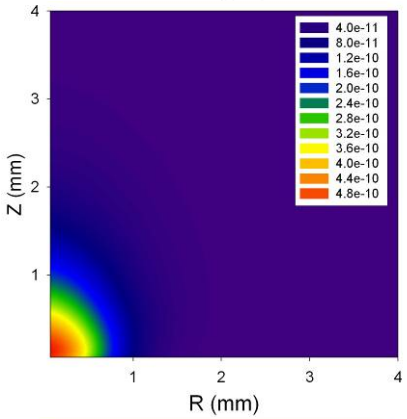

$(\sigma_a = 0.4 mm^{-1})$

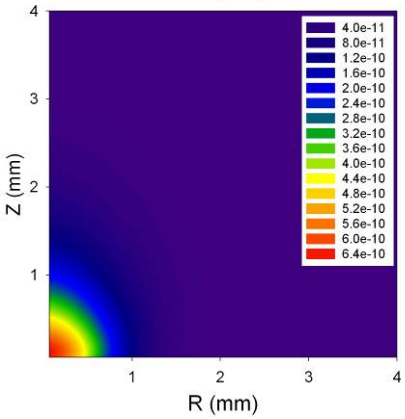

Figure 2.19 The accumulation of divergence of radiative heat flux at t = 400 ps with various absorption coefficient medium.

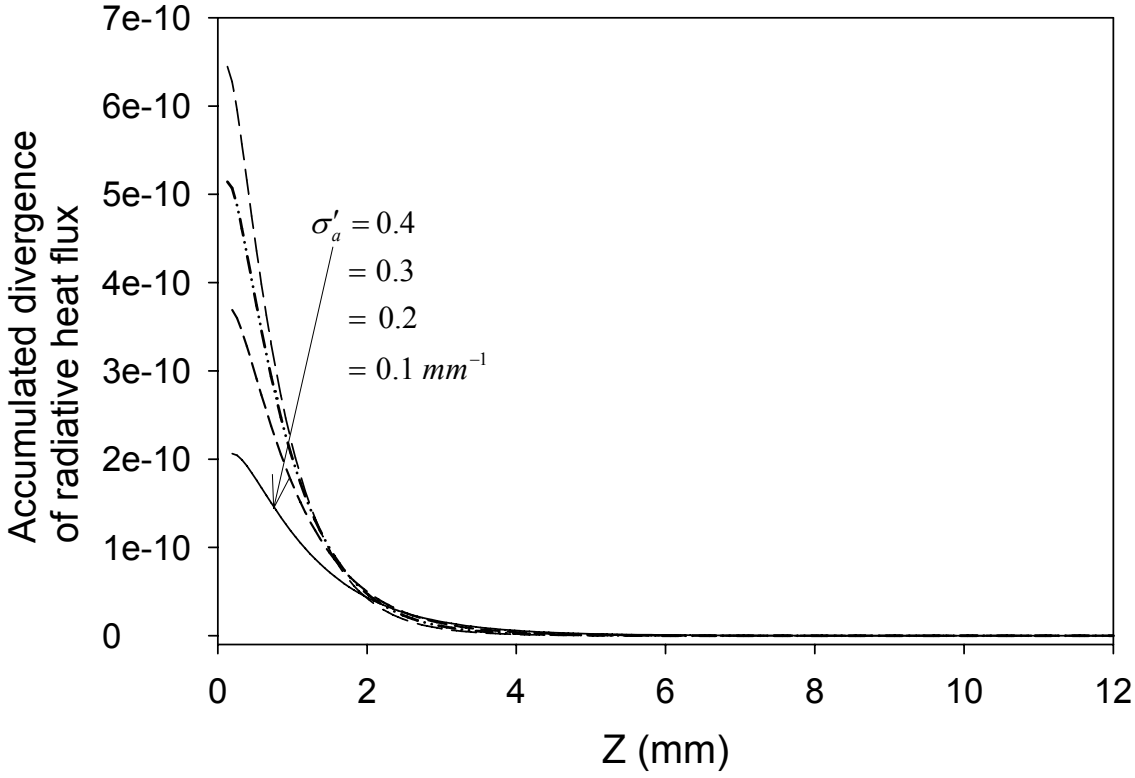

Figure 2.20 The comparison of accumulated divergence of radiative heat flux along the optical axis at t = 400 ps with various absorption coefficient medium.

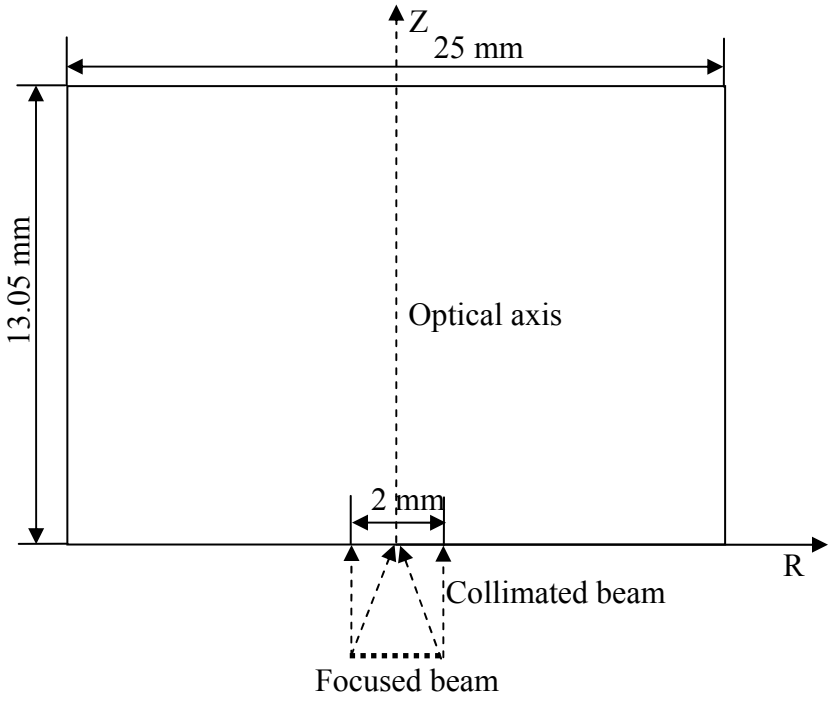

Figure 2.21 The geometric sketch of tissue phantom (side view)

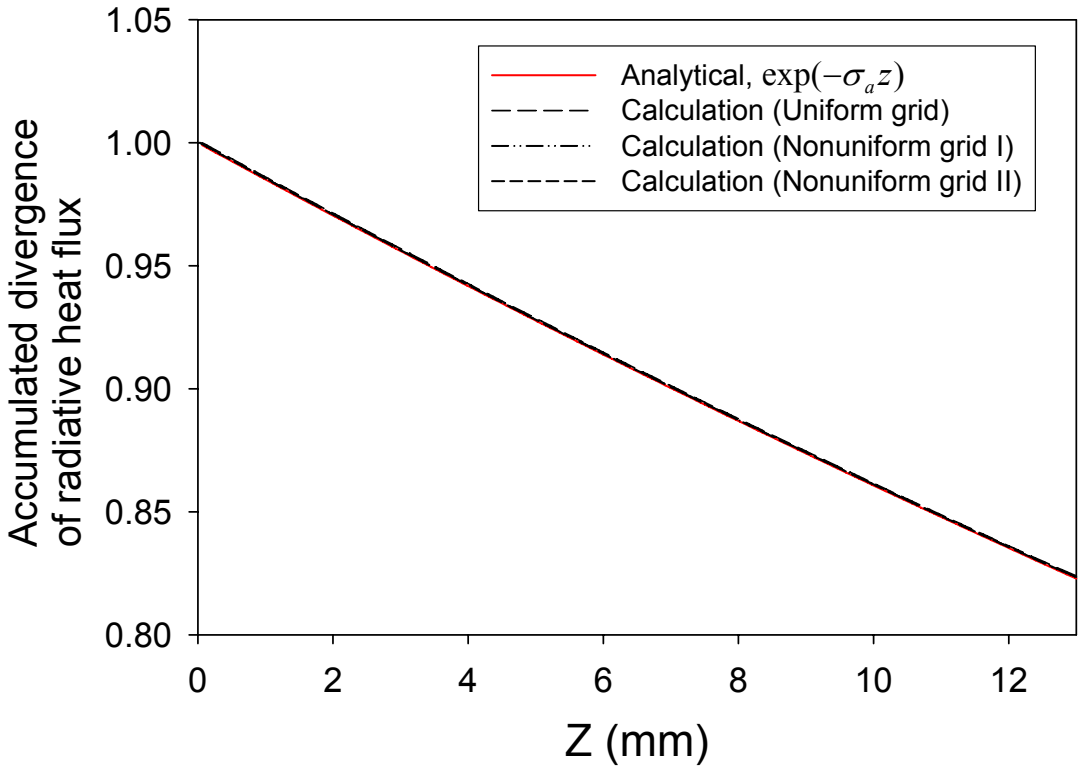

Figure 2.22 The grid size influence with the accumulated divergence of radiative heat flux along the optical axis at t = 400 ps with a fully absorbing medium ($\sigma_a = 0.015\,mm^{-1}$). The collimated laser beam is used.

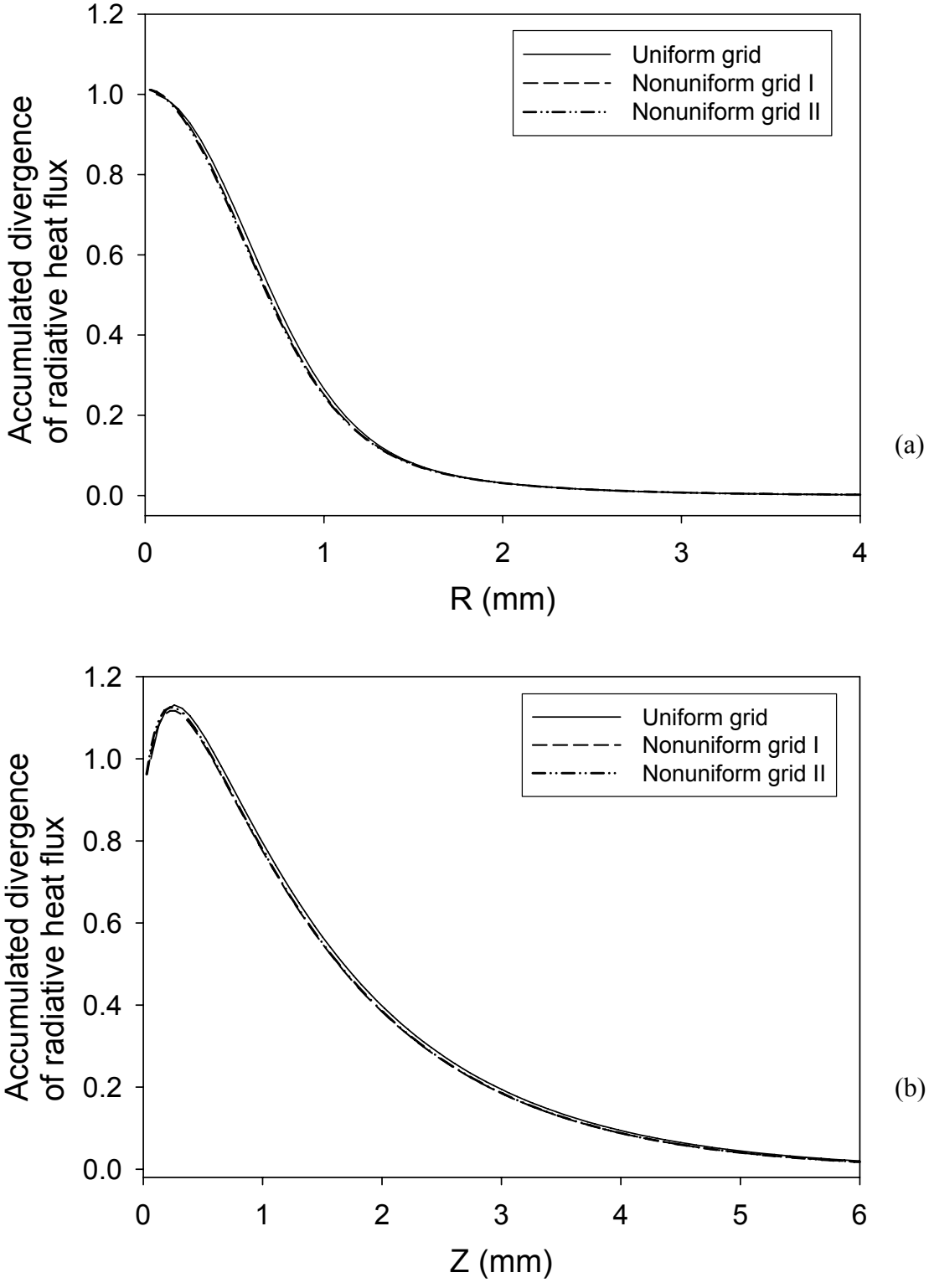

Figure 2.23 The grid size influence with the accumulated divergence of radiative heat flux radial direction along the tissue surface (a) and axial direction along the optical axis (b) at t = 400 ps with a scattering medium ($\sigma_a = 0.015\,mm^{-1}, \sigma_s' = 2\,mm^{-1}$). The collimated laser beam is used.

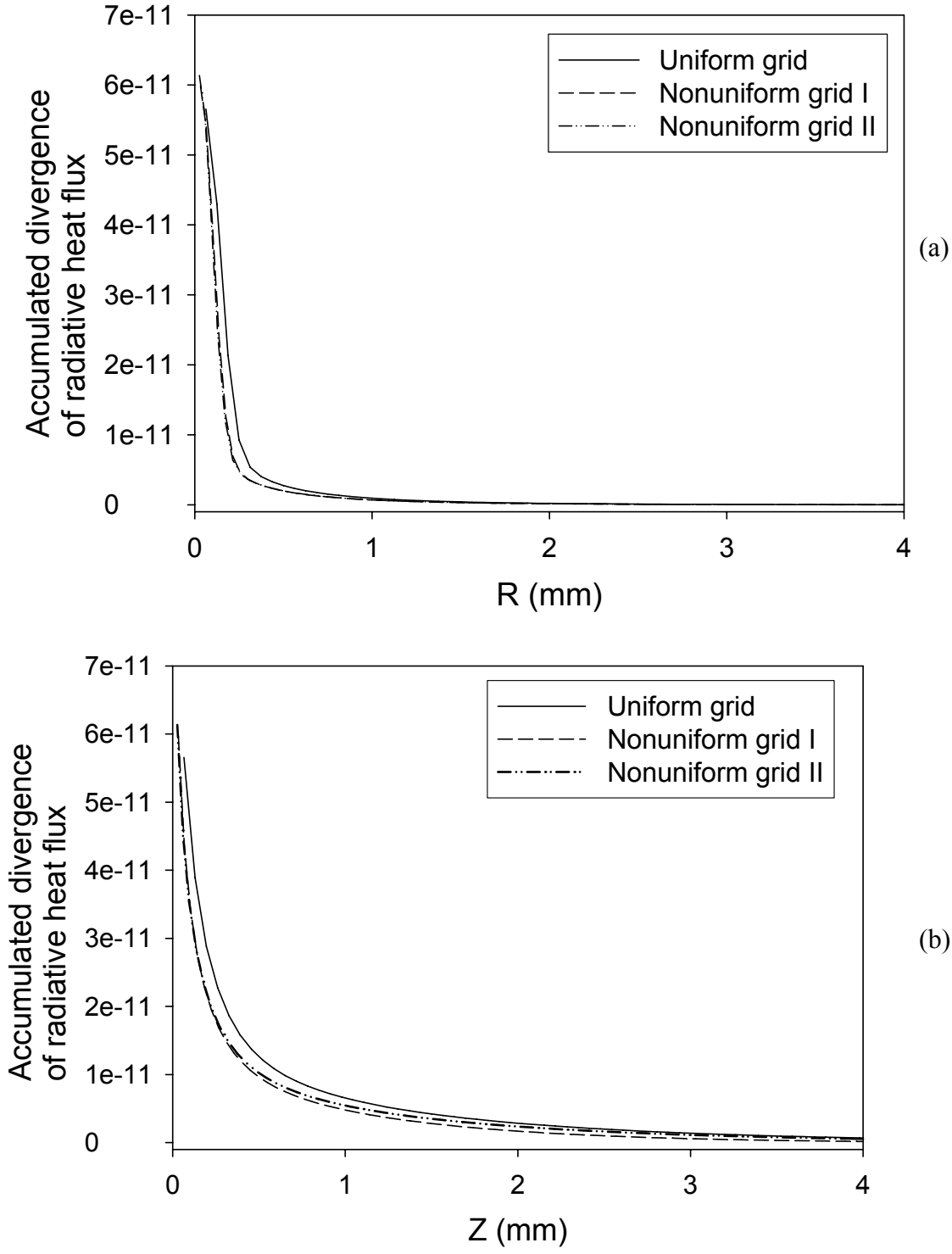

Figure 2.24 The grid size influence with the accumulated divergence of radiative heat flux along the optical axis at t = 400 ps with a scattering medium ($\sigma_a = 0.015 mm^{-1}, \sigma_s' = 2 mm^{-1}$). The focused laser beam is used.

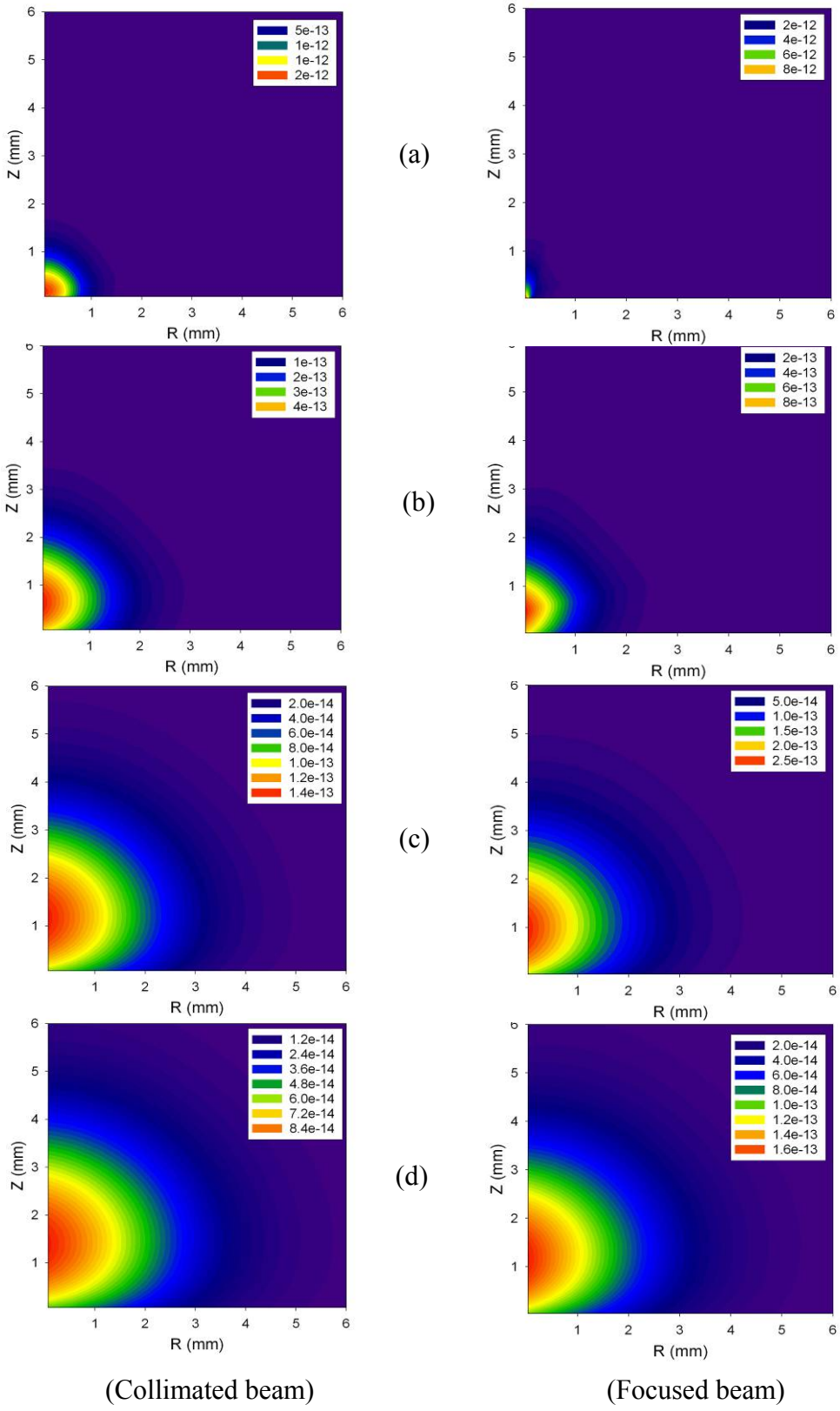

Figure 2.25 The comparison of divergence of radiative heat flux between collimated laser and focused laser at certain time instant: (a) t = 20 ps, (b) t = 40 ps, (c) t = 60 ps, and (d) t = 80ps.

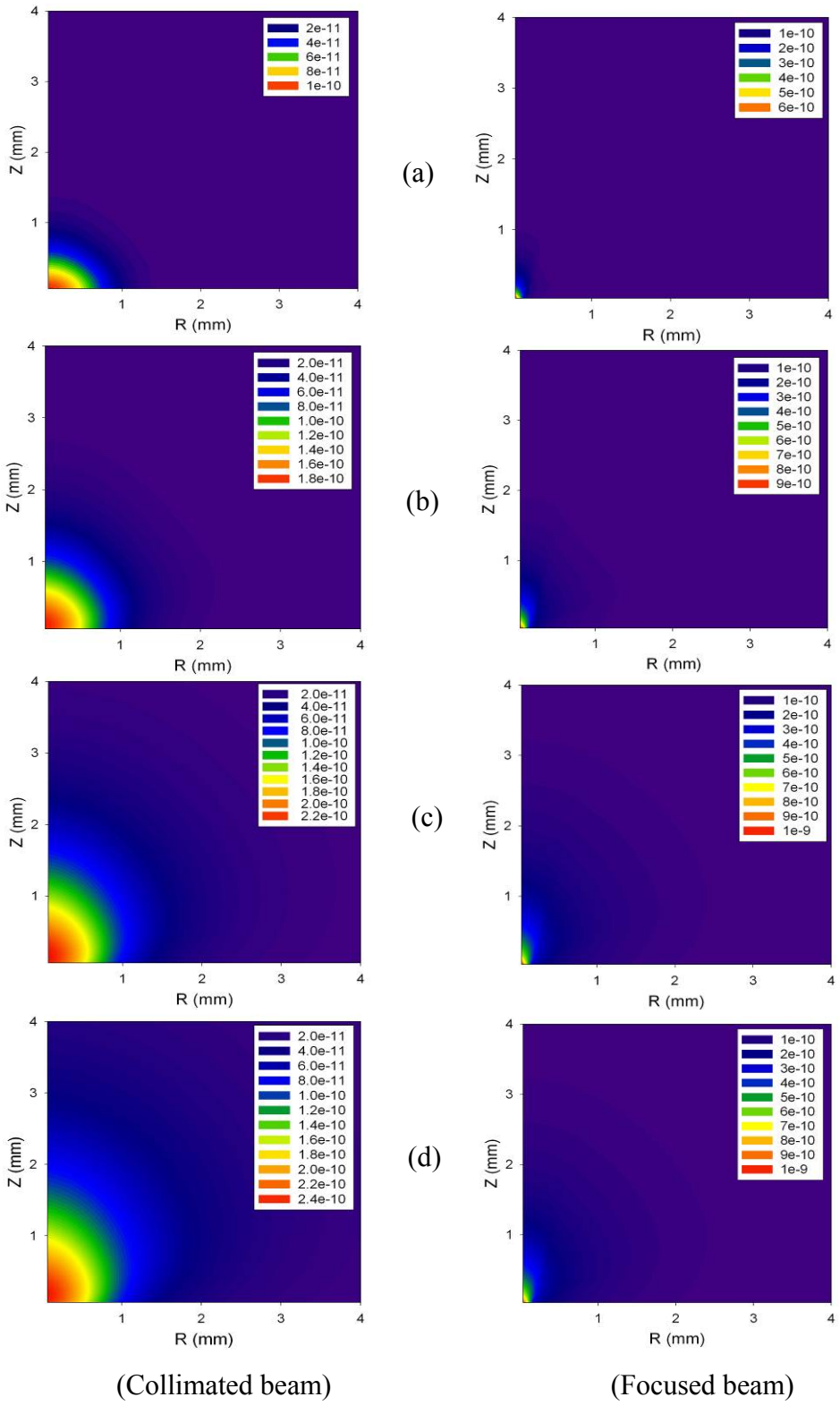

Figure 2.26 The comparison of accumulated divergence of radiative heat flux between collimated laser and focused laser at certain time instant: (a) t = 20 ps, (b) t = 40 ps, (c) t = 100 ps, and (d) t = 200ps.

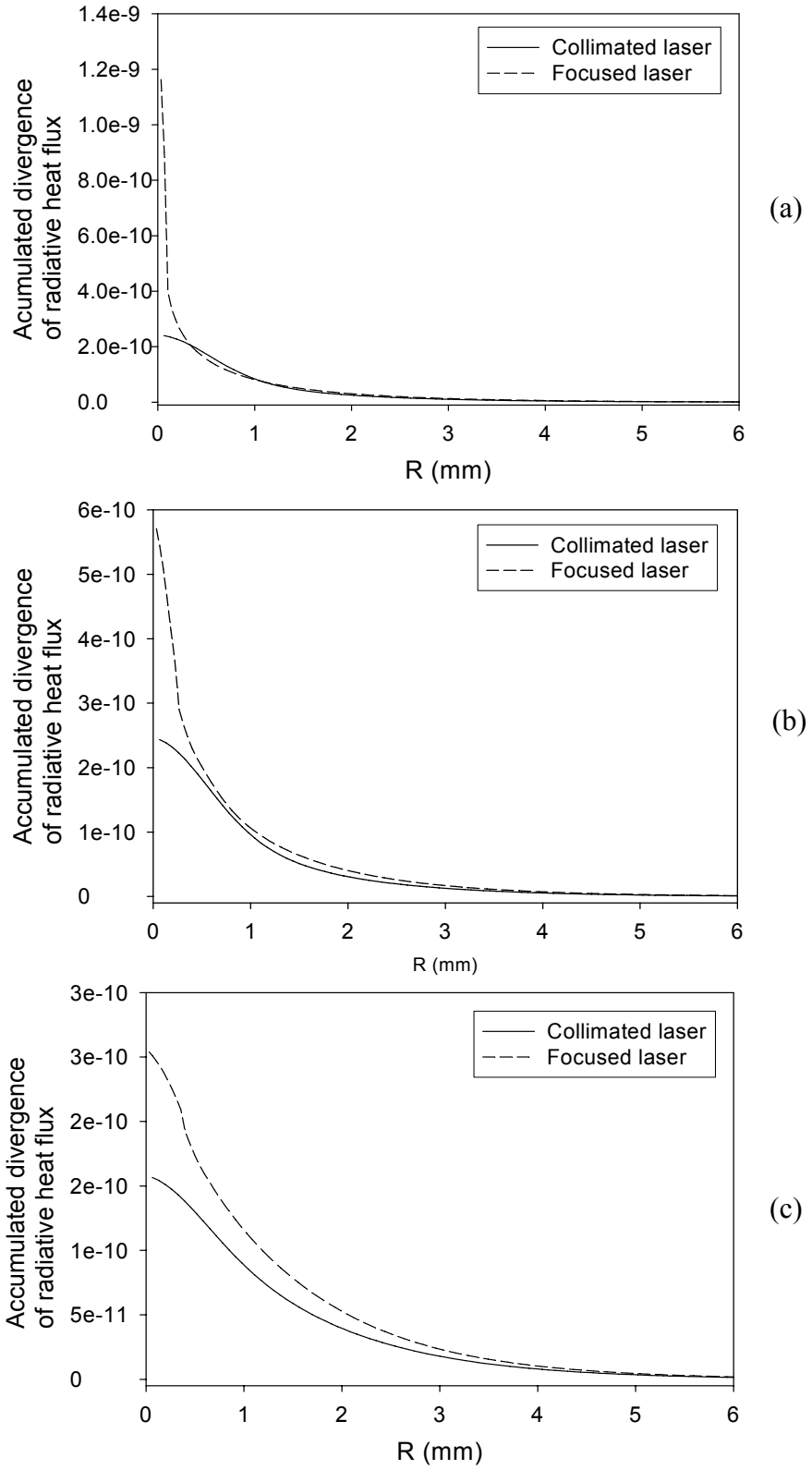

Figure 2.27 The comparison of accumulated divergence of radiative heat flux profile along the radial direction between collimated laser and focused laser at t =200ps: (a) Z = 0, (b) Z = 0.25 mm, and (c) Z = 1 mm.

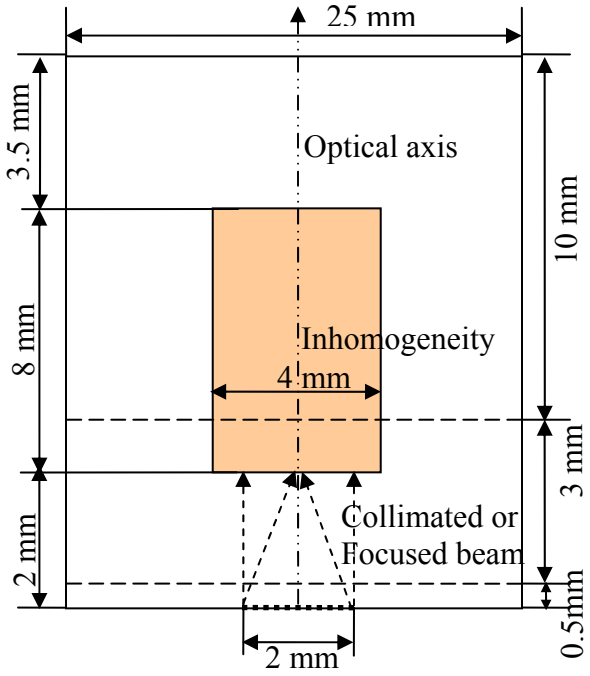

Figure 2.28 Geometric sketch of three layered tissue with inhomogeneity

LAYER	THICKNESS(MM)	ABSORPTION COEFFICIENT (σ_a) (MM^{-1})	REDUCED SCATTERING COEFFICIENT (σ_s') (MM^{-1})
EPIDERMIS	0.5	0.355	0.824
DERMIS	3	0.049	0.049
FATTY TISSUE	10	0.050	0.55
INHOMOGENITY	8	0.0509	1.23

Table 2.3 The tissue optical properties for multi layered tissue.

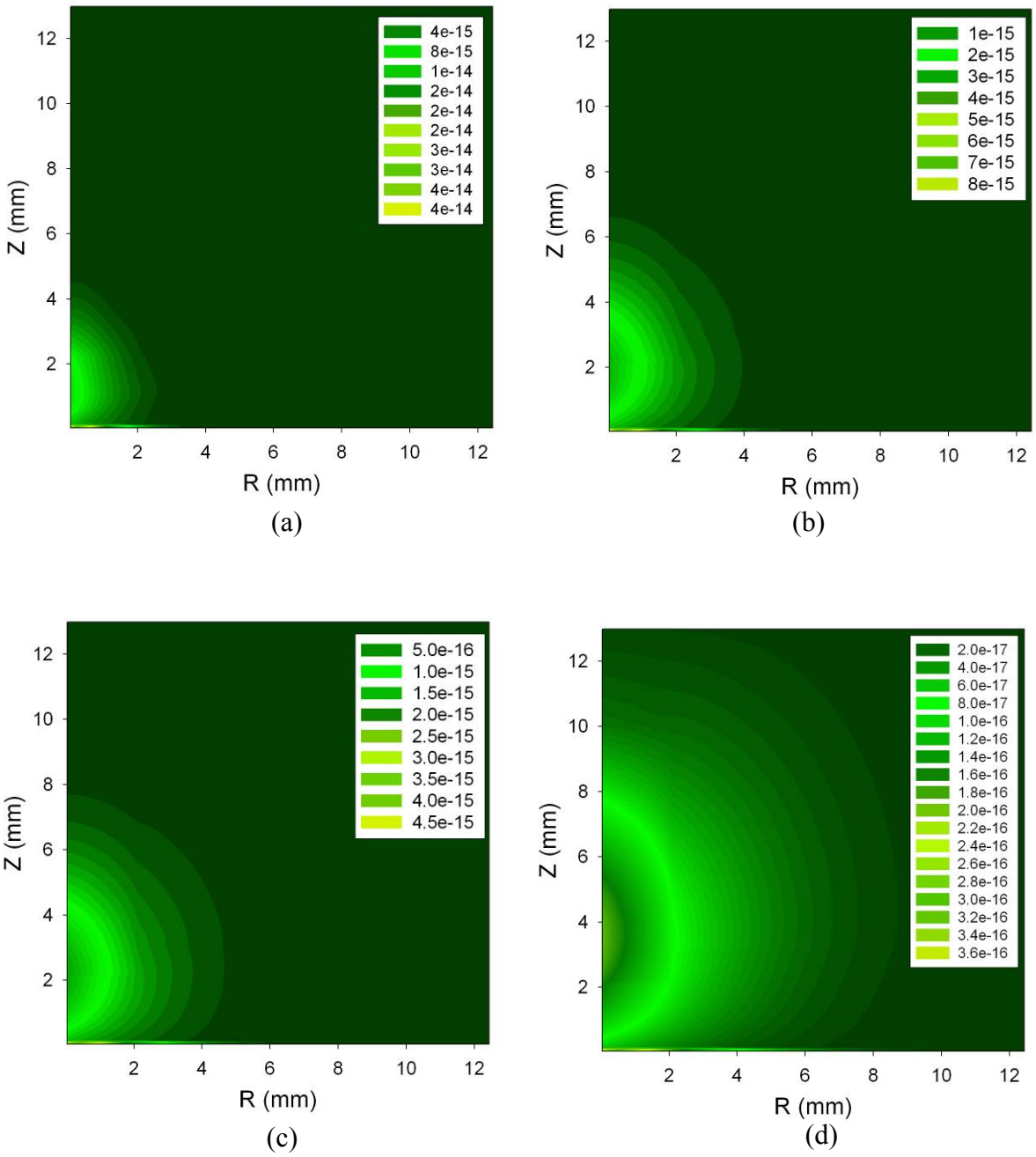

Figure 2.29 The contours of divergence of radiative heat flux at certain time instant: (a) t = 40 ps, (b) t = 80 ps, (c) t = 200 ps, and (d) t = 400 ps. (Collimated laser)

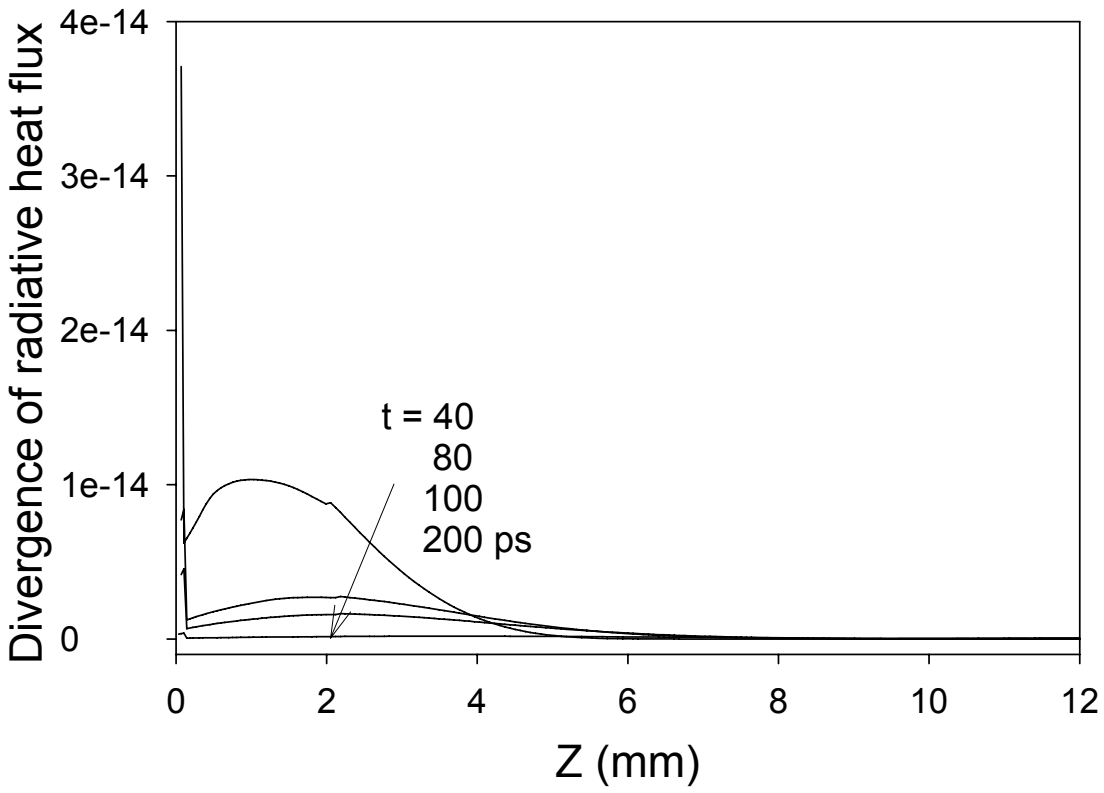

Figure 2.30 The axial profiles of divergence of radiative heat flux along the optical axis. (Collimated laser)

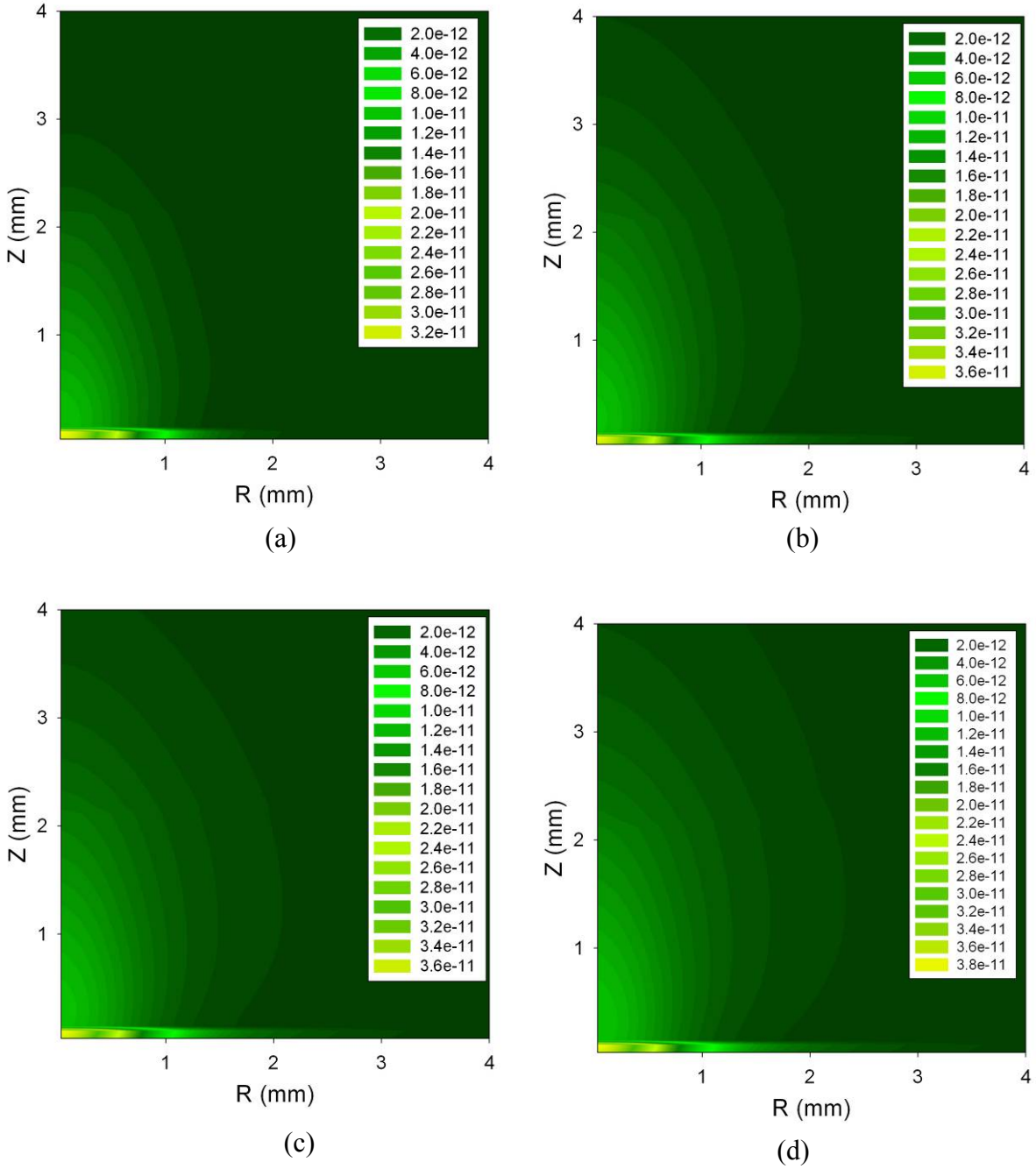

Figure 2.31 The accumulated contours of divergence of radiative heat flux at certain time instant: (a) t = 40 ps, (b) t = 80 ps, (c) t = 100 ps, and (d) t = 200 ps. (Collimated laser)

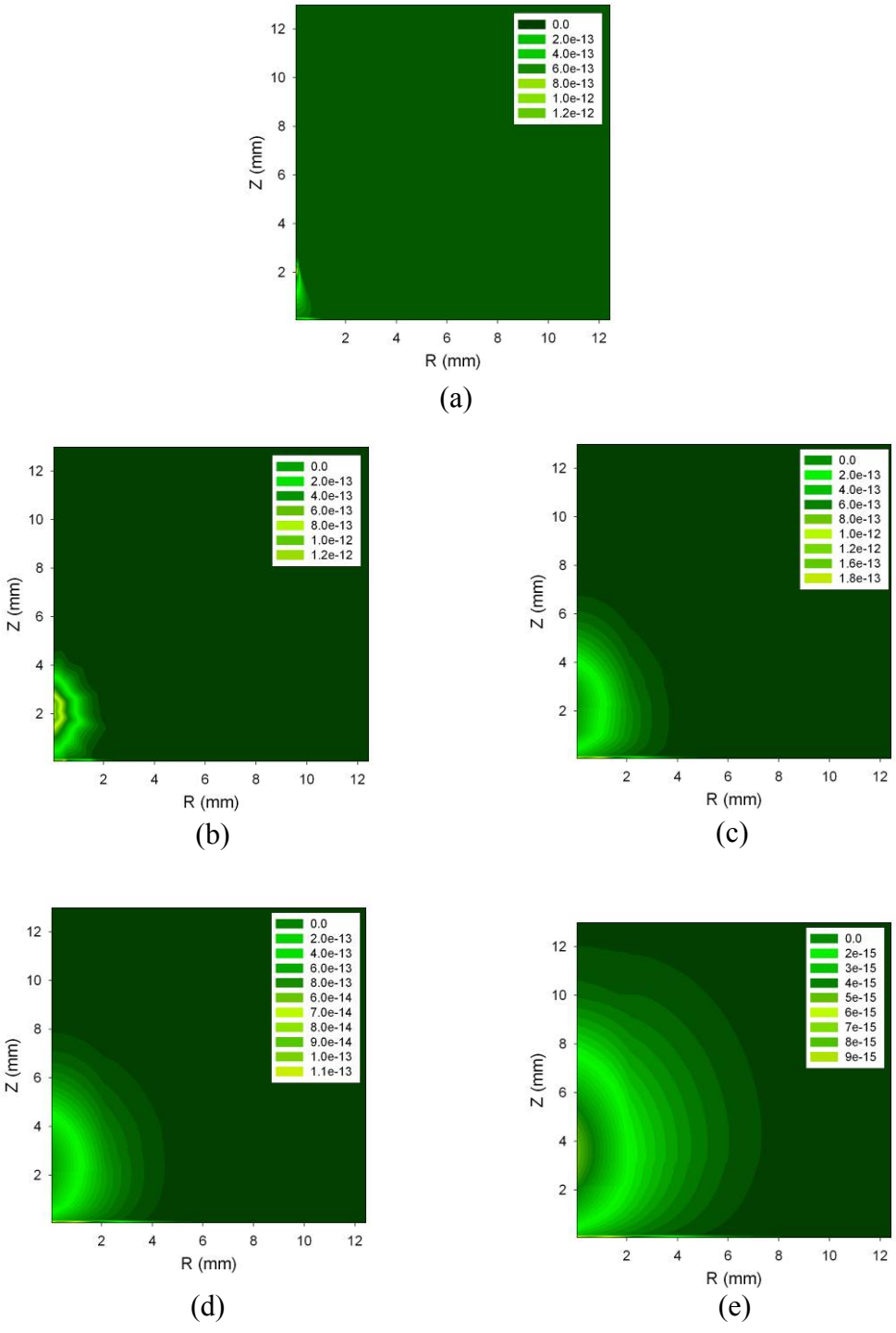

Figure 2.32 The contours of divergence of radiative heat flux at certain time instant: (a) t = 20 ps, (b) t = 40 ps, (c) t = 80 ps, (c) t = 100 ps, and (e) t = 200 ps. (Focused laser beam)

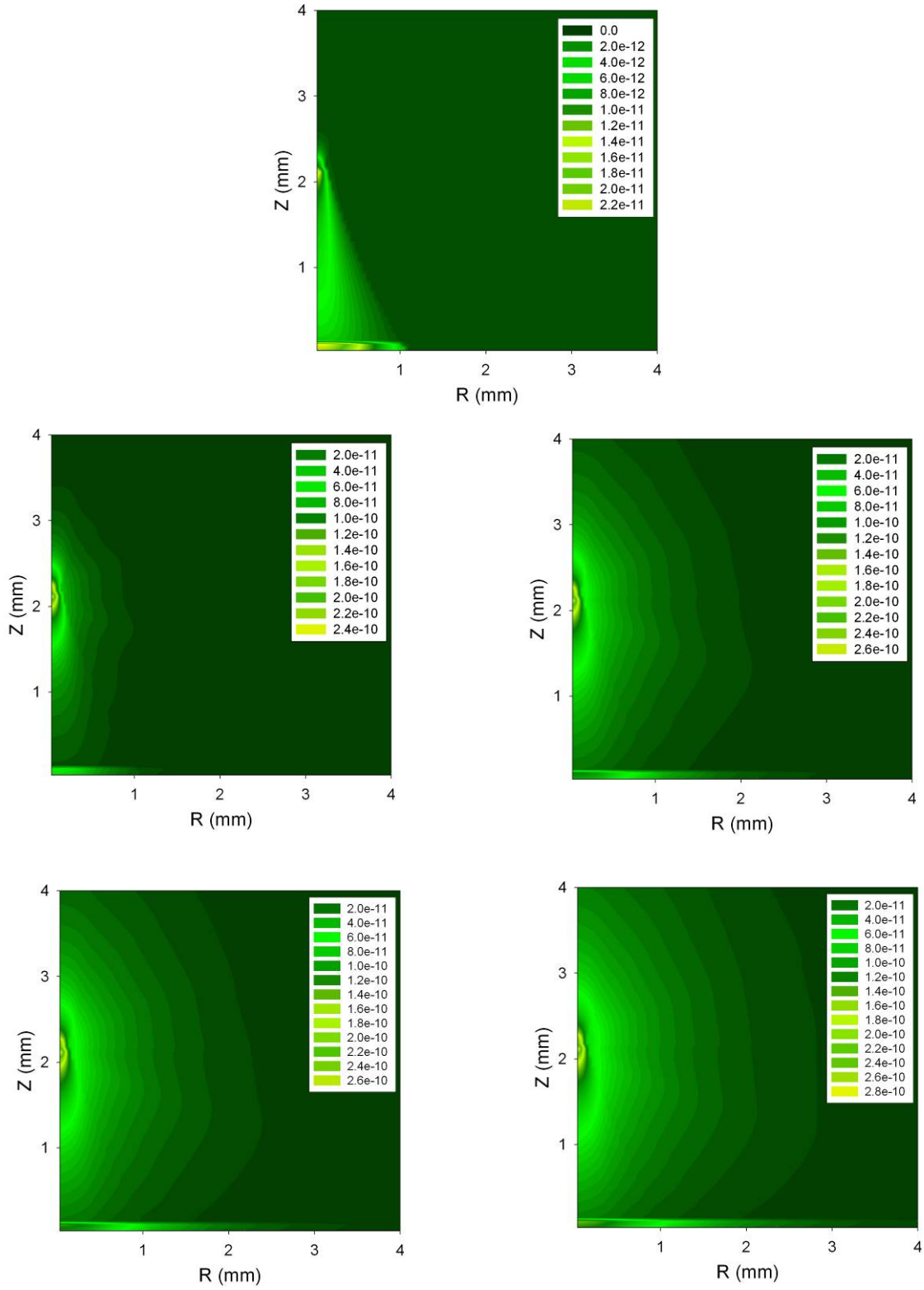

Figure 2.33 The accumulated contours of divergence of radiative heat flux at certain time instant: (a) t = 20 ps, (b) t = 40 ps, (c) t = 80 ps, (d) t = 200 ps, and (e) t = 400 ps.

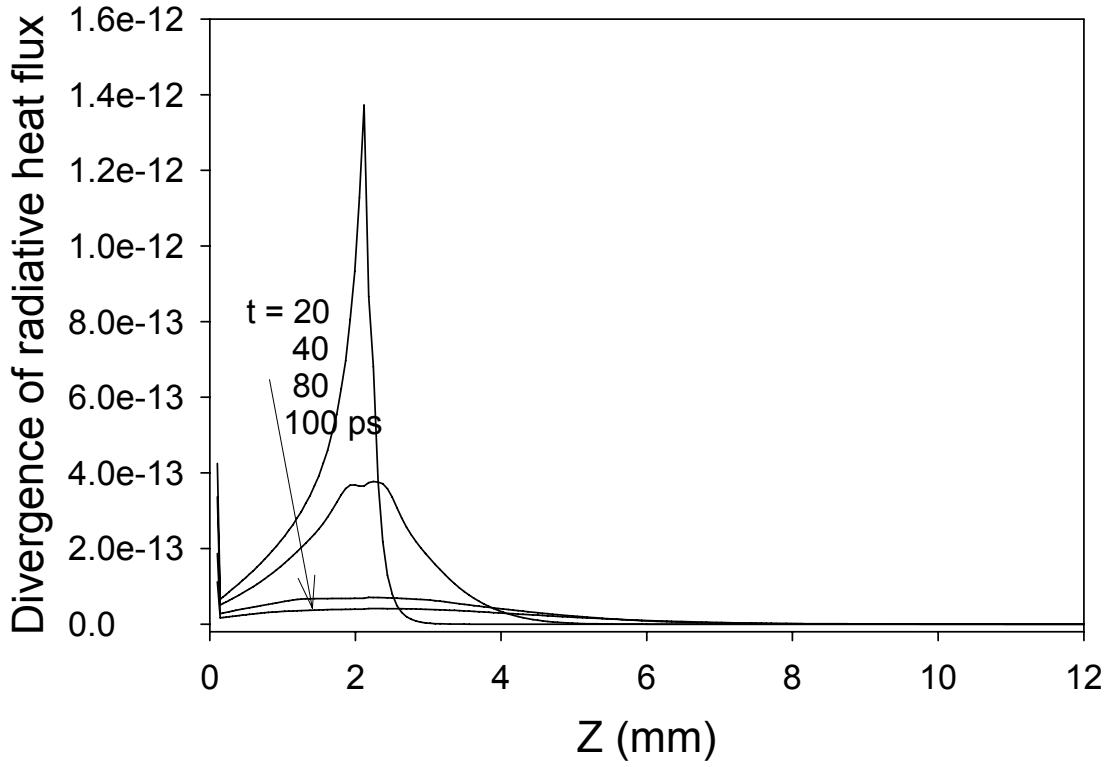

(a)

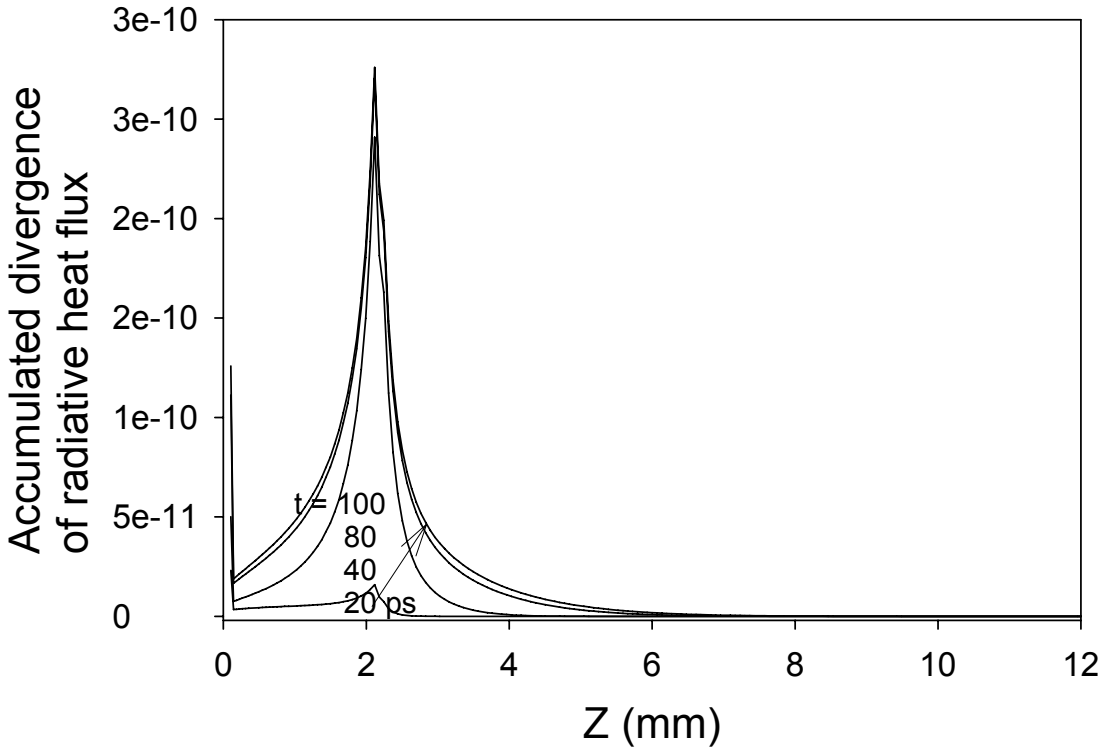

(b)

Figure 2.34 The divergence of radiative heat flux (a) and the accumulated divergence of radiative heat flux (b) along the optical axis at certain time instant.

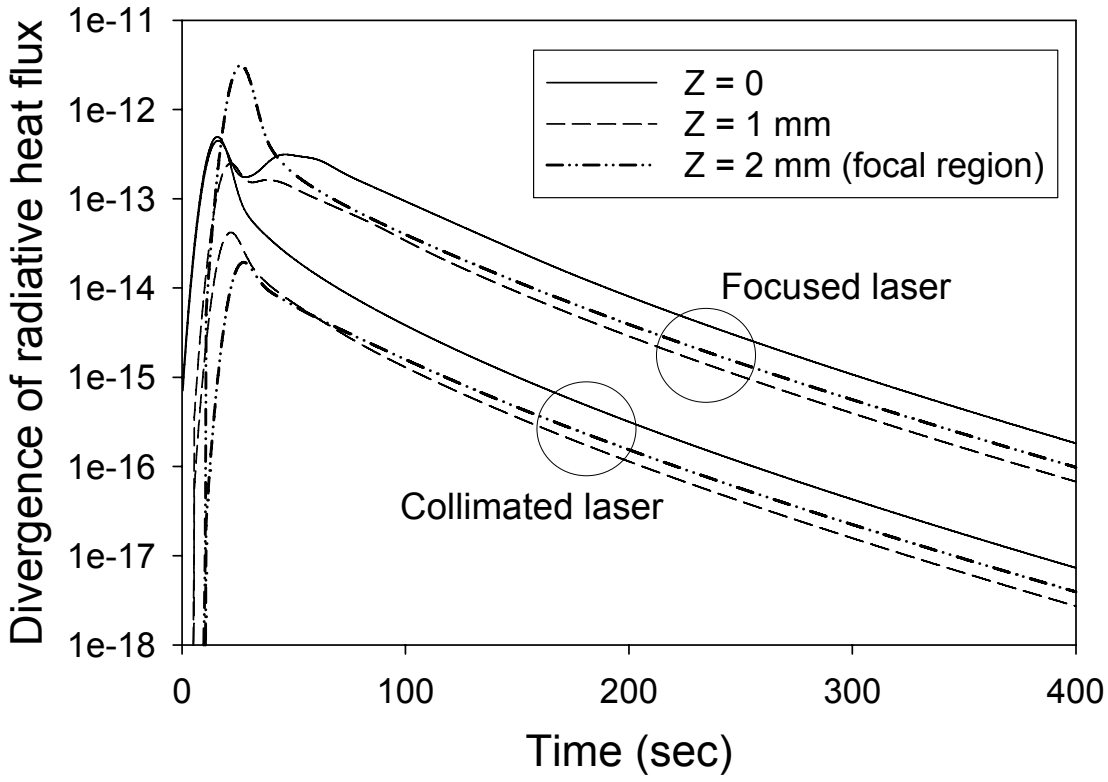

Figure 2.35 The comparison between collimated laser beam and focused laser beam with the temporal profiles of the divergence of radiative heat flux at selective locations along the optical axis.

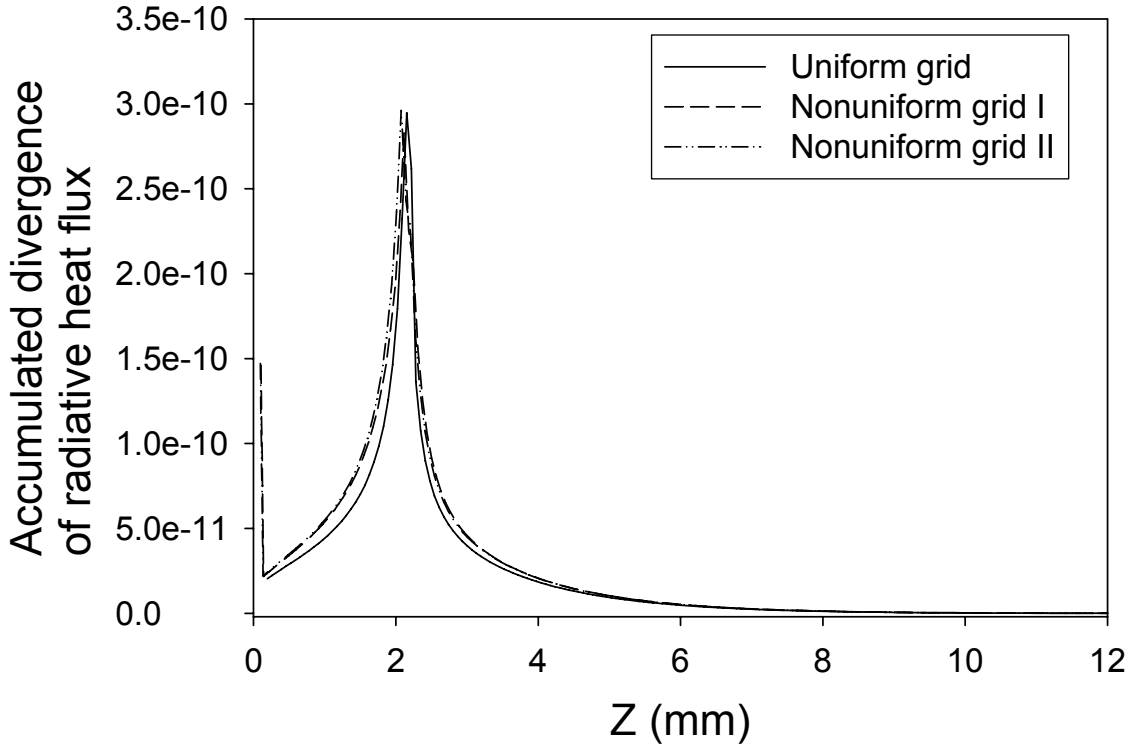

(a)

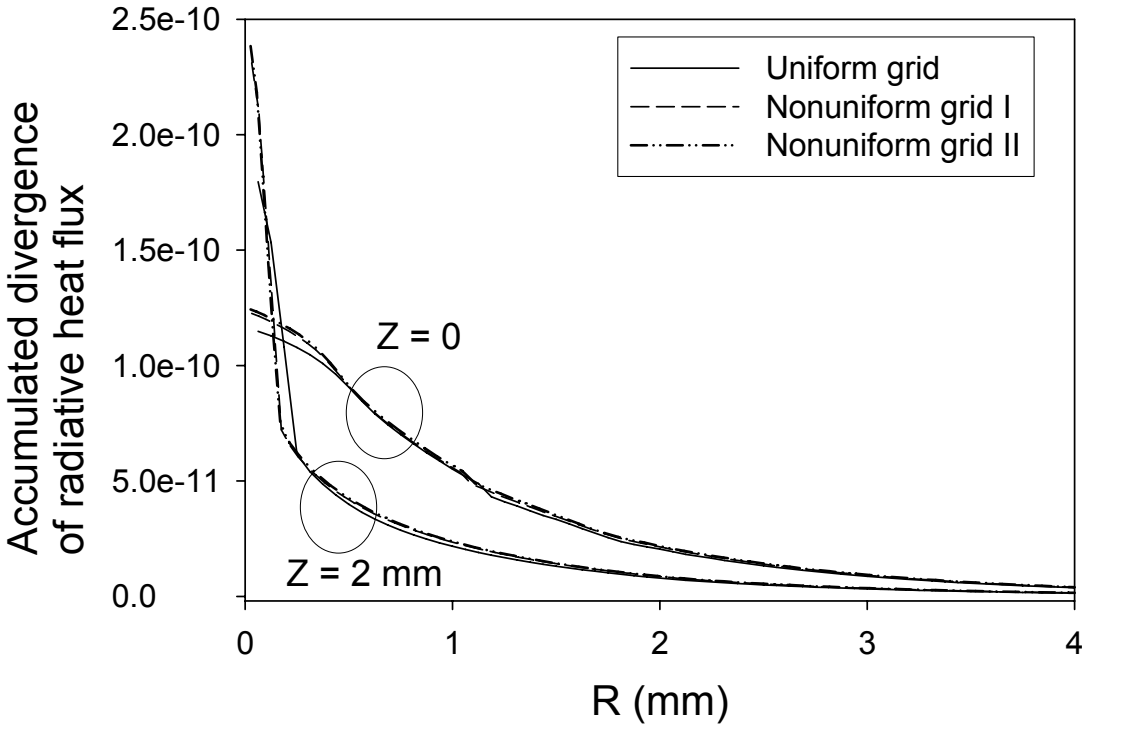

(b)

Figure 2.36 The grid system comparison with accumulated divergence of radiative heat flux at t = 200 ps (a) Axial profiles along the optical axis and (b) Radial profiles along the tissue surface.

Chapter 3

The transient heat conduction

In this chapter, the transient heat conduction is modeled with both hyperbolic conduction and parabolic heat conduction. To predict the thermal response prediction during the short pulse laser irradiation, the heat conduction should be modeled. The transient heat conduction model will be formulated. The numerical method will be introduced. The solution of certain problem will be validated with existing analytical solution.

3.1 Mathematical models

The local temperature response for the axisymmetric cylindrical geometric enclosure is governed by the following energy equation,

$$\rho C_p \frac{\partial T(r,z,t)}{\partial t} = -\nabla \cdot \left[\mathbf{q}_{cond}(r,z,t) + \mathbf{q}_{rad}(r,z,t)\right], \tag{3.1}$$

where ρ is the density, C_p is the specific heat, and T is the temperature. The $\mathbf{q}_{cond}(r,z,t)$ and $\mathbf{q}_{rad}(r,z,t)$ represent the conductive heat flux vector and radiative heat flux vector, respectively. If only conductive heat transfer is considered, the radiative heat flux vector can be neglected. The radiative heat flux vector plays the role of the source term in the

energy equation. In hyperbolic thermal wave theory, the conductive heat flux vector is expressed by [37]

$$\tau \frac{\partial \mathbf{q}_{cond}(r,z,t)}{\partial t} + \mathbf{q}_{cond}(r,z,t) = -k\nabla T(r,z,t)\,, \tag{3.2}$$

where the thermal relaxation time τ is introduced. The speed of thermal wave is

$$c_t = \sqrt{\alpha / \tau}\,. \tag{3.3}$$

where α is the thermal diffusivity. When $\tau \to 0,\ c_t \to \infty$; and Eq. (3.3) regresses to the traditional Fourier expression.

$$\rho C_p \frac{\partial T(r,z,t)}{\partial t} = -\left(\frac{\partial q_{cond,r}(r,z,t)}{\partial r} + \frac{q_{cond,r}(r,z,t)}{r} + \frac{\partial q_{cond,z}(r,z,t)}{\partial z} \right). \tag{3.4}$$

For the sake of analysis, the hyperbolic conduction equations are converted to vector form with non-dimensional variables as follows:

$$\frac{\partial \mathbf{E}}{\partial \xi} + \frac{\partial \mathbf{F}}{\partial \chi} + \frac{\partial \mathbf{G}}{\partial \eta} + \mathbf{H} = 0 \tag{3.5a}$$

where

$$\mathbf{E} = \begin{bmatrix} \theta \\ Q_\chi \\ Q_\eta \end{bmatrix},\ \mathbf{F} = \begin{bmatrix} Q_\chi \\ \theta \\ 0 \end{bmatrix},\ \mathbf{G} = \begin{bmatrix} Q_\eta \\ 0 \\ \theta \end{bmatrix},\ \mathbf{H} = \begin{bmatrix} Q_\chi / \chi \\ Q_\chi \\ Q_\eta \end{bmatrix}, \tag{3.5b}$$

and the non-dimensional variables are defined as:

$$\chi = \frac{r}{\sqrt{\alpha\tau}},\ \eta = \frac{z}{\sqrt{\alpha\tau}},\ \xi = \frac{t}{\tau}\ ,$$

$$Q_\chi = \frac{q_{cond,r}\sqrt{\alpha\tau}}{k(T_{ref} - T_i)},\ Q_\eta = \frac{q_{cond,z}\sqrt{\alpha\tau}}{k(T_{ref} - T_i)},\ \theta = \frac{T - T_i}{T_{ref} - T_i}\,. \tag{3.6}$$

where T_{ref} is the reference temperature and T_i is the initial temperature.

3.2 Numerical scheme-MacCormack's predictor-corrector scheme

A survey of numerical schemes for the solution of the hyperbolic heat conduction equation can be grouped into three categories: analytical, finite-difference, and finite-element methods. Due to the complexity of the hyperbolic heat conduction equation, only a simply cases can be solved analytically. Analytical solution has been developed using methods of Laplace transform [54-56], Fourier transform [57, 58], Green's function [59, 60], and integral equation [61].

Many numerical methods have been developed to solve the hyperbolic heat conduction problem. MacCormack's predictor-corrector scheme has been known to deal with thermal wave propagation very well in 1-D problems [62, 63]. Chen and Lin devised a finite-difference scheme based on Laplace transform and control-volume methods together with a hyperbolic shape function to solve the hyperbolic heat conduction [64]. Specially tailored transfinite-element [65] and explicit Lax-Wendroff-based finite-element methods [66] have been developed to study heat conduction involving non-Fourier effect. For the present study, MacCormack's predictor-corrector scheme is employed in following reasons:

(1) It is proved to deal well with thermal wave propagation.

(2) The discretization is relatively simple.

(3) The calculation time is quite fast. It is most important factor due to combine with the radiative heat transfer problem.

Here it is extended to the 2-D axisymmetric cylindrical problems. The discretized forms of the non-dimensional hyperbolic conduction equations are as follows:

Predictor:

$$\widetilde{\mathbf{E}}_{i,j}^{n+1} = \mathbf{E}_{i,j}^{n} - \nu_x\left(\mathbf{F}_{i+1,j}^{n} - \mathbf{F}_{i,j}^{n}\right) - \nu_y\left(\mathbf{G}_{i,j+1}^{n} - \mathbf{G}_{i,j}^{n}\right) - \Delta\xi\mathbf{H}_{i,j}^{n} \tag{3.7a}$$

Corrector:

$$\mathbf{E}_{i,j}^{n+1} = \frac{1}{2}\left[\mathbf{E}_{i,j}^{n} + \widetilde{\mathbf{E}}_{i,j}^{n+1} - \nu_x\left(\widetilde{\mathbf{F}}_{i,j}^{n+1} - \widetilde{\mathbf{F}}_{i-1,j}^{n+1}\right) - \nu_y\left(\widetilde{\mathbf{G}}_{i,j}^{n+1} - \widetilde{\mathbf{G}}_{i,j-1}^{n+1}\right) - \Delta\xi\widetilde{\mathbf{H}}_{i,j}^{n+1}\right] \tag{3.7b}$$

If those equation can be rewritten in the scalar expression as,

Predictor:

$$\widetilde{Q}_{x\,i,j}^{n+1} = (1-\Delta\xi)\,Q_{x\,i,j}^{n} - \frac{\Delta\xi}{\Delta\chi}\left(\theta_{i+1,j}^{n} - \theta_{i,j}^{n}\right) \tag{3.8a}$$

$$\widetilde{Q}_{\eta\,i,j}^{n+1} = (1-\Delta\xi)\,Q_{\eta\,i,j}^{n} - \frac{\Delta\xi}{\Delta\eta}\left(\theta_{i,j+1}^{n} - \theta_{i,j}^{n}\right) \tag{3.8b}$$

$$\widetilde{\theta}_{i,j}^{n+1} = \theta_{i,j}^{n} - \frac{\Delta\xi}{\Delta\chi}\left(Q_{\chi i+1,j}^{n} - Q_{\chi i,j}^{n}\right) - \frac{\Delta\xi}{\Delta\eta}\left(Q_{\eta i,j+1}^{n} - Q_{\eta i,j}^{n}\right) \tag{3.8c}$$

Corrector:

$$Q_{x\,i,j}^{n+1} = \frac{1}{2}\left[Q_{x\,i,j}^{n} + \widetilde{Q}_{x\,i,j}^{n+1} - \frac{\Delta\xi}{\Delta\chi}\left(\widetilde{\theta}_{i,j}^{n+1} - \widetilde{\theta}_{i-1,j}^{n+1}\right) - \Delta\xi\,\widetilde{Q}_{x\,i,j}^{n+1}\right] \tag{3.8d}$$

$$Q_{\eta\,i,j}^{n+1} = \frac{1}{2}\left[Q_{\eta\,i,j}^{n} + \widetilde{Q}_{\eta\,i,j}^{n+1} - \frac{\Delta\xi}{\Delta\eta}\left(\widetilde{\theta}_{i,j}^{n+1} - \widetilde{\theta}_{i,j-1}^{n+1}\right) - \Delta\xi\,\widetilde{Q}_{\eta\,i,j}^{n+1}\right] \tag{3.8e}$$

$$\theta_{i,j}^{n+1} = \frac{1}{2}[\theta_{i,j}^{n} + \widetilde{\theta}_{i,j}^{n+1} - \frac{\Delta\xi}{\Delta\chi}(\widetilde{Q}_{\chi\,i,j}^{n+1} - \widetilde{Q}_{\chi\,i-1,j}^{n+1}) - \frac{\Delta\xi}{\Delta\eta}(\widetilde{Q}_{\eta\,i,j}^{n+1} - \widetilde{Q}_{\eta\,i,j-1}^{n+1})] \tag{3.8f}$$

Von Neumann stability analysis is conducted and the stability criterion is:

$$\nu_x^2 + \nu_y^2 \le 1 \tag{3.9}$$

The two Courant numbers are defined as $\nu_x = \Delta\xi/\Delta\chi$ and $\nu_y = \Delta\xi/\Delta\eta$.

MacCormack's scheme is explicit and has second-order accuracy. The modified equation is determined as

$$\frac{\partial \mathbf{E}}{\partial \xi}+\frac{\partial \mathbf{F}}{\partial \chi}+\frac{\partial \mathbf{G}}{\partial \eta}+\mathbf{H}+\frac{\partial}{\partial \chi}\left(\Delta_2\mathbf{F}+\Delta_3\mathbf{F}\right)+\frac{\partial}{\partial \eta}\left(\Delta_2\mathbf{G}+\Delta_3\mathbf{G}\right)+O(\Delta^4)=0\,, \qquad (3.10a)$$

where the error terms are

$$\Delta_2\mathbf{F}=\frac{1}{3!}(\Delta\chi)^2\left[\left(1-\nu_x^2\right)\frac{\partial^2\mathbf{F}}{\partial\chi^2}\right],\ \Delta_2\mathbf{G}=\frac{1}{3!}(\Delta\eta)^2\left[\left(1-\nu_y^2\right)\frac{\partial^2\mathbf{G}}{\partial\eta^2}\right], \qquad (3.10b)$$

$$\Delta_3\mathbf{F}=\frac{1}{4!}(\Delta\chi)^3\left[3\nu_x\left(1-\nu_x^2\right)\frac{\partial^3\mathbf{F}}{\partial\chi^3}\right],\ \Delta_3\mathbf{G}=\frac{1}{4!}(\Delta\eta)^3\left[3\nu_y\left(1-\nu_y^2\right)\frac{\partial^3\mathbf{G}}{\partial\eta^3}\right]. \qquad (3.10c)$$

Because of the stability constrain, the Courant numbers cannot be unity. Thus, the error terms in Eq. (3.10) exist and correction of the error terms in Eq. (3.5) is important because it is the modified equation that is actually solved when Eq. (3.5) is integrated by MacCormack's scheme. This can be done by subtracting the error terms from Eq. (3.5), which then becomes

$$\frac{\partial \mathbf{E}}{\partial \xi}+\frac{\partial \mathbf{F}_0}{\partial \chi}+\frac{\partial \mathbf{G}_0}{\partial \eta}+\mathbf{H}=0\,, \qquad (3.11a)$$

where

$$\mathbf{F}_0=\mathbf{F}-\Delta_2\mathbf{F}-\Delta_3\mathbf{F}\,, \qquad (3.11b)$$

$$\mathbf{G}_0=\mathbf{G}-\Delta_2\mathbf{G}-\Delta_3\mathbf{G}\,. \qquad (3.11c)$$

When MacCormack's method is applied to Eq. (3.11), the resulting modified equation does not contain the second-order and third-order error terms. In the present computations, the error terms are discretized by second-order accurate approximations.

3.3 The test of MacCormack's predictor-corrector scheme

The current computational code is validated through comparison of numerical results with analytical solutions. Let's consider a hyperbolic heat conduction problem in a

semi-infinite region due to axisymmetric continuous or pulsed surface heat sources as Figure 3.1. The problem has been described and analytically solved by Kim et al. [55]. The irradiation source is simplified as a surface heat flux. In the calculations both the non-dimensional radius and thickness of the cylinder are set at 1.5.

3.3.1 Boundary, initial conditions and source term

The initial and boundary conditions are followed by compared problem's one [55] directly and specified as below,

$$T = T_0, \qquad \text{for } t = 0 \tag{3.12a}$$

$$\frac{\partial T}{\partial t} = 0, \qquad \text{for } t = 0 \tag{3.12b}$$

$$q_z = q_0 \; f(t)\, e^{\frac{-r^2}{R^2}}, \qquad \text{at } z = 0 \tag{3.12c}$$

The source term is implemented by the entire surface heat flux as Figure 3.1. Where, Gaussian heat flux is employed. The parameter R is a characteristic beam radius which represents the circular boundary within the Gaussian source that contains 63 % of the total power incident to the surface. The function $f(t)$ represents the temporal profile.

$$f(t) = 1, \qquad \text{for Continuous source} \tag{3.13a}$$

$$f(t) = u(t) - t(t_0), \qquad \text{for Single pulse source} \tag{3.13b}$$

where, $u(t)$ is the step function and pulse duration is t-t_0.

3.3.2 The validation result

Figures 3.2 (a) and (b) show the comparisons of the calculations with the analytical exact solutions for the continuous and single pulse sources, respectively. The

non-dimensional temperature profiles along the cylinder centerline at different time instants are selected for comparison. Various grid sizes are considered in the calculations with a constant Courant number of 0.5. It is seen that the numerical results for the case with a continuous source match excellently with the exact solutions. The sharp wave fronts are well captured. The numerical results for the case with a single pulse source generally match with the exact solutions. The grid size influences the quality of the simulated wave fronts in Figure 3.2 (b). With coarse grid sizes the dissipative effect is obvious and the gradients at the wave fronts tilt. With refining grid sizes the sharp wave fronts are well captured. However, it is worthy of mentioning that the refining of grid system will increase computer memory and CPU time; and there is always a compromise between accuracy and computation costs.

Figure 3.3 shows the comparison result with temporal temperature profiles between numerical and analytical solution. The temporal profiles are compared at the selective location in the cylinder centerline. The results are matched well in both locations. By the error analysis, the maximum error is within 2 %.

Figure 3.4 demonstrates the importance of the error terms correction in MacCormack's scheme using the above exemplary problem. The grid size is $\Delta\chi = \Delta\eta =$ 0.001 and the Courant number is still 0.5. Strong numerical oscillations at the wave fronts are observed in the numerical results without correction of the error terms. These oscillations are due to the dominance of the odd derivate error terms over the even derivate term. However, the numerical oscillations are eliminated when the error terms are corrected.

3.3.3 Parabolic heat conduction

The parabolic heat conduction is also modeled and solved to compare the hyperbolic conduction. The governing equation can be achieved by the elimination of first term of Eq. (3.2). Similar with previous approach, the parabolic conduction equations are converted to vector form with non-dimensional variables as follows:

$$\frac{\partial \mathbf{E}}{\partial \xi}+\frac{\partial \mathbf{F}}{\partial \chi}+\frac{\partial \mathbf{G}}{\partial \eta}+\mathbf{H}=0 \tag{3.14a}$$

where

$$\mathbf{E}=\begin{bmatrix}\theta\\0\\0\end{bmatrix},\ \mathbf{F}=\begin{bmatrix}Q_\chi\\\theta\\0\end{bmatrix},\ \mathbf{G}=\begin{bmatrix}Q_\eta\\0\\\theta\end{bmatrix},\ \mathbf{H}=\begin{bmatrix}Q_\chi/\chi\\Q_\chi\\Q_\eta\end{bmatrix}, \tag{3.14b}$$

The discretized equation can be derived as follow:

$$\theta_{i,j}^{n+1}=\theta_{i,j}^{n}-\frac{\Delta\xi}{\Delta\chi}\left[Q_{\chi i+1,j}^{n}-Q_{xi,j}^{n}\right]-\frac{\Delta\xi}{\Delta\eta}\left[Q_{\eta i,j+1}^{n}-Q_{\eta i,j}^{n}\right]-\frac{\Delta\xi}{2}\left[Q_{\chi i,j}^{n}-Q_{xi-1,j}^{n}\right] \tag{3.15a}$$

$$Q_{\chi}^{n}=-\left[\frac{\theta_{i+1,j}^{n}-\theta_{i,j}^{n}}{\Delta\chi}\right] \tag{3.15b}$$

$$Q_{\eta}^{n}=-\left[\frac{\theta_{i,j+1}^{n}-\theta_{i,j}^{n}}{\Delta\eta}\right] \tag{3.15c}$$

Von Neumann stability analysis is conducted and the stability criterion is:

$$\frac{\Delta\xi}{\Delta\chi^{2}}+\frac{\Delta\xi}{\Delta\eta^{2}}\le\frac{1}{2} \tag{3.16}$$

The comparison is conducted with analytical solution. In Figure 3.5, the temperature profile at two selected time instants along the cylinder centerline is shown.

The numerical result for parabolic conduction model is well matched with analytical solution. In Figure 3.6, the comparison is conducted with temporal temperature profiles. Both continuous and pulsed source results are shown in good agreement with analytical solution.

3.4 Summary

In this chapter, the hyperbolic and parabolic heat conduction were modeled and solved with numerical method. For the hyperbolic conduction, the MacCormack's predictor-corrector scheme was employed. The grid system was tested and selected. As the fine grid is selected, the numerical result was well matched with analytical solution. The governing equation was corrected until second order error terms. With the error terms correction, the strong numerical oscillations at the wave fronts can be reduced. The numerical results were well matched with analytical solution generally.

For the parabolic conduction model, the fully explicit method was used. The calculation results were shown in good agreement with analytical solution.

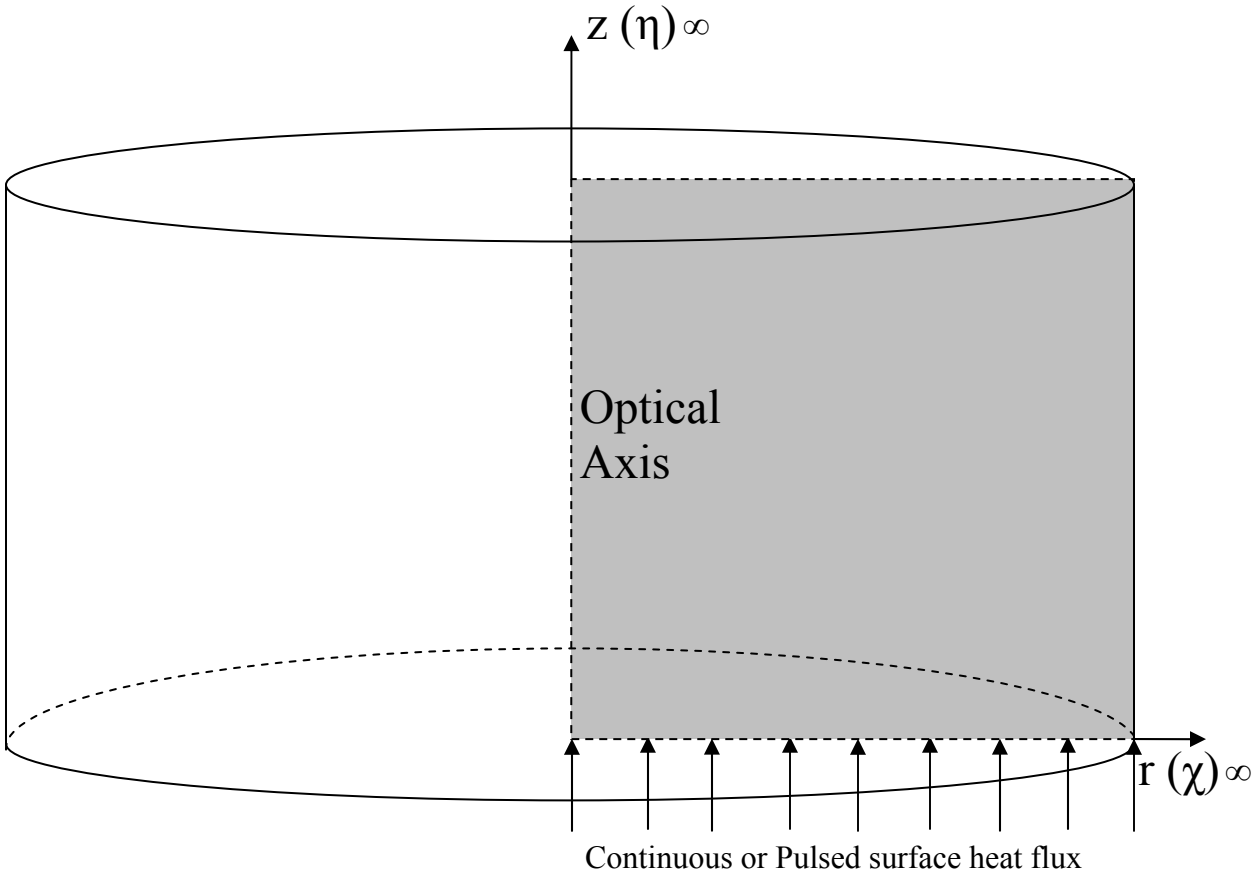

Figure 3.1 The schematic diagram for axisymmetric cylinder with surface heat flux source

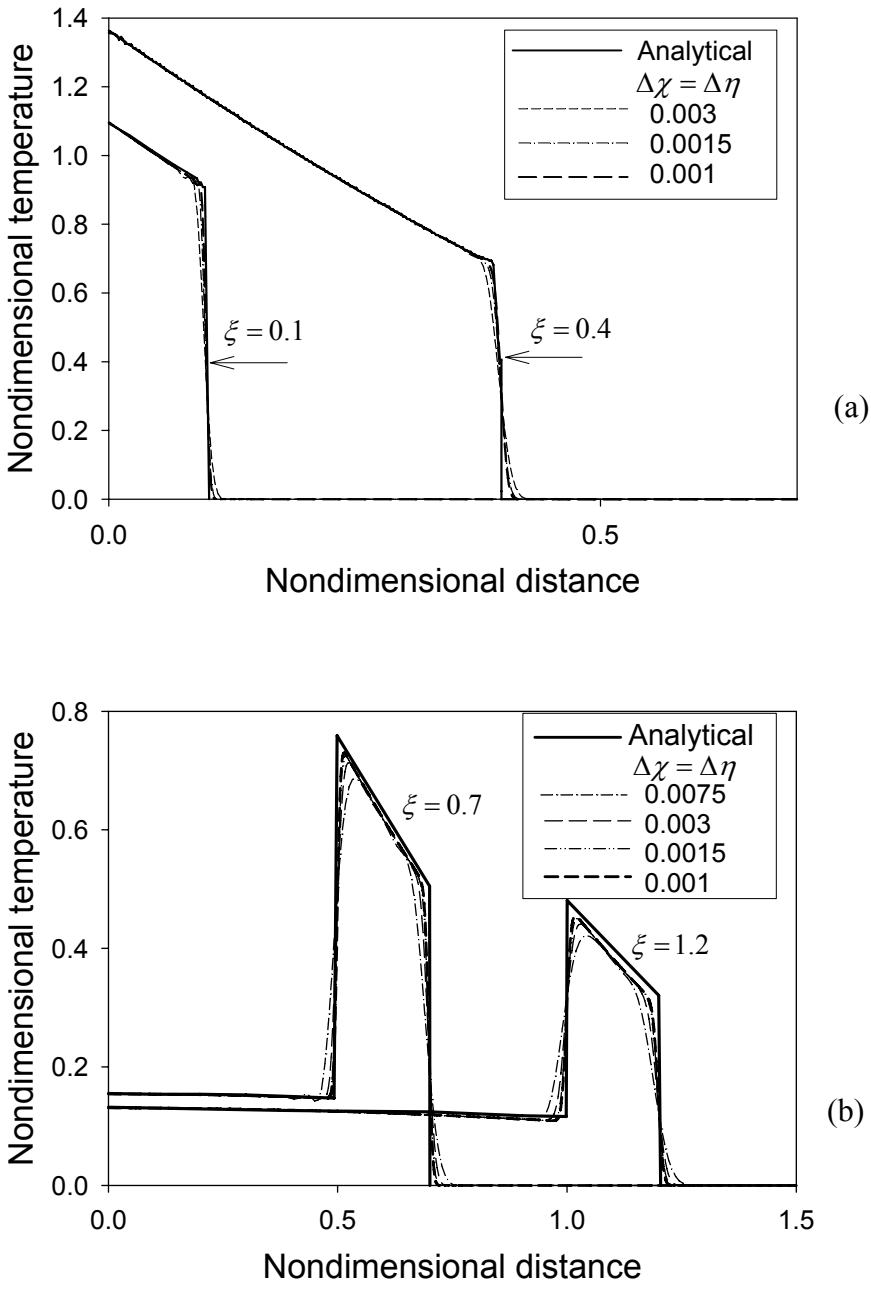

Figure 3.2 Comparison of the numerical results of hyperbolic conduction with the analytical solution [55] of the temperature profiles along the cylinder centerline: (a) continuous source; and (b) single pulse source.

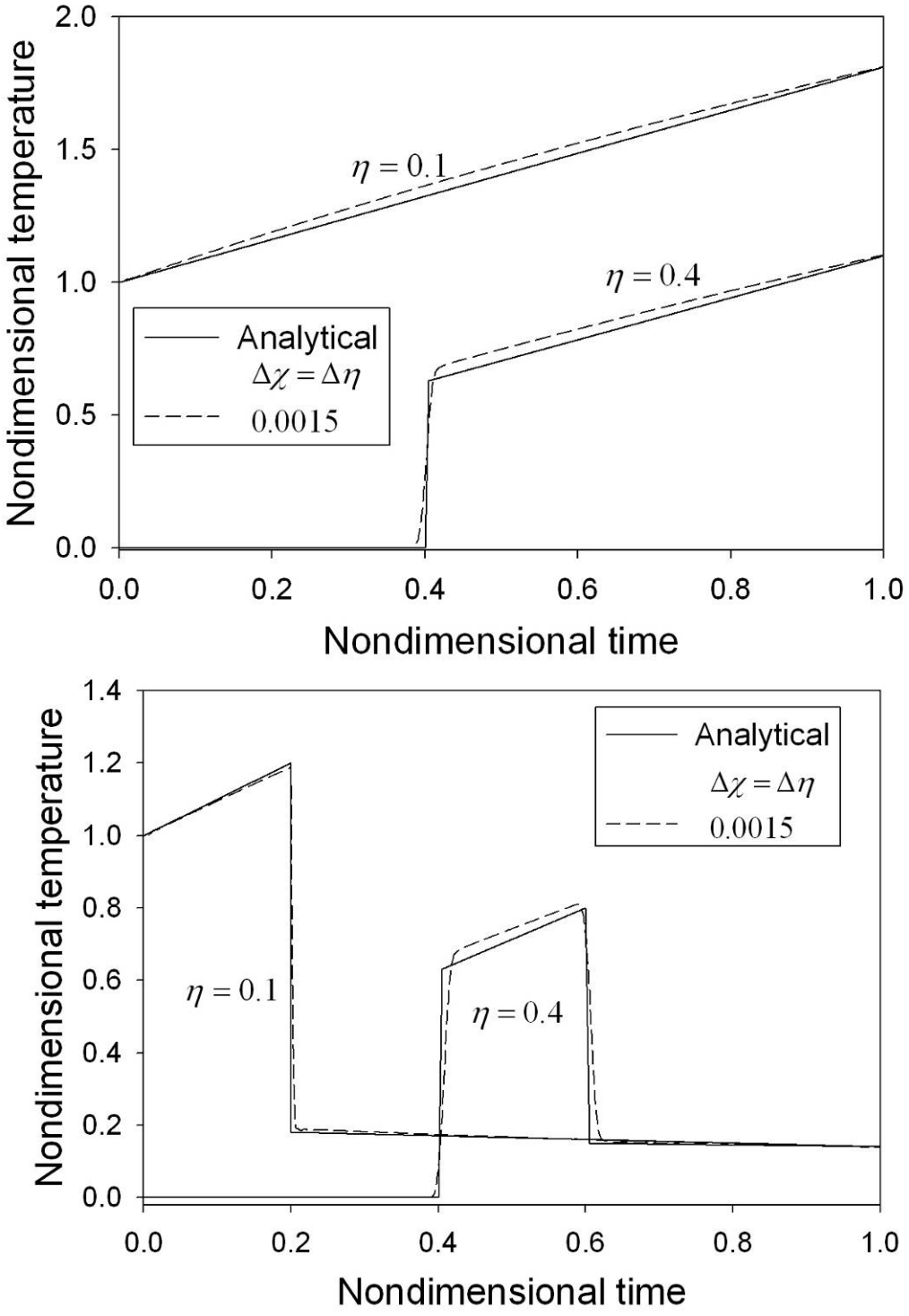

Figure 3.3 Comparison of the numerical results of hyperbolic conduction with the analytical solution [55] of the temporal temperature profiles at selective positions in the cylinder centerline: (a) continuous source; and (b) single pulse source.

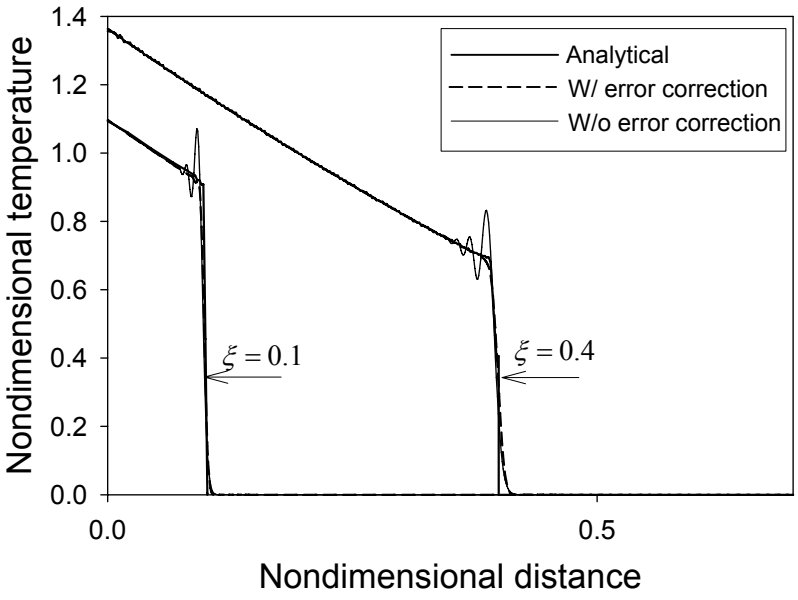

(a)

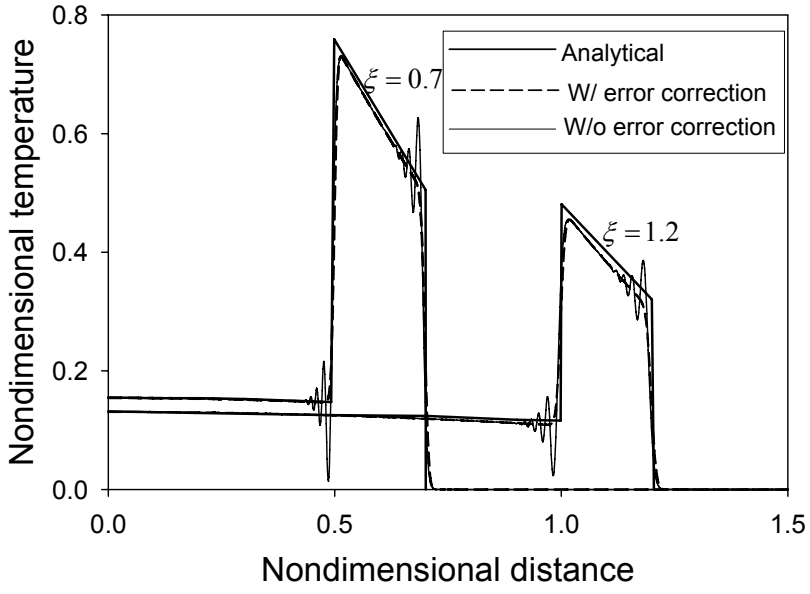

(b)

Figure 3.4 Comparisons of the calculated temperature profiles for hyperbolic conduction along the cylinder centerline with and without error terms correction: (a) continuous source; and (b)single pulse source.

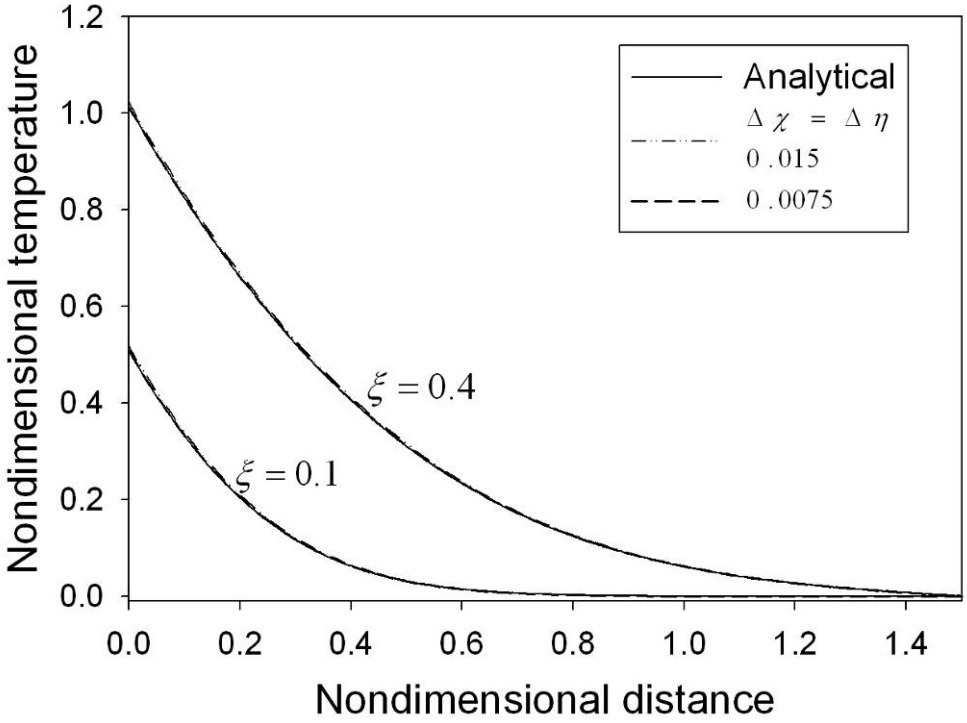

Figure 3.5 Comparison of the numerical results of parabolic conduction with the analytical solution [55] of the temperature profiles along the cylinder centerline with continuous surface source

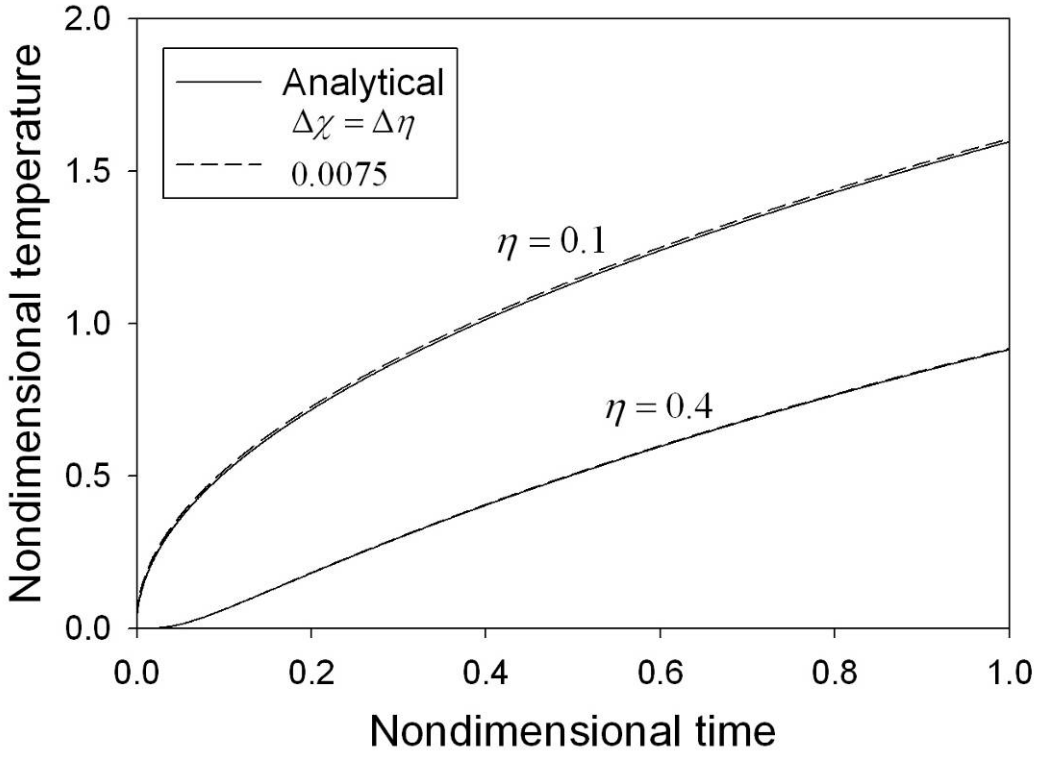

(a)

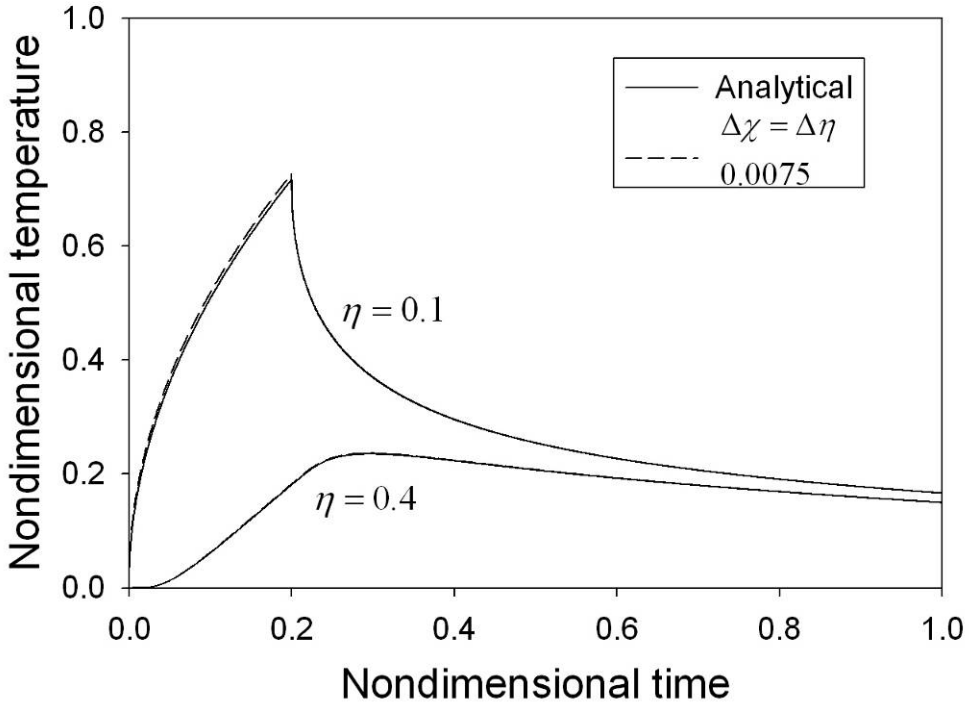

(b)

Figure 3.6 Comparison of the numerical results of parabolic conduction with the analytical solution [55] of the temporal temperature profiles at selective positions in the cylinder centerline: (a) continuous source; and (b) single pulse source.

Chapter 4

Multi-time-scale heat transfer modeling of turbid tissues exposed to short-pulsed irradiations

Many of the clinical procedures with lasers use the so-called non-ablative thermal mode of laser-tissue interaction [1, 2]; that is, tissue is heated and irreversibly damaged by absorption of the laser energy. The degree and extent of tissue thermal damage depends on the rate of heat generation and transfer. Fundamentals to these applications are knowledge of multi-time-scale heat transfer in biological tissues which includes ultrafast laser radiation transport in the micro/nano time scale and transient bio-heat transfer in the meso-time scale.

To analyze thermal response of a laser irradiated tissue and to avoid thermal damage to surrounding healthy tissue, combined thermal radiation and bio-heat modes must be considered. In the present study, I investigate the thermal response of biological tissues to short-pulsed irradiation and the importance of hyperbolic heat conduction in the prediction of accurate temperature distribution and development in the turbid tissue.

In this chapter, the heat transfer procedure is modeled by two steps. The first step is the radiation transfer dominant period during 1 ms. The 10 ps pulsed laser irradiate with pulse train until achieving proper radiation energy absorption. The radiation energy absorption is accumulated until radiation transfer reaches to the steady state. The second

step is the dissipation of absorbing radiation energy, which is modeled by the hyperbolic conduction and compared with the parabolic conduction.

4.1 Mathematical models

4.1.1 The heat transfer modeling

The local temperature response is governed by the following energy equation:

$$\rho C_p \frac{\partial T(r,z,t)}{\partial t} = -\nabla \cdot \left[\mathbf{q}_{cond}(r,z,t) + \mathbf{q}_{rad}(r,z,t)\right], \tag{4.1}$$

where ρ is the density, C_p is the specific heat, and T is the temperature. In hyperbolic thermal wave theory, the conductive heat flux vector is expressed by:

$$\tau \frac{\partial \mathbf{q}_{cond}(r,z,t)}{\partial t} + \mathbf{q}_{cond}(r,z,t) = -k\nabla T(r,z,t), \tag{4.2}$$

where the thermal relaxation time τ is introduced. The speed of thermal wave is

$$c_t = \sqrt{\alpha / \tau}. \tag{4.3}$$

where α is the thermal diffusivity. When $\tau \to 0$, $c_t \to \infty$; and Eq. (4.3) regresses to the traditional Fourier expression.

In the case of $t_p << \tau$, the dimensional analysis of Eqs. (4.1) and (4.2) reveals that within the short pulse duration neither thermal wave nor heat diffusion is important. The laser exposure time, t_r induced by pulsed train is 1 ms, and it is much smaller than thermal relaxation time. The radiative heat transfer will be dominant during this time period. It results in a much localized temperature response that can be described by

$$\rho C_p \frac{\partial T(r,z,t)}{\partial t} = -\nabla \cdot \mathbf{q}_{rad}(r,z,t). \tag{4.4}$$

In the meso-time scale after the turning-off of the short irradiation (1 ms), the energy equation in the axisymmetric cylindrical coordinates system is simplified as

$$\rho C_p \frac{\partial T(r,z,t)}{\partial t} = -\left(\frac{\partial q_{cond,r}(r,z,t)}{\partial r} + \frac{q_{cond,r}(r,z,t)}{r} + \frac{\partial q_{cond,z}(r,z,t)}{\partial z} \right). \tag{4.5}$$

For the sake of analysis, the hyperbolic conduction equations are converted to vector form with non-dimensional variables as follows:

$$\frac{\partial \mathbf{E}}{\partial \xi} + \frac{\partial \mathbf{F}}{\partial \chi} + \frac{\partial \mathbf{G}}{\partial \eta} + \mathbf{H} = 0 \tag{4.6a}$$

where

$$\mathbf{E} = \begin{bmatrix} \theta \\ Q_\chi \\ Q_\eta \end{bmatrix}, \ \mathbf{F} = \begin{bmatrix} Q_\chi \\ \theta \\ 0 \end{bmatrix}, \ \mathbf{G} = \begin{bmatrix} Q_\eta \\ 0 \\ \theta \end{bmatrix}, \ \mathbf{H} = \begin{bmatrix} Q_\chi / \chi \\ Q_\chi \\ Q_\eta \end{bmatrix}, \tag{4.6b}$$

and the non-dimensional variables are defined as:

$$\chi = \frac{r}{\sqrt{\alpha \tau}}, \ \eta = \frac{z}{\sqrt{\alpha \tau}}, \ \xi = \frac{t}{\tau} \ ,$$

$$Q_\chi = \frac{q_{cond,r}\sqrt{\alpha \tau}}{k(T_{ref} - T_i)}, \ Q_\eta = \frac{q_{cond,z}\sqrt{\alpha \tau}}{k(T_{ref} - T_i)}, \ \theta = \frac{T - T_i}{T_{ref} - T_i} \ . \tag{4.7}$$

In which T_i and T_{ref} are the tissue initial and reference temperatures, respectively. The reference temperature that represents the desirable temperature response induced by the irradiation is 65 °C in the present calculations. This quantity was reported as a proper temperature in laser tissue welding to achieve optimum welding strength.

4.1.2 The initial and boundary conditions

The tissue is assumed to be at a constant and uniform temperature of 37 °C initially. Except for the laser incident surface which is exposed to the ambient air at room temperature of 25 °C, all other surfaces of the tissue cylinder are surrounded with tissue; and thus, remained at the constant temperature. Thus, the initial and boundary conditions for the hyperbolic heat conduction model are given as

$$\theta = Q_\chi = Q_\eta = 0, \qquad \text{for } \xi = 0. \tag{4.16a}$$

$$\frac{\partial \theta(\chi,\eta,\xi)}{\partial \chi} = 0, \qquad \text{at } \chi = 0. \tag{4.16b}$$

$$Q_\eta = h^*(\theta_\infty - \theta), \qquad \text{at } \eta = 0. \tag{4.16c}$$

$$\theta = 0, \qquad \text{at } \chi = \chi_{\max} \text{ or } \eta = \eta_{\max}. \tag{4.16d}$$

where θ_∞ the non-dimensional ambient temperature and non-dimensional convective heat transfer coefficient is defined as $h^* = \sqrt{\alpha\tau}h/k$.

4.1.3 General assumptions

In the present models the following assumptions are adopted:

(1) The volume-average method is used for predicting local temperature response during a short irradiation period. Since the thermal wave speed in tissues is generally in the order of 10^{-4} mm/ms, the propagation of a thermal wave is 10^{-4} mm in 1 ms. As compared with the dimension of a turbid tissue (1 – 100 mm), thermal propagation and diffusion are negligible within 1 ms.

(2) Tissue radiation emission is neglected because the tissue blackbody intensity is much smaller than the incident laser intensity.

(3) Tissue optical and thermal properties are thermally stable during the heat transfer process.

(4) Blood perfusion and thermal evaporation and/or phase change of tissue during the heat transfer process are not considered.

4.2 Properties of tissue

4.2.1 Optical properties of tissue

In order to discuss light transport in tissue medium, the knowledge of optical properties should be preceding. The optical properties are changing by laser wavelength. The optical properties using in this chapter is summarized in Table 4.1

4.2.2 Thermal properties of tissue

The measurement of thermal diffusivity is important not only to predict temperature response but to find out thermal wave speed. Fortunately, the thermal diffusivity of live organ has relatively small variation compared with optical properties. Cohen measured the human skin thermal diffusivity as $\alpha = 0.142\, mm^2 / s$ in 70% water contained tissue condition [67].

4.3 Results and discussion

In Figure 4.1, the tissue model with cylinder shape is sketched and the optical properties are noted in table 4.1

Figure 4.2 shows the contours of the temperature fields in the dermis tissue subject to a 10 ps pulse at four different time instants. At t = 20 ps, the temperature field

is confined in a superficial regime around the laser spot. At t = 40 ps, the temperature field is penetrated axially due to radiation propagation. Also the magnitude of temperature at t = 40 ps is greater than that at t = 20 ps, because of the continuous absorption of the Gaussian irradiation (up to $3t_p$). The temperature fields at t = 100 and 500 ps are further enlarged as compared with the figure at t = 40 ps. However, the expansion speed of the temperature field gradually slows down. This is because the local temperature response depends on the local volume-average accumulation of radiation energy absorption. When the incident pulse is turned off after $3t_p$, the source for radiation absorption comes only from the scattered radiation. As time elapses, the scattered radiation becomes weaker and weaker.

In Figure 4.3, the heart tissue (Endocardium) is selected. Absorption and scattering properties of heart tissue is so small that the laser light penetrates into the deeper tissue medium. Then the temperature fields of it propagate deeply as shown in Figure. The speed of the temperature propagation is slower than dermis tissue case and the temperature increment after 100 ps is still predicted.

Figure 4.4 shows the temperature responses of three tissue types to a single 10 ps pulse at three selected positions in the centerline ($\chi = 0$; $\eta = 0,\ 0.5$, and 1). It is seen that, at the location of $\eta = 1$ the temperature in the heart tissue is much higher than the temperatures in the aorta and dermis tissues. The large absorption of the dermis tissue will confine the laser radiation in a small area. When the changes of the temporal temperatures at all locations become very flat, pseudo steady state of the temperature response is then reached. The time for achieving the pseudo steady state responding to a single short pulse depends mainly on the tissue properties. It is found that longer time is

required for weakly absorbing tissues, such as the heart tissue. Generally the temperature field will reach to pseudo steady state condition in 1 ns for all the considered tissues.

The pulse train response in the μs/ms time scales with negligible thermal wave and diffusion is then a simple addition of the pseudo steady state temperature of the single pulses. In Figure 4.5, the temporal temperature responses of the dermis tissue subject to pulse train irradiation (10^5 short pulses within 1 ms) are plotted at three selective positions. The responses are linear at all positions unless they are inspected in the ps/ns time scales as shown in Figure 4.4. In the following figures, the irradiation condition is assumed to be a pulse train of 10^5 pulses in 1 ms.

In the present studies, the incident laser power is adjusted to let the maximum temperature at the laser spot be a unity. Figure 4.6 shows the relationships between the maximum temperature at the laser spot center and the laser power density with pulse train irradiation for the four tissues. The smaller the tissue absorption coefficient, the higher is the required laser power. Thus, increasing tissue absorption in the target area is important in laser surgery and treatment applications. This can be realized through proper selection of laser wavelength [1], use of endogenous or exogenous chromophores [3, 12], etc. It should be mentioned that relationships are linear when tissue emission is neglected. A logarithmic scale is used in the abscissa in Figure 4.6.

The immediate temperature fields induced purely by radiation absorption of the pulse train are compared in Figure 4.7 between different tissue types. It is seen that the temperature patterns vary, depending on the tissue extinction coefficient. In the uterus tissue (has the largest σ_e among the four tissues), the temperature is concentrated in a very small region. In the heart tissue (has the smallest σ_e among the four tissues), the

temperature field penetrates to deep tissue. The temperature fields are similar in the aorta and dermis tissues because they have similar σ_e values.

Thermal wave propagation follows the immediate local temperature rise, but it is only significant in the meso-time scale. In Figure 4.8, the temporal temperature profiles in the dermis tissue at several selected locations are displayed. Strong wave behavior is observed when $0 < \xi < 4$ where the temperature changes periodically with decreasing amplitude. To understand the differences between the hyperbolic heat conduction and traditional Fourier parabolic heat diffusion, the results predicted by the parabolic diffusion model are also plotted in Figure 4.8. In the parabolic diffusion prediction, the temperature decays exponentially and more slowly than the hyperbolic counterpart. It is noticeable that the hyperbolic wave model predicts larger maximum temperatures at positions beyond the laser spot center than the parabolic diffusion model. When the time reaches to 10 thermal relaxation times, the thermal waves fade away and the predictions between the hyperbolic and parabolic models are consistent.

Figure 4.9 shows the contours of the temperature fields in the dermis tissue at various time stages. The results from both the hyperbolic and parabolic models are given for comparison. In the temperature distributions predicted by the hyperbolic model, clear wave front propagation is observed. The temperatures in the wave fronts are generally high, leading to larger magnitudes in the temperature spectra in the contours of hyperbolic modeling. As time elapses, the wave front weakens and a diffusion field is quickly developing behind the front. The temperature fields predicted by the parabolic model are concentrated in the vicinity around the laser spot and a large temperature gradient exists there.

In Figure 4.10, the maximum temperature maps in the dermis tissue are plotted for comparison between the hyperbolic and parabolic models, where the maximum temperature for each location during the entire hyperbolic or parabolic heat transfer process is selected. The maps are useful for estimating the thermal damage zone. It is found that in a small zone around the laser incident spot, the maximum temperature is determined by the direct radiation absorption. While in other regions, the hyperbolic model generally predicts larger maximum temperature than the parabolic model. Thus, its thermal damage zone is larger than that predicted by the parabolic model. This finding could be significant for many laser biomedical applications. The temperature difference between the two model predictions is further visualized in Figure 4.11. A 7% non-dimensional temperature increase is observed in some region with the hyperbolic prediction.

Figure 4.12 shows the nondimensional temperature profiles along the optical axis at certain time instant in heart tissue. By the radiation energy absorption, the temperature profile is achieved at 1 ms. Then the temperature profiles drop down as time advancing due to the hyperbolic conduction phenomena. The thermal wave propagation is observed clearly in early time instants and the amplitude of it decreases as time proceeding. Unique feature of thermal wave reflection takes places and it travels from the tissue end wall to the tissue surface as certain thermal speed.

In Figure 4.13, the temperature fields of heart tissue at various time stages are displayed and hyperbolic and parabolic conduction models are compared. The distribution of temperature field is similar between two models. However, the discontinuity of distribution is observed in the hyperbolic conduction model. At $\xi = 2$,

there exist two discontinuity locations of $\eta = 2$ and $\eta = 8$. Front thermal wave travels from tissue surface and second one returns from the end of tissue wall. At delayed time instants, the thermal wave of front location decays and shows almost diffusion aspect but the reflecting thermal wave is clearly shown in Figures.

The comparison between the two conduction models is conducted with temperature profiles along the optical axis in Figure 4.14. In early time instants, the thermal wave propagation is obvious in hyperbolic conduction model and the profiles become similar to the profiles of parabolic conduction model at $\xi = 8$.

Figure 4.15 shows the temporal temperature profiles along the tissue surface at selective locations. It shows the periodic thermal wave propagation to the radial direction as well as axial direction. The maximum temperature increment at each location in the hyperbolic conduction model is higher. The peak locations of it are shifted due to the thermal wave effect.

4.4 Summary

The combined radiation and conduction heat transfer model is proposed and employed to simulate multi-time-scale heat transfer in turbid tissues subject to short-pulsed irradiation. This model integrates three steps. In the first step, ultrafast radiation heat transfer of a tissue subject to a single ultrashort pulse irradiation is modeled; and an initial local temperature response at the ps/ns time scale is obtained. Pseudo steady state temperature response in the tissues is found within 1 ns. If the incident pulse or pulse train is in the μs/ms time scales, the temperature response is a simple accumulation of the pseudo steady state temperature for all the pulses. In the second step, thermal wave

propagation is considered at the meso-time scale. In the third step, thermal waves fade away and the parabolic heat diffusion predominates.

Accurate radiation heat transfer modeling is needed in order to predict local temperature rise due to radiation absorption because biological tissues are generally highly scattering. The temperature distribution pattern of a tissue induced by direct radiation absorption depends on the absorption coefficient as well as the extinction coefficient. For the uterus tissue, high temperature is concentrated in a very small region. While for the heart tissue, high temperature penetrates to deep tissue. The temperature fields are similar in the aorta and dermis tissues because of small difference in their extinction coefficients.

The temperatures in the dermis tissue subject to a pulse train irradiation predicted by the hyperbolic heat conduction are compared with the parabolic heat diffusion predictions. In the hyperbolic conduction modeling, temperature changes periodically with decreasing amplitude. In the parabolic conduction modeling, however, temperature rises first and then decays exponentially. After several thermal relaxation times the thermal wave behavior is substantially weakened and the predictions between the hyperbolic and parabolic models are consistent. The obtained maximum local temperature maps show that the hyperbolic model predicts a larger thermal damage zone than the parabolic model.

The temperature field in the heart tissue propagates deeply into the tissue medium since it has a small absorption and scattering characteristics. The thermal wave reflection is observed in heart tissue. As time advancing, the temperature field becomes consistent between the two conduction models.

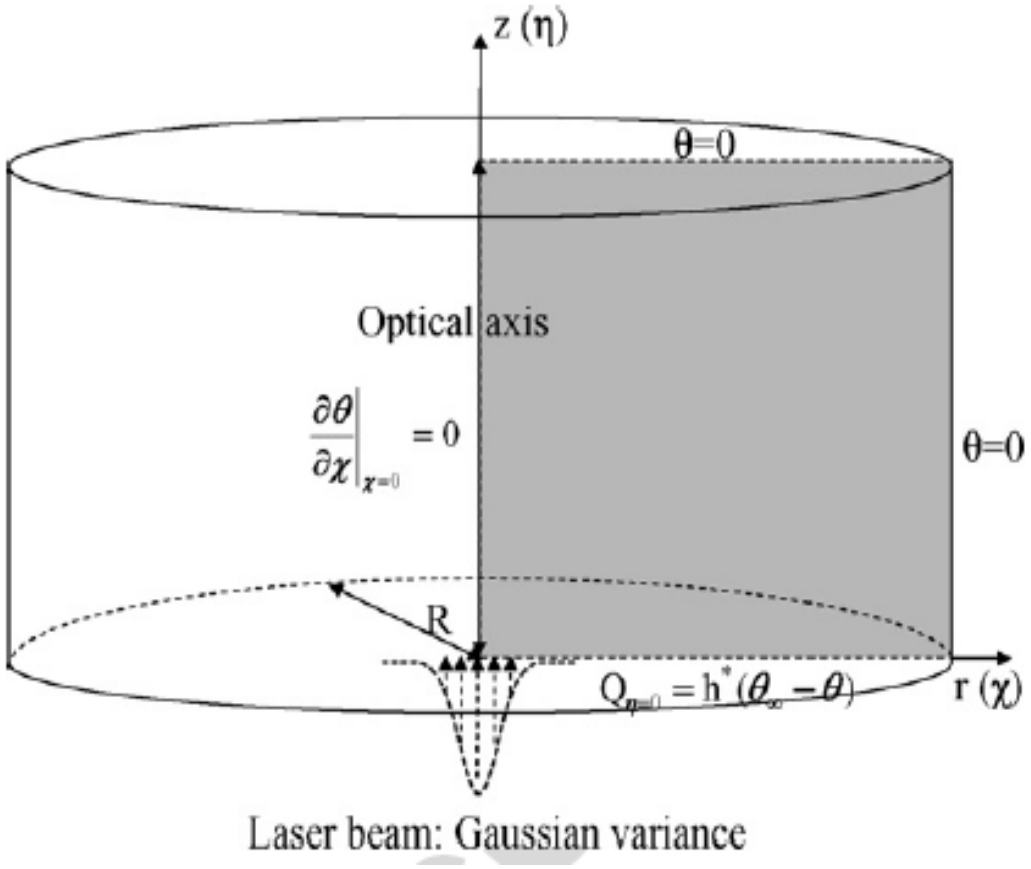

Figure 4.1 Geometric sketch of tissue model.

Tissue type	Wavelength (mm)	Absorption (mm^{-1})	Reduced scattering (mm^{-1})	Citation
Human dermis	633	0.27	3.55	[52]
Human aorta	632.8	0.052	4.1	[52]
Heart (Endocardium)	1060	0.007	0.367	[52]
Human uterus	635	0.035	12.214	[52]

Table 4.1 The optical properties of selective tissues.

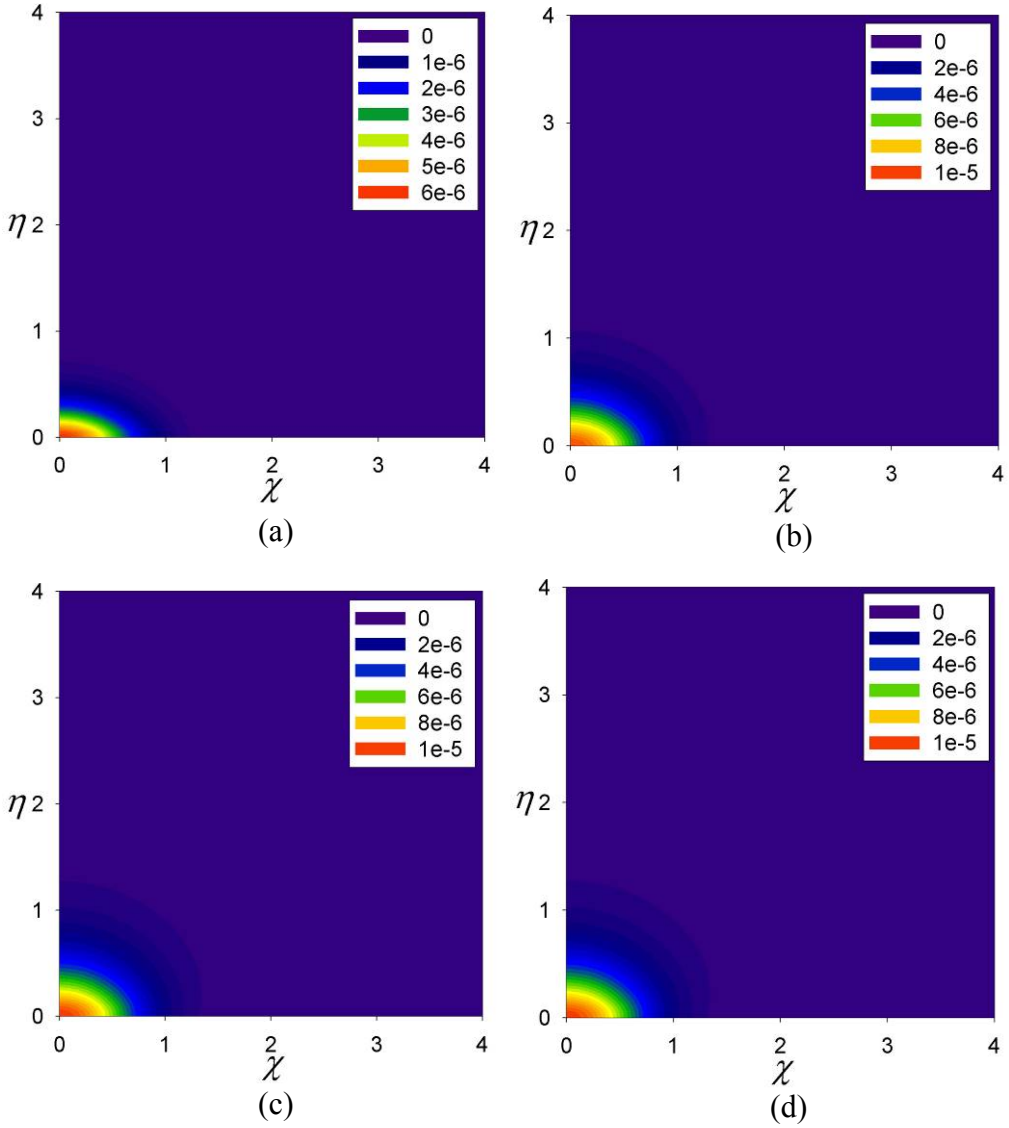

Figure 4.2 Contours of non-dimensional temperature fields of the dermis tissue subject to an ultrashort pulse irradiation at selected time instants at (a) t = 20 ps; (b) t = 40 ps; (c) t = 100 ps; and (d) t = 500ps.

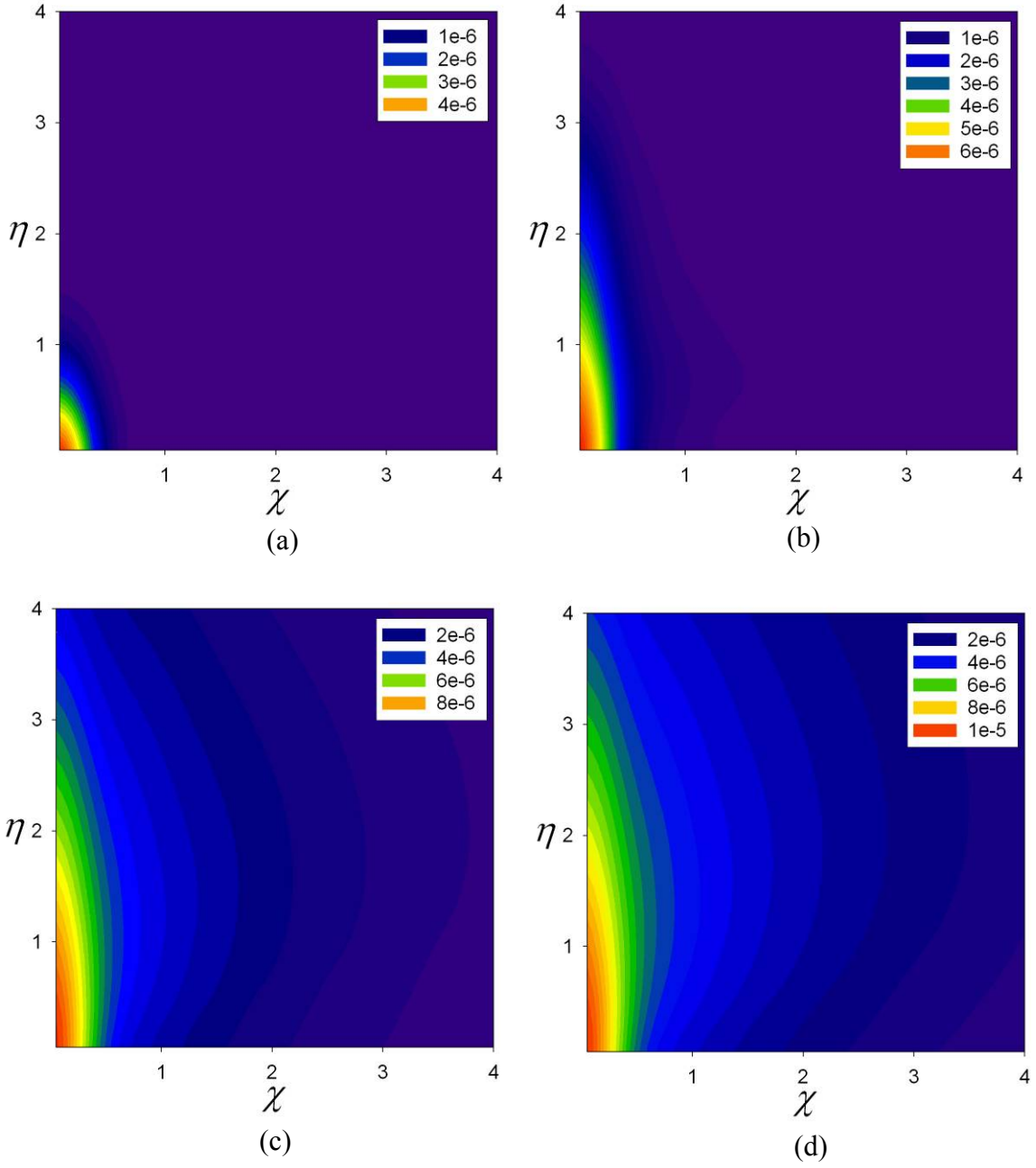

Figure 4.3 Contours of non-dimensional temperature fields of the Heart tissue subject to an ultrashort pulse irradiation at selected time instants at (a) t = 20 ps; (b) t = 40 ps; (c) t = 100 ps; and (d) t = 500ps.

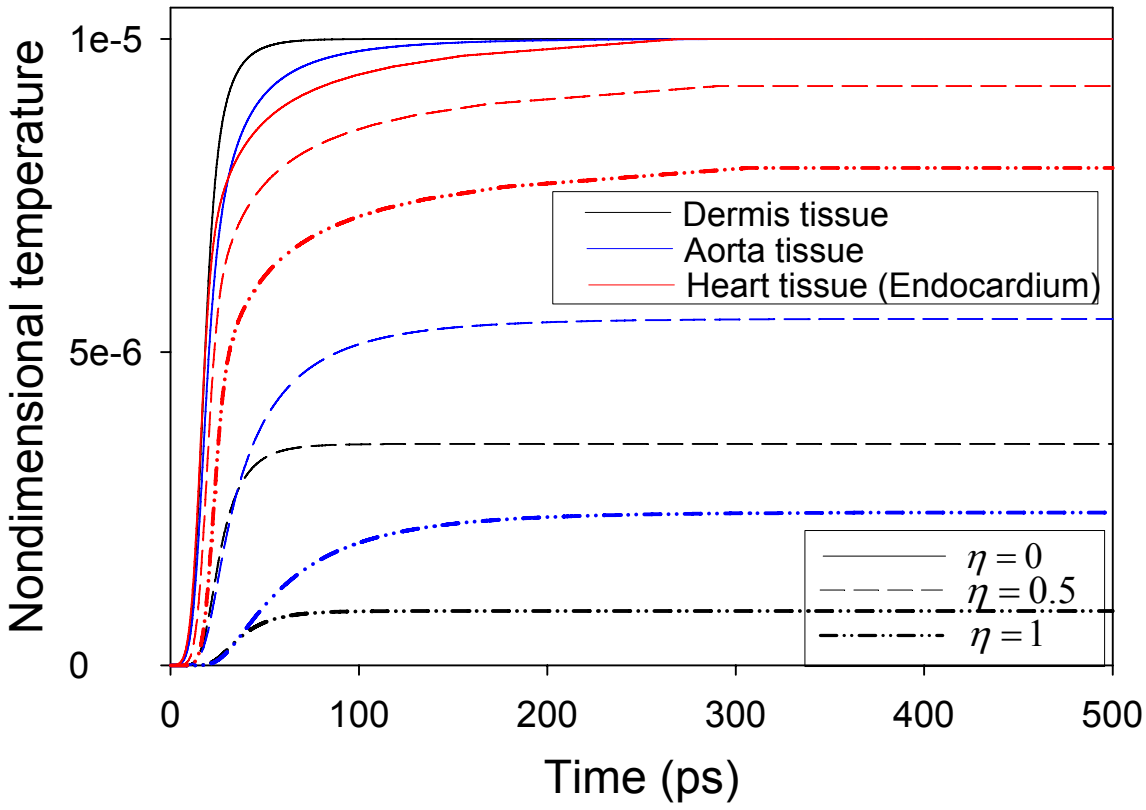

Figure 4.4 Temporal profiles of the non-dimensional temperatures at different locations in the tissues subject to an ultrashort pulse irradiation.

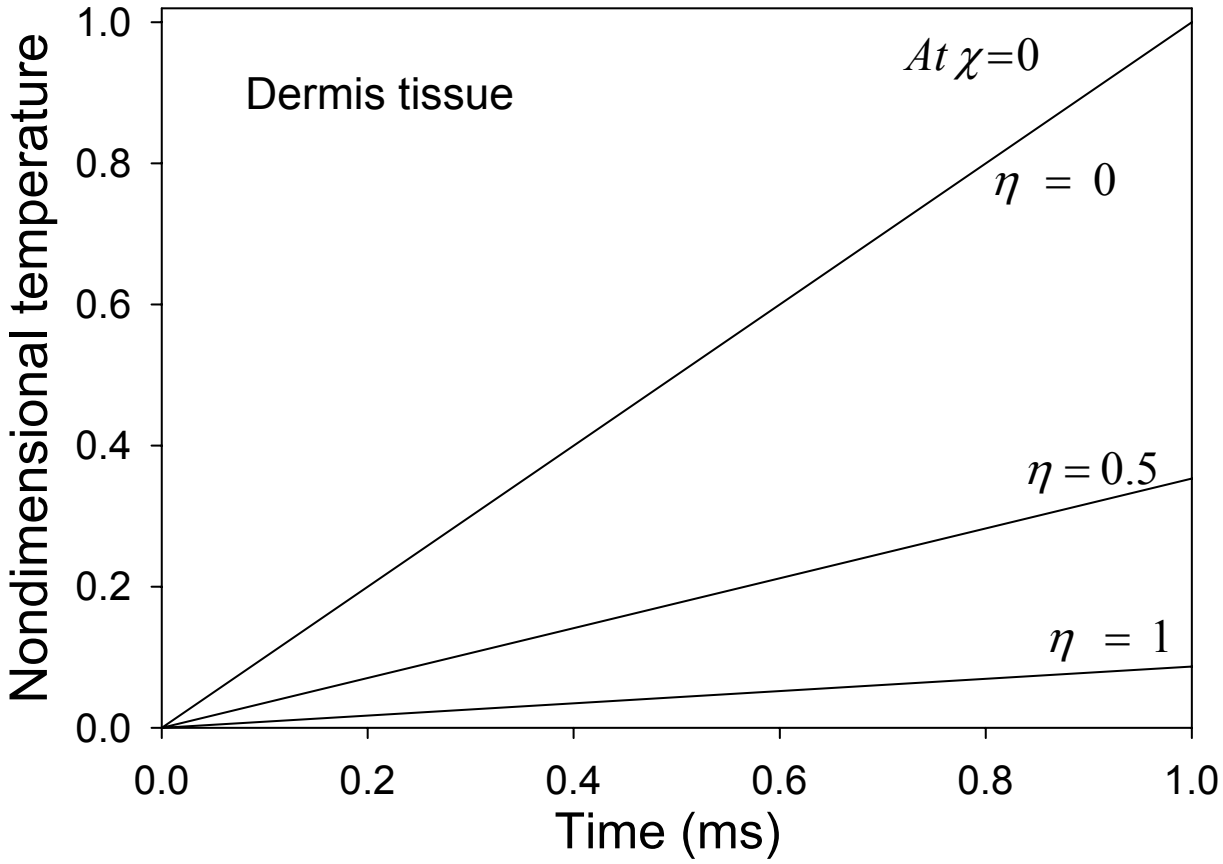

Figure 4.5 Temporal profiles of the non-dimensional temperatures in the dermis tissue exposed to 1 ms pulse train irradiation.

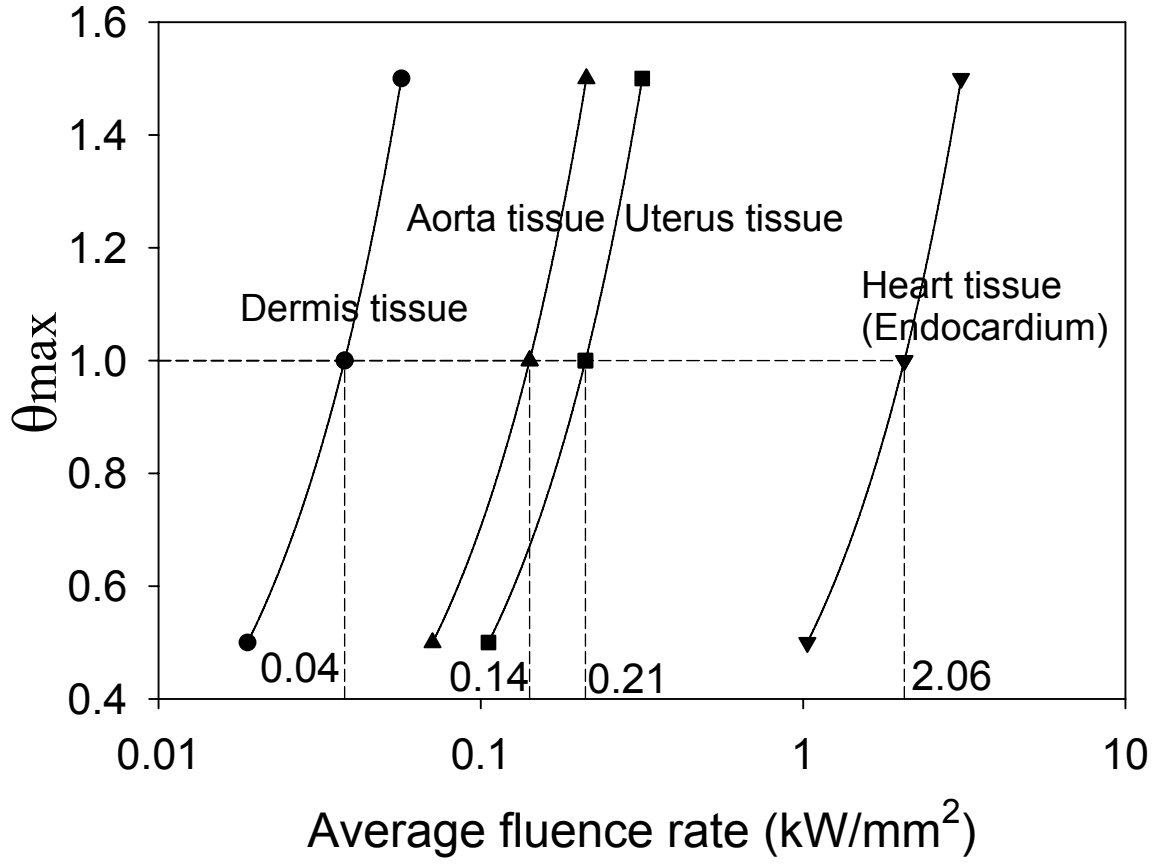

Figure 4.6 The incident laser power versus the maximum temperature at the laser spot center for various tissues.

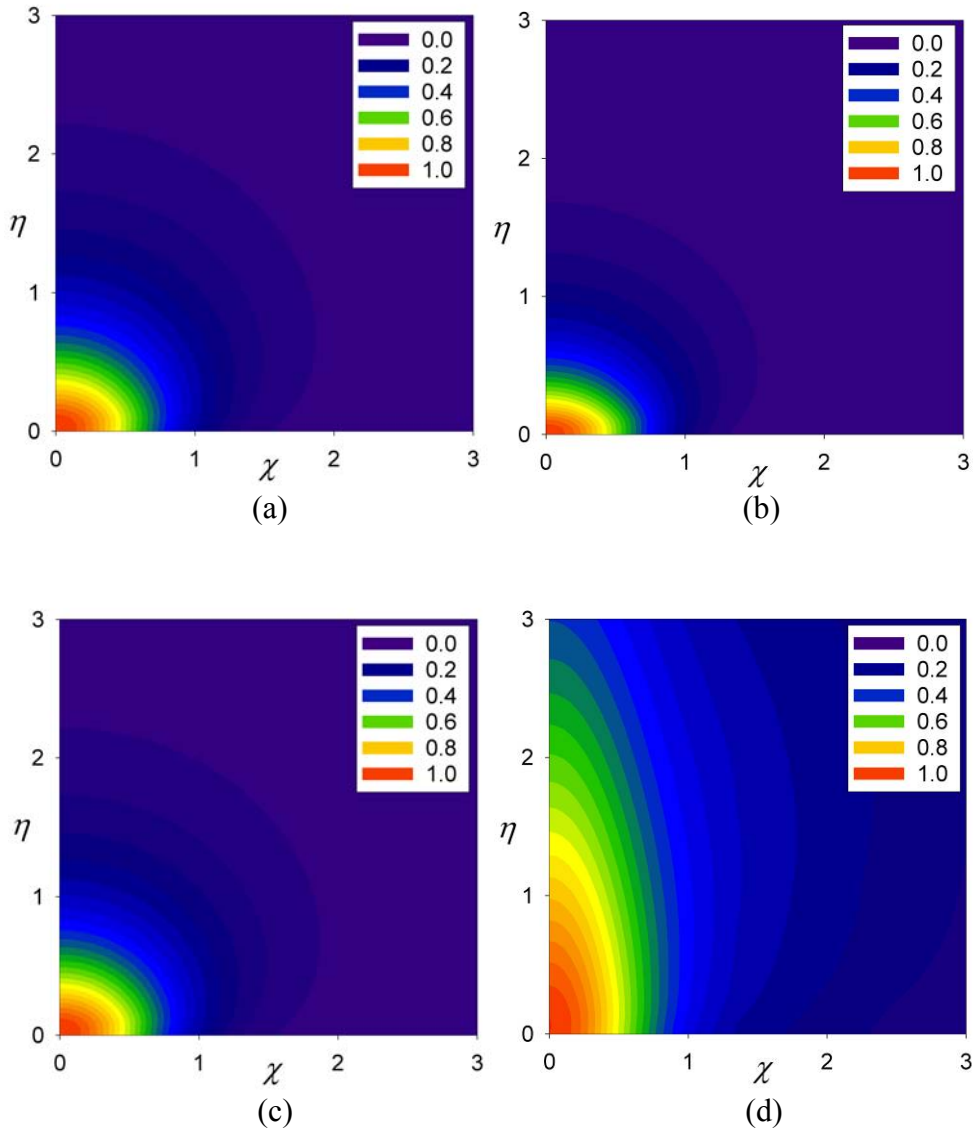

Figure 4.7 Comparisons of the non-dimensional temperature fields induced by the 1ms pulse train radiation heat transfer: (a) dermis tissue; (b) uterus tissue; (c) aorta tissue; and (d) heart tissue.

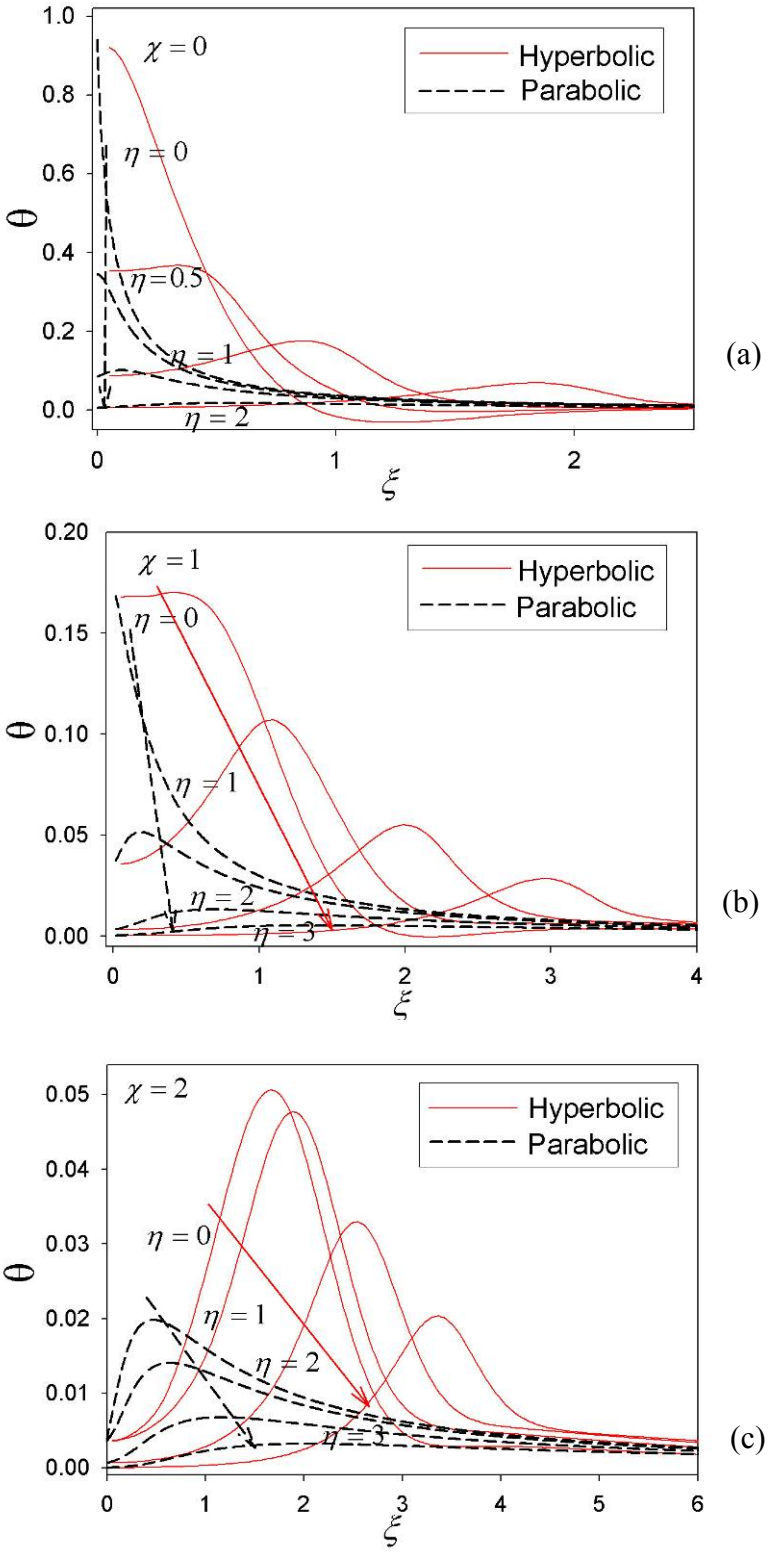

Figure 4.8 Comparison of temporal profiles of the non-dimensional temperature in the dermis tissue between hyperbolic conduction and parabolic diffusion predictions.

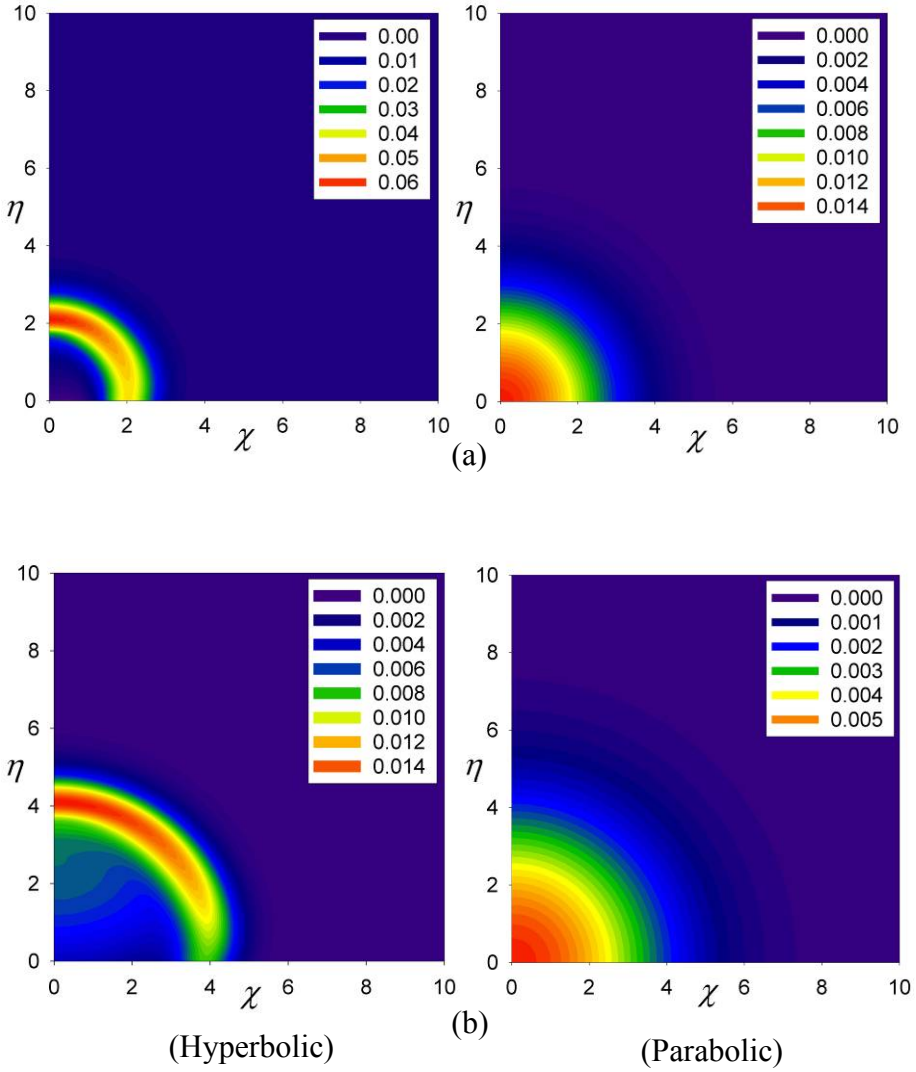

Figure 4.9 (1). Comparisons of non-dimensional temperature fields in the dermis tissue between hyperbolic conduction and parabolic diffusion models at four different meso-time: (a) $\xi = 2$; (b) $\xi = 4$; (c) $\xi = 6$; and (d) $\xi = 8$.

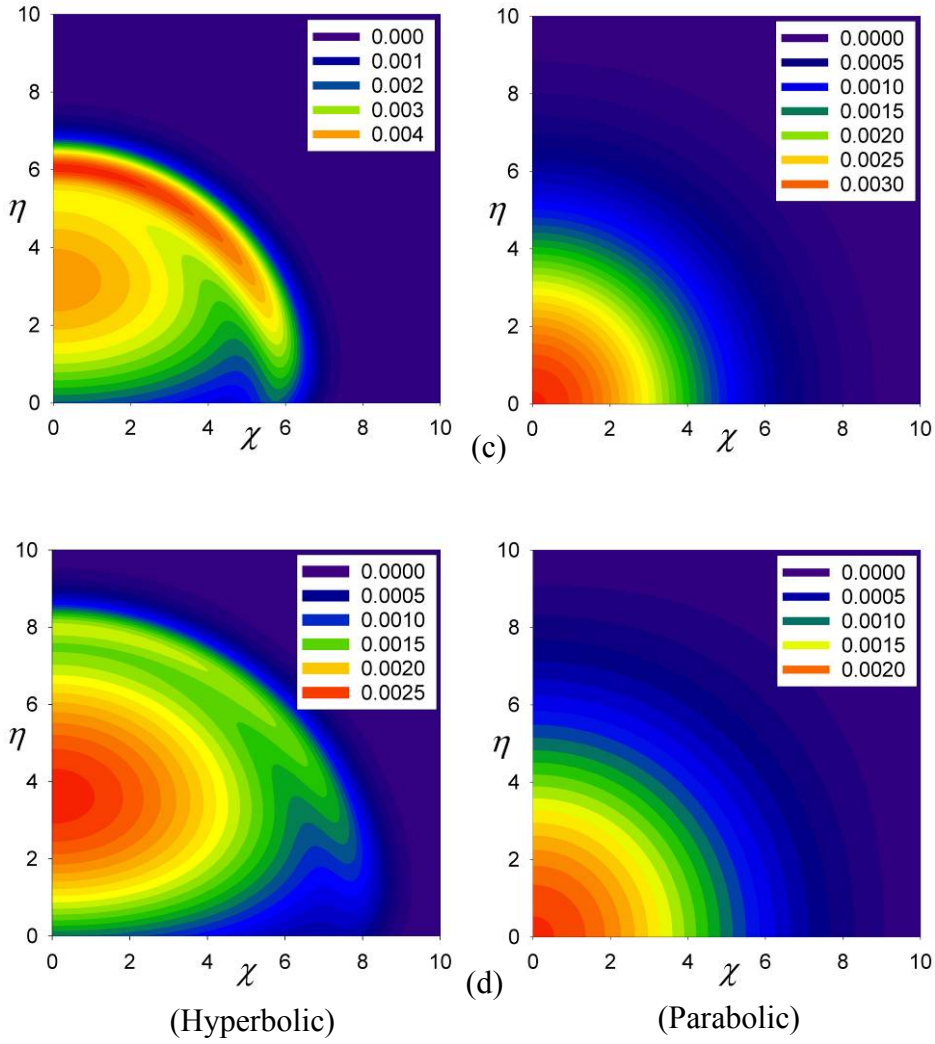

Figure 4.9 (2) Comparisons of non-dimensional temperature fields in the dermis tissue between hyperbolic conduction and parabolic diffusion models at four different meso-time: (a) $\xi = 2$; (b) $\xi = 4$; (c) $\xi = 6$; and (d) $\xi = 8$.

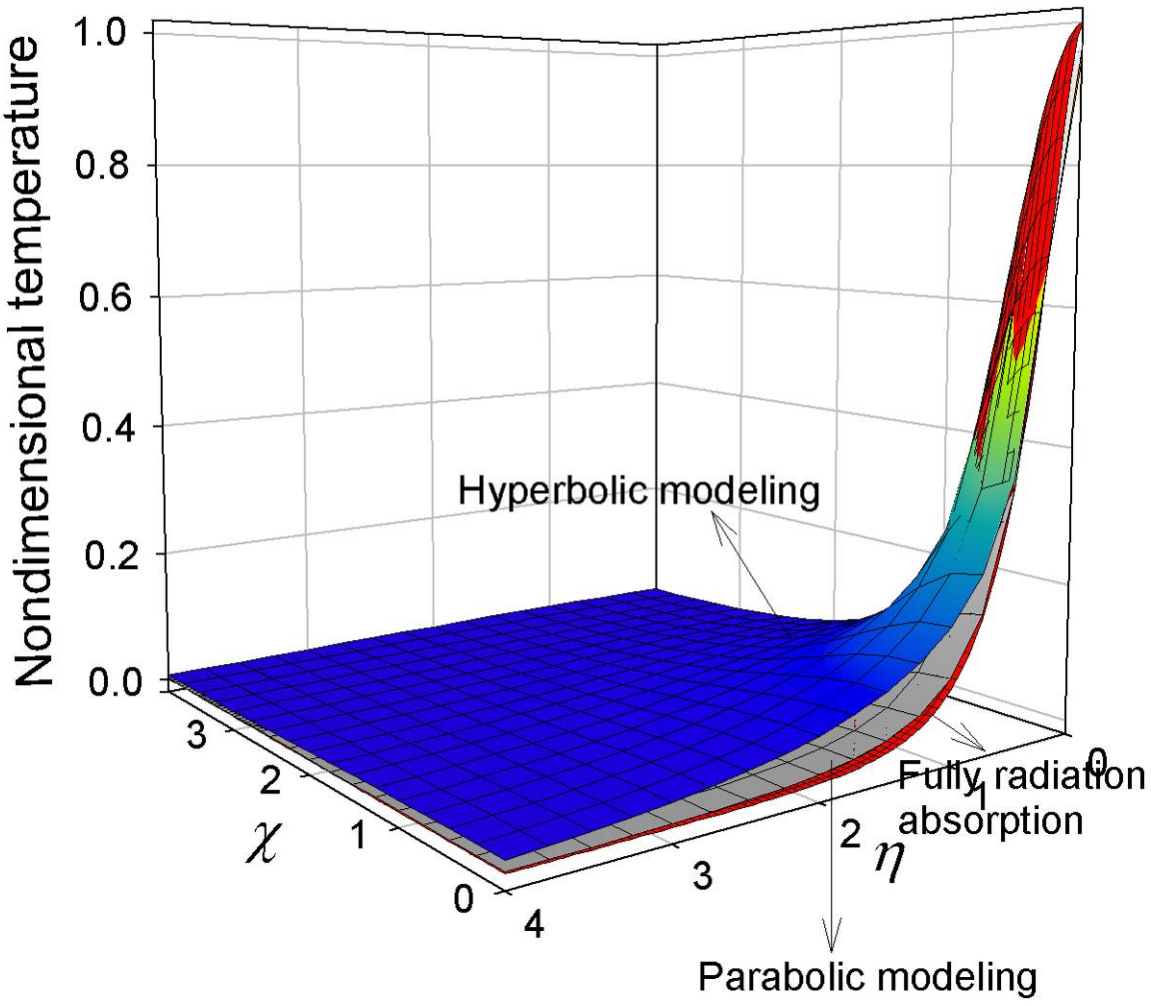

Figure 4.10 Comparisons of the maximum temperature maps in the dermis tissue due to purely radiation heat transfer or combined heat transfer predicted by the hyperbolic and parabolic models, respectively.

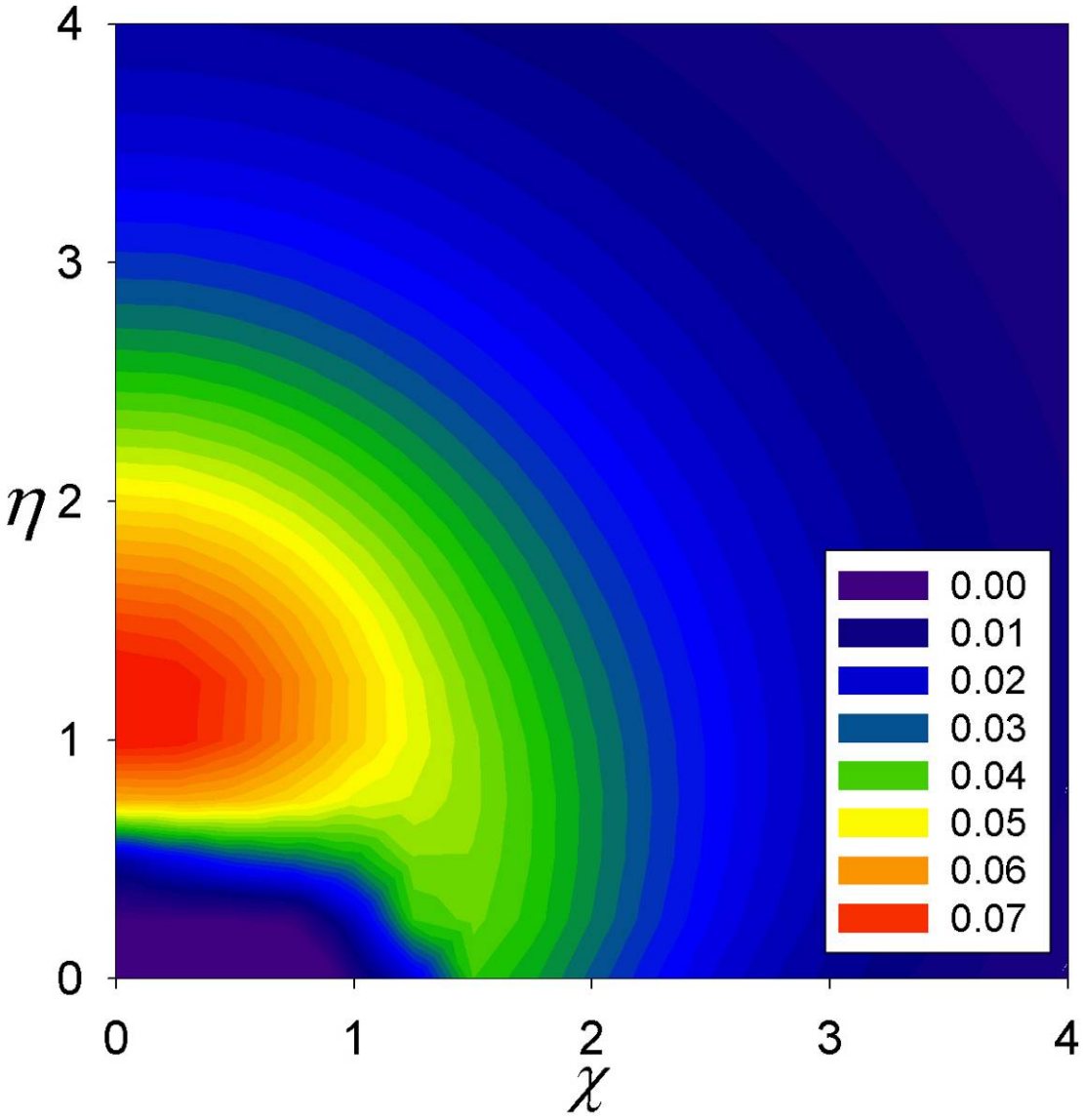

Figure 4.11 Contour of maximum temperature difference image between hyperbolic and parabolic model.

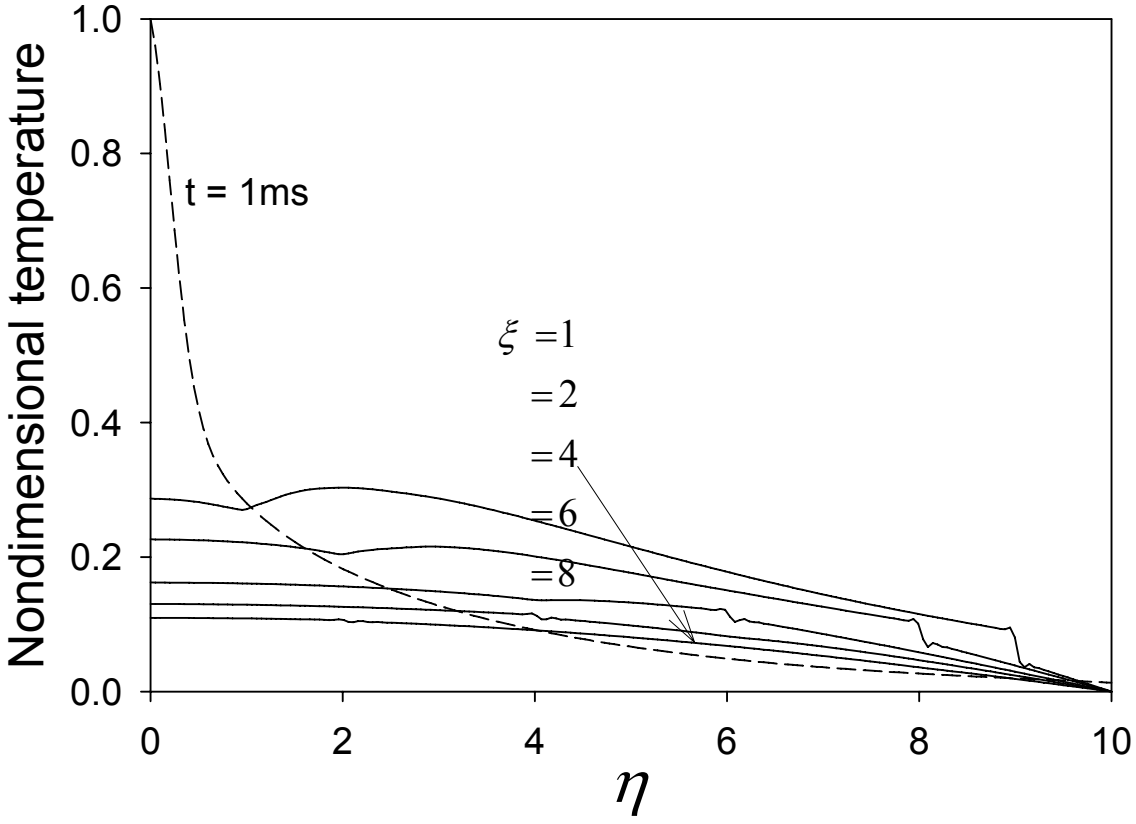

Figure 4.12 The nondimensional temperature profiles along the optical axis at certain time instant (Heart tissue: Endorcardium).

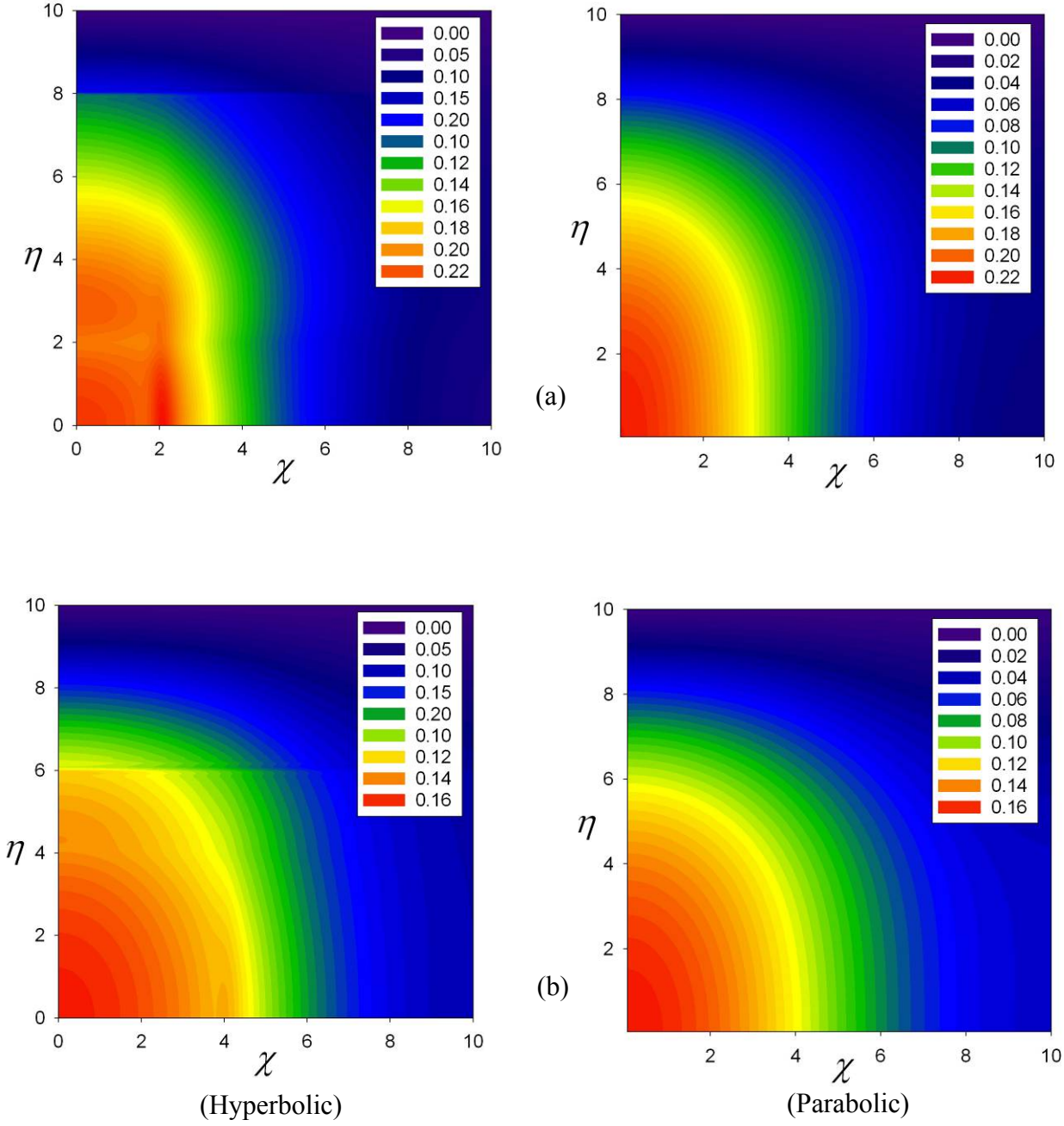

Figure 4.13(1) Comparisons of non-dimensional temperature fields in the heart tissue between hyperbolic conduction and parabolic diffusion models at four different meso-time: (a) $\xi = 2$; (b) $\xi = 4$; (c) $\xi = 6$; and (d) $\xi = 8$.

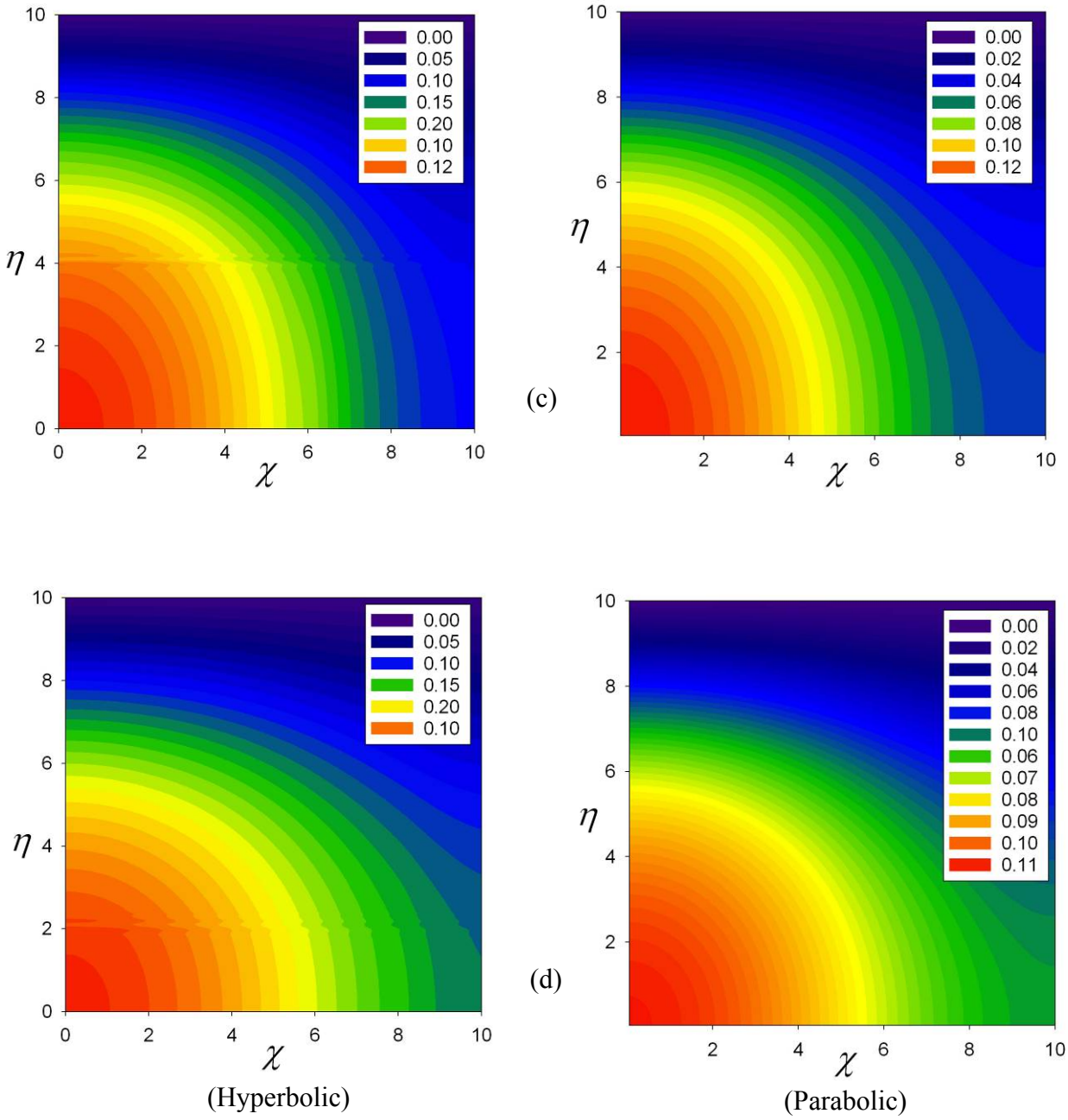

Figure 4.13 (2) Comparisons of non-dimensional temperature fields in the heart tissue between hyperbolic conduction and parabolic diffusion models at four different meso-time: (a) $\xi = 2$; (b) $\xi = 4$; (c) $\xi = 6$; and (d) $\xi = 8$.

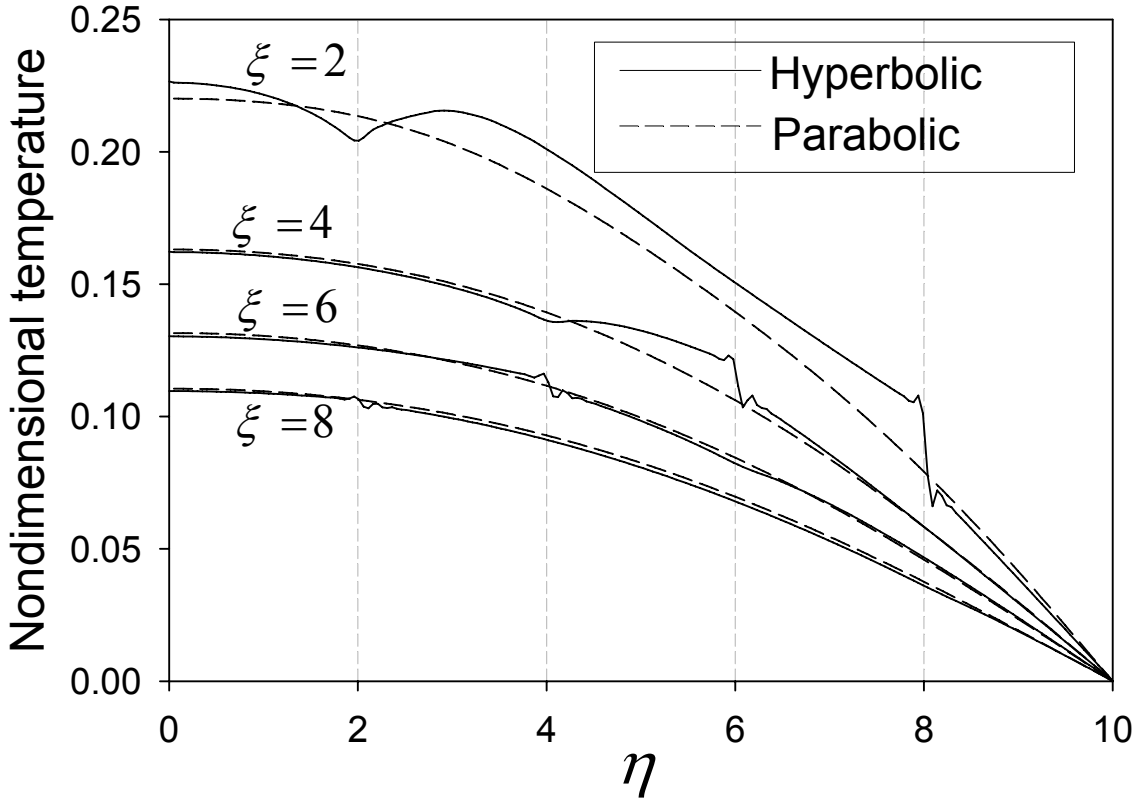

Figure 4.14 The temperature profiles along the optical axis at certain time instant in the heart tissue.

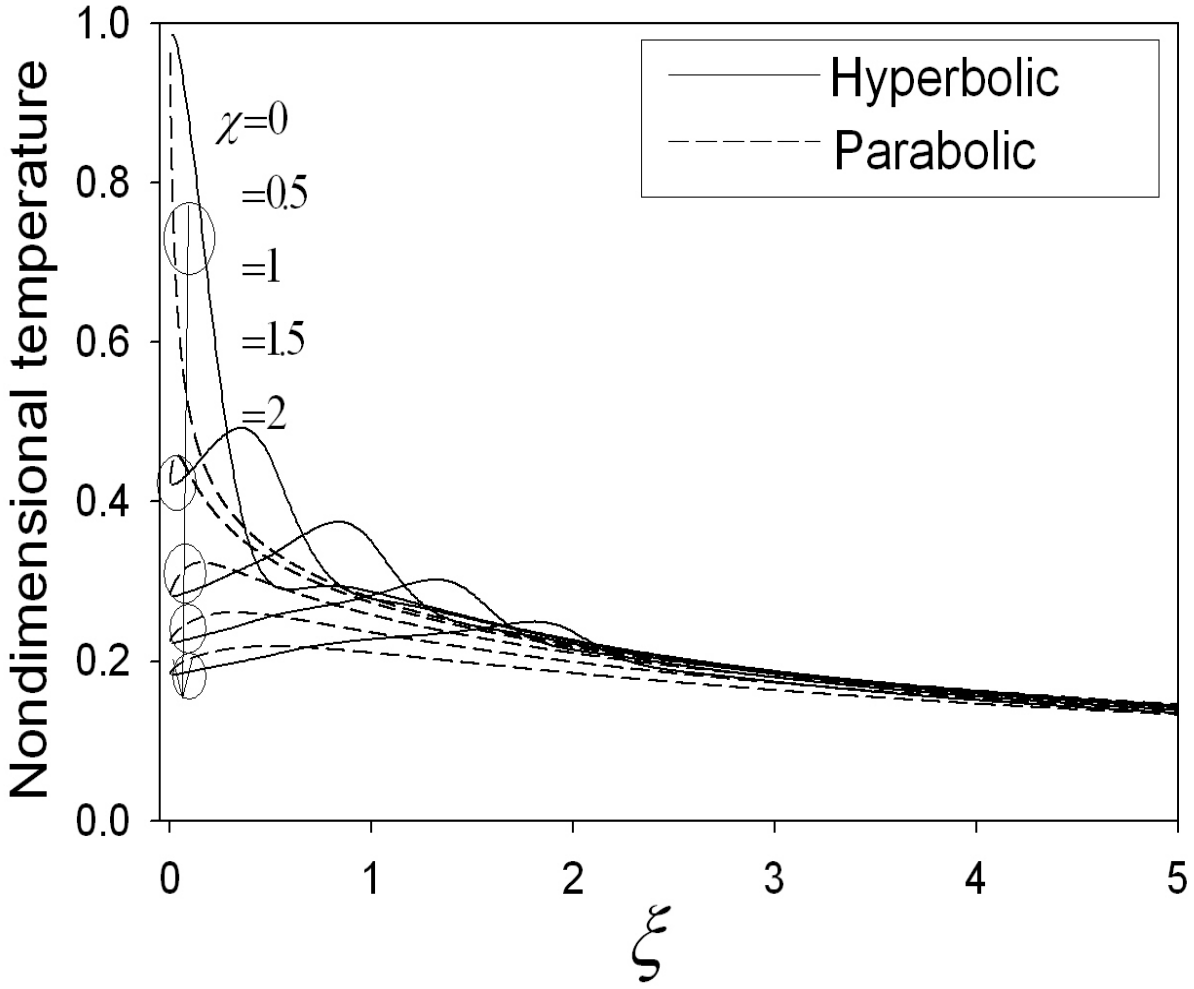

Figure 4.15 The temporal temperature profiles along the tissue surface at selective locations in the heart tissue.

Chapter 5

Experimental study for hyperbolic conduction

In this chapter, the experimental study to examine the hyperbolic conduction phenomena. The 1D model is assumed for the experimental model. Compared with the numerical approaches solving the hyperbolic conduction model, the experimental success or meaningful data is relatively few. It may be the first validation of hyperbolic heat conduction applying to organic tissue experimentally [39]. With the advent of ultrafast laser system, the hyperbolic heat conduction problem has been widely studied relating matter of short-pulsed laser metal heating. Qiu and Tien [40] validated the hyperbolic conduction model comparing with experimental data with gold metal irradiating 96 *fs* pulsed laser. More recently, Herwig and Beckert failed to validate the hyperbolic conduction phenomena with their own experimental [68]. They could not observe any sharp wave front in their experiment. Similar experiments are conducted in this chapter to evaluate the hyperbolic conduction.

5.1 Experimental setup

5.1.1 Temperature measurement system

5.1.1.1 Thermocouple

The T type thermocouple is used as the temperature sensor. Its product number is COCO-010 and it is made by the Omega Company. The wire diameter is 0.25 mm. The maximum temperature measurement range is over 149 °C. The response time of this thermocouple is shorter than 0.1 sec. The T type thermocouple, with a positive copper wire and a negative Constantan wire is recommend for use in mildly oxidizing and reducing atmospheres up to 400 °C. They are suitable for applications where moisture is present. This alloy is recommended for low temperature work since the homogeneity of the component wires can be maintained better than other base metal wires. Therefore, errors due to inhomogeneity of wires in zones of temperature gradient are greatly reduced. The accuracy of various types of thermocouples is summarized in Table 1. There are international standards that specify the amount by which sensors may deviate from ideal behavior. These figures are reproduced here. The table shows the maximum permitted error in thermocouples which comply with IEC 584-2 (1982) and in PRTDs (platinum resistance temperature devices) which comply with BS 1904 (1984) Class A. In mild operating temperature range (0-200 °C), the T type thermocouple shows the best accuracy.

5.1.1.2 Data acquisition system

To record the temperature, the thermocouple is connected to the data acquisition system. The data acquisition system is composed with thermocouple input module, slot chassis, and cables. It is purchased from the National Instrument. The 8 channel thermocouple input module (model number: SCXI-1112) is used, which the 8 multiple temperature measurements are possible. The thermocouple input module is embedded in

the slot chassis (model number: SCXI-1000). The data acquisition system is shown in Figure 5.1 (a) and (b).

5.1.1.3 The thermocouple calibration

Before performing experiment, the thermocouple is calibrated. The temperature of water in water vessel is measured. The three point temperatures measured are 0, 33, and 62 °C. For measuring a 0 °C, the ice water is prepared. The temperature measurement is waited until the thermal equilibrium is reached. The water vessel is heated in the microwave and the temperature measurement is performed at 33 and 62 °C. The temperature calibrated data is shown in Figure 5.2. It shows the good match with the curve which is provided NIST. The temperature and reading voltage can be displayed in the computer screen by the Labview software interface.

5.1.2 Sample preparation and experimental setup

For the experiment, the fresh chicken breast tissue which is production of Tyson is used. The chicken breast tissue is contained in the 4 °C refrigerator before performing experiment. The tissue sample is cut in a cubic shape as a size of $8 \times 8 \times 5 mm$. It is put above the Styrofoam box. The thermocouples are embedded into the chicken breast tissue. The exact locations of thermocouples are investigated after the chicken breast tissue is sliced. After the tissue sample reaches to the thermally equilibrium to the experimental environment, the test is conducted. The Styrofoam box is suddenly is switched to the ice block. The temperature response is recorded by the data acquisition system. The schematic diagram of experimental design is shown in Figure 5.3.

5.2 Experimental Results and discussion

If this problem is approximated as an 1D parabolic heat conduction problem like as,

$$\frac{\partial^2 T(x,t)}{\partial x^2} = \frac{1}{\alpha}\frac{\partial T(x,t)}{\partial t} \qquad \text{in } 0 < x < \infty, \quad t > 0 \qquad \text{(Eq.5.1)}$$

$$T(x,t) = 0 \qquad \text{at } x = 0, \qquad t > 0 \qquad \text{(Eq.5.2)}$$

$$T(x,t) = T_0 \qquad \text{for t = 0 in } 0 \le x \le \infty \qquad \text{(Eq.5.3)}$$

The solution can be achieved like as [69],

$$\frac{T(x,t)}{T_0} = erf\left(\frac{x}{\sqrt{4\alpha t}}\right) \qquad \text{(Eq.5.4)}$$

where, T_0 is the initial temperature of the tissue sample and α is the thermal diffusivity. The initial temperature is same as the room temperature since the tissue reaches the thermal equilibrium to the room air. Several experimental tests are attempted. Each experimental is repeated two times. The data shown in Figure 5.4 are averaged value of two time tests. The experimental results are followed by the parabolic heat conduction model. There is no obvious wave front or sudden temperature gradient change. However, by this experiment the thermal diffusivity of chicken breast tissue can be predicted. The prediction of α is summarized as a range of 0.102-0.109 mm^2/s in Table 5.2. It is an good agreement result of previous measurement data. Fontana et al. measured the thermal diffusivity of chicken breast as a 0.11 mm^2/s [70].

Another experiment is conducted to evaluate hyperbolic conduction. The thermocouple is embedded to near the surface contact region between tissue sample and ice block. The thermocouple location is 0.1± 0.05 mm. The tests are repeated three times

during three days. The test results are shown in Figure 5.5. In the enlarged Figure, the sudden jump of temperature response is observed. The different locations of wave front are observed. The thermocouple locations may be various due to the multiple experiments. The vibration of thermocouple may cause the noise of one temperature response. In two profiles, two gradients of temperature response are observed. These profiles show initial slow change of temperature and sudden drop of temperature. Recently, Antaki did a new interpretation of hyperbolic heat conduction [71]. In this paper, he developed the DPL (Dual Phase Lag) model for the hyperbolic conduction. Dual phase lags are τ_q and τ_T of heat flux and temperature gradient, respectively. The temperature gradient contributed this smooth change of gradient profile [71, 72].

In Figure 5.6, the experimental data are compared with analytical solution of parabolic conduction model. Three locations of temperature response are plotted individually. The experimental data are quite deviated from the parabolic conduction model. For the parabolic conduction model, the temperature response always shows smooth and continuous profile. Whereas, there exists sudden change of temperature response and a wave front is observed in one of the experiments. It shows more close phenomena of hyperbolic conduction.

5.3 Summary

The experimental study was conducted to evaluate hyperbolic conduction phenomena. The temperature measurement system was set up with T type thermocouple and data acquisition system. T type thermocouple was selected due to the high accuracy and fast response time. With the data acquisition system, the multiple location

measurement can be possible. The fresh chicken breast tissue was used for the tissue sample. The tissue sample in room temperature was suddenly contacted to the ice block. By the measurement of longer time temperature response, the thermal diffusivity was predicted. The problem was approximated as an 1D parabolic heat conduction problem. After the analytical solution was derived, the experimental data was compared. The thermal diffusivity of tissue sample is predicted as a range of 0.102-0.109 mm^2/s. The temperature measurement was performed at near the contact location, $0.1\pm0.05mm$. The temperature response of the experimental data showed different behavior with parabolic conduction model. There exists sudden change of temperature gradient and a sharp wave front was observed in one of experiments, which are the typical aspect of hyperbolic conduction model. Some results were more close to the DPL model recently developed and interpreted.

Temperature	B Type	E Type	J type	K Type	N Type	R Type	S Type	T Type
-200	-	-	-	3	3	-	-	3
-100	-	-	-	2.5	2.5	-	-	1.5
0	-	1.7	1.5	1.5	1.5	1	1	0.5
200	-	1.7	1.5	1.5	1.5	1	1	0.8
400	-	2	1.6	1.6	1.6	1	1	-
600	1.5	3	2.4	2.4	2.4	1	1	-
800	2	4	-	3.2	3.2	1	1	-
1000	2.5	-	-	4	4	1	1	-
1200	3	-	-	9	9	1.3	1.3	-
1400	3.5	-	-	-	-	1.9	1.9	-

Table 5.1 The measurement accuracy table with various types of thermocouples in different temperature conditions.

(a)

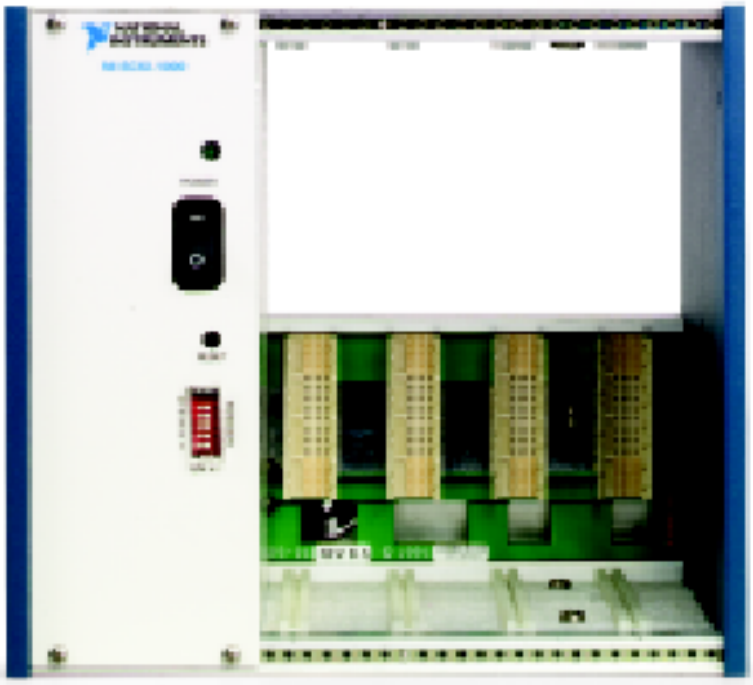

(b)

Figure 5.1 The data acquisition system of the National Instrument. (a) The 8 channel thermocouple input module (b) The 4 slot Chassis

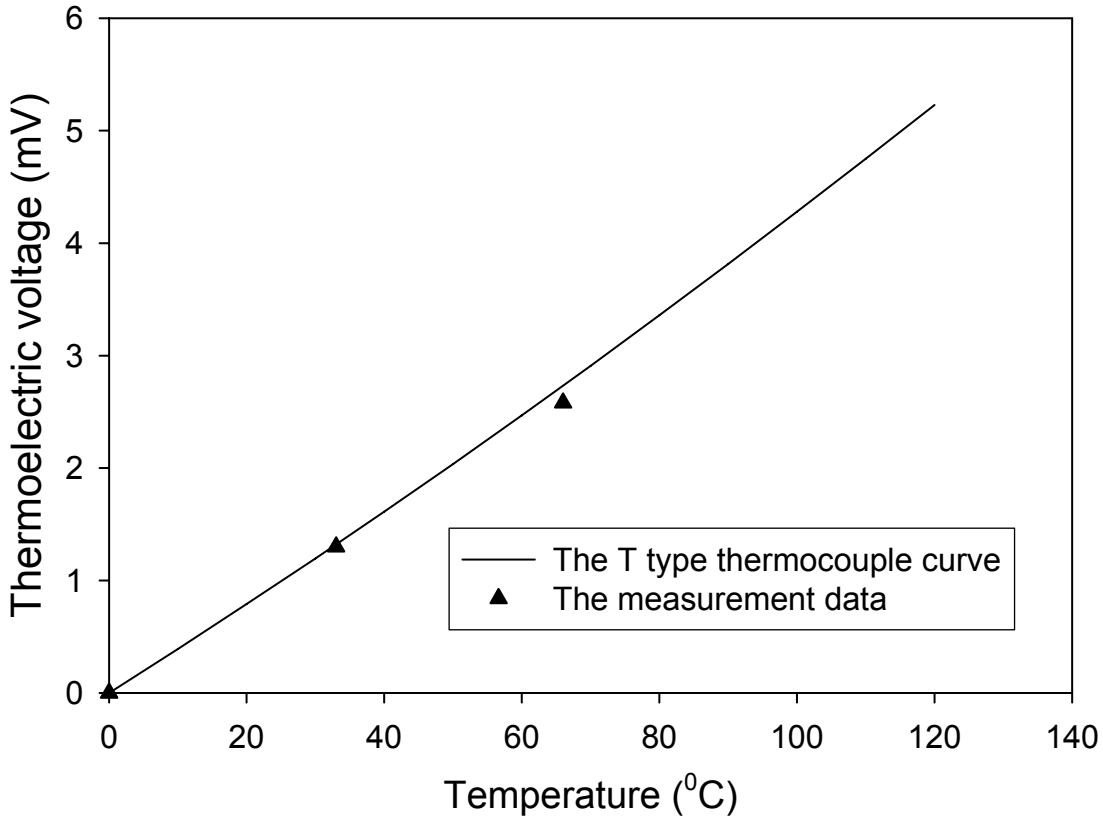

Figure 5.2 The thermocouple calibration result. The measurement data is compared with T type thermocouple curve.

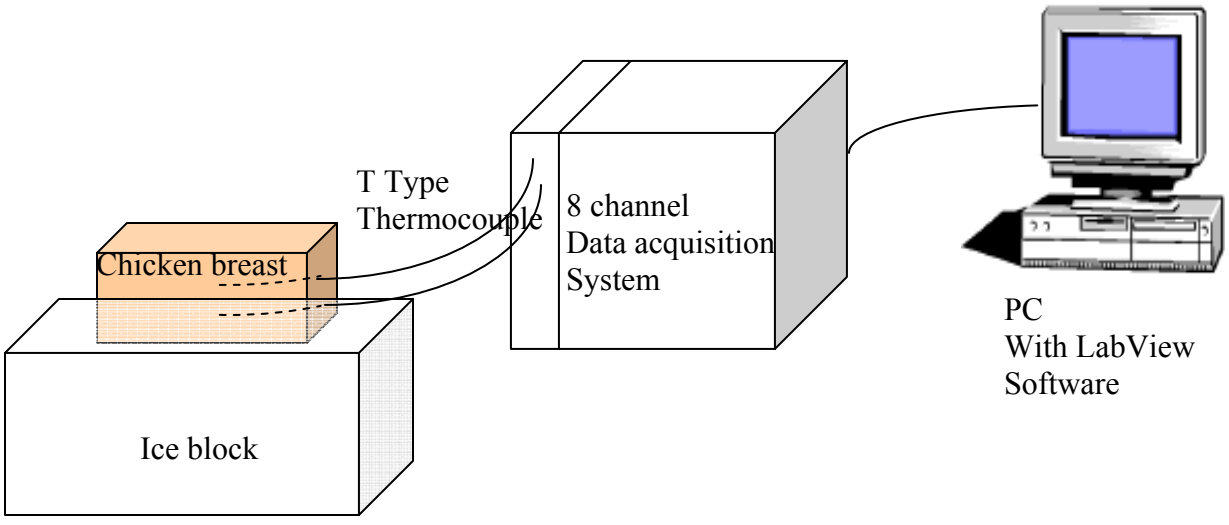

Figure 5.3 (a) The photo of experimental set up and (b) The schematic sketch of experimental design

	X(mm)	Nondimensional Temperature (T/T_0)	$\frac{x}{\sqrt{4\alpha t}}$	$\alpha\,(mm^2/s)$	$\overline{\alpha}\,(mm^2/s)$
Experimental 1	8.6	0.578	0.568	0.104	0.109
	5.2	0.359	0.329	0.114	
Experimental 2	5.8	0.424	0.385	0.103	0.102
	4.4	0.325	0.296	0.1	
Experimental 3	6.7	0.475	0.449	0.101	0.109
	3.6	0.250	0.225	0.116	

Table 5.2 The result of prediction of thermal diffusivity

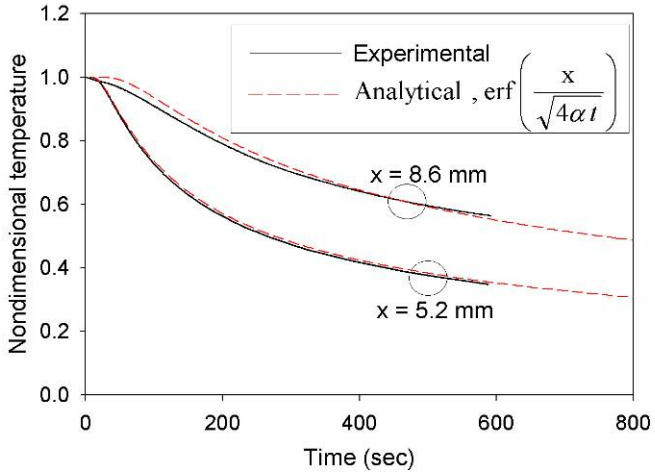

(a) Experiment 1

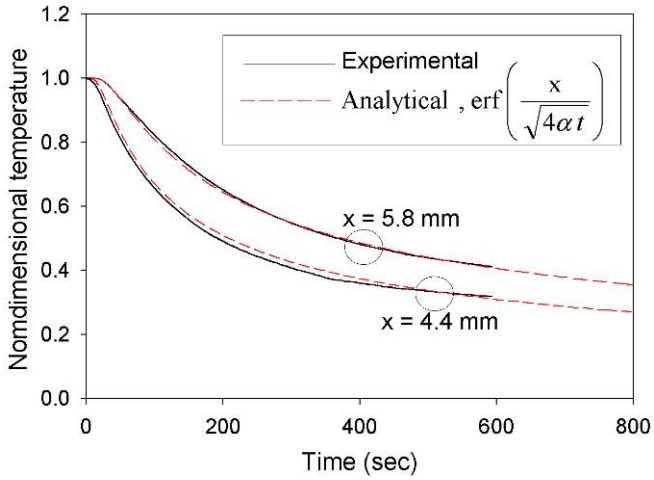

(b) Experiment 2

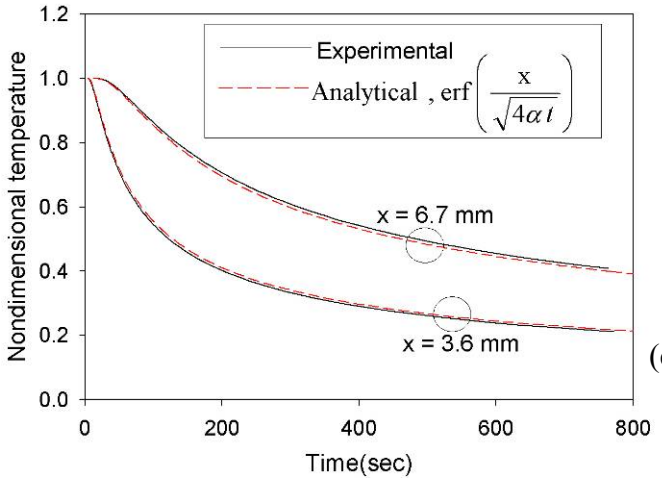

(c) Experiment 3

Figure 5.4 The transient temperature response to measure thermal diffusivity.

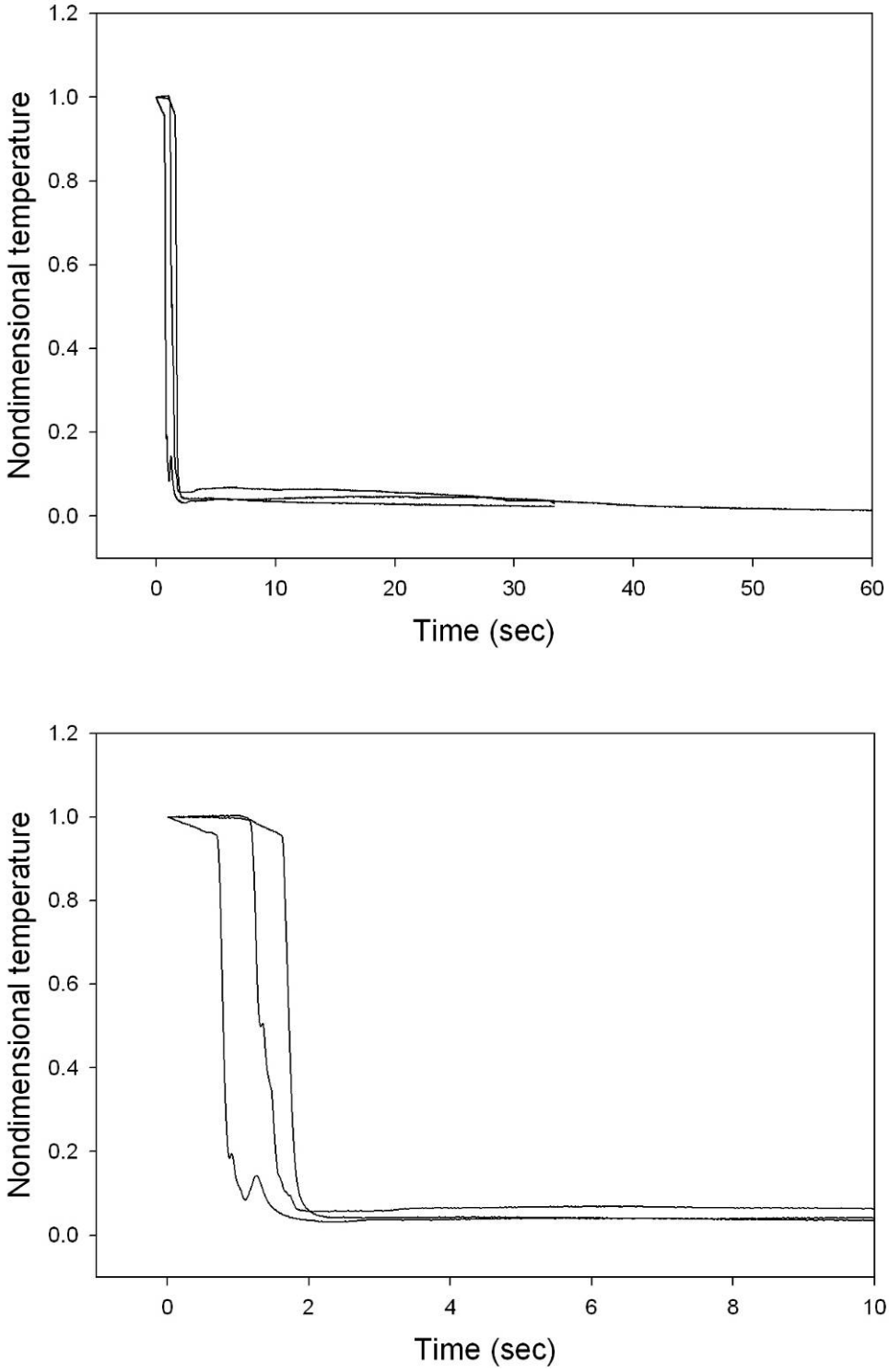

Figure 5.5 The temperature response at the location of 0.1 mm.

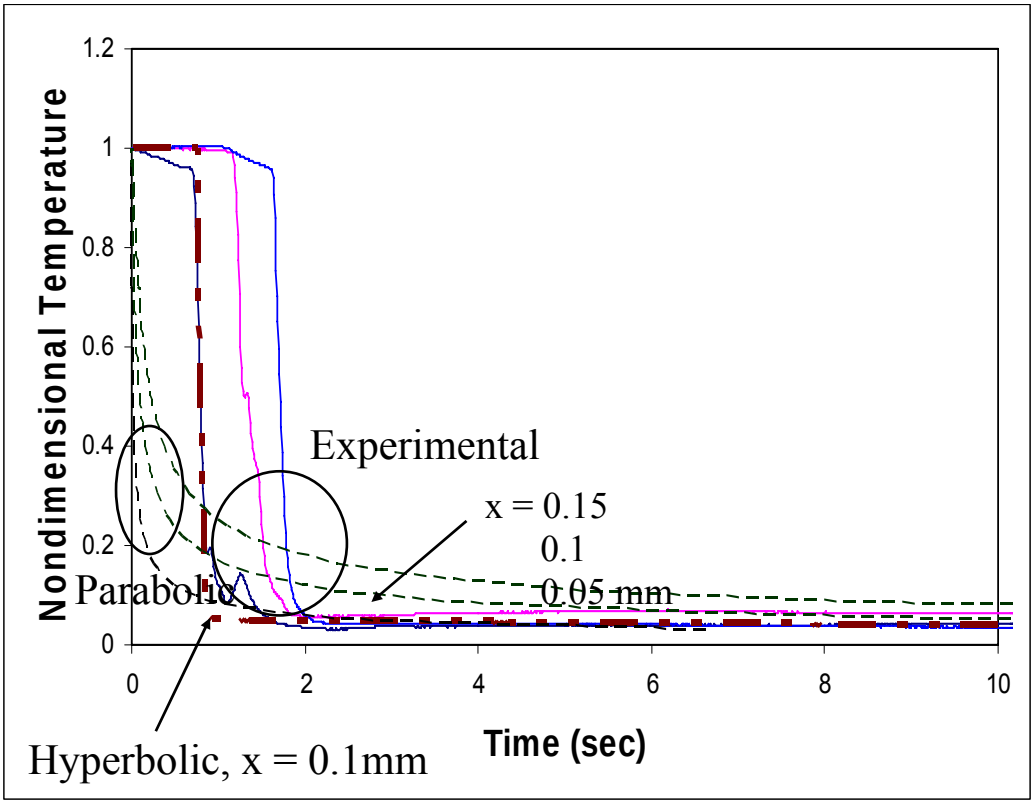

Figure 5.6 The comparison of temperature response profile between experimental data and parabolic conduction model.

Chapter 6

Benchmarking study with experimental data

In this chapter, the numerical simulation result is compared with the experimental results. The experimental data are provided by the Prof. Mitra group in the Florida Institute Technology. In comparison I, the collimated laser is used as laser source. From comparison II to IV, the focused laser beam is utilized. Propagation of focused laser beam has been studied for the cases of homogeneous or more complicated tissue models [77-79]. The main purpose of the focused laser is to enhance the peak absorbing radiation energy [80] and to increase temperature rising at the focused region. It is applied to the vascular laser therapy of dark port wine skin and higher temperature distribution is found out in the target region [81]. The focused laser beam is also studied in confocal microscopy for imaging application [82]. The objective of this chapter is to validate the numerical result by the comparison with experimental data and is to investigate the influence of the focused laser beam. The influence of grid system is also studied.

6.1 Comparison I – Collimated laser source

6.1.1 Experimental condition

In this comparison, short pulse laser with 200 ps pulse duration in 514 nm wavelength is considered. The energy of one pulse laser is 1.68212 nJ. The

1.3376×10^{8} short pulse laser whose radius 1mm irradiated until 14 sec and the average power of it is 225 mW. The experimental condition is depicted in Figure 6.1. The tissue absorption coefficient, σ_a , is $0.015\,mm^{-1}$ and reduced scattering coefficient, σ_s' , is $2\,mm^{-1}$. The tissue reflective index is 1.54. The thermal properties are determined as $\rho = 1000\,kg/m^3$, $k = 0.35\ W/mK$, and $C_p = 4200\ J/kgK$.

6.1.2 Mathematical model

The scenario of short pulse laser irradiation is shown in Figure 6.2. One pulse train is composed of 44643 short pulses and 42000 pulse trains irradiate until 14 sec. Then the average power (P_{ave}) of the laser can be calculated,

$$P_{ave} = \frac{E_{pulse}\times N_p}{t_r} = \frac{(1.68212\times10^{-9})\times1.3376\times10^{8}\times14}{14} = 225\,mW \tag{6.1}$$

where, E_{pulse} is energy per pulse, t_r is the laser exposure time, and P_{ave} are given by experimental conditions. N_p is the number of pulse.

In this experiment, the laser irradiates until relative longer time period compared with chapter 4 model and heat conduction model always occur with radiative transfer. Thus, the mathematical model is formulated as,

$$\rho C_p \frac{\partial T(r,z,t)}{\partial t} = -\left(\frac{\partial q_{cond,r}(r,z,t)}{\partial r} + \frac{q_{cond,r}(r,z,t)}{r} + \frac{\partial q_{cond,z}(r,z,t)}{\partial z}\right) - \nabla\cdot\mathbf{q}_{rad}(r,z,t) \tag{6.2}$$

where, the term of divergence of radiative heat flux plays an role as source in the energy equation (6.2). Similar method of chapter 4, the hyperbolic conduction equations are converted to vector form with non-dimensional variables as follows:

$$\frac{\partial \mathbf{E}}{\partial \xi}+\frac{\partial \mathbf{F}}{\partial \chi}+\frac{\partial \mathbf{G}}{\partial \eta}+\mathbf{H}=0 \tag{6.3a}$$

where

$$\mathbf{E}=\begin{bmatrix}\theta\\ Q_\chi\\ Q_\eta\end{bmatrix},\ \mathbf{F}=\begin{bmatrix}Q_\chi\\ \theta\\ 0\end{bmatrix},\ \mathbf{G}=\begin{bmatrix}Q_\eta\\ 0\\ \theta\end{bmatrix},\ \mathbf{H}=\begin{bmatrix}Q_\chi/\chi+S\\ Q_\chi\\ Q_\eta\end{bmatrix}, \tag{6.3b}$$

in which, the nondimensional variables are introduced in the previous chapter except source term,

$$S=\frac{\nabla\cdot q_{rad}\,\alpha\tau}{k(T_{ref}-T_i)} \tag{6.3c}$$

The initial temperature is defined as 25°C in experimental and boundary conditions are

$$\frac{\partial\theta(\chi,\eta,\xi)}{\partial\chi}=0, \qquad \text{at } \chi=0. \tag{6.4a}$$

$$\frac{\partial\theta(\chi,\eta,\xi)}{\partial\chi}=0, \qquad \text{at } \chi=\chi_{\max}. \tag{6.4b}$$

$$Q_\eta=h^*(\theta_\infty-\theta), \qquad \text{at } \eta=0. \tag{6.4c}$$

$$\frac{\partial\theta(\chi,\eta,\xi)}{\partial\eta}=0, \qquad \text{at } \eta=\eta_{\max} \tag{6.4d}$$

To compare the experimental data, the nondimensional variables are converted into the dimensional value again. To calculate of the divergence of radiative heat flux, the TDOM is applied using 200 ps laser. Reaching the steady state, it is plugged to the Equation (6.2).

6.1.3 Results and discussion

In Figures 6.3 & 6.4, the temperature distributions at 14 sec time instant both radial and axial directions are compared with experimental data. For the hyperbolic conduction, the 15 sec thermal relaxation time is selected and parabolic conduction model is also. The general tendency of profile shows a similar agreement between simulation and experimental data in radial direction at the surface. The temperature distribution along the radial axis shows the higher gradient in the hyperbolic conduction model and the temperature prediction is higher than experimental data in the laser deposition region. The temperature prediction at tissue surface by the parabolic model is under estimated.

In Figure 6.5, the temperature evolution along the surface region is depicted as time advancing. The temperature increases as time passing but the speed of temperature increment decelerates due to the conduction influence. The profiles show the Gaussian shape and become steeper along the radial direction in longer time stage. The axial temperature distribution along the optical axis is shown in Figure 6.6. As time marching, the temperature propagates deeper inside medium.

The comparison between hyperbolic and parabolic model is conducted with a temporal temperature profiles in Figure 6.7. The three locations along the optical axis are selected. For the hyperbolic model, the 15 sec thermal relaxation time is chosen. At Z=0, the temperature quickly increases in hyperbolic model and the temperature difference between two models is largest. Similar tendency is predicted at Z = 1mm and 2 mm and the temperature difference decreases. The temperature prediction difference is most severe near the tissue surface medium, where is the important concerning region in laser

tissue treatment application. In longer time stage, the temperature shows the similar value at each point between two models.

The contour plot is shown at certain time instants in Figure 6.8. The temperature field is enlarged to the inside medium in longer time stage and it shows higher magnitude as well. The temperature filed of parabolic model is more spread compared with hyperbolic model. For the hyperbolic model, the temperature shows higher and it is concentrated in the laser deposition area.

In Figures 6.9 & 6.10, the parametric study of thermal relaxation time is conducted. As higher thermal wave relaxation time is plugged, the higher temperature gradient along the radial direction is predicted in the hyperbolic model since the strong heat flux rate can occur. Interestingly, the temperature profile of hyperbolic model becomes identical to the parabolic mode as small thermal wave relaxation time. Since the thermal wave speed is faster when the thermal relaxation time is small. Ultimately, if the thermal wave speed is infinite, i.e. $\tau = 0$, it becomes parabolic model. The surface peak temperature prediction using 10 sec τ is very close to the experimental one. However, the deviation result from the experimental data takes place from about 1mm to 6 mm in the radial distance. The axial temperature distribution along the optical axis is investigated in Figure 6.10. Surface temperature point shows a good agreement between hyperbolic model result and experimental data but overestimation result is predicted compared with experimental data at Z = 2 mm and 4 mm. Still hyperbolic conduction model is better approximation rather than parabolic model.

6.2 Comparison II- Light is focused to the tissue surface

6.2.1 Experimental condition

In previous comparison using collimated laser, the temperature increment is not quite enough for laser treatment application. Then, the laser light is focused to the tissue surface as shown in Figure 6.11. Other laser parameters and tissue phantom are same as comparison I.

6.2.2 Mathematical model

The focused laser beam diameter can be calculated by the equation (6.4) as,

$$d_f = \frac{4}{\pi} \cdot \lambda \cdot \frac{f}{D} \tag{6.4}$$

where, λ is the wavelength, f is the focal length, and D is the beam diameter before focusing. By the experimental conditions, $\lambda = 514nm, f = 400\,mm,$ and $D = 2mm$. Then, the focused beam diameter can be achieved as 0.13 mm.

For focused laser beam intensity is specified as Equation (6.5),

$$I_c(r,z,t) = (1-R)q_0 \exp\left\{-4\ln 2 \times [(t - z/c)/t_p - 1.5]^2\right\} \times \exp(-2r^2/v_i^2) \times \exp(-\sigma_e z) \times \frac{\int_0^{v_i} \exp(-2r^2/v_i^2)dr}{\int_0^{r_f} \exp(-2r^2/r_f^2)dr} \tag{6.5}$$

in which, v_i is the beam radius at the certain axial position and it is approximated that the maximum laser intensity drops to e^{-2} value. r_f is the focused beam radius, which is 0.065 *mm*. Other parameters are already defined in chapter 2. To supply the same amount of radiation energy during focusing laser propagation as shown in Figure 6.12, the compensation is conducted by the integration.

6.2.3 Results and discussion

Radial temperature distribution along the tissue surface at t = 14 sec is shown in Figure 6.13. The dramatic matching between experimental data and model with the hyperbolic conduction is depicted. The maximum temperature increment is about 40 °C and it is a suitable temperature for laser welding or surgery. The temperature prediction with the parabolic conduction model is underestimated about 8 °C. Also, the temperature distribution along the optical axial is investigated in Figure 6.14. It shows a good agreement between experimental and numerical one. The maximum temperature increment is almost identical value and it is important area for laser tissue treatment. Higher temperature gradient along the line exists for focused laser beam and the temperature increment is trivial after Z = 4 mm.

The temporal temperature profiles are compared between two conduction models in Figure 6.15. For the hyperbolic conduction model, the sudden temperature increment is predicted at the tissue surface (Z = 0). It is due to the high concentration of radiation energy by focusing of laser beam. It causes the steep gradient of radiation energy between focused area and other tissue region. In this situation, the thermal wave can be predictable. Similar aspect is observed in the Z = 1mm. However, the absorbing radiation energy is not too high to show the thermal wave. At the position Z = 2mm, the temperature profiles between two models show similar tendency.

In Figure 6.16, the temperature field as time marching are shown with contours. At early time instant (t = 3.5 sec), the temperature field is highly concentrated to the tissue surface region. The temperature field is more confined in the hyperbolic model.

The magnitude of it is larger as well. In the longer time instant, the distribution of temperature field becomes similar.

In Figure 6.17, the focused laser beam is compared with collimated one with the surface temperature profiles, which is modeled by the hyperbolic conduction. The prediction higher temperature profiles using focused laser beam is clear. For the focused laser beam, the temperature field is mainly accumulated to the laser focal region. For the collimated laser, the temperature profiles more spread to the radial direction.

In Figures 6.18 and 6.19, the grid systems are compared. Previous results used in this comparison are implemented with nonuniform grid I. The grid system and numerical scheme were discussed in previous chapter and detail things will be omitted in this chapter. Generally speaking, the result of temperature prediction used all grid systems show the very close values. The difference is observable close the optical axis (R = 0). The fine grid systems are employed in the nonuniform grid system in this area. There exists high gradient of absorption radiation energy in the case of focusing laser beam and the fine grid is necessary to capture it. Then, more accurate matching with experimental is observed.

6.3 Comparison III- Laser beam is focused to 2mm below the tissue surface

6.3.1 Experimental condition

In this experiment, the Q-switched Nd:YAG is utilized. It has 200 ns pulse duration and the wavelength is tuned up 1064 nm. The pulse train frequency is 1 kHz and irradiated until 10 sec. The average power of laser is 1.3 W and laser beam is focused to 2 mm below the tissue surface. The tissue geometric sketch is shown in Figure 6.20. The

inhomogeneity tissue is embedded inside the normal tissue. The optical properties of homogeneous tissue are mimicked as human skin tissue like $\sigma_a = 0.0509\,mm^{-1}$ and $\sigma_s' = 0.614\,mm^{-1}$. The reduced scattering coefficient of inhomogeneity medium is $1.228\,mm^{-1}$ and absorption coefficient is same as homogeneous tissue. The laser beam propagation for this comparison is depicted in Figure 6.21.

6.3.2 Results and discussion

In Figure 6.22, the temperature distribution along the optical axis compared between experimental data and hyperbolic conduction model with 15 sec thermal wave relaxation time. Also, the different grid systems are compared. The calculation result with finer grid is more close to the experimental data, especially maximum temperature. However, at the surface region is predicted higher temperature compared with experimental result. For the parabolic conduction model, there exists more deviation from the experimental data. The maximum temperature prediction with the parabolic model is almost 10 °C less than experimental data.

The radial temperature distribution at focused region (Z = 2mm) is shown in Figure 6.23. Even though the temperature field at the tail of the beam radius is over estimated in numerical one, the agreement is quite good. Also, the nonuniform grid system is superior. Again, the temperature prediction of parabolic model is under estimated.

In the Figure 6.24, the 17 sec thermal relaxation time is used for the hyperbolic model. The value of thermal relaxation time depends on the propagation velocity of thermal wave which is dependent on material structure and property. Although its value

has been measured for biological media such as bologna meat samples [Mitra], the exact value of thermal relaxation time (typically having values in the range of 10 to 20 seconds) is unknown for most of the tissues. Also, it is hard to predict in case of inhomonogeneous tissue. The result using 17 sec thermal relaxation time is more close to the maximum temperature region.

In the Figure 6.25, the temporal temperature profiles at selective positions are plotted with hyperbolic conduction model. Of course, this is an imaginary simulation. In actual case, the tissue sample will have thermal damage if the laser exposure time is extended. It is easily predicted that the temperature increment is highest in focal region. The thermal wave is also observed in this position. The tendency of temperature increment is similar between at Z = 1 mm and Z = 3 mm since it is the symmetric location against focal region. However, the higher temperature increment is predicted at Z = 1mm due to the close location of the laser deposition area. As time advancing, the temperature profiles converge to the one value from the Z = 0 to the Z = 2 mm. It means that temperature mainly accumulates from the tissue surface to the focal area.

The evolution of temperature profiles as time passing is shown in Figure 6.26. For the hyperbolic conduction, the temperature concentration around the focal region is observed in early time moment with high magnitude of it. In longer time instant, the parabolic model catch up hyperbolic model. The temperature gradient along the z axis from tissue to the focal region becomes smaller.

The temperature field distribution as time marching is depicted in Figure 6.27. The temperature field propagates from the focal region to the whole tissue medium. It is

noticed that the thermal damage area is the focal region and the tissue surface region may be in thermal damage in the longer time period.

6.4 Comparison IV- Laser beam is focused to 2mm below the three layered tissue surface

6.4.1 Experimental condition

Conventionally, the skin tissue is treated to the single layered tissue for the simplicity. But in the real nature, the skin tissue is multi layered medium having different thickness and optical properties. In this experiment, the layered tissue is set up shown as in Figure 6.28. The optical properties of layered tissue are shown in Table 6.1 and geometric sketch is in Figure 6.28. Other laser parameters are same as comparison III model.

6.4.2 Results and discussion

In Figure 6.29, the experimental data is compared with simulation result. For the hyperbolic conduction model, 15 sec τ is used. In the axial profiles, the temperature prediction by the hyperbolic model dramatically matches to the experimental data. Again, the surface temperature increment and maximum temperature increment at the focal region is well matched. Radial profile at Z = 2mm shows also good matching for hyperbolic model. It means that hyperbolic model with proper τ is essential to predict temperature rise involving short pulse laser application. The parabolic model always shows the under estimation of temperature increment.

The parametric study with various thermal relaxation times is conducted in Figure 6.30. The unique feature of axial variation is the existence of the thermal damping wave in front of the focal region. It is inducted by the high concentration of radiation energy absorption in the top layer of the skin (epidermis) having high absorption coefficient. The wave feature is validated with different τ. If the τ is small, the speed of thermal wave propagation becomes rapid. Then, it can propagate faster along the axial distance. The figure shows it clearly. Also, small τ causes the tiny heat flux rate and the amplitude of damping wave becomes small. Ultimately, the parabolic model which has infinite thermal wave speed can not predict any thermal wave damping feature. In the surface region, higher temperature increment is expected compared with single layered tissue in comparison III. The tissue top surface (epidermis) has high absorption property which results in higher temperature rise at the surface in three-layer model than that of single-layer model. By this parametric study, the result with 17 sec τ is more similar to the experimental data.

In Figure 6.31, the radial temperature profile along the tissue surface is plotted with various τ situations. The higher temperature increment is observed with the high τ especially the close region R = 0. Also, the 17 sec τ is good approximation to predict in the three layered tissue.

With the 17 sec thermal relaxation time for the hyperbolic conduction model, the temperature field propagation is compared with parabolic model in Figure 6.32. The high temperature field is confined to the focal area both models. For the hyperbolic conduction model, the higher temperature field is more confined to the focal area in early time instant (t = 2.5 sec and 5 sec). It is observed that the thermal damping wave propagates from the

tissue surface into the inside tissue medium as time marching. At t = 20 sec, the temperature distribution becomes similar shape.

6.5 Summary

The numerical results are compared with the experimental data. The laser source is collimated beam or focused one. The short pulse train is irradiated until certain time instant. In comparison I using collimated laser beam, the general tendency of temperature profile is close to experimental data for the hyperbolic conduction model. For the parabolic conduction model, the temperature is underestimated. However, the temperature prediction deviates from the experimental data tail region both radial and axial direction. The error can occur by the misplacement of thermocouples or inaccurate thermal camera imaging. The temporal temperature behavior is predicted during laser irradiation. The temperature field propagates from the laser deposition area to inside tissue medium as increasing laser irradiation time.

In comparison II, the laser beam is focused in the tissue surface and higher temperature increment is observed at the focal region. The result of hyperbolic model is well matched to the experimental data both radial and axial directions. The temperature field at early time instant is well confined for the hyperbolic model. The finite grid around focal area is helpful to predict sudden temperature change.

Q-switched Nd:YAG laser is used in comparison III and inhomogeneity medium is embedded inside of the tissue phantom. The laser beam focused into the inhomogeneity medium, where is below 2mm from the tissue surface. The high temperature increment is observed at the beam focal region. The temperature prediction by the hyperbolic model is

more close to the experimental data. The 17 sec thermal relaxation time provides better matching to the experimental data and it may be proper approximation of this tissue phantom. To increase calculation accuracy, nonuniform grid is utilized and shows more close matching with experimental data.

To mimic the skin tissue in reality, the tissue is modeled is three layered tissue. Epidermis which is top surface tissue has a high absorbing optical property. The laser beam is focused to the inhomogeneous medium which is located to below 2 mm from the tissue surface. In comparison IV, a good agreement was found between hyperbolic model and experimental results. The thermal damping wave propagation is observed induced by the high radiation absorption from the tissue surface. The location and amplitude of thermal damping wave is depending on the thermal relaxation time or thermal wave speed. As small thermal relaxation time employed, the wave move fast and the amplitude of it decreases.

Based on these benchmarking studies, the hyperbolic model provides accurate temperature prediction incorporation with short pulse laser irradiation. The thermal wave propagation can be observable depending on the tissue optical properties. The higher temperature increment is predicted to the focal area. To capture of it, the fine grid system is helpful.

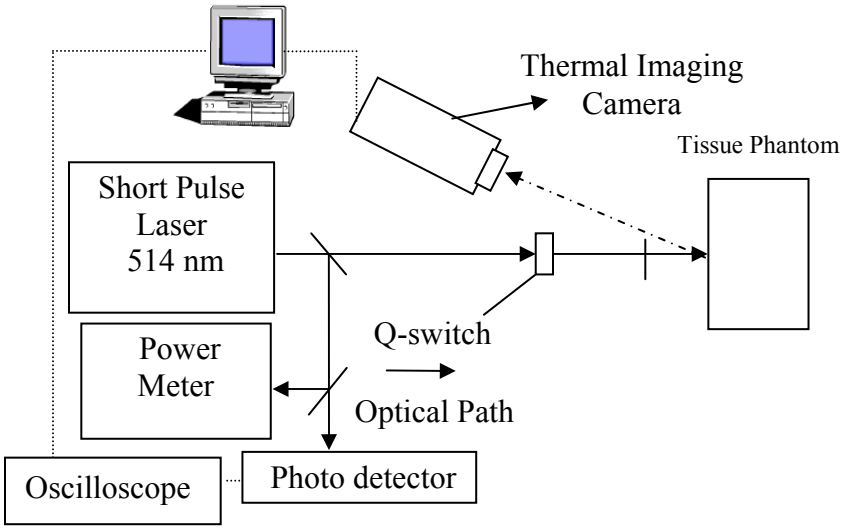

Figure 6.1 Schematic of the experimental set-up for tissue which is designed by Prof. Mitra group

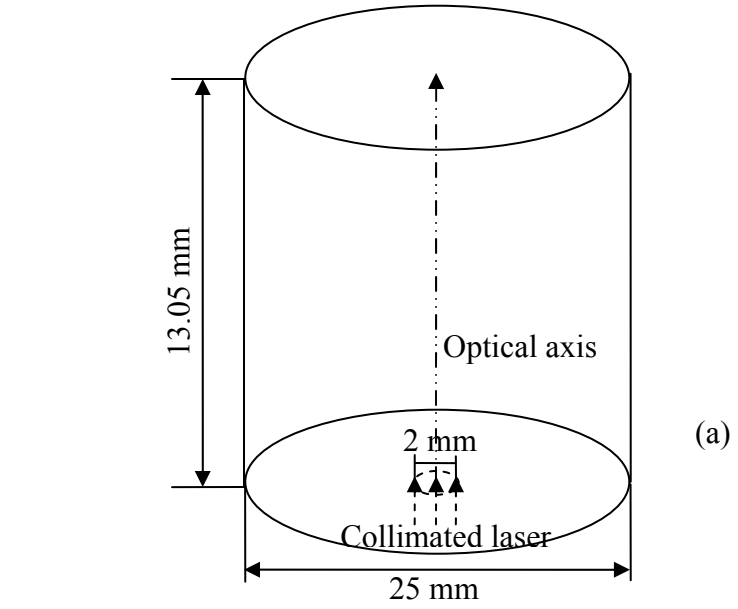

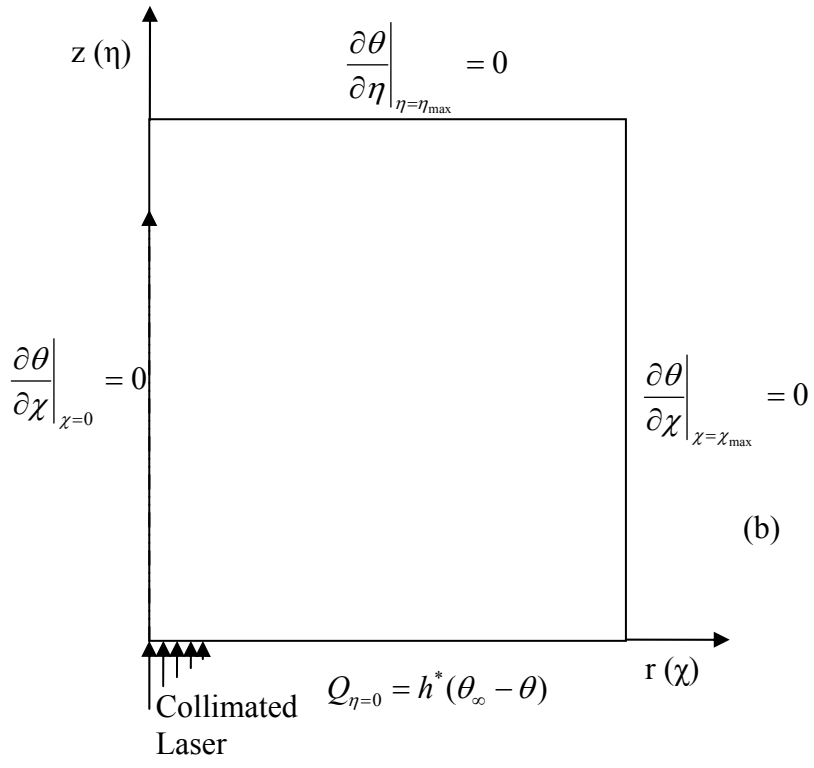

Figure 6.2 Geometric sketch of comparison I: (a) Transparent view and (b) Side view

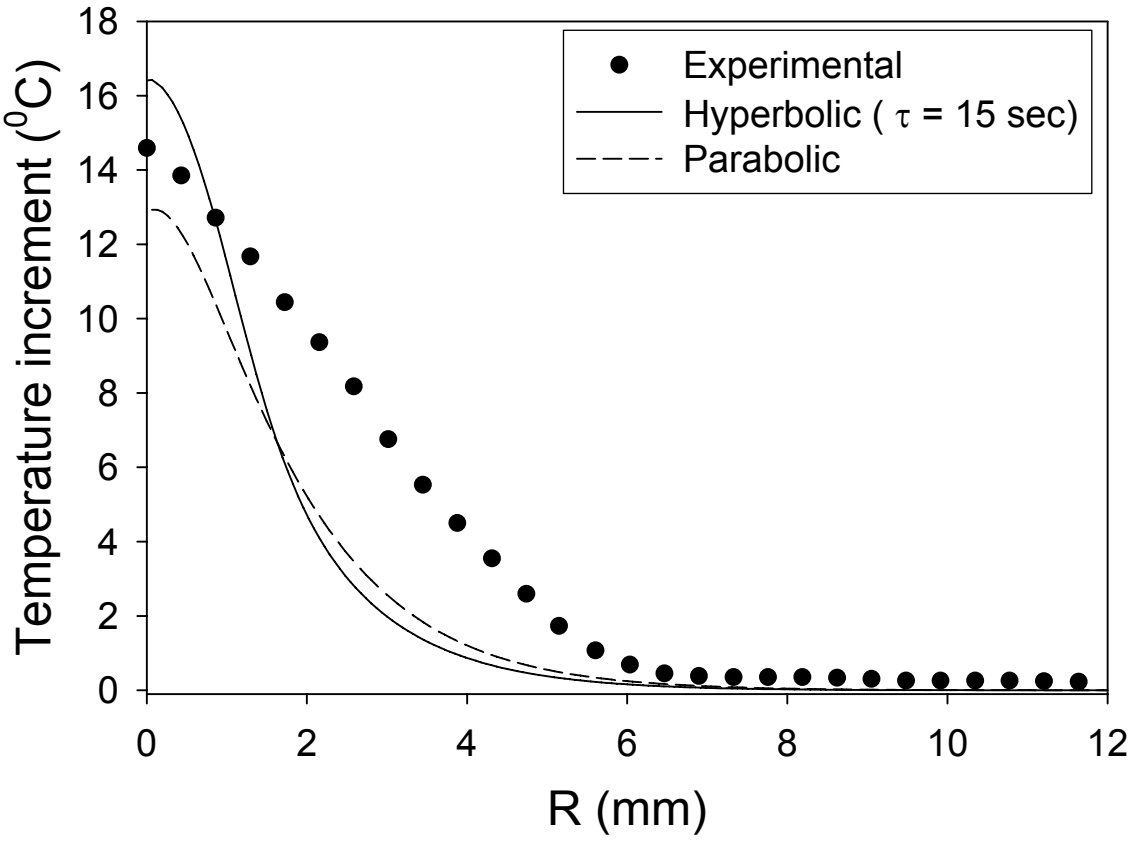

Figure 6.3 The radial temperature distribution at the tissue surface at t = 14 sec.

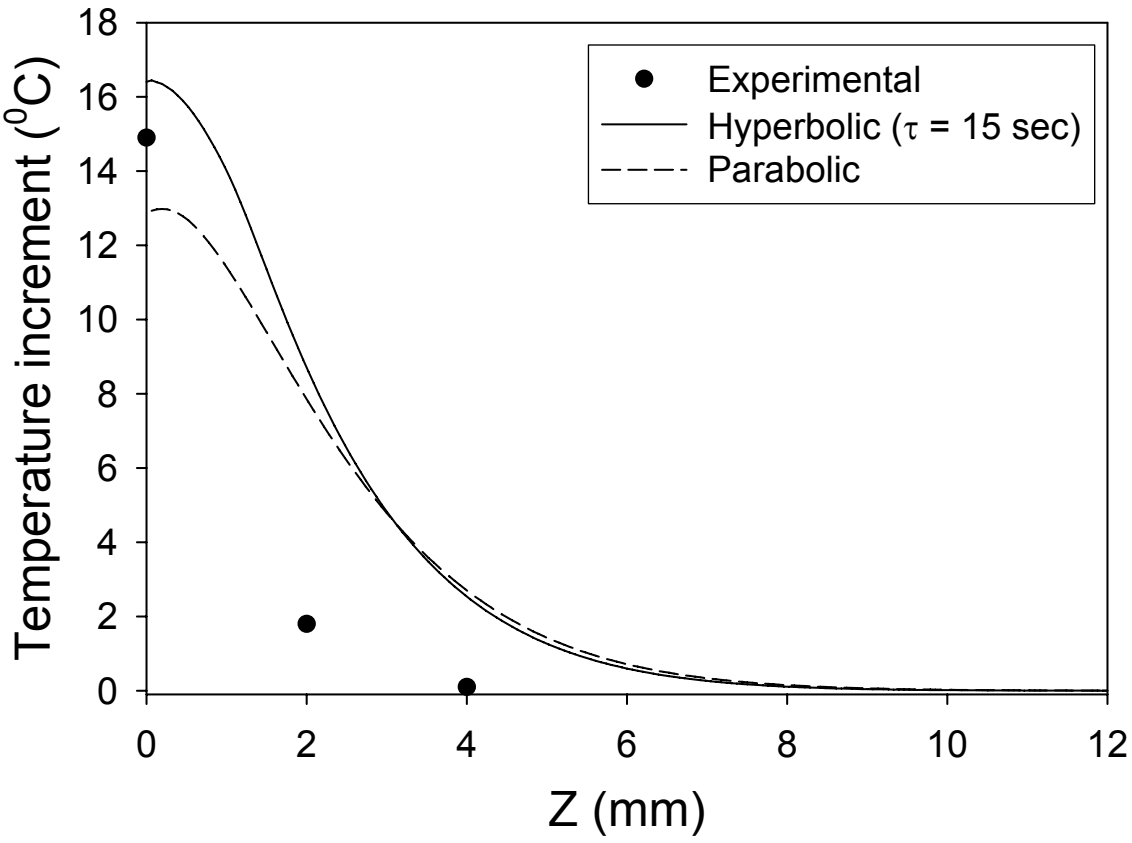

Figure 6.4 The axial temperature distribution along the optical axis at t = 14 sec.

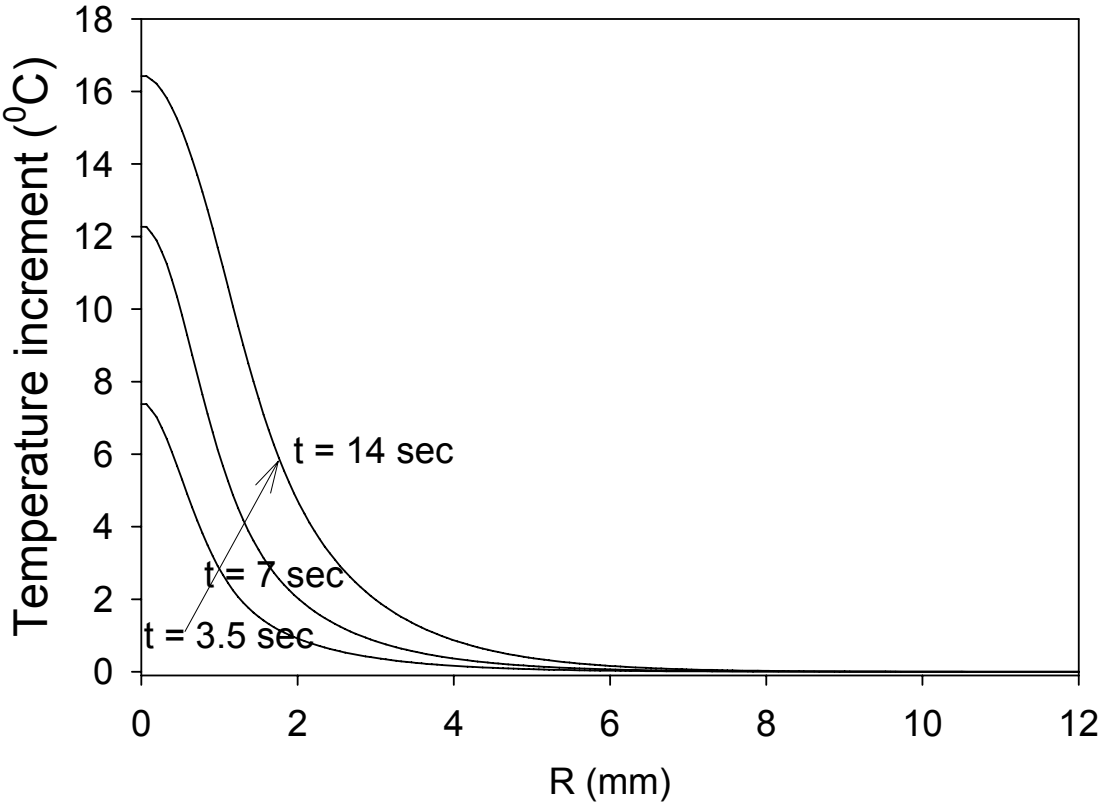

Figure 6.5 The change of radial temperature profiles at the tissue surface as time advancing

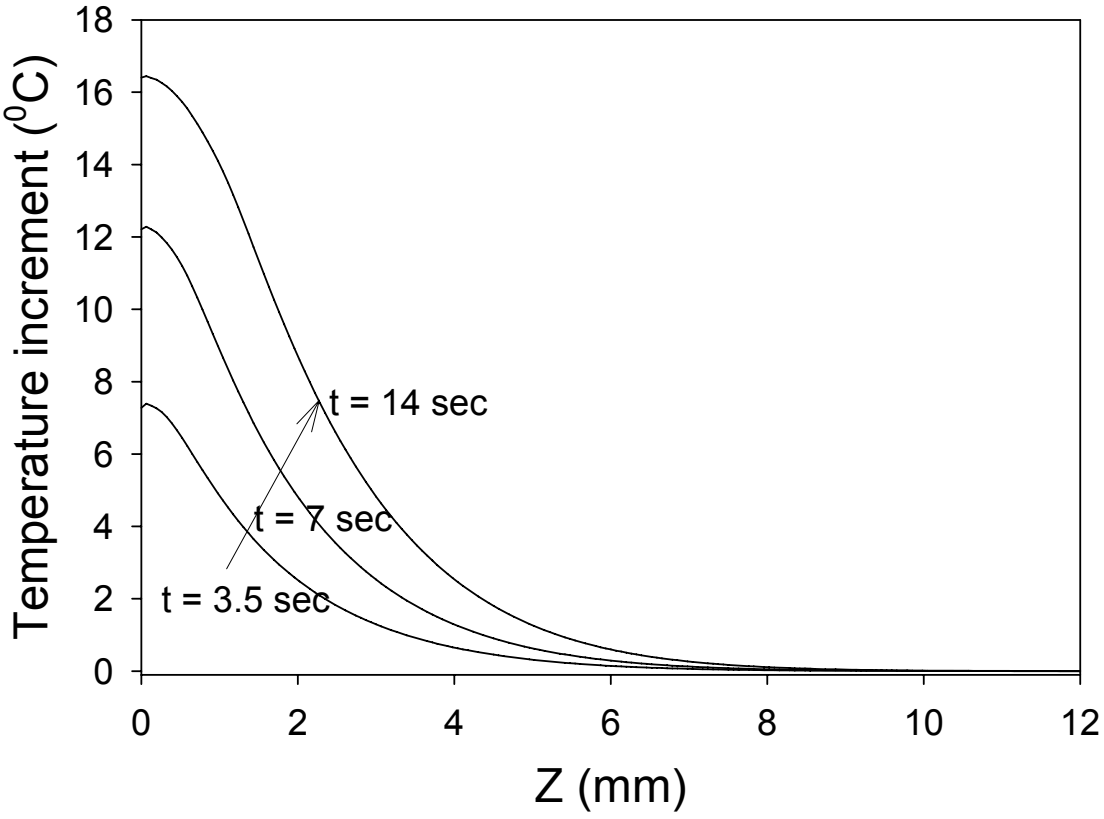

Figure 6.6 The change of axial temperature profiles along the optical axis as time advancing

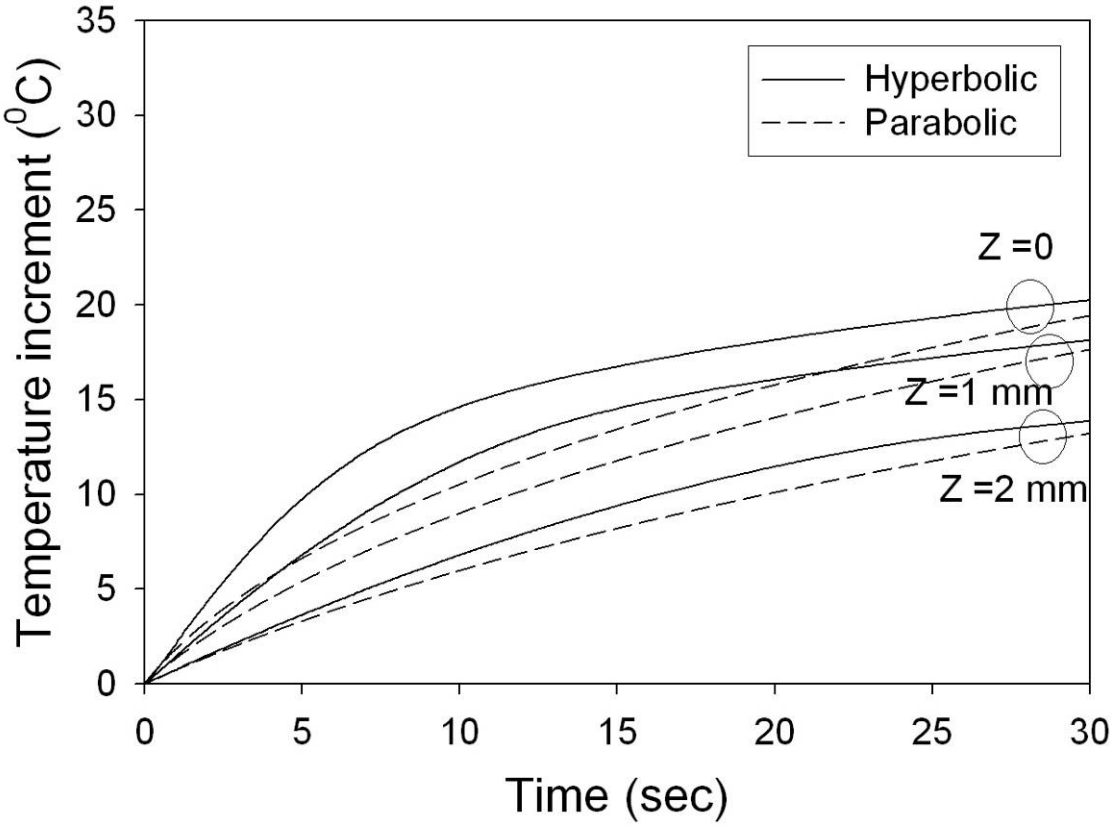

Figure 6.7 The temporal temperature profiles at selective positions along the optical axis. Hyperbolic and parabolic models are compared.

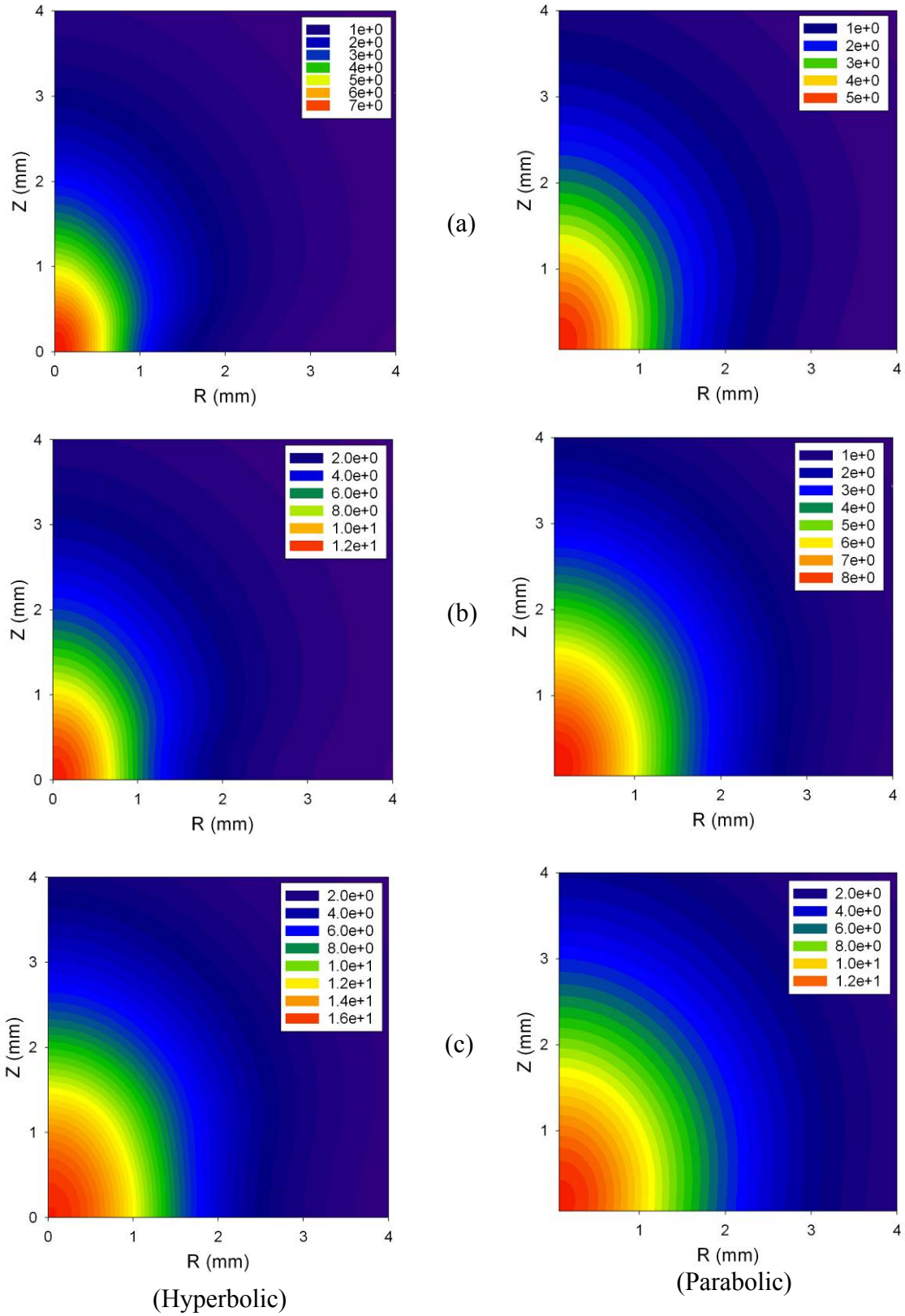

Figure 6.8 The contour of temperature field at certain time instants: (a) t = 3.5 sec, (b) t = 7 sec, and (c) t = 14 sec. (Collimated laser beam)

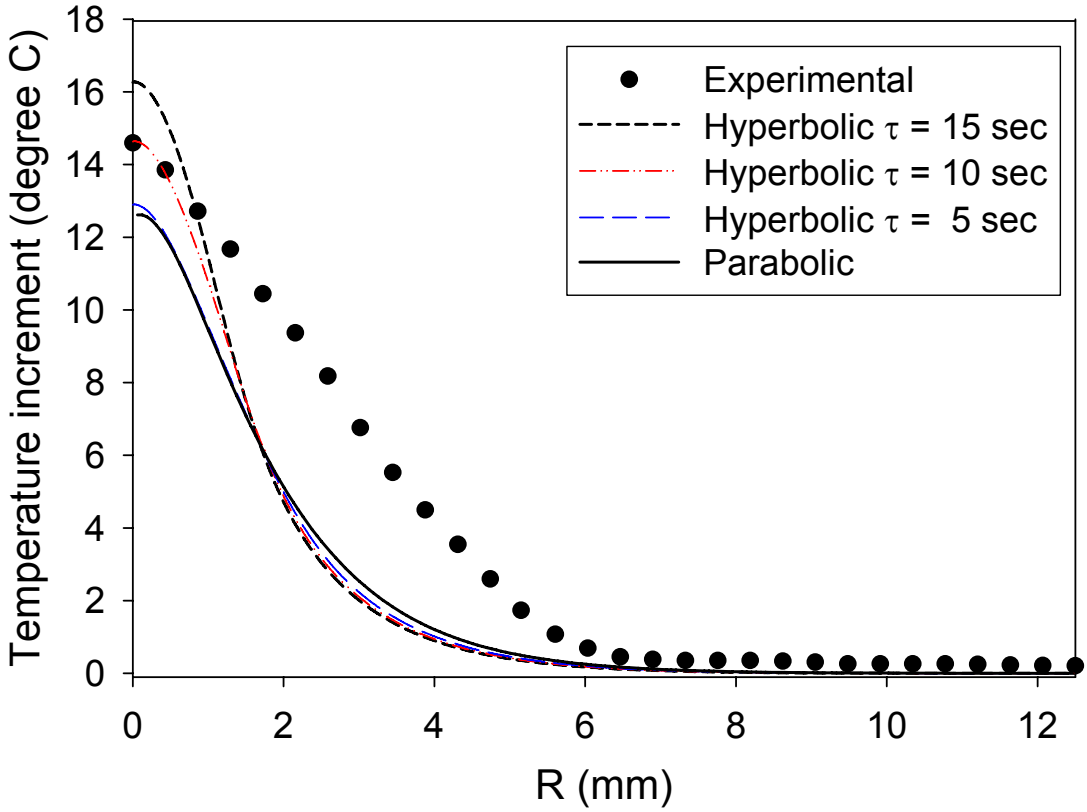

Figure 6.9 The parametric study of thermal relaxation time – The temperature profile along the radial direction at 14 sec.

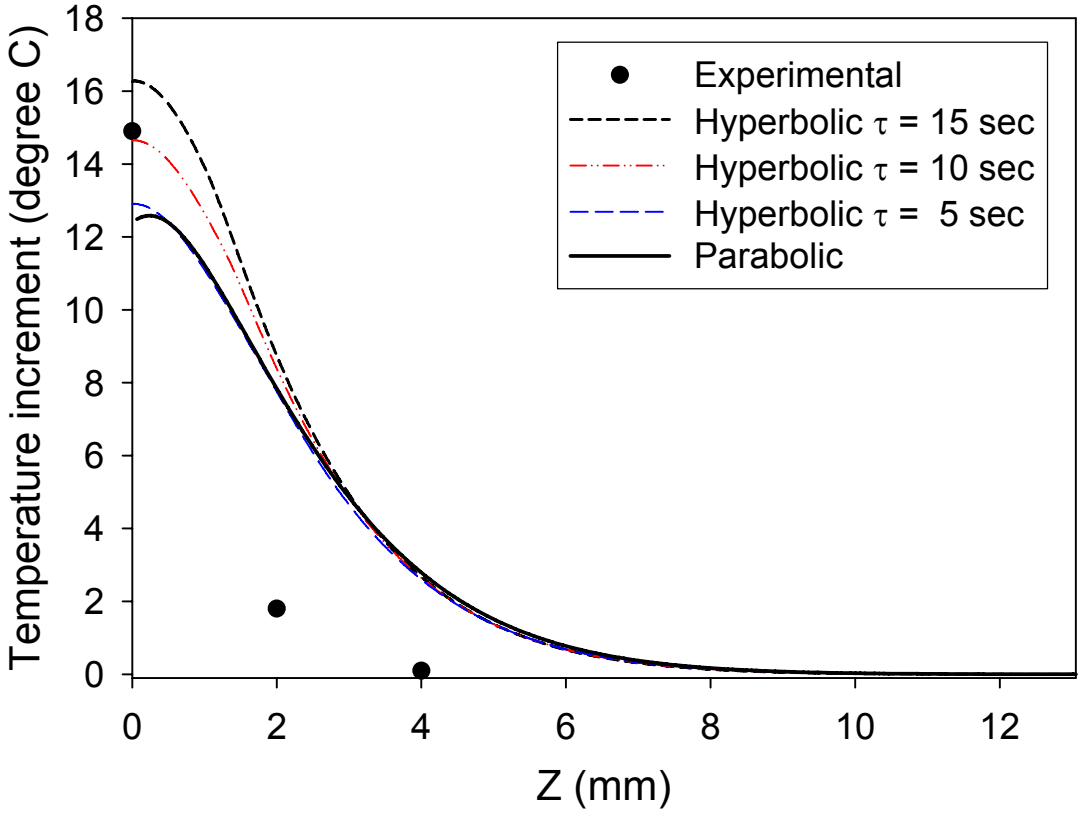

Figure 6.10 The parametric study of thermal relaxation time – The temperature profile along the optical axis at 14 sec.

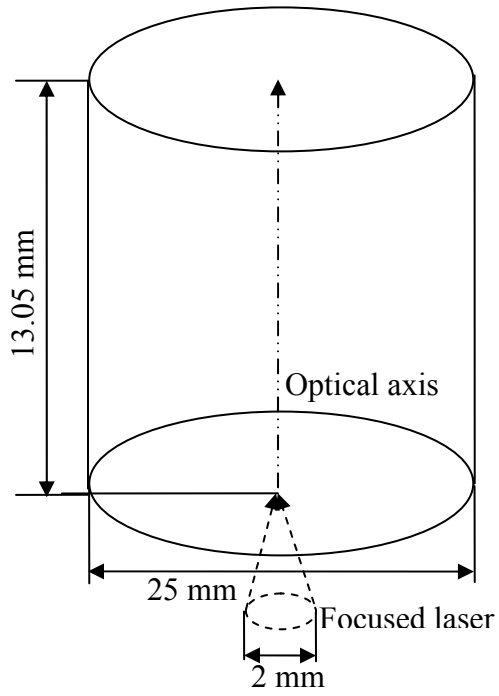

Figure 6.11 Geometric sketch of comparison II

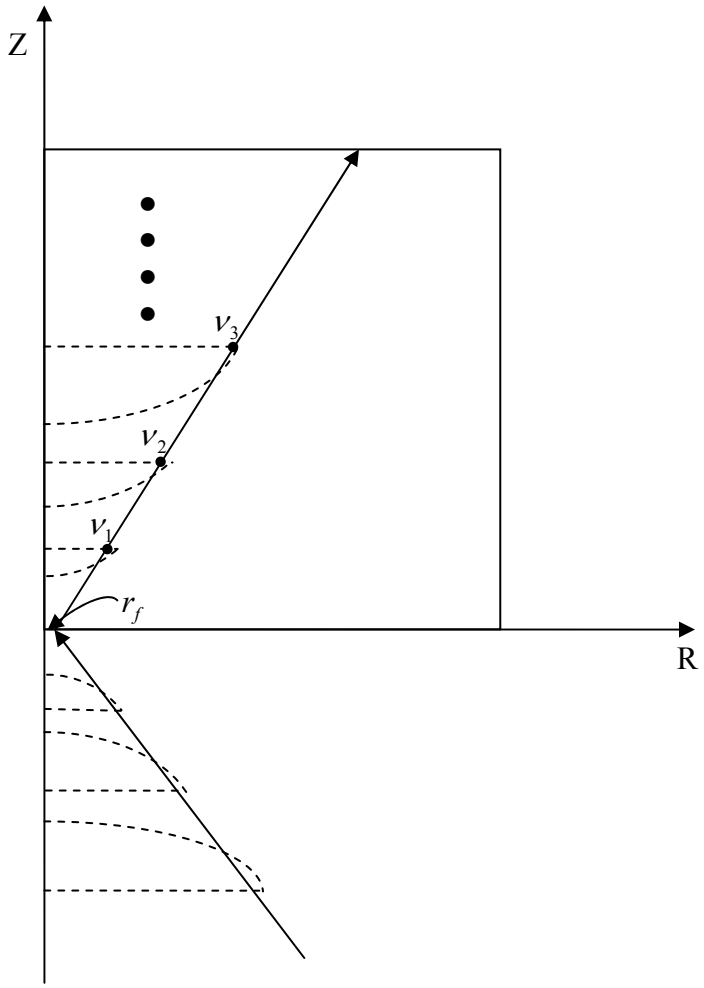

Figure 6.12 The sketch of the focused beam propagation.

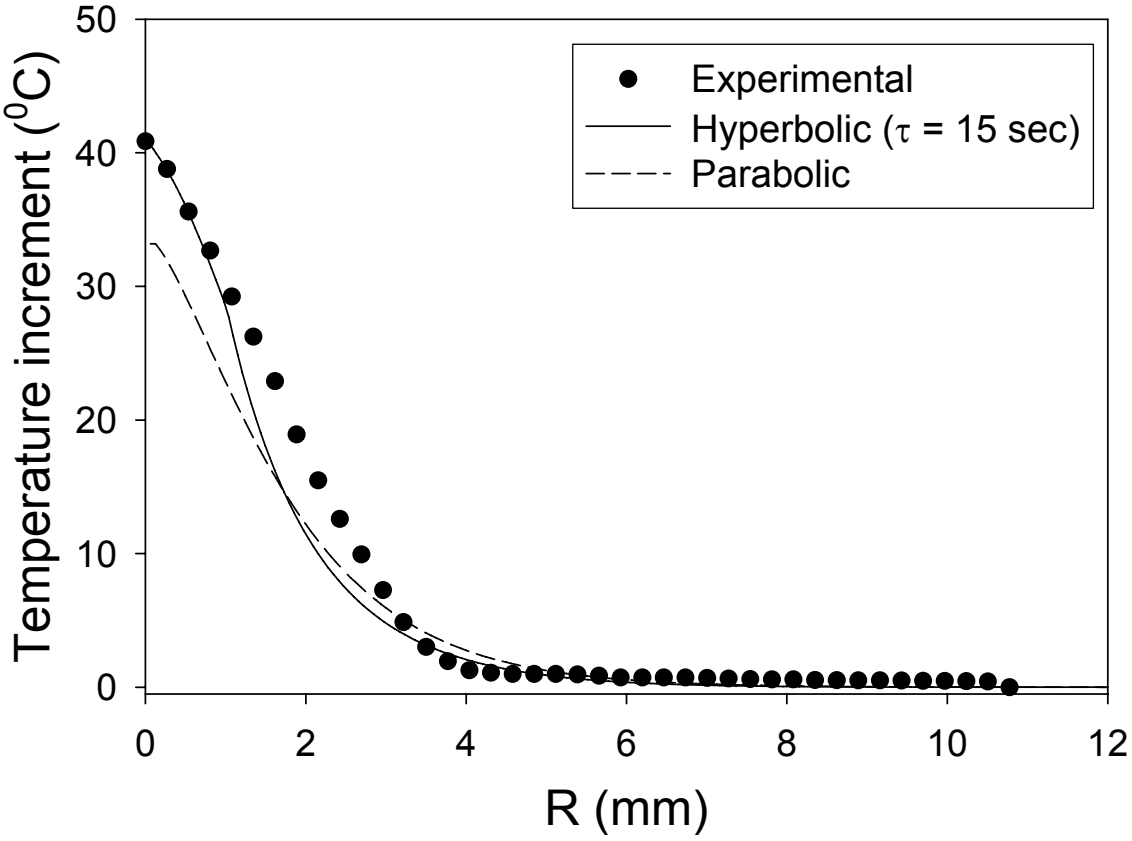

Figure 6.13 The radial temperature distribution at the tissue surface with focused laser beam: t = 14 sec instant.

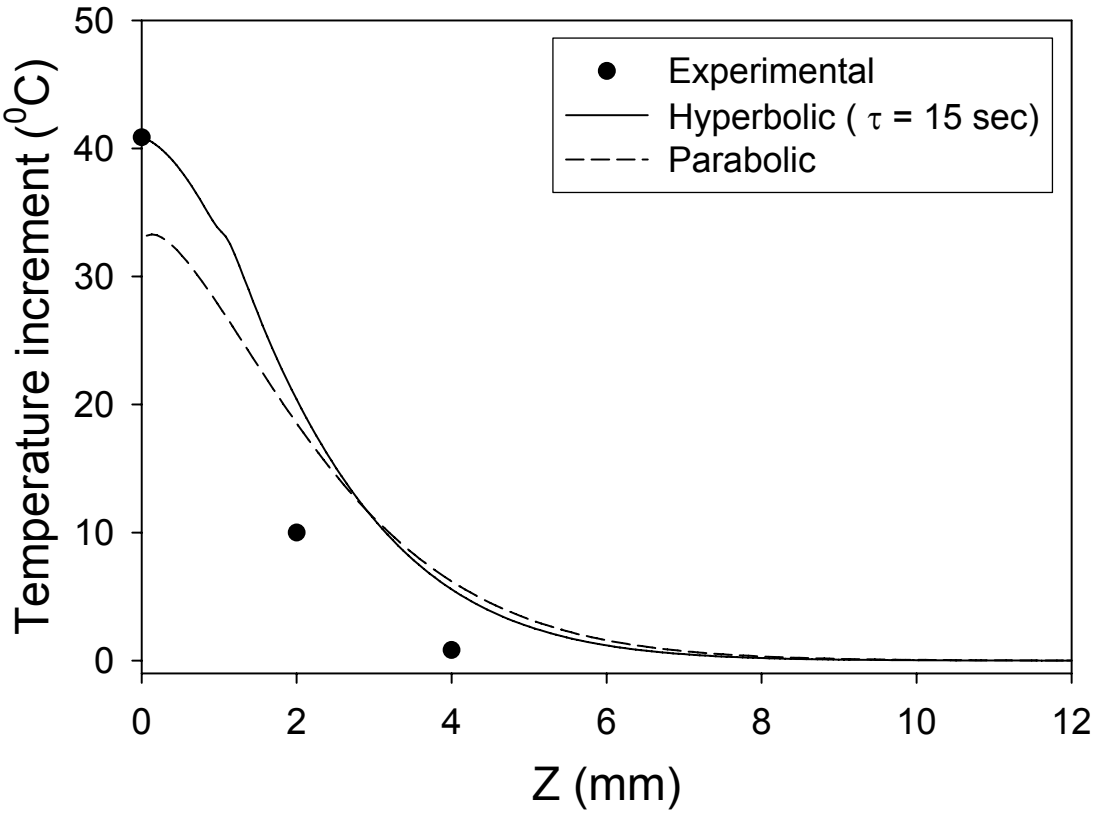

Figure 6.14 The axial temperature distribution along the optical axis with focused laser beam: t = 14 sec instant.

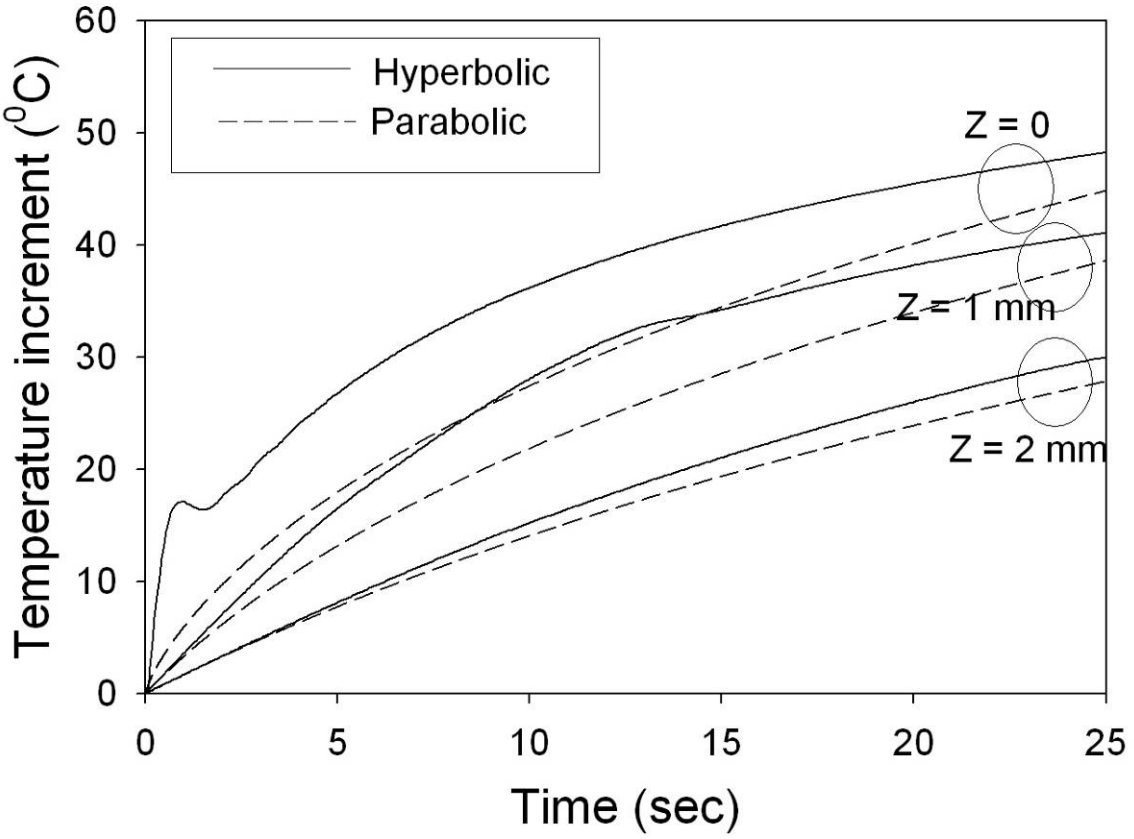

Figure 6.15 The temporal temperature profiles at selective at selective positions along the optical axis.

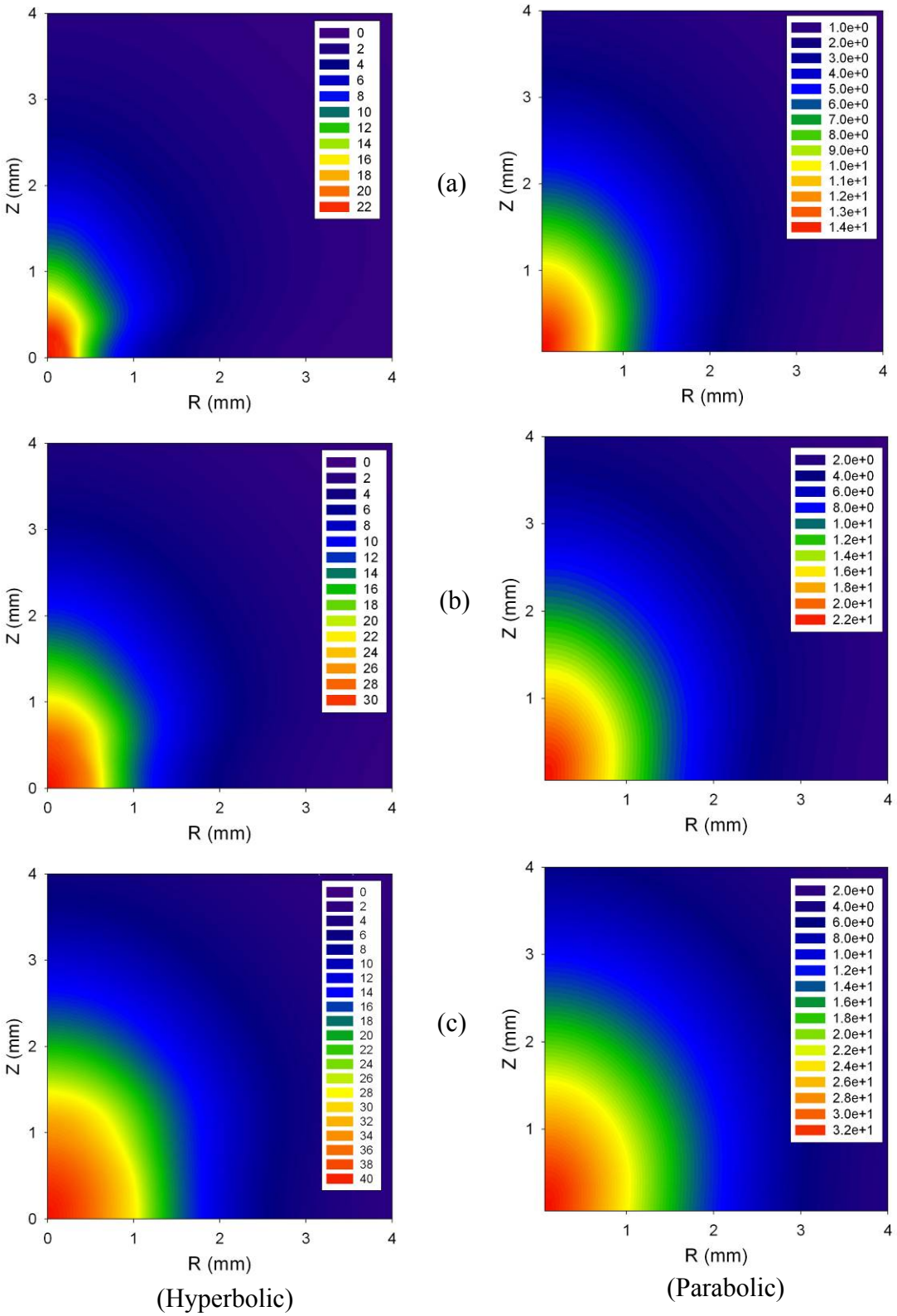

Figure 6.16 The contour of temperature field at certain time instants: (a) t = 3.5 sec, (b) t = 7 sec, and (c) t = 14 sec. (Focused laser beam)

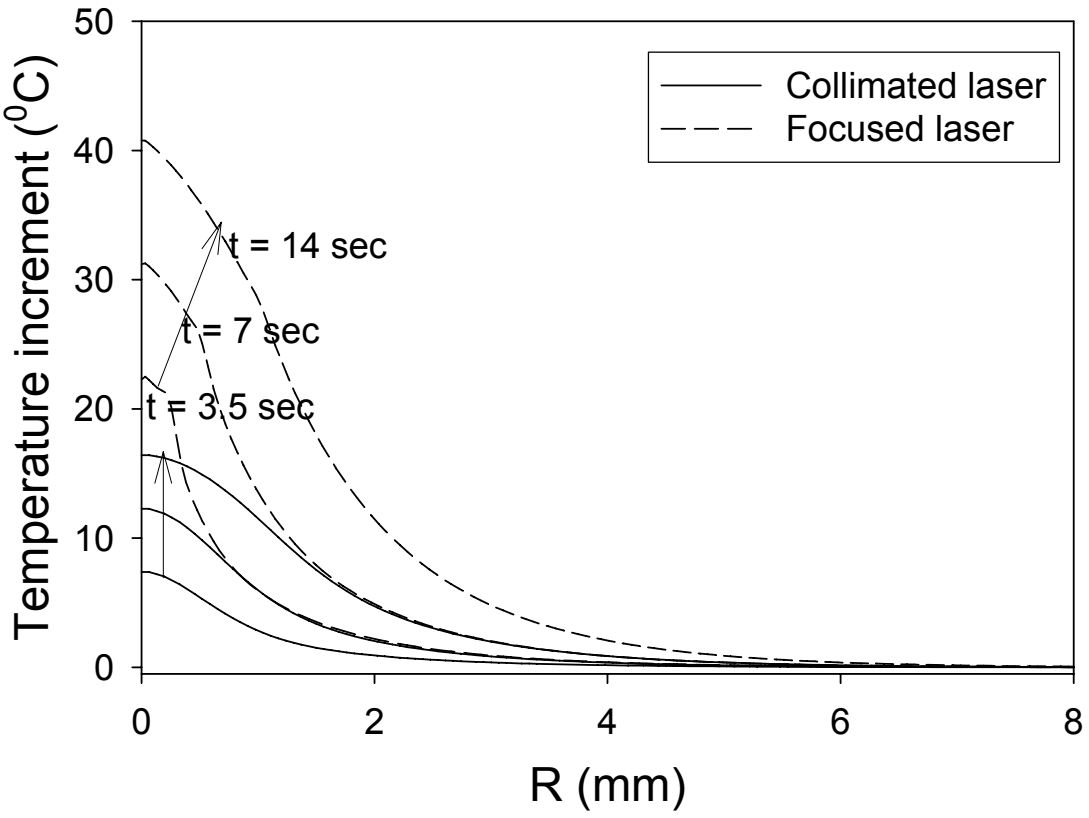

Figure 6.17 The comparison between focused laser beam and collimated laser beam with the temperature profiles along the tissue surface.

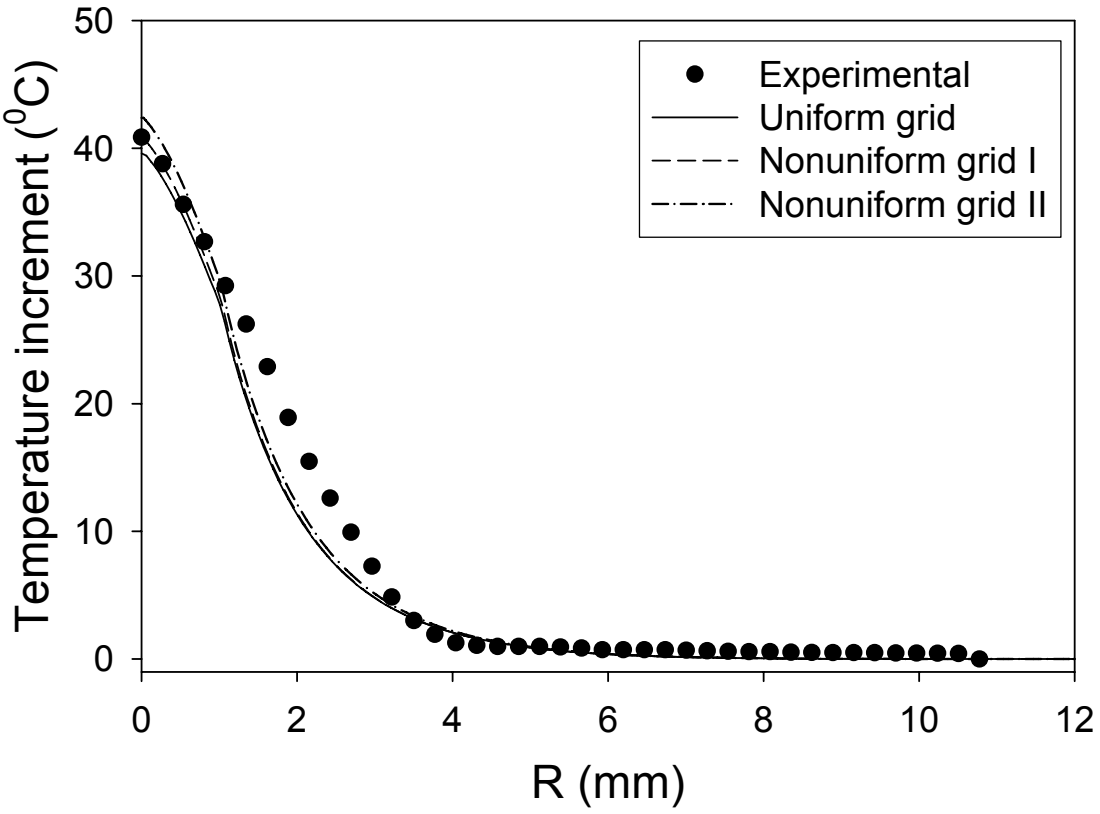

Figure 6.18 The grid system comparison with the temperature profiles along the tissue surface at t =14 sec.

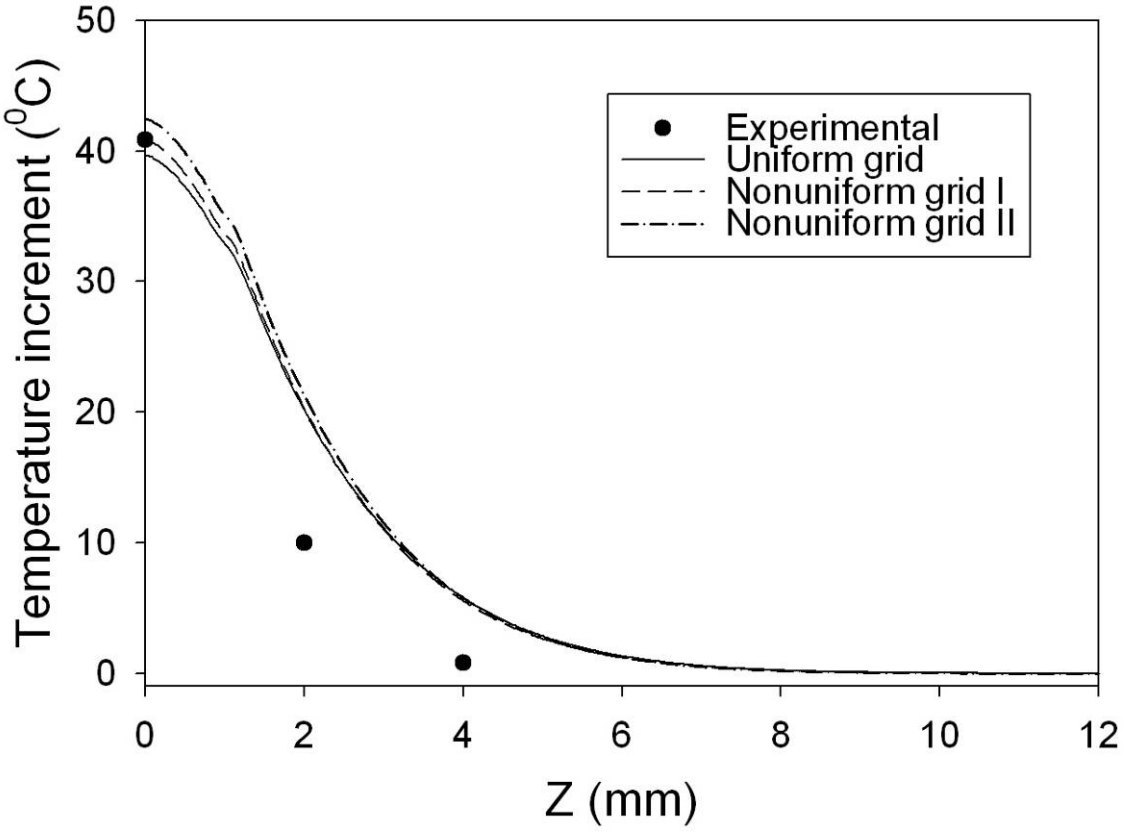

Figure 6.19 The grid system comparison with the temperature profiles along the optical axis at t =14 sec.

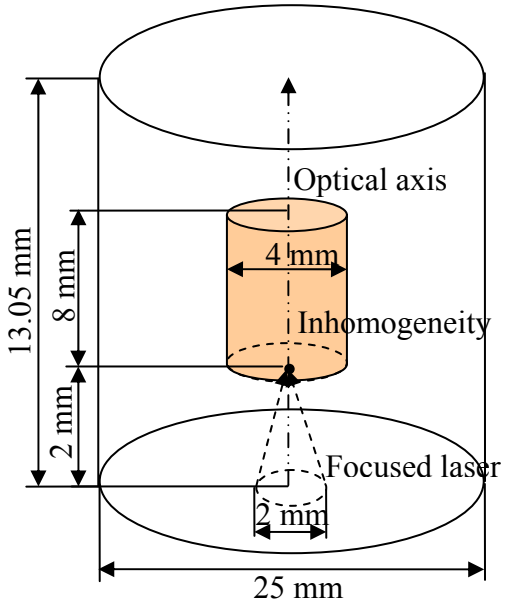

Figure 6.20 Geometric sketch of comparison III.

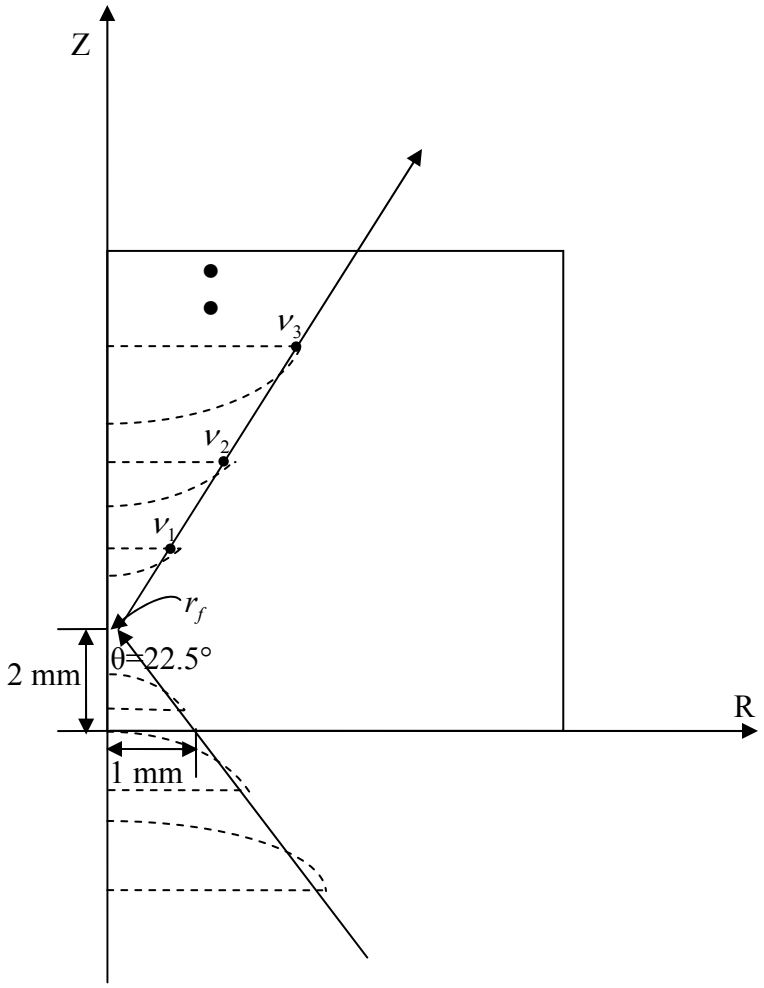

Figure 6.21 The sketch of the focused beam propagation. The beam is focused below 2mm from the surface.

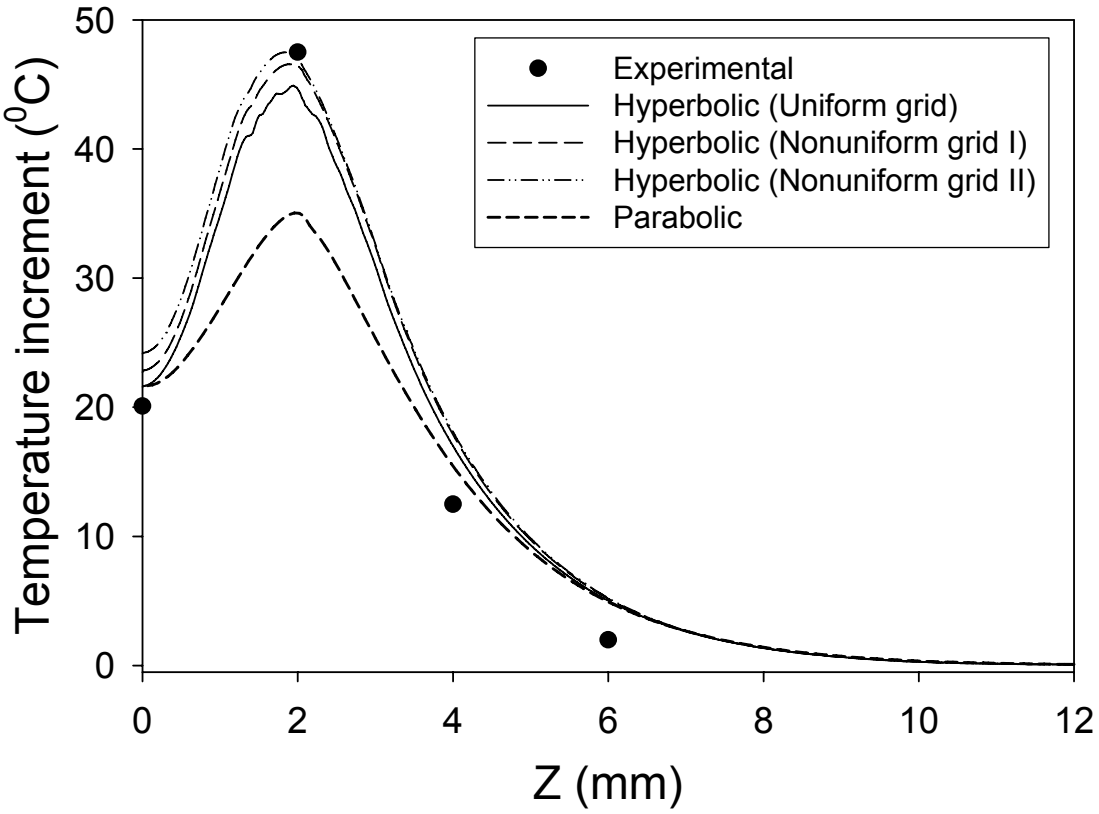

Figure 6.22 The axial temperature profile along the optical axis at t = 10sec.

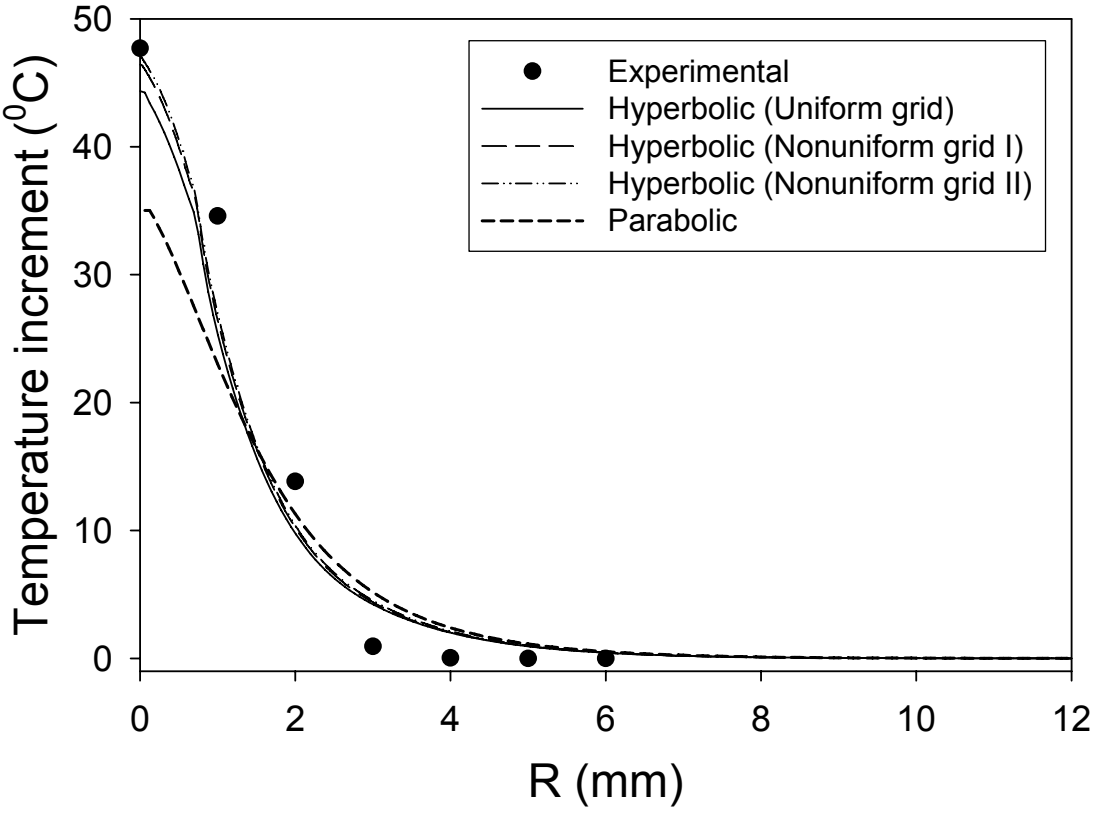

Figure 6.23 The radial temperature profile along the tissue surface at t = 10sec.

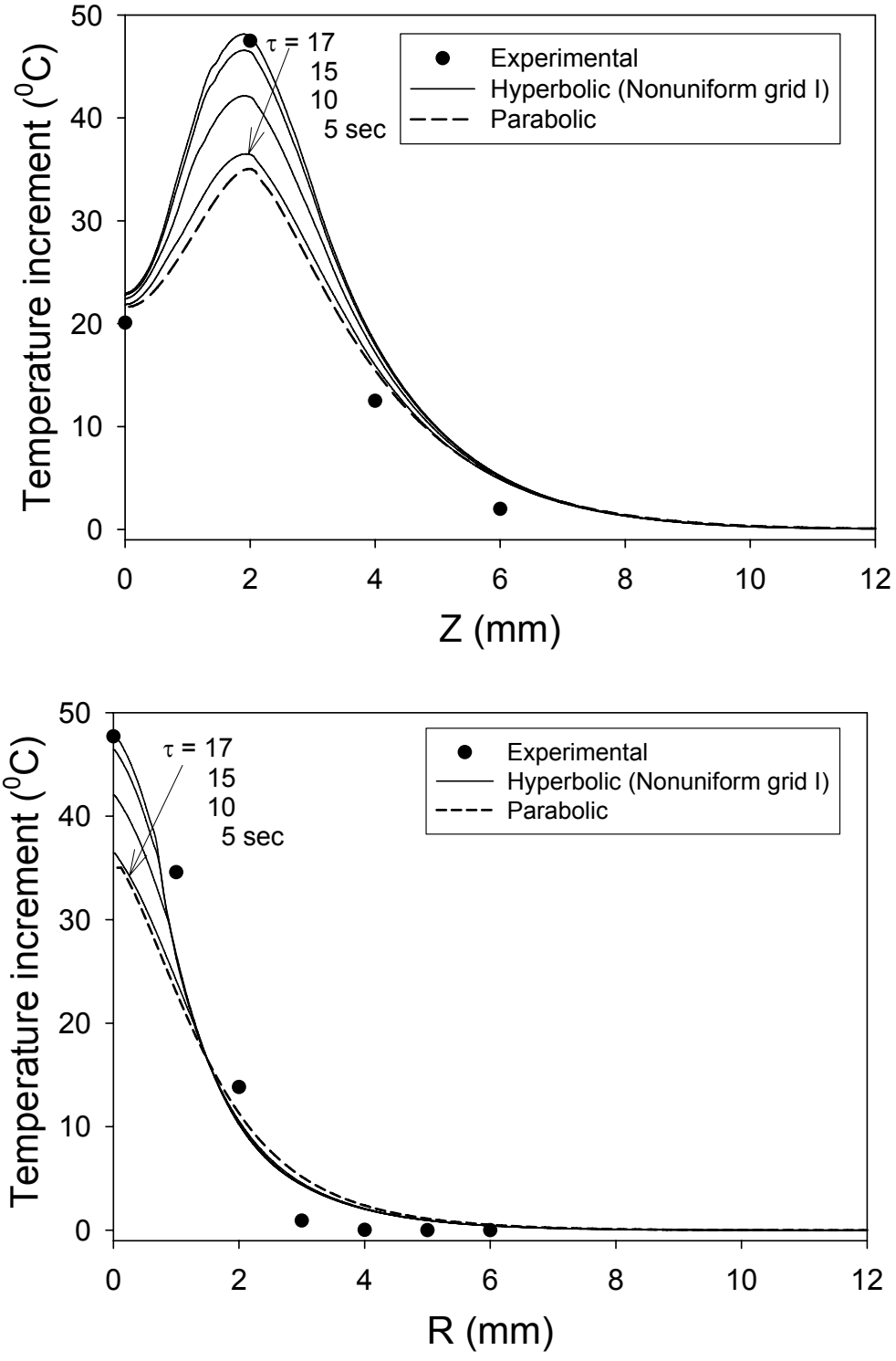

Figure 6.24 The parametric study of thermal relaxation time.

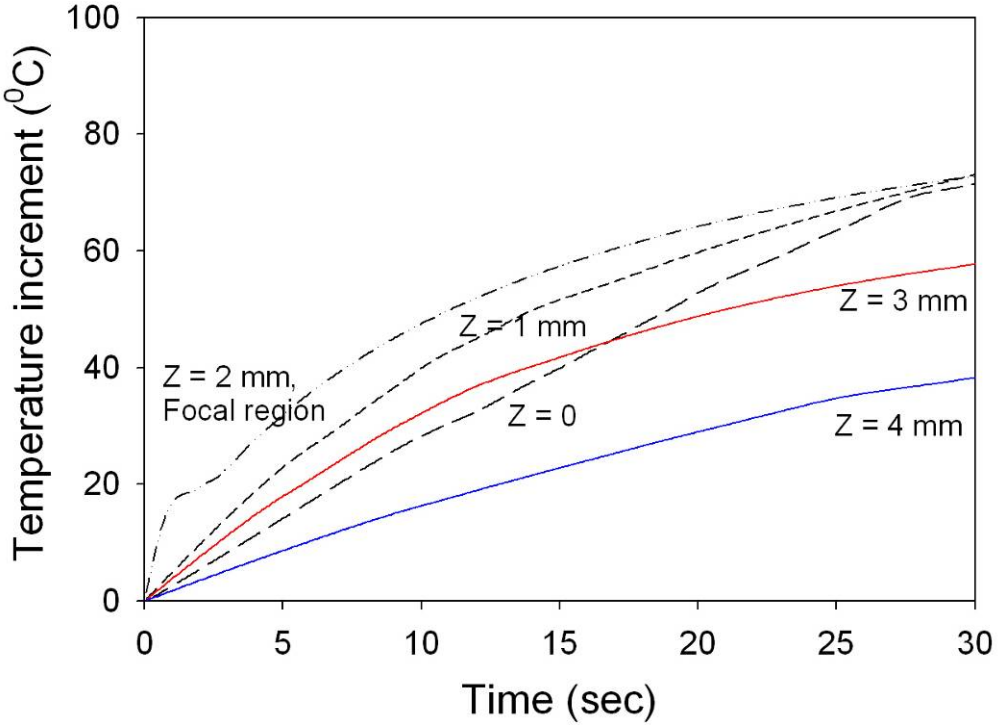

Figure 6.25 The temporal temperature profiles at selective positions along the optical axis: τ = 15 sec is used.

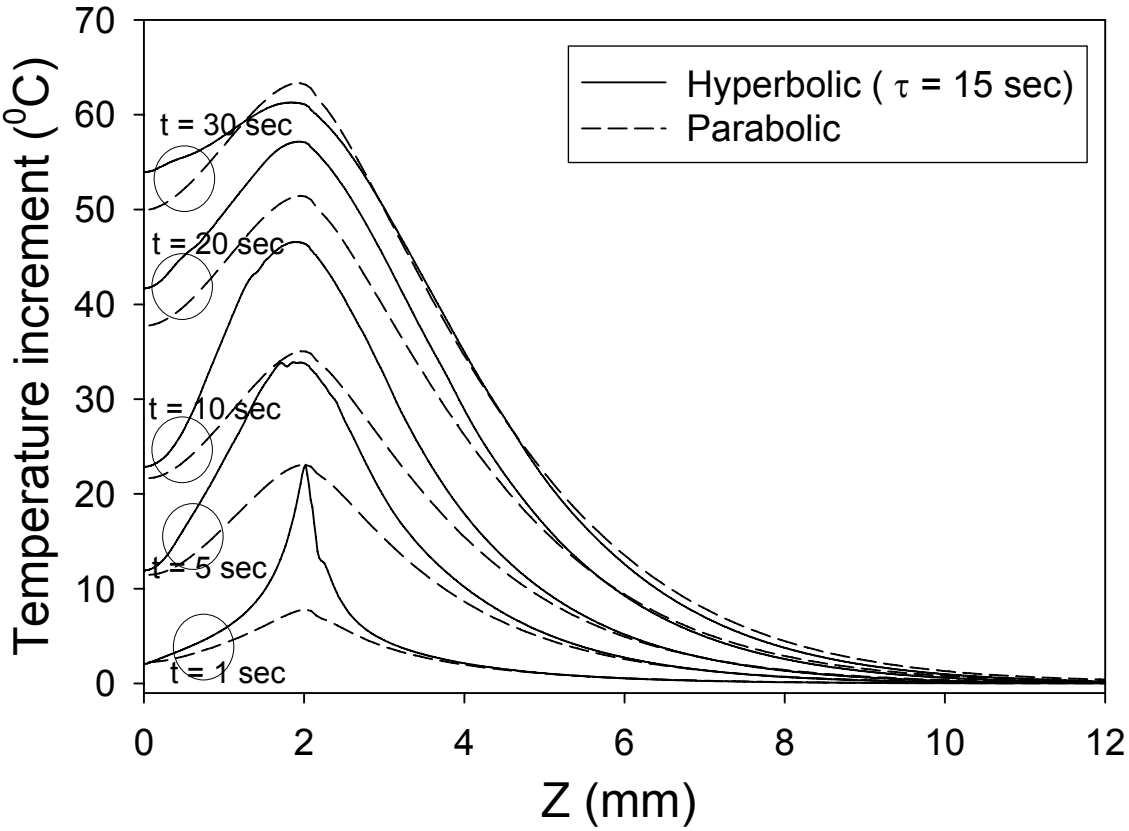

Figure 6.26 The evolution of temperature profiles as time marching.

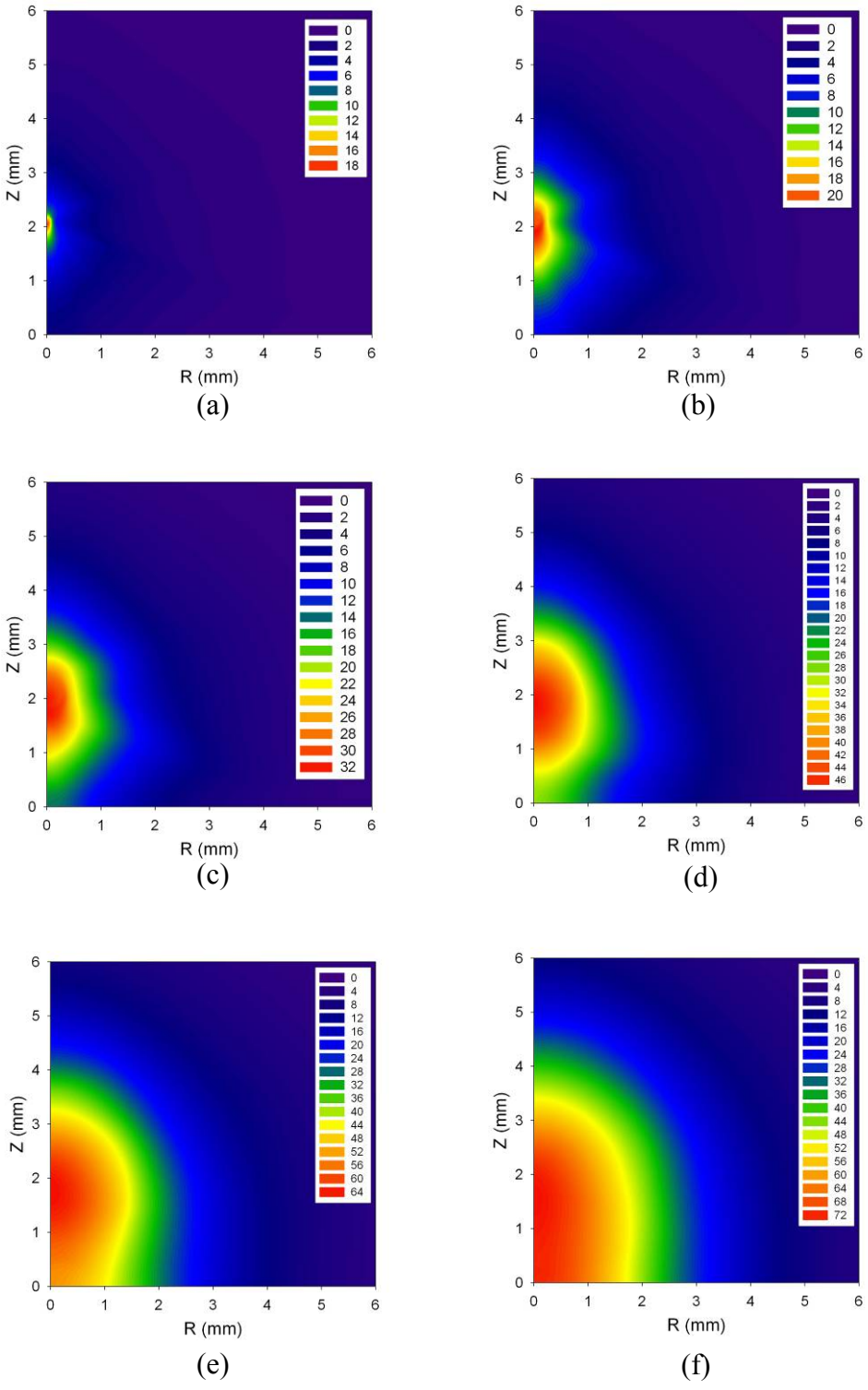

Figure 6.27 The contours of temperature field propagation as time marching in hyperbolic conduction (τ = 17): (a) t = 1sec, (b) t = 2.5 sec, (c) t = 5 sec, (d) t = 10 sec, (e) t = 20 sec, and (f) t = 30sec.

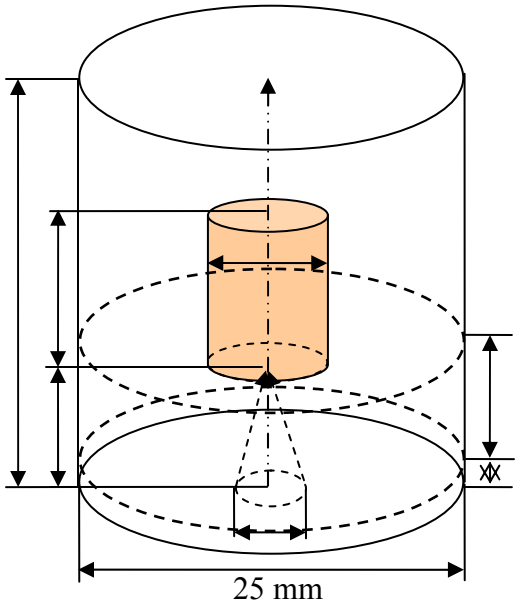

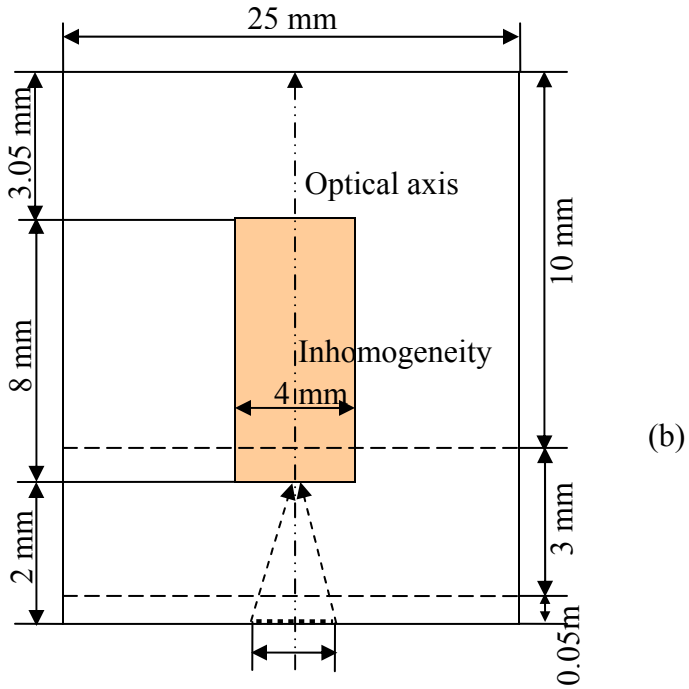

Figure 6.28 Geometric sketch of comparison IV: (a) Transparent view and (b) Side view.

Layer	Thickness	Absorption Coefficient (σ_a) (mm^{-1})	Reduced scattering Coefficient (σ_s') (mm^{-1})
Epidermis	0.05 mm	0.355	0.824
Dermis	3 mm	0.049	0.824
Fatty tissue	10 mm	0.050	0.55

Table 6.1 The length scale of three layered tissue and optical properties.

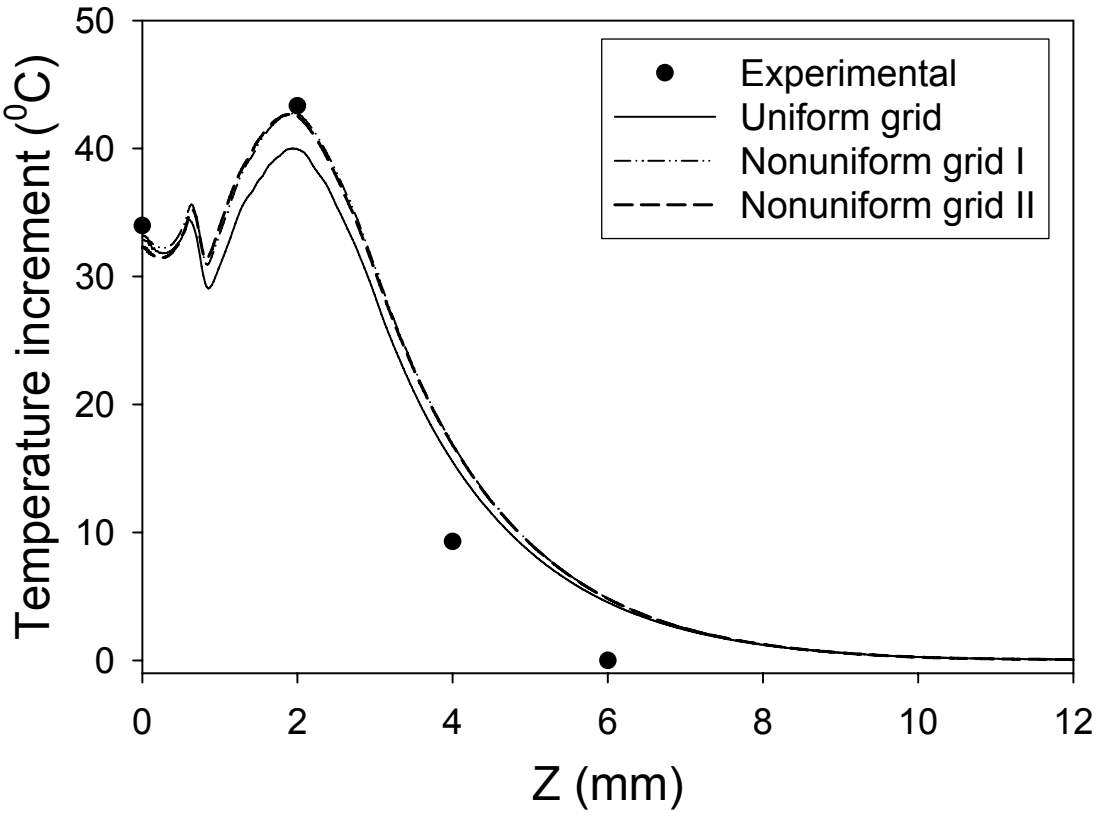

Figure 6.29 The comparison between experimental data and simulation result at t = 10 sec. (a) Z axial along the optical axis

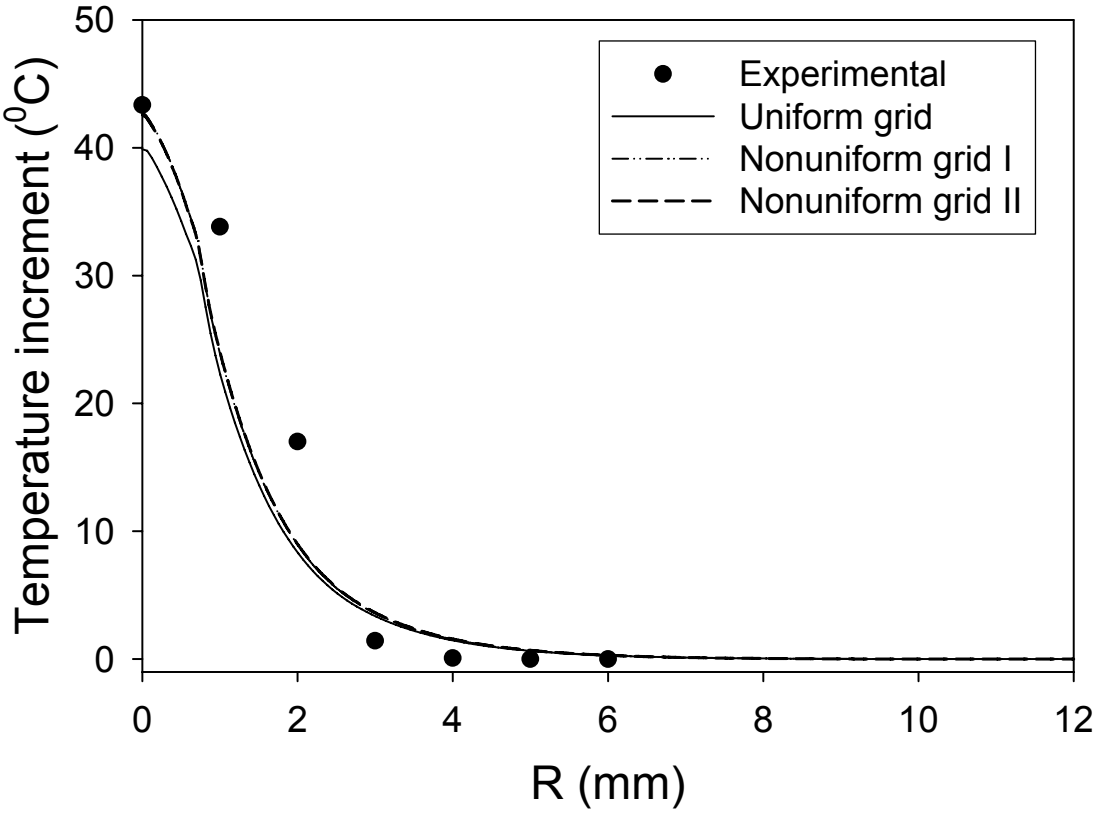

Figure 6.29 (continued). The comparison between experimental data and simulation result at t = 10 sec. (b) Radial direction at Z = 2mm.

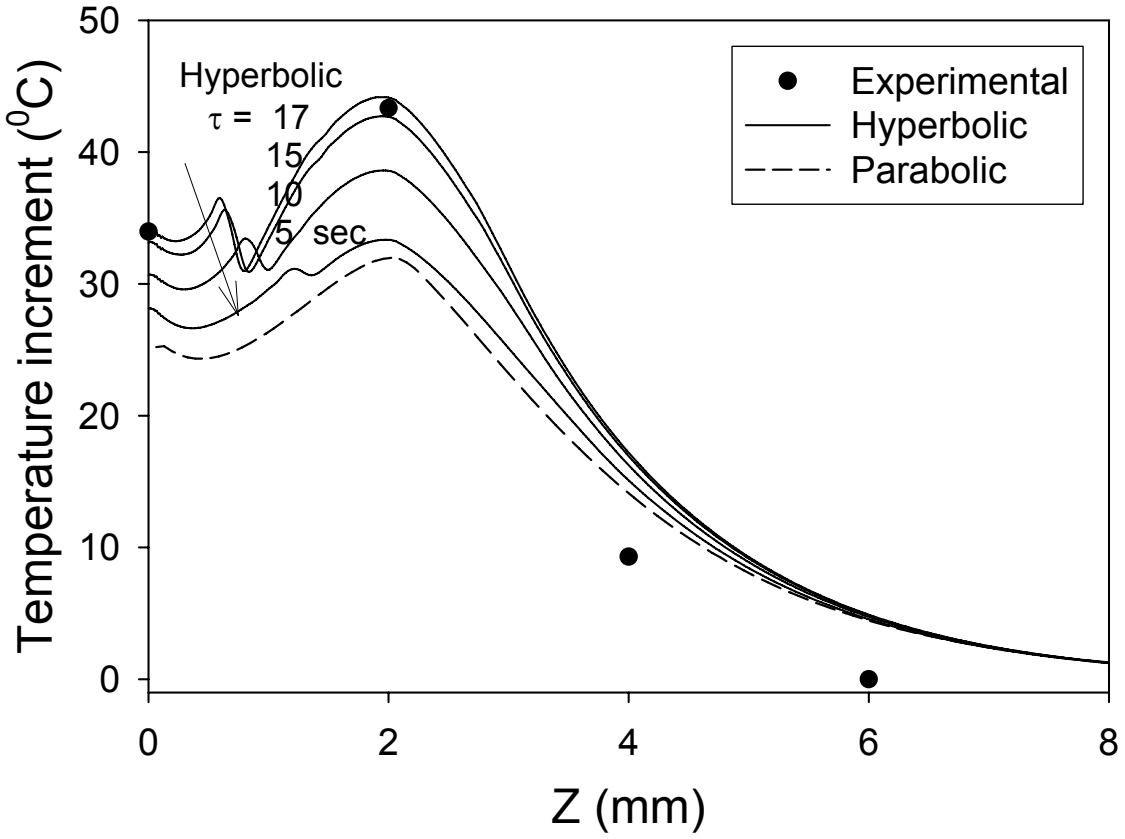

Figure 6.30 The parametric study of thermal relaxation time. (The axial profile)

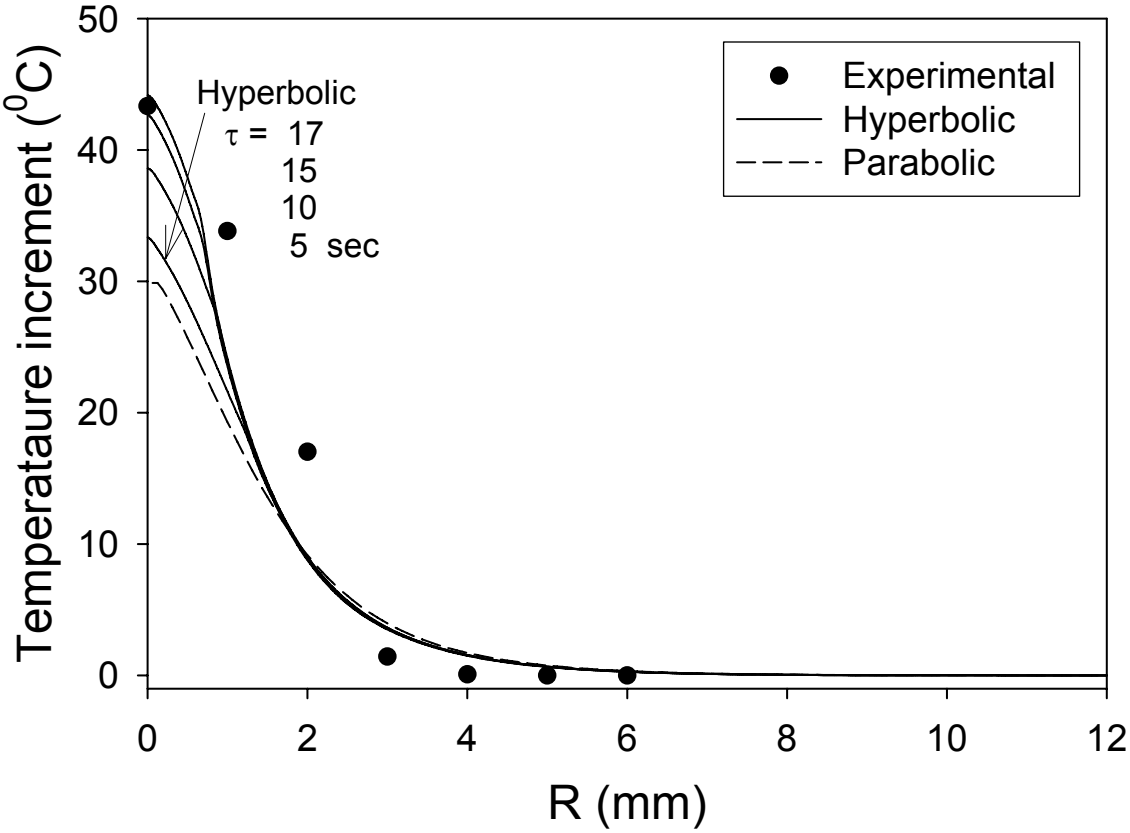

Figure 6.31 The parametric study of thermal relaxation time. (The radial profile at Z = 2mm)

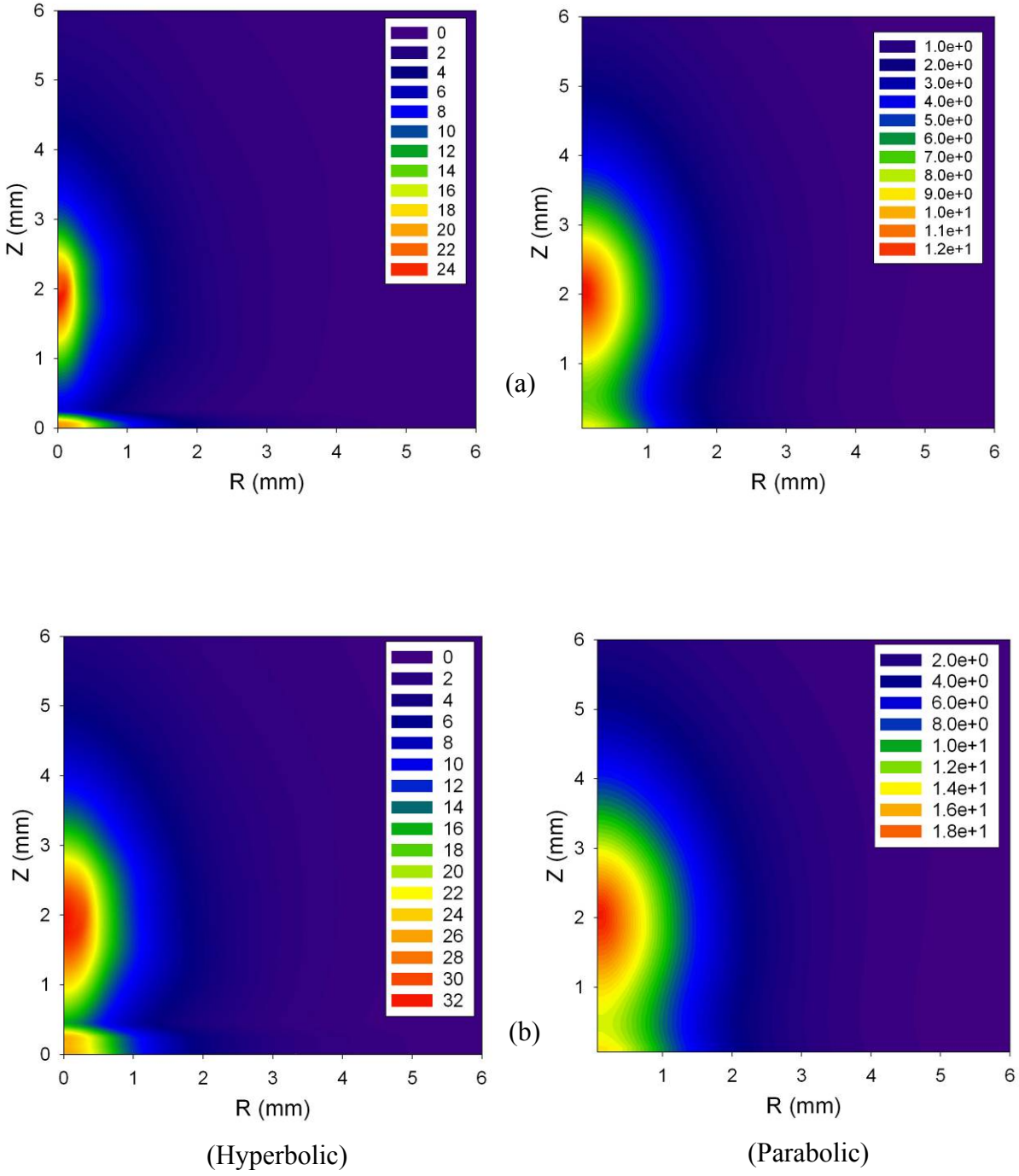

Figure 6.32 The contours of temperature field at selective time instants. The hyperbolic conduction model (τ = 17 sec) and compared with parabolic conduction model: (a) t =2.5 sec and (b) t = 5 sec.

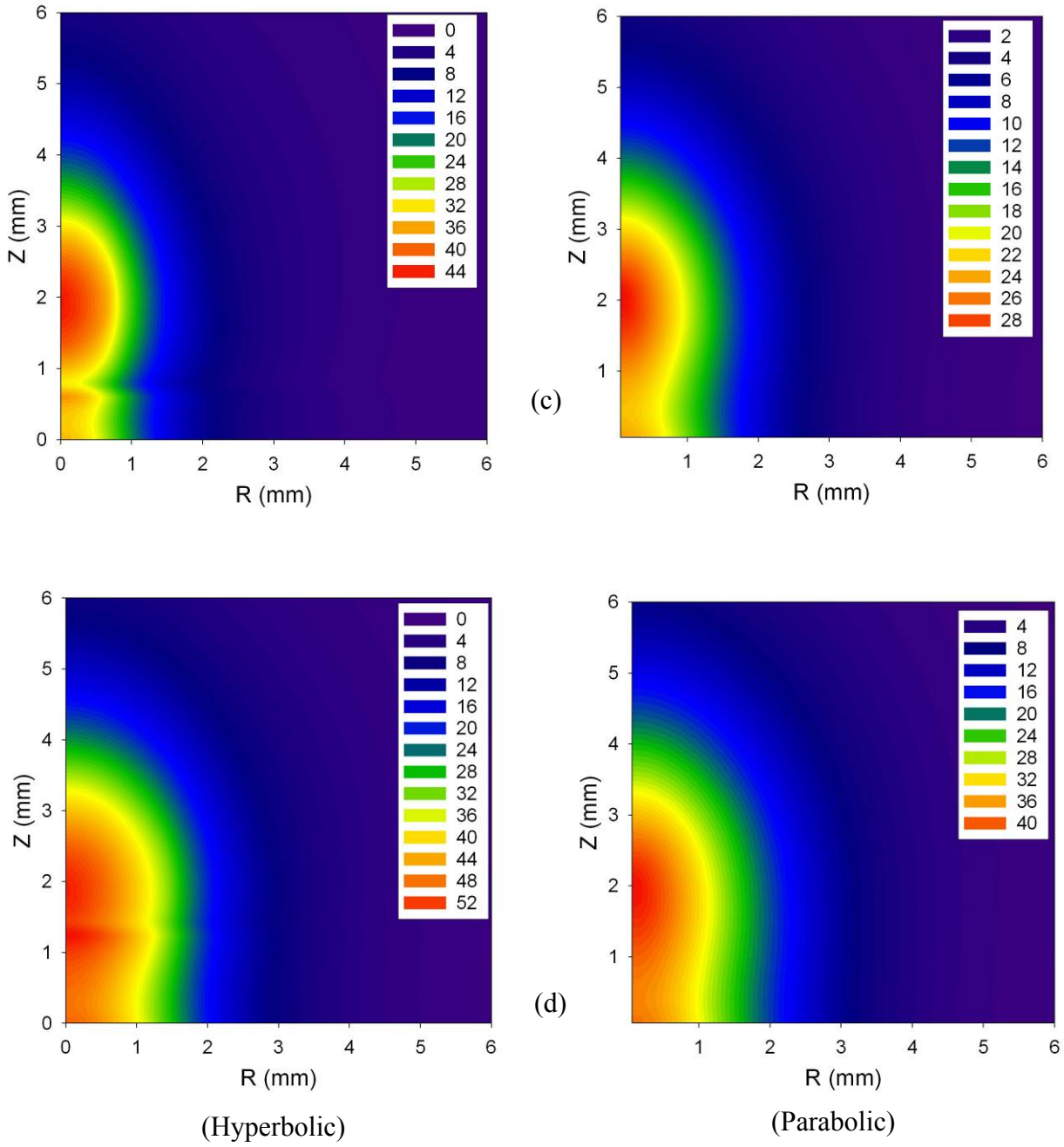

Figure 6.32 (Continued) The contours of temperature field at selective time instants. The hyperbolic conduction model (τ = 17 sec) and compared with parabolic conduction model: (a) t =10 sec and (b) t = 20 sec.

Chapter 7

Conclusion and Future work

7.1 Conclusion

The primary purpose of this study was to investigate the short pulsed laser transfer mechanism subjected in the tissue medium.

In chapter 1, the study was introduced by the explanation of background and literature survey. The objective and uniqueness of study were also emphasized.

In chapter 2, the transient radiative heat transfer irradiated to the short pulsed laser was modeled, formulated, and solved using TDOM (Transient Discrete Ordinates Method). The cylindrical shape tissue was modeled. By the tissue optical parametric study, high scattering medium showed the steep spatial gradient of divergence of radiative heat flux profile. The high concentration of radiation energy absorbing was predicted in high absorbing optical property medium. The focused laser beam can amplify radiation energy absorption. To increase calculation efficiency, the nonuniform grid was employed for the focused laser beam case. Several layered tissue with inhomogeneity was modeled to mimic real tissue phantom.

In chapter 3, the transient heat conduction problem was dealt with. Both hyperbolic and parabolic conduction models were formulated and solved. For the hyperbolic conduction, MacCorkmack's predictor and corrector scheme employed. The

error term was corrected and the noise was diminished around wave dump region. The solutions of two heat conduction models were validated with analytical solution. Both continuous and pulsed surface heat sources, the numerical result and analytical one were matched very well.

In chapter 4, the radiative heat transfer and hyperbolic conduction was combined. Initially the tissue was irradiated until 1ms and hyperbolic conduction was followed. After radiation energy was directly absorbed in the tissue medium and heat was dissipated by the conduction process. The thermal wave propagation had been observed and maximum temperature field of the hyperbolic model was higher near 7% than the parabolic model.

In chapter 5, the experimental study was conducted to evaluate hyperbolic heat conduction. The fresh chicken breast tissue was used as the tissue sample. After it was maintained room temperature, the ice block was suddenly contacted to one side of tissue sample. When the location of thermocouple is far from the contacting position, the thermal wave phenomenon was not observed. By the long time temperature measurement, the thermal diffusivity is predicted as a range of 0.102-0.109 mm^2/s. A sudden change of temperature is observed in near contacting position.

In chapter 6, the benchmarking study with experimental data was performed. The experimental data was provided by the Prof. Kunar Mitra's group. Generally, the hyperbolic model combined with radiative heat transfer showed very similar result with the experimental data. The hyperbolic model also showed high temperature increment near the laser deposition area. The focused laser beam played a role of temperature

amplification around focal region. In calculation result, the movement of thermal wave had been found out due to the high absorption of radiation energy.

7.2 Future works

Though numerical result was showed similar value with experimental one, there exists a little deviation in some cases. A possible reason of it, the measurement of optical properties, and thermal properties are misled. The heat conduction model needs to consider water evaporation, surface heat convection effect, phase change of tissue surface region, and so on. Recently, hyperbolic conduction model is interpreted by Antaki, where he suggested the dual phase lag model. One of the experimental data is shown more close to this model. Experimental study is crucial to validate the hyperbolic conduction. Many trials of experimental study should be conducted.

Appendix A

Characterization study of laser exposure time

This Appendix includes the characterization study of laser exposure time. The short-pulsed laser is irradiated until 1 ms in Chapter 4 and it is extended until a second regime in Chapter 6. The reason of restriction of laser exposure time is to minimize the conductive heat transfer. The rational of it is that only radiative heat transfer occurs until 1 ms and the conductive heat transfer is followed by. To justify this rational, the comparison study is conducted. The short-pulsed laser is irradiated until 1 second in modeled dermis tissue. One model is only considering radiative transfer. Other two models are that combined radiation and hyperbolic or parabolic conduction. In Figure A1, the contribution of conductive heat transfer starts around 0.1 second regime. It is decelerated inside tissue medium. In enlarged Figure until 0.01 sec, the profiles are almost identical. In Figure A2, the comparison is conducted with contour plots. Generally, the plots show similar aspect all models until 0.1 sec. Then, we can justify that the contribution of conduction is trivial before 1 ms with very safely and only consideration of radiation is a reasonable assumption.

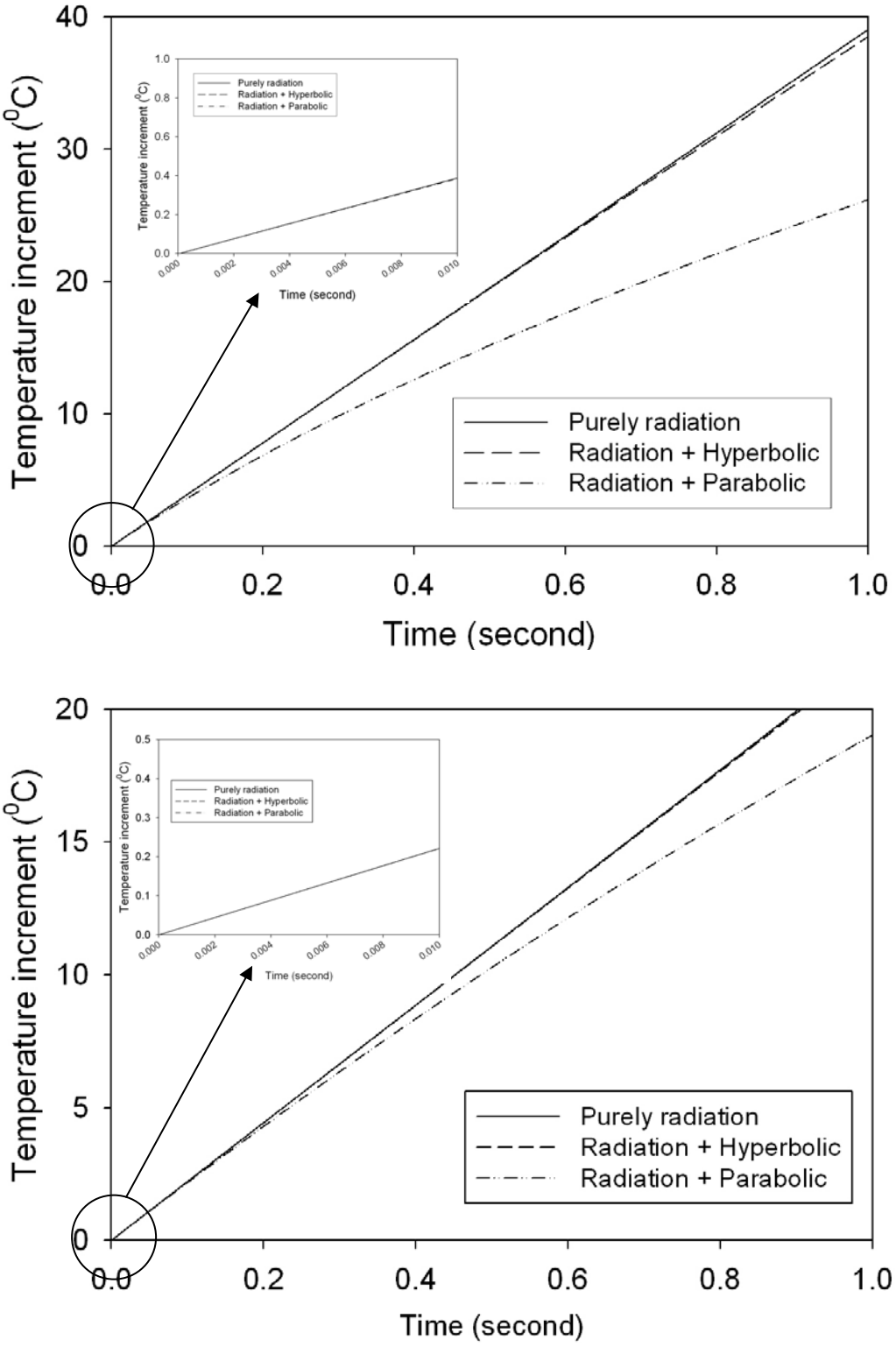

Figure A1 The investigation of conductive heat transfer influence by temporal temperature profiles along the optical axis (a) surface, z = 0 mm and (b) z = 0.05 mm

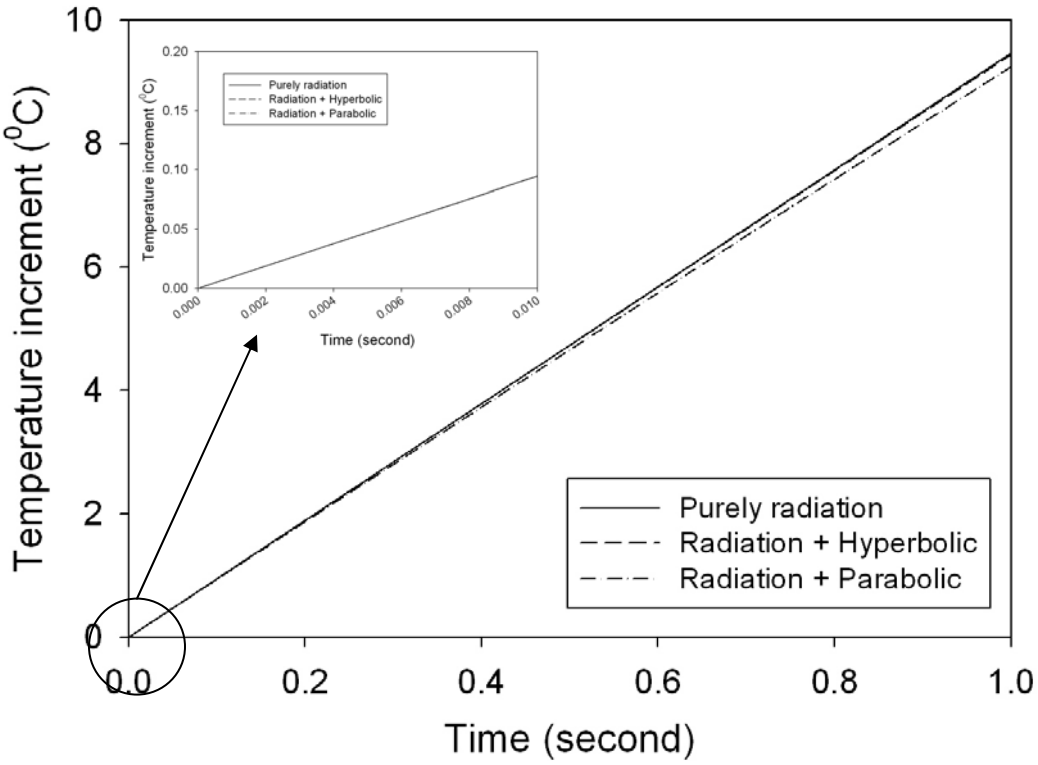

Figure A1 (continued) The investigation of conductive heat transfer influence by temporal temperature profiles along the optical axis (c) z = 1mm.

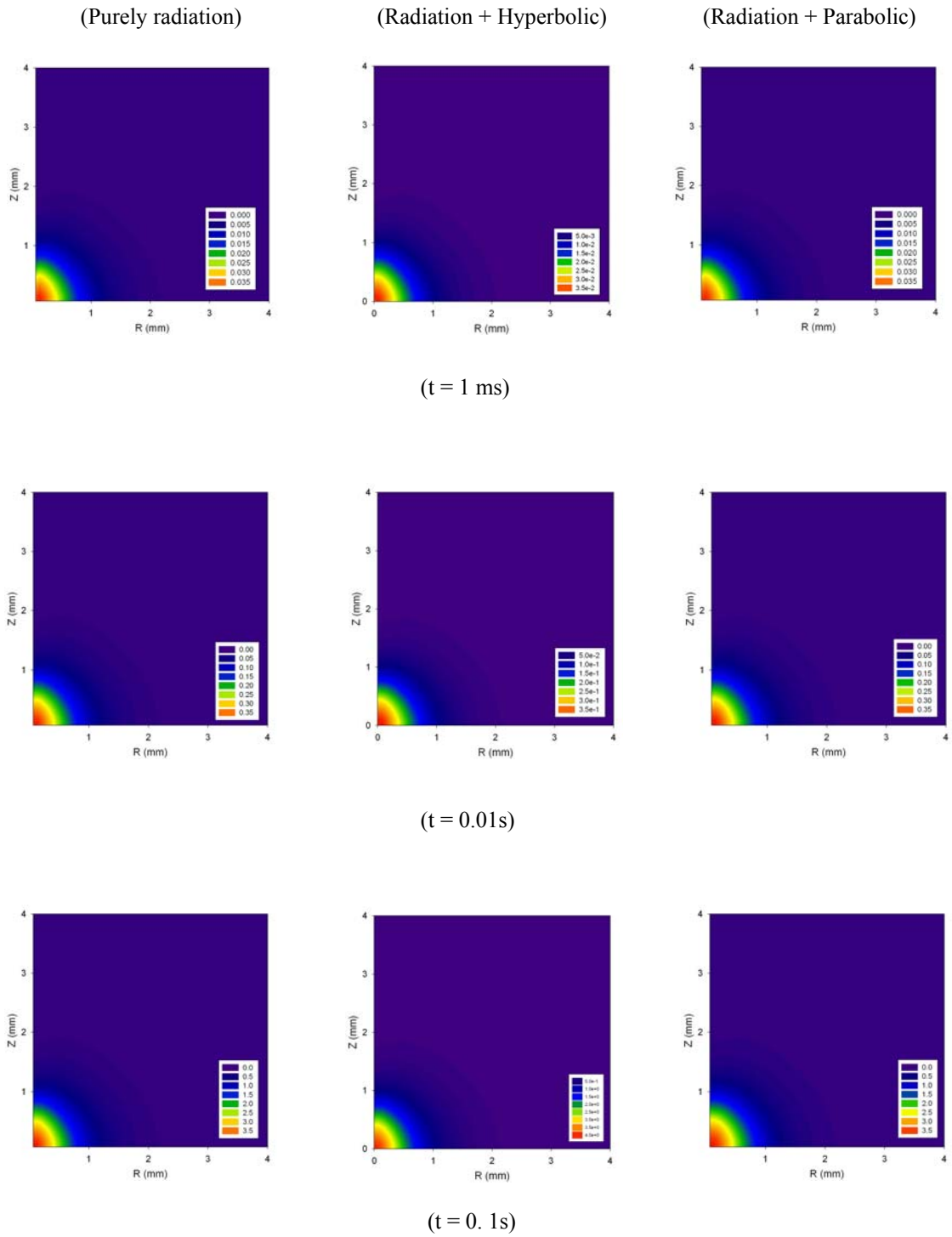

Figure A2 The contour plot to compare several scenarios.

References

[1] R.R. Anderson and J.A. Parrish, 1983, "Selective photothermolysis: precise microsurgery by selective absorption of pulsed radiation," *Science*, **220** pp.524-527.

[2] M.H. Niemz, 1996, "Laser-Tissue Interactions," Chap. 3 (Springer, New York).

[3] L.S. Bass and M.R. Treat, 1995, "Laser tissue welding: a comprehensive review of current and future applications," *Lasers Surg. Med.,* **17** pp.315-349.

[4] R.R. Anderson, 2003, "Dermatological history of the ruby laser: the long story of short pulses," *Arch Dermatol*, **139**, pp.70-74.

[5] A. Igarashi, J. Kato, Y. Takase, and Y. Hirai, 2008, "Influence of Output Energy and Pulse Repetition Rate of the Er:YAG Laser on Dentin Ablation," *Photomedicine and laser surgery*, **26**, pp.189-195.

[6] Y. Yamada, 1995, "Light-tissue interactions and optical imaging in biomedicine," *Annu. Rev. Heat Transfer,* **6**, pp.1-59.

[7] H. Quan and Z. Guo, 2004, "Fast 3-D optical imaging with transient fluorescence signals," *Optics Express,* **12**, pp.449-457.

[8] Z. Guo, S.K. Wan, D.A. August, J. Ying, S.M. Dunn and J.L. Semmlow, 2006, "Optical imaging of breast tumor through temporal log-slope difference mappings," *Comput. Biol. Med.*, **36**, pp.209 -223.

[9] S. Kumar and R. Richards, 2006, "Optical molecular imaging agents for cancer diagnostics and therapeutics," *Nonomedicine*, **1**, pp.23-30.

[10] T. Yuasa et al, 2001, "Transillumination optical sensing for biomedicine and diagnostics: Feasibility of early diagnosis for rheumatoid arthritis," *Analytical science*, **17**, pp.i515-i518.

[11] H. Shangguan, L.W. Casperson, K.W. Gregory, and S.A. Prahl, 1997, "Penetration of fluorescent particles in gelatin during laser thrombolysis,"

[12] F.H. Loesel, F.P. Fisher, H. Suhan, and J. F. Bille, 1998, "Non-thermal ablation of neural tissue with femtosecond laser pulses," *Appl. Phys. B.,* **66**, pp.121-128.

[13] M.H. Niemz, 1998, "Ultrashort laser pulses in dentistry: advantages and limitations," *Proc. SPIE.,* **3255**, pp.84-91.

[14] H. Lubatschowski, A. Heisterkamp, F. Will, A. Singh, J. Serbin, A. Ostendorf, O. Kermani, R. Heermann, H. Welling and W. Ertmer, 2003, "Medical applications for ultrafast laser pulses," *RIKEN Review*, **50**, pp.113-118.

[15] K.H. Kim and Z. Guo, 2004, "Ultrafast radiation heat transfer in laser tissue welding and soldering," *Heat Transfer Part A: Applications*, **46**, pp.23-40.

[16] A. M. Gobin et al., 2005, "Near infrared laser-tissue welding using nonoshells as an exogenous absorber," *Laser surgery and medicine*, **9999**, pp.1-7.

[17] E.V. Ross, G. Naseef, C Lin, and M. Kelly, 1998, "Comparison of response of tattoos to picosecond and nanosecond Q-switched neodymium: YAG lasers," *Arch. Dermatol,* **134**, pp.167-171.

[18] S. Kumar and K. Mitra, 1999, "Microscale aspects of thermal radiation transport and laser applications," *Adv. Heat Transfer*, **33**, pp.87-294.

[19] W.S. Warren, D. Fu, T. Ye, H Liu, and M.C. Fischer, 2007, "Tissue imaging with shaped femtosecond laser pulses," *Ultrafast Phenomena XV*, 807

[20] D Fu et al, 2007, "High resolution in vivo imaging of blood vessels without labeling," *Optics letters*, **32**, pp.2641-2643.

[21] Z. Guo and S. Kumar, 2001, "Radiation element method for transient hyperbolic radiative transfer in plane-parallel inhomogeneous media," *Numerical Heat Transfer Part B,* **39**, pp.371 - 387.

[22] Z. Guo, S. Kumar and K.C. San, 2000, "Multi-dimensional Monte Carlo simulation of short pulse laser radiation transport in scattering media," *J. Thermophysics Heat Transfer*, **14**, pp.504 - 511.

[23] Z. Guo and S. Kumar, 2001, "Discrete-ordinates solution of short-pulsed laser transport in two-dimensional turbid media," *Appl. Opt.,* **40**, pp.3156-3163.

[24] Z. Guo and S. Kumar, 2002, "Three-dimensional discrete ordinates method in transient radiative transfer," *J. Thermophysics Heat Transfer*, **16**, pp.289-296.

[25] Z. Guo and K.H. Kim, 2003, "Ultrafast-laser-radiation transfer in heterogeneous tissues with the discrete-ordinates method," *Appl. Opt.,* **42**, pp.2897-2905.

[26] L.S. Bass, and M.R. Treat, 1995, "Laser tissue welding: A comprehensive review of current and future applications," *Lasers Surg. Med.,* **17**, pp.315-349.

[27] B. Lobel, O.Eyal, N. Kariv, and A. Katzir, 2000, "Temperature controlled CO_2 laser welding of soft tissue: Urinary bladder welding in different animal models (Rats, Rabbits, and Cats)," *Lasers Surg. Med.,* **26**, pp.4-12.

[28] M.C. Pierce, S.D. Jackson, M.R. Dickinson, and T.A. King, 1999, "Laser-Tissue interaction with a high-power 2-μm fiber laser: Preliminary studies with soft tissue," *Lasers Surg. Med.,* **25**, pp.407-413.

[29] B.J.F. Wong, T.E. Milner, B. Anvari, A. Sviridov, A. Omel'chenko, V.V. Bagratashvili, E.N. Sobol, and J.S. Nelson, 1998, "Measurement of radiometric surface temperature and integrated back-scattered light intensity during feedback controlled laser-assisted cartilage reshaping," *Lasers Med. Sci.,* **13**, pp.66-72.

[30] S.H. Diaz, G. Aguilar, E.J. Lavernia, and B.J.F. Wong, 2001, "Modeling the thermal response of porcine cartilage to laser irradiation," *IEEE Journal on Selected Topics in Quantum Electronics,* **7,** pp.944-951.

[31] H. Arkin, L.X. Xu and K.R. Holmes, 1994, "Recent developments in modeling heat transfer in blood perfused tissues," *IEEE Trans Biomed Eng*., **41**, pp.97-107.

[32] H.H. Pennes, 1948, "Analysis of tissue and arterial blood temperatures in resting force arm," *J. Appl. Physiology*, **1**, pp.93-122.

[33] A. Shitzer and R.C. Eberhart, 1985, "Heat transfer in medicine and biology," Plenum Press, New York, **vol. 1 and 2.**

[34] A.J. Welch and M.J.C. van Germert, 1995, "Optical-thermal response of laser-irradiation tissue," Plenum Press, New York, **ch. 11.**

[35] A.J. Welch, E.H. Wissler, and L.A. Priebe, 1980, "Significance of blood flow in calculations of temperature in laser irradiated tissue*," IEEE Trans. Biomed. Eng.,* **BME-27**, pp.164-166.

[36] J.H. Torres, M. Motamedi, J.A. Pearce, and A.J. Welch, 1993, "Experimental evaluation of mathematical models for predicting the thermal response of tissue to laser irradiation," *Appl. Opt.,* **32**, pp.597-606.

[37] D.D. Joseph and L. Preziosi, 1989, "Heat waves," *Rev. Modern Phys.,* **61**, pp. 41-73.

[38] A. Vedavarz, S. Kumar and M.K. Moallemi, 1994, "Significance of non-fourier heat waves in conduction," *J. Heat transfer*, **116**, pp. 221-224.

[39] K. Mitra, S. Kumar, A. Vedavarz and M. Moallemi, 1995, "Experimental evidence of hyperbolic heat conduction in processed meat," *J. Heat Transfer*, 117, pp.568-573.

[40] T.Q. Qiu and C.L. Tien, 1993, "Heat transfer mechanisms during short-pulse laser heating of metals," *J. Heat Transfer*, **115**, pp.835-841.

[41] W. Shen and S. Han, 2002, "Numerical solution of two-dimensional axisymmetric hyperbolic heat conduction," *Computational Mechanics*, **29**, pp.122-128.

[42] A. Banerjee, A.A. Ogale, C. Das, K. Mitra and C. Subramanian, 2005, "Temperature distribution in different materials due to short pulse laser irradiation," *Heat Transfer Eng*., **26**, pp.41-49.

[43] S. Kumar, K. Mitra, and Y.Yamada, 1996, "Hyperbolic damped-wave models for transient light-pulse propagation in scattering media," *Appl. Opt*., **35**, pp.3372-3378.

[44] K. Mitra and S. Kumar, 1999, "Development and comparison of models for light pulse transport through scattering absorbing media," *Appl. Opt*., **38**, pp.188-196.

[45] K. Mitra, M.S. Lai, and S. Kumar, "Transient radiation transport in participating media within a rectangular enclosure," *J. Thermophys.,* **11**. pp.409-414.

[46] Z.M. Tan and P. Hsu, 2001, "An integral formulation of transient radiative transfer," *J. Heat Transfer*, **123**, pp.466-475.

[47] M.C. Gemert and A.J. Welch, 1989, "Time constants in thermal laser medicine," *Lasers in Surgery and Medicine*, **9**, pp.405-421.

[48] G. Shafirstein et al., 2004, "A new mathematical approach to the diffusion approximation theory for selective photothermolysis modeling and its implication in laser treatment of port-wine stains," *Lasers in Surgery and Medicine*, **34**, pp.335-347.

[49] A.J. Welch and C.M. Gardner, 1997, "Monte Carlo model for determination of the role of heat generation in laser-irradiated tissue," *J. Biomech Eng*., **119**, pp.489-495.

[50] Z. Guo, S. K. Wan, K.-H. Kim, and C. Kosaruja, 2003, "Comparing diffusion approximation with radiation transfer analysis for light transport in tissues," *Optical Review*, **10**, pp. 415-421.

[51] Modest, 1993, "Radiative heat transfer," chapter 2, McGraw-Hill.

[52] W.F Cheong, S.A. Prahl, and A.J. Welch, 1990, "A review of the optical properties of biological tissues," *IEEE Journal of Quantum electronics*, **26**, pp.2166-2185.

[53] B.G. Carson and K.D. Lathrop, 1968, "Transport theory-The method of discrete ordinates*," Computing Methods in Reactor Physics*, Gordon & Breach, New York.

[54] G.F. Carey and M. Tsai, 1982, "Hyperbolic heat transfer with reflection," *Numer. Heat Transfer*, **5**, pp.309-327.

[55] W.S. Kim, L.G. Hector Jr. and M.N. Ozisik, 1990, "Hyperbolic heat conduction due to axisymmetric continuous or pulsed surface heat sources," *J. Appl. Phys.,* **8,** pp. 5478-5485.

[56] B. Pulvirenti, and E.R. Schio, 1999, "Non-Fourier heat conduction by axisymmetric thermal waves in an infinite solid medium" *Heat and Mass Transfer*, **35**, pp.1-8.

[57] I.A. Novikov, 1996, "Harmonic thermal waves in materials with thermal memory," *J. Appl. Phys.,* **81**, pp.1067-1072.

[58] C.J. Cho and W.N. Juhng, 2000, "Non-Fourier heat conduction in a slab subjected to periodic surface heating," *J. Korean Physics Society*, **36**, pp.209-214.

[59] M.N. Ozisik and B. Vick, 1984, "Propagation and reflection of thermal waves in finite medium," *Int. J. Heat Mass Transfer*, **27**, pp.1845-1854.

[60] D.W. Tang and N. Araki, "1999, "Wavy, wavelike, diffusive thermal response of finite rigid slabs to high-speed heating of laser-pulses," *Int. J. Heat Mass Transfer*, **42**, pp.855-860.

[61] C.Y. Wu, 1988, "Integral equation solution for hyperbolic heat conduction with surface radiation," *Int. Commun. Heat Mass Transfer*, **15**, pp.365-374.

[62] D.E. Glass, M.N. Ozisik, D.S. McRae, B. Vick, 1985, "On the numerical solution of hyperbolic heat conduction," *Numerical Heat Transfer*, **8**, pp.497-504.

[63] D.E. Glass, M.N. Ozisik, D.S. McRae and B. Vick, 1985, "Hyperbolic heat conduction with surface radiation," *Int. J. Heat Mass Transfer*, **28**, pp.1823-1830.

[64] H.T. Chen and J.Y. Lin, 1993, "Numerical analysis for hyperbolic heat conduction," *Int. J. Heat Mass Transfer*, **36**, pp.2891-2898.

[65] K.K. Tamma and S.B. Railkar, 1989, "Specially tailored transfinite-element formulations for hyperbolic heat conduction involving non-Fourier effects*," Numer. Heat Transfer,* **15**, pp.211-226.

[66] K.K. Tamma and R.R. Namburu, 1991, "Hyperbolic heat conduction problems: Numerical solutions via explicit Lax-Wendroff-based finite element formulations," *AIAA J. Thermophys. Heat Transfer*, **5**, pp. 232-239.

[67] M.L. Cohen, 1977, "Measurement of the thermal properties of human skin," *A Review J. Invest. Dermatol*., **69**, pp.333-338.

[68] H. Herwig and K. Beckert, 2000, "Fourier versus non-Fourier heat conduction in materials with a nonhomogeneous inner structure," *J. Heat Transfer*, **122**, pp.363-365.

[69] M.N Ozisik, 1993, "Heat conduction," Chapter 2, John Wiley & Sons, New York.

[70] A.J Fontana et al., 2001, "Simultaneous thermal conductivity, thermal resistivity, and thermal diffusivity measurement of selected foods and soils," *ASME Meeting, Sacramento, California*, paper number: 01-6101, pp.1-7.

[71] P.J. Antaki, 2005, "New interpretation of non-Fourier heat conduction in processed meat," *J. Heat Transfer*, **127**, pp.189-193.

[72] D.W Tang and N. Araki, 1998, "Wavy, wavelike, diffusive thermal response of finite rigid slabs to high-speed heating of laser-pulses," *Int. J. Heat Mass Transfer*, **42**, pp.855-860.

[73] S.K. Wan and Z. Guo, 2006, "Correlative studies in optical reflectance measurements of cerebral blood oxygenation," *Journal of Quantitative Spectroscopy & Radiative Transfer*, **98**, pp. 189-201.

[74] S.K. Wan, Z. Guo, S. Kumar, J. Aber and B. A. Garetz, 2004, "Noninvasive detection of inhomogeneities in turbid media with time-resolved log-slope analysis," *Journal of Quantitative Spectroscopy & Radiative Transfer*, **84**, pp. 493-500.

[75] A. Banerjee, A.A. Ogale, C. Das, K. Mitra and C. Subramanian, 2005, "Temperature distribution in different materials due to short pulse laser irradiation," *Heat Transfer Eng*., **26**, pp.41-49.

[76] B.J. Waters, R.G. Squires, and N.M. Laurendeau, 1988, "Morphological development and intrinsic reactivity for combustion of two microporous carbon chars," *Combust. Sci. and Tech.*, **62**, pp.187-209.

[77] E. Stoykova, and O. Sabotinov, 2004, "Precise optical dosimetry in low level laser therapy of soft tissues in oral cavity," *Proc. SPIE*., **5449**, pp. 474-480.

[78] Z. Song , Ke Dong, X.H. Hu, and J.Q. Liu,1999, "Monte Carlo simulation of converging laser beams propagation in biological materials," *Appl. Opt*., **38**, pp.2944-2949.

[79] J. Lu, X. Hu, and Ke Dong, 1999, "Modeling of the rough-interface effect on a converging light beam propagation in a skin tissue phantom," *Appl. Opt*., **39**, pp.5890-5897.

[80] L.V. Wang and G. Liang, 1999, "Absorption distribution of an optical beam focused into a turbid medium," *Appl. Opt*., **38**, pp.4951-4958.

[81] J.W. Tunnell, L.V. Wang, and B. Anvari, 2003, "Optimum pulse duration and radiant exposure for vascular laser therapy of dark port-wine skin: a theoretical study," *Appl. Opt*., **42**, pp.1367-1378.

[82] A. Singh and K.P. Gopinathan, 1988, "Confocal microscopy-a powerful technique for biological research," *Curr. Sci*., **74**, pp.841-851.

[83] J.P. Ritz, A. Roggan, C. Isbert, G. Muller, H.J. Buhr, and C.T. Germer, 2001, "Optical properties of native and coagulated porcine liver tissue between 400 and 2400 nm, *Lasers Surg. Med.,* **29**, pp.205-212.

[84] B.J. Tromberg, O. Coquoz, J. Fishkin, T Pham, E.R. Anderson, J. Butler, M. Cahn, J.D. Gross, V. Venugopalan, and D. Pham, 1997, "Non-invasive measurements of breast tissue optical properties using frequency-domain photon migration," *Philos. Trans. R. Soc. Lond. B: Biol. Sci*., **352**, pp.661-668.

Curriculum Vita

Kyunghan Kim

Education

2008 Ph.D in Mechanical and Aerospace Engineering
Rutgers, The State University of New Jersey, New Brunswick, NJ

2003 Master Degree in Mechanical and Aerospace Engineering
Rutgers, The State University of New Jersey, New Brunswick, NJ

2001 Bachelor Degree in Mechanical Engineering and Automation Engineering
Inha University, Incheon, South Korea

Work Experience

2007-2008 Senior Scientist, Princeton Biomeditech

2004-2007 Research Assistant, Mechanical and Aerospace Engineering
Rutgers, The State University of New Jersey, New Brunswick, NJ

2001-2002 Teaching Assistant, Mechanical and Aerospace Engineering
Rutgers, The State University of New Jersey, New Brunswick, NJ

Publication

2008 M. Jaunich, S. Raje, **K.H. Kim**, K. Mitra, and Z. Guo, 2008, "Bio-heat transfer analysis during short pulse laser irradiation of tissues," *Int. J. Heat Mass Transfer*, (in press).

2007 **K.H. Kim** and Z. Guo, 2007, "Multi-time-scale heat transfer modeling of turbid tissues exposed to short-pulsed irradiations", *Computer Methods and Programs in Biomedicine*, vol. 86, pp. 112-123.

2004 **K.H. Kim** and Z. Guo, 2004, "Ultrafast radiation heat transfer in laser tissue welding and soldering," *Numerical Heat Transfer Part A: Applications*, Vol. 46, No. 1, pp. 23-40.

2003 Z. Guo and **K.H. Kim**, 2003, "Ultrafast-laser-radiation transfer in heterogeneous tissues with the discrete-ordinates method," *Applied Optics*, vol. 42, No. 16, pp. 2897-2905.
Z. Guo, S. K. Wan, **K.H. Kim**, and C. Kosaruja, 2003, "Comparing diffusion approximation with radiation transfer analysis for light transport in tissues", *Optical Review*, Vol. 10, No. 5, pp. 415-421.